Orbital to millennial-scale atmosphere-ocean-cryosphere interactions and interhemispheric teleconnections in the Southeast Pacific (IODP Site U1542)

by

Vincent Rigalleau

Supervisor
Dr. Frank Lamy

Referees
Prof. Dr. Ralf Tiedemann
Prof. Dr. Carina Lange

A doctoral thesis submitted in fulfilment of the requirements for the degree of
Doctor Rerum Naturalium (Dr. rer. nat.)

in the

Department of Geosciences
at the University of Bremen

2024

Datum des Kolloquiums: 24.01.2025

Versicherung an Eides Statt / *Affirmation in lieu of an oath*

gem. § 5 Abs. 5 der Promotionsordnung vom 28.04.2021 /
according to § 5 (5) of the Doctoral Degree Rules and Regulations of 28 April, 2021

Ich / I, ____
(Vorname / First *Name*, Name / *Name*, Anschrift / *Address*, ggf. Matr.-Nr. / *student ID no., if applicable)*

versichere an Eides Statt durch meine Unterschrift, dass ich die vorliegende Dissertation selbständig und ohne fremde Hilfe angefertigt und alle Stellen, die ich wörtlich dem Sinne nach aus Veröffentlichungen entnommen habe, als solche kenntlich gemacht habe, mich auch keiner anderen als der angegebenen Literatur oder sonstiger Hilfsmittel bedient habe und die zu Prüfungszwecken beigelegte elektronische Version (PDF) der Dissertation mit der abgegebenen gedruckten Version identisch ist. / *With my signature I affirm in lieu of an oath that I prepared the submitted dissertation independently and without illicit assistance from third parties, that I appropriately referenced any text or content from other sources, that I used only literature and resources listed in the dissertation, and that the electronic (PDF) and printed versions of the dissertation are identical.*

Ich versichere an Eides Statt, dass ich die vorgenannten Angaben nach bestem Wissen und Gewissen gemacht habe und dass die Angaben der Wahrheit entsprechen und ich nichts verschwiegen habe*. / I affirm in lieu of an oath that the information provided herein to the best of my knowledge is true and complete.*

Die Strafbarkeit einer falschen eidesstattlichen Versicherung ist mir bekannt, namentlich die Strafandrohung gemäß § 156 StGB bis zu drei Jahren Freiheitsstrafe oder Geldstrafe bei vorsätzlicher Begehung der Tat bzw. gemäß § 161 Abs. 1 StGB bis zu einem Jahr Freiheitsstrafe oder Geldstrafe bei fahrlässiger Begehung. / *I am aware that a false affidavit is a criminal offence which is punishable by law in accordance with § 156 of the German Criminal Code (StGB) with up to three years imprisonment or a fine in case of intention, or in accordance with § 161 (1) of the German Criminal Code with up to one year imprisonment or a fine in case of negligence.*

______________________________ ______________________________

Ort / *Place*, Datum / *Date* Unterschrift / *Signature*

Abstract

From orbital (10 to 100 thousand years or kyr) to millennial (1 to 10 kyr) timescales, the Southern Ocean is thought to substantially modulate global climate and ocean variability. Most critical factors include the Southern Ocean's impact on surface, intermediate, and deep-water circulation affecting global heat, salt, and nutrient distribution and the processes influencing storage and outgassing of atmospheric CO_2. This PhD thesis is focused on the reconstruction of past climatic variability in the Southeast Pacific spanning the past 800,000 years, based on the analysis of different organic paleoclimatic tracers, in a sedimentary archive from International Ocean Discovery Program (IODP Site U1542, situated on the southern Chilean margin. This work has generated a series of millennial-scale resolution paleoclimatic records of sea surface temperature (SST), bottom current velocity, accumulation of terrestrial organic compounds from leaf waxes and soil bacteria, and ice-rafted debris. Results show that SST covaries with the strength of the Antarctic Circumpolar Current (ACC). The millennial-scale variability appears to be a persistent and inherent feature of the climate over the last eight glacial cycles. The recurrence of millennial-scale events is independent of the glacial state, but the amplitude increases when the glacial state lasts longer. The sediment record at Site U1542 underlines a persistent close link between millennial-scale climatic events from both hemispheres and that the millennial-scale fluctuations of the ACC covary with atmospheric CO_2 release over the past 800,000 years. In a second application of the proxy datasets, the location of Site U1542 near the former Patagonian ice sheet (PIS), enabled the reconstruction of the past variability of the PIS on multiple glacial cycles using terrestrial proxies leaf waxes compounds and ice-rafted debris. The timing of terrestrial sediment deposition aligns notably with the extent of PIS moraines. These data reveal a close connection between sediment export and SST in the Southeast Pacific, suggesting that the PIS extent is controlled by ocean temperature forcing. The third study of this thesis aims to explore the meridional sea surface changes of the Southern Ocean using a biomarker tracer for polar water masses. A compilation of Southern Ocean records highlights a long period of retreated polar water between 410 and 310 kyr, following the Mid-Brunhes Transition. This retreat notably mirrors low atmospheric CO_2 concentrations, emphasizing the role of the Southern Ocean in the global carbon budget. Overall, the records developed from the sedimentary archive Site U1542 provide an unprecedented picture of orbital and millennial-scale Southern Ocean variability over the past 800,000 years, highlighting the close atmosphere-ocean-cryosphere interactions of Earth's climate.

Zusammenfassung

Es wird angenommen, dass der Südliche Ozean das globale Klima und die Variabilität der Ozeane auf orbitalen (10 bis 100 Tausend Jahre oder kyr) bis hin zu millennialen (1 bis 10 kyr) Zeitskalen erheblichbeeinflusst. Die wichtigsten Faktoren sind die Auswirkungen des Südlichen Ozeans auf die Zirkulation von Oberflächen-, Zwischen- und Tiefenwasser, die die globale Verteilung von Wärme, Salz und Nährstoffen beeinflussen, sowie die Prozesse, die die Speicherung und Freisetzung von atmosphärischem CO_2 beeinflussen. Diese Doktorarbeit konzentriert sich auf die Rekonstruktion der klimatischen Variabilität im Südostpazifik in den letzten 800.000 Jahren, basierend auf der Analyse verschiedener organischer paläoklimatischer Tracer aus den Sedimenten eines Kerns des International Ocean Discovery Program (IODP Site U1542), der sich am südlichen Rand Chiles befindet. In dieser Arbeit wurde eine Zeitreihe paläoklimatischer Aufzeichnungen mit millennialer Auflösung von Meeresoberflächentemperaturen (SST), Bodengeschwindigkeiten, Akkumulation terrestrischer organischer Verbindungen von Blattwachsen und Bodenbakterien sowie eisgeschlepptem Schutt erzeugt. Die Ergebnisse zeigen, dass SST mit der Stärke des Antarktischen Zirkumpolarstroms (ACC) korreliert. Die millenniale Variabilität scheint ein dauerhaftes und inhärentes Merkmal des Klimas über die letzten acht Glazialzyklen zu sein. Das Wiederauftreten von Ereignissen im millennialen Maßstab ist unabhängig vom glazialen Zustand, aber die Amplitude nimmt zu, wenn der glaziale Zustand länger andauert. Die analysierten Sedimente an Site U1542 unterstreicht eine anhaltend enge Verbindung zwischen klimatischen Ereignissen im millennialen Maßstab aus beiden Hemisphären und dass die Schwankungen des ACC im millennialen Maßstab mit der Freisetzung von atmosphärischem CO_2 in den letzten 800.000 Jahren korrelieren. In einer zweiten Anwendung der Proxy-Datensätze ermöglichte die Lage von Site U1542 in der Nähe des ehemaligen Patagonischen Eisschilds (PIS) die Rekonstruktion der vergangenen Variabilität des PIS über mehrere glaziale Zyklen mithilfe terrestrischer Proxies, Blattwachskomponenten und eisgeschlepptem Schutt. Der Zeitpunkt der terrestrischen Sedimentablagerung stimmt bemerkenswert gut mit dem Umfang der PIS-Moränen überein. Diese Daten zeigen eine enge Verbindung zwischen Sedimentexport und SST im Südostpazifik und deuten darauf hin, dass das Ausmaß des PIS durch den Ozeantemperaturzwang gesteuert wird. Die dritte Studie dieser Arbeit zielt darauf ab, die meridionalen Veränderungen der Meeresoberfläche des Südlichen Ozeans mithilfe eines Biomarker-Tracers für polare Wassermassen zu untersuchen. Eine Zusammenstellung von Aufzeichnungen des Südlichen

Ozeans zeigt eine lange Periode zurückgezogener polarer Wassermassen zwischen 410 und 310 kyr nach dem Mid-Brunhes-Übergang. Dieser Rückzug spiegelt bemerkenswerterweise niedrige atmosphärische CO_2-Konzentrationen wider und betont die Rolle des Südlichen Ozeans im globalen Kohlenstoffhaushalt. Insgesamt bieten die Aufzeichnungen aus dem sedimentären Archiv Site U1542 ein beispielloses Bild der Variabilität des Südlichen Ozeans auf orbitaler und millennialer Skala in den letzten 800.000 Jahren und heben die engen Wechselwirkungen zwischen Atmosphäre, Ozean und Kryosphäre des Erdklimas hervor.

Abbreviations

- **AABW** = Antarctic Bottom Water;
- **AAIW** = Antarctic Intermediate Water;
- **AASW** = Antarctic Surface Water;
- **ACC** = Antarctic Circumpolar Current;
- **AL** = Agulhas Leakage;
- **AMOC** = Atlantic Meridional Overturning Circulation;
- $\mathbf{C}_{37:4}$ = tetra-unsaturated C_{37} alkenones;
- **CDW** = Circumpolar Deep Water;
- **DBD** = Dry Bulk Density;
- **DP** = Drake Passage;
- **DO events** = Dansgaard-Oeschger events;
- **DSDP** = Deep Sea Drilling Program;
- **G/IG** = Glacial/Interglacial;
- **GDGT** = Glycerol Dialkyls Glycerol Tetraethers;
- **IRD** = Ice-Rafted Debris;
- **ITCZ** = Intertropical Convergence Zone;
- **IODP** = International Ocean Discovery Program;
- **Ka** = 'thousands of years ago' as a unit of age or time before present;
- **Kyr** = 'thousands of years' as a unit of time;
- **LR04** = Lisiecki and Raymo's 2004 benthic oxygen isotope stack;
- **LSR** = Linear Sedimentation Rate;
- **Ma** = 'millions of years ago' as a unit of age or time before present;

- **MAR** = Mass Accumulation Rate;
- **MBE-MBT** = Mid-Brunhes Event/Transition;
- **MIS** = Marine Isotope Stage;
- **MPT** = Mid-Pleistocene Transition;
- **Myr** = 'millions of years' as a unit of time;
- **NADW** = North Atlantic Deep Water;
- **NB** = Northern Boundary;
- **ODP** = Ocean Drilling Program;
- **PDW** = Pacific Deep Water;
- **PF** = Polar Front;
- **PIS** = Patagonian Ice-Sheet;
- **R/V** = Research Vessel;
- **SACCF** = Southern ACC Front;
- **SAF** = Subantarctic Front;
- **SAMW** = Subantarctic Mode Water;
- **SAZ** = Subantarctic Zone;
- **SO** = Southern Ocean;
- **SS** = 'Sortable Silt' fraction of the terrigenous sediment, following *McCave et al.* [1995];
- **SST** = Sea surface temperature;
- **STF** = Subtropical Front;
- **SWW** = Southern Westerly Wind;
- $\mathbf{U}^{k}_{37}$, $\mathbf{U}^{k'}_{37}$ = unsaturated ketones indices;
- **WSI** = Winter Sea Ice;

Preface

Since the first civilizations, the climate has been marked by a series of abrupt events, primarily cooling periods or long-lasting droughts, which are recorded in the Northern Hemisphere climatic records and often coincide with important societal changes in human history. For instance, in Mesopotamia, the collapse of the Akkadian empire may have been induced by a dry spell of several centuries occurring 4.2 thousand years before present (kyr BP), (*Gibbons*, 1993). The decline of the late Bronze Age occurring in the late thirteenth and twelfth centuries B.C. ($\sim$2.2 kyr BP), is closely related to social, political, and economic decisions made by Eastern Mediterranean civilizations which likely originated from changes in precipitation that significantly affected agricultural productivity (*Kaniewski et al.*, 2008; *Weiss*, 1982). The pandemic plague outbreaks affecting Roman Italy during the Late Antique Little Ice Age were amplified by local climate conditions (*Zonneveld et al.*, 2024). Lastly, both the agricultural revolution in Great Britain from the mid-18th century onwards and the succession of bad harvests that stimulated the social crisis at the dawn of the French Revolution at the end of the same century were probably triggered by the Little Ice Age (*Fagan*, 2019; *Le Roy Ladurie*, 2011). Although, by this time, anthropogenic activity such as agriculture and conquests was already affecting the climate (*Ruddiman*, 2017), these millennial-scale climatic events, whether anthropogenically enhanced or not, were triggered by reduced solar activity and volcanic eruptions. For instance, Gerard Bond found in Northern Hemisphere deep-sea cores that these millennial-scale climate events fluctuated in association with variations in solar output through the Holocene, with potential feedback from ocean circulation (*Bond et al.*, 2001). *Hodell et al.* [2001] linked century-scale variability in Yucatan droughts and solar forcing. They argued that some of the maxima in the 208-year drought cycle corresponded with discontinuities in Maya cultural evolution, suggesting that the Maya were affected by these bicentennial oscillations in precipitation and that they ultimately precipitated their downfall. Given the impacts of natural abrupt climatic events on human activity and civilizations over the past several millennia, it is worth considering that modern-day civilization could be comparably affected. Moreover, modern anthropogenic impacts on climate cannot be quantified and addressed without first distinguishing them from natural events. From this perspective, it appears crucial to better understand the origin of natural millennial-scale climate variability to comprehend the influence of climate on modern civilization.

Contents

Chapter 1

Introduction

In the last million years of Earth's history, evidence in the geological record indicates a cyclical pattern of massive glaciations interspersed by warmer periods (*Emiliani*, 1955). The alternation between glacial stages (*Agassiz et al.*, 1840) and brief warm periods (interglacials) define the Quaternary glaciations. The last glacial period (71-11.7 thousand years or kyr), was marked by pronounced (amplitudes between 9 and 13°C; *Kindler et al.*, 2014) and rapid alternations between cold (stadial) and warm (interstadial) climate conditions (*Dansgaard et al.*, 1993). Historically described in Greenland ice cores for the last glacial period, these millennial-scale fluctuations, called Dansgaard-Oeschger (D-O) events, were later identified in North-Atlantic sediment cores (*Bond et al.*, 1993). More recently, D-O-type variability has been found at low latitudes from monsoonal regions such as the Brazilian margin (*Arz et al.*, 1998) and in the Asian-monsoon speleothems records (*Cheng et al.*, 2016), as well as in the Southern Ocean (*Euler and Ninnemann*, 2010; *Kanfoush et al.*, 2000) and northwest of the Drake Passage (DP) (*Lamy et al.*, 2015).

Despite extensive documentation in terrestrial, marine, and ice records, D-O events continue to pose a challenge in terms of identifying a coherent triggering mechanism (*Li and Born*, 2019; *Petersen et al.*, 2013; *Zhang et al.*, 2014). Early in the study of millennial-scale variability, Gerard Bond found in Northern Hemisphere deep-sea cores that these millennial-scale climate events fluctuated in association with the variations in solar output throughout the Holocene (*Bond et al.*, 1997, 2001). He further identified a 1470 $\pm$ 500-year cyclicity in the occurrence of these events, although this latter point is debatable (*e.g.*, *Obrochta et al.*, 2012; *Schulz et al.*, 1999). There is no consensus on solar output as a unique forcing (*Paul and Schulz*, 2002), and Bond and co-authors further suggested potential feedback from ocean circulation. The state-of-the-art explanation involves the weakening/collapse of Atlantic Meridional Overturning Circulation (*Clark* *et al.*, 2002), likely triggered by freshwater input (*e.g.*, *Ganopolski and Rahmstorf*, 2001; *Rahmstorf*, 2002; *Zhang et al.*, 2014). In addition to freshwater input, the Southern Ocean is thought to play a major role in AMOC stability (*Marshall and Speer*, 2012), and consequently, D-O events (*Oka et al.*, 2021). For instance, changes in the meridional overturning circulation are controlled by two inter-basin gateways; the Agulhas leakage (also called the warm-water route) and the Drake Passage (DP) throughflow (the cold-water route) (*Knorr and Lohmann*, 2003). The former connects the Indian Ocean to the Atlantic Ocean and shows significant variability (*Bard and Rickaby*, 2009; *Beal et al.*, 2011). The latter connects the Pacific and the Atlantic Ocean and shows significant millennial-scale correlation with Northern Hemisphere D-O events (*Wu et al.*, 2021). These authors show an acceleration of the DP throughflow during the Antarctic Isotope Maximum (AIM), the Southern Hemisphere counterpart of D-O events (*Blunier et al.*, 1998; *EPICA Community Members*, 2006).

Beyond the last glacial cycle and the reach of Greenland ice cores, sediment records covering several glacial cycles documenting millennial-scale climatic changes are rare, particularly in the Southern Hemisphere. For instance, a review by *Lang and Wolff* [2011] compiles 37 ice, marine, and terrestrial paleoclimate high-resolution records covering the last 800 kyr, yet includes only three records south of 5°S. These include two sediment records (Site 1123 and Site 1090) and the well-known ice core drilled at EPICA Dome C (EDC). More recent studies can be added to this global review, such as the Dongge Cave speleothem record (*Cheng et al.*, 2016) and the very recent sedimentary archive Site U1385 (*Hodell et al.*, 2023), both located in the Northern Hemisphere. In the Southern Hemisphere, sediment cores such as the composite records GeoB3375-1-GeoB15016 (*Lamy et al.*, 2019), Site U1476 (*Nuber et al.*, 2023), or an accumulation rate record of the planktic foraminiferal species *Globorotalia menardii* from the Agulhas leakage (*Caley et al.*, 2012) exist but lack millennial-scale resolution. Antarctic ice core records are good candidates for monitoring millennial-scale variability in older glacial stages. However, the continental isolation and low accumulation rates limit the ability of Antarctic records to fully capture abrupt global climatic events (*Jouzel et al.*, 2007). Moreover, an important drawback arises in the deeper parts of the ice cores where the resolution decreases due to compaction of the ice (*Barker et al.*, 2011; *Jouzel et al.*, 2007), leaving the Southern Hemisphere devoid of a millennial-scale resolving record covering multiple glacial cycles. Consequently, our understanding of millennial-scale climatic events in the Southern Hemisphere remains limited.

To address this problem, a millennial-scale resolving record covering multiple glacial cycles is necessary to understand the Southern Ocean's role and response to the D-O events. On July 5th and 6th 2019, the drilling vessel JOIDES *Resolution* successfully recovered a 250-meter sedimentary sequence on the Chilean margin during the International Ocean Discovery Program (IODP) Expedition 383 (*Lamy et al.*, 2021). Situated in a strategic position, the drilling site subsequently designated as Site U1542, represents a climatic record of the northernmost part of the Antarctic Circumpolar Current (ACC) reaching the Drake Passage (see section 3.2 for further details). This presents an opportunity to investigate the role of the Antarctic Circumpolar Current (ACC), and particularly the DP throughflow, in millennial-scale climatic events. Thus, a first question can be formulated:

Research Question 1: How does the Antarctic Circumpolar Current and particularly the Drake Passage throughflow condition meridional overturning circulation, a key feature of global millennial-scale climates events across multiple glacial cycles?

Chapter 5 addresses the aforementioned questions using two different proxies[1] : the grain-size parameters to infer paleo-flow speeds of near-bottom currents and the alkenones unsaturation index, a biomarker-derived sea surface temperature proxy (see Chapter 4 for further details). These new records are compared on an orbital and millennial-scale with North Atlantic records to better understand the interhemispheric teleconnections induced by the global overturning circulation, as well as the atmospheric CO_2 record to assess the role of the ACC in atmospheric-ocean exchanges.

On these time scales, mid-latitude ice sheets play a dynamic role by amplifying, pacing, and driving local to global climate changes, notably by processes such as sea level rise and decline, albedo effect, and sediment production (*Clark et al.*, 1999). For instance, the Patagonian ice sheet (PIS), the largest mid-latitude ice sheet, significantly impacts global climate by exporting soluble iron (Fe) to the Fe-deficient Southern Ocean which stimulates net primary production and carbon sequestration, thereby contributing to up to 40 ppm atmospheric CO_2 drawdown during ice ages (*Brovkin et al.*, 2007). Understanding the forces that drive and shape the Patagonian ice sheet is thus crucial to better comprehend atmosphere-ocean-cryosphere interactions. Previously, the geographic maximum extent of the ice sheet was mainly determined through continental ice-derived sedimentary sequences on land, dated by radionuclides. Unfortunately, older glaciations are often eroded by the more recent glacial advance, resulting in an incomplete picture. Based on the sedimentary record Site U1542, the second part of this thesis aims to produce the first detailed, continuous history of the Patagonian ice sheet at orbital and sub-orbital times scales over the last million years, with a focus on the second question of this thesis:

[1]Paleoclimate proxies are indirect data from materials preserved in the various environmental records (marine sediment in our case) that are associated with different climate variables and can be analysed to provide information on past climates.

Research Question 2: What forces drive the Patagonian ice sheet across glacial/interglacial timescales and how has its evolution impacted Earth's global climate?

Chapter 6 aims to reconstruct the history of the Patagonian Ice Sheet over the past 790 kyr using ice-rafted debris and terrigenous accumulation rates, as well as terrestrial biomarkers. Biomarkers are molecular proxies with numerous applications in paleoclimatology (see Chapter 4 for further details). 3 different groups of well-establish biomarkers are used: the alkenones unsaturation index as a proxy for sea surface temperature in Chapter 5, while Chapter 6 focuses on the *n*-alkanes from terrestrial plants together with the ubiquitous Glycerol Diakyls Glycerol Tetraethers (GDGT) to reconstruct continental changes. All these biomarkers are derived in this work from a single sample extract, providing a wealth of information from various indices.

Due to the diversity of the molecules, the field of biomarker research is versatile and continually evolving, offering new answers to complex challenges as highlighted by Timothy and Geoffrey Eglinton "*The utility and applications of biomarkers may only be limited by our imagination*" (*Eglinton and Eglinton*, 2008). Among biomarker indices, the tetra-unsaturated alkenone was historically avoided due to uncertainty regarding its source (*Rosell-Melé et al.*, 2002). Often associated with annual mean sea ice concentrations(*e.g.*, IP_{25}; *Wang et al.*, 2021), polar diatom and dinocysts (*Horikawa et al.*, 2015), and ice-rafted debris (*Bard et al.*, 2000), the tetra-unsaturated alkenone appears to be a tracer for high latitude surface polar water (*Martínez-Garcia et al.*, 2010; *McClymont et al.*, 2008), hence relevant for the broader aim of this thesis consisting in understanding the role of Southern Ocean in orbital to millennial climate variability. Chapter 7 aims to precisely focus on the tetra-unsaturated alkenone and shed light on the third question of this thesis;

Research Question 3: Which paleoenvironmental conditions control the tetra-unsaturated alkenone ratio and how has this ratio varied across the previous eight glacial cycles in the Southern Ocean?

Chapter 7 explores the significance of the tetra-unsaturated alkenone signal by comparing it with commonly associated proxies from various Southern Ocean records. In the second part, a stack of Southern Ocean tetra-unsaturated alkenone data is developed to provide a broader context of climatic variability such as atmospheric CO_2 concentrations.

The remainder of the thesis is structured as follows; a brief overview of the spatial and temporal context will be given in Chapter 2, beginning with the last 800 kyr of Earth's history, continuing with the past and present Southern Ocean specifically, and finally focusing on the Southeast Pacific. Chapter 3 aims to describe the sedimentary archive

Site U1542, the principal material of this work. Chapter 4 introduces the biomarkers and describes the methods used to extract them from the sediment archive Site U1542. Following this, Chapter 5, Chapter 6, and Chapter 7 aim to address the three aforementioned questions respectively. These chapters are manuscripts in review or will be submitted to academic journals and can thus be read independently from each other, which explains the slight repetition between chapters. Lastly, this thesis will conclude with a discussion of the findings and their implications in Chapter 8.

Chapter 2

Earth's system and paleoclimate background

2.1 A brief overview of climate over the past one million years

Cesare Emiliani published in 1955 a revolutionary study, considered as pioneering in the field of Palaeoceanography, which established a relationship between stable isotopes in sediment cores and environmental variables (*Emiliani*, 1955). Emiliani investigated oxygen isotope ratios ($^{18}O/^{16}O$, $\delta^{18}O$) in foraminifera shells, which reflect the temperature at which these foraminifera grew. By analysing these foraminifera shells all along a one-million-year sediment record, he realised that ice ages are part of long-term cyclic climate change. This strongly supported Milankovitch's visionary work, which suggested that variations in Earth's orbits, induce variations in high northern latitudes insolation, driving the waxing and waning of Northern Hemisphere ice sheets (*Milankovitch*, 1941). This theory was revisited by *Hays et al.* [1976] who confirmed the periodic nature of Quaternary ice ages through statistical analysis of $\delta^{18}O$ records measured in marine sediment cores. Their findings matched the changes in Earth's orbit and axis, hence confirming Milankovitch's theory and establishing orbital changes as a "pacemaker" of climate variability.

Orbital control of global climate

The variations in Earth's orbits are led by three astronomical parameters known as eccentricity, obliquity, and precession responsible for variations in insolation (Fig. 2.1) (*Laskar et al.*, 2004). The eccentricity is related to the shape of Earth's orbits varying around the sun between nearly circular to elliptic due to gravitational forces between the nearest planets (Jupiter, Mars, and Venus) and the Earth. In a more elliptic orbit (*i.e.*, high eccentricity), the Earth receives more unequal solar radiation during a year, leading to hotter but shorter summers. In turn, a circular orbit (*i.e.*, low eccentricity) will create longer, but cooler summers (*Berger et al.*, 1992). The eccentricity cycles present periodicities of 100 kyr, 413 kyr, and roughly 2 Myr (*Laskar et al.*, 2004). The obliquity involves changes in the tilt of the earth's axis. The tilt's angle varies between 22.4° and 24.5° on a regular 41-kyr cycle. This parameter controls mainly the seasonality, where a strong tilt leads to higher insolation in summer and lower insolation in winter, whereas a weak tilt causes less variability between summer and winter, of a particular influence in high latitudes (*Laskar et al.*, 2004). The last parameter, precession, impedes the rotational axis to describe a circular motion, or "wobble", and is particularly influencing the insolation at lower latitudes since the "wobble" motion is largest around the equator. A precessional cycle is completed at either 19 kyr or 23 kyr.

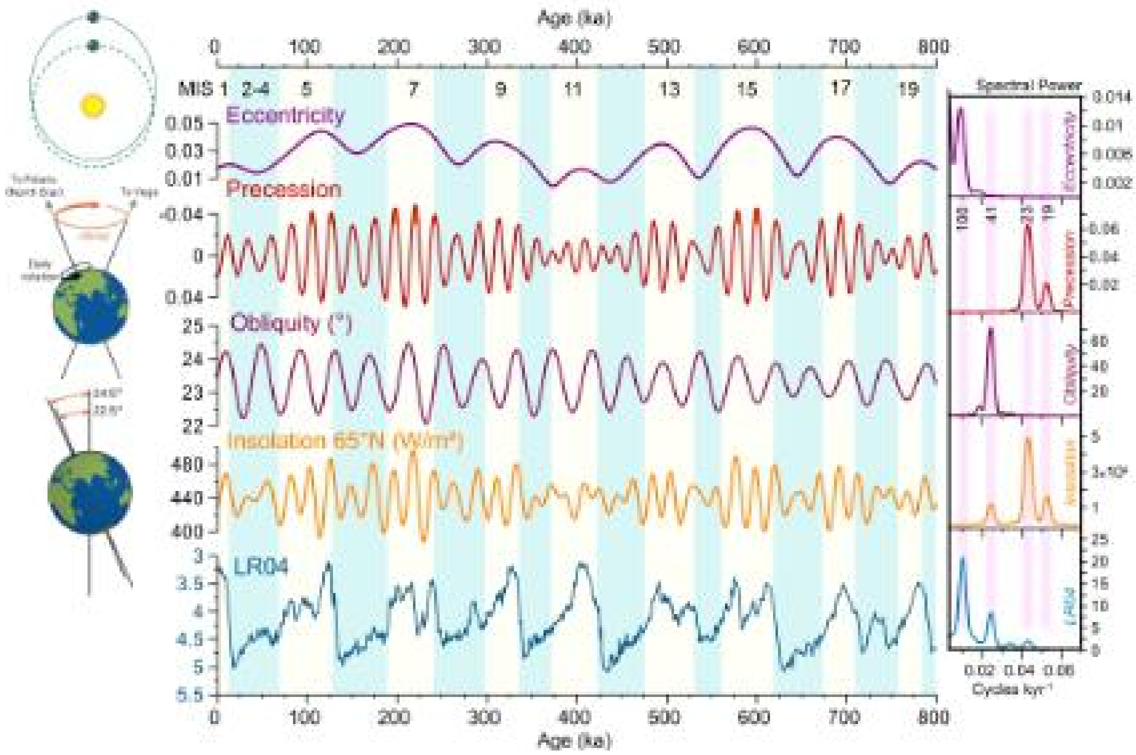

Figure 2.1: **Eccentricity, precession, and obliquity** are the 3 main orbital parameters controlling changes in insolation (*Laskar et al.*, 2004 LR04 stack from *Lisiecki and Raymo* [2005] shows the glacial cycles characteristic of the Quaternary period. On the right are spectral analyses of each component. Insolation at 65°N is often plotted as it strongly correlates with global climate. North Hemisphere ice sheets have a strong influence on global climate.

However, the compilation of benthic marine $\delta^{18}O$ records, providing perhaps the clearest overview of Quaternary climate (*Lisiecki and Raymo*, 2005), suggests that climate fluctuations since 800 kyr alternates between glacial and interglacial states are rather asymmetric, with a gradual build-up followed by rapid abrupt termination of ice ages as shown in figure 2.1.

The glacial cycles are paced with a ~100-kyr cycle, sharing common spectral power with eccentricity even though its involvement in insolation changes is rather weak (*Berger and Loutre*, 1991). This unknown mechanism linking glacial cycles to eccentricity corresponds to the well-known feature of the "100-kyr problem" (*Hays et al.*, 1976). Several theories, using independent dating methods to circumvent circular reasoning, suggest that the 100-kyr cycle regulating the Quaternary ice ages since the Mid-Pleistocene Transition[1] is rather a combination of multiple obliquity cycles (*Huybers and Wunsch*, 2005; *Imbrie and Imbrie*, 1980), together with the additional influence of precession pacing the glacial-interglacial transitions (*Cheng et al.*, 2016).

The role of CO_2

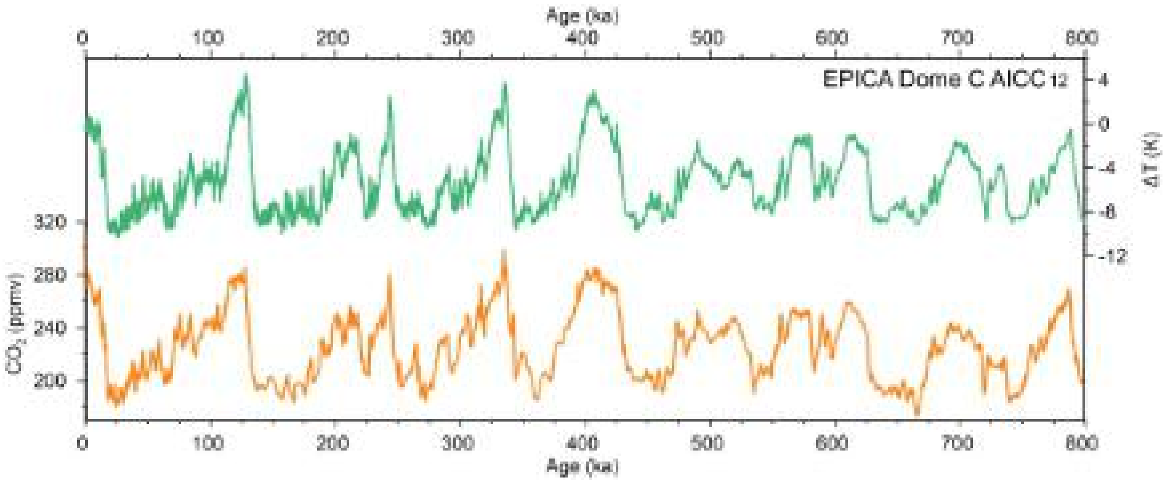

Figure 2.2: **Changes in atmospheric temperatures (green) and atmospheric CO_2 concentration** (orange) from EPICA Dome C Antarctic ice cores (*Jouzel et al.*, 2007; *Lüthi et al.*, 2008.

Yet, if internal feedbacks, such as the ocean circulation (*Toggweiler*, 2008), or ice-albedo (*Hays et al.*, 1976) are thought to play a role, the importance of atmospheric CO_2 concentrations in triggering, amplifying, and modulating changes in glacial-interglacial climate during the Pleistocene is commonly accepted as demonstrated by the close co-

[1] The Mid Pleistocene Transition relates the gradual changes of glacial cycles from a 41 kyr cycle into a 100 kyr cycle, starting 1.2 Ma and ending 800 ka, hence earlier than the scope of this thesis.

variation between air temperature and the partial pressure of CO_2 in the atmosphere (pCO_2) measured in Antarctica ice-cores (Fig. 2.2).

For instance, the transition from MIS 12 to MIS 11 in the middle of the Brunhes Chronozone shows a global climate shift toward warmer interglacials (*Jouzel et al.*, 2007), with higher concentrations of pCO_2 (*Lüthi et al.*, 2008), resulting in increased amplitude of G/IG variability (*Jansen et al.*, 1986). The origin of this "Mid-Brunhes" Event or Transition (MBE - MBT) is thought to be linked to changes in the Southern Ocean ventilation and deep-ocean temperature (*Yin*, 2013) and is discussed in more detail in Chapter 7.

Millennial timescales

The close relation between global climate and pCO_2 prevail on millennial timescales (between 10^3 and 10^4 years) (*Ahn and Brook*, 2008). Millennial-scale variability is characterized by rapid Dansgaard-Oeschger (D-O) events in the Northern Hemisphere, and Antarctic Isotope Maximum (AIM) in the Southern Hemisphere, presenting more gradual millennial changes with smaller amplitudes (*Blunier et al.*, 1998; *EPICA Community Members*, 2006). The interhemispheric comparison presented in figure 2.2 shows an antiphase of Greenland (D-O Events) and Antarctic (AIM) $\delta^{18}O$ changes (primarily representing high latitude atmospheric temperatures) during the last glacial period. The bipolar seesaw concept explains the observed antiphase in interhemispheric temperature variations at millennial time scales by sudden changes in the thermohaline circulation, distributing heat in the polar regions. During Heinrich Event, the Atlantic Overturning Circulation (AMOC) turns down via enhanced freshwater influx (during Heinrich Events) to the North Atlantic. This leads to a cooling in the Northern Hemisphere warming in the Southern Hemisphere, explaining the asynchronicity (*Knutti et al.*, 2004). Once the AMOC turns on again, the poleward heat transfer resumes, and the Northern Hemisphere warms while the Southern Hemisphere cools down.

To sum up, the Earth's climate over the past one million years presents a long-term glacial/interglacial variability superimposed by millennial-scale variability. While the long-term pattern is paced by changes in orbital parameters, the millennial-scale forcings are more complex, though it is generally assumed that the global ocean circulation plays a major control. In the following section, I give a brief overview of the global oceanic circulation, with special attention on the Southern Ocean.

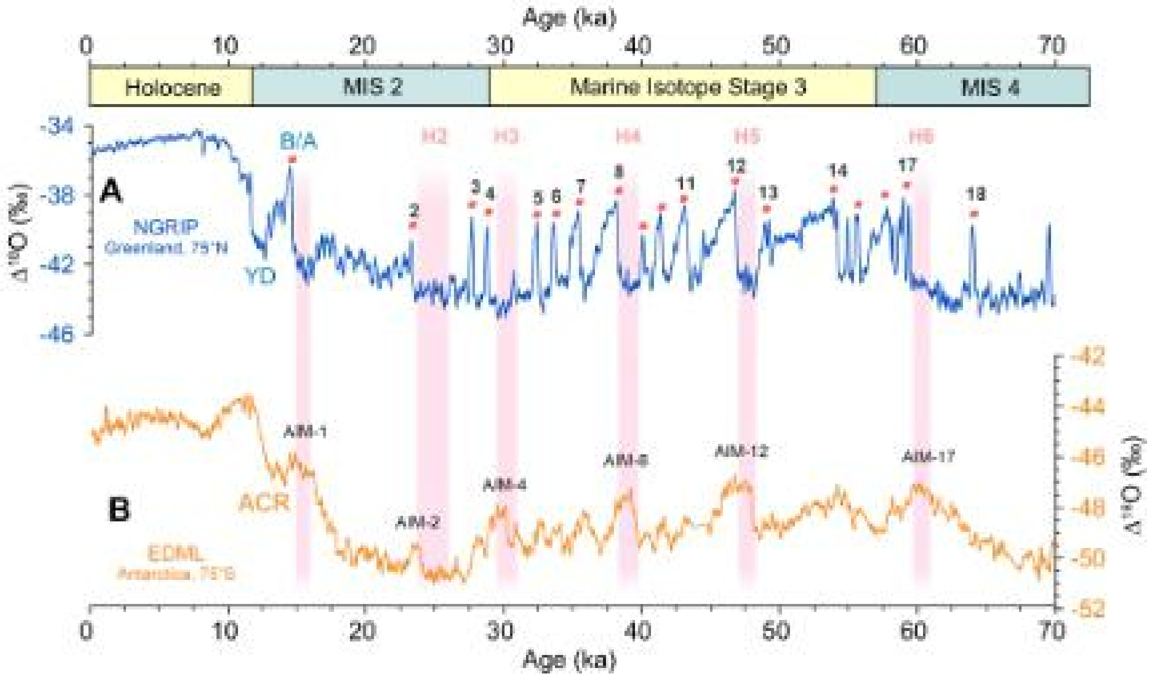

Figure 2.3: **interhemispheric timing of millennial-scale climate events over the past 70 kyr.** Greenland temperature proxy, $\delta^{18}O_{ice}$ in blue and Antarctica temperature proxy, δ^{18}Oice in orange. Red numbers denote DO events. AIM = Antarctic Isotope Maxima, YD = Younger Dryas, B/A = Bølling–Allerød, ACR = Antarctic Cold Reversal.

2.2 Modern Earth's system configuration

Above, we have introduced the influence of the global thermohaline circulation, transporting heat from low to high latitudes, and redistributing salt, nutrients, and carbon. In a simple way, the dynamic water flow consists of upwelling in some places whereby cold saltier water sinks in others (*Talley*, 2013). Perhaps the most important, at least the one that received the most attention, is the AMOC or "great ocean conveyor" (*Broecker*, 1991), with the formation of North Atlantic Deep-Water (NADW) that further returning via upwelling in the Indian and the Pacific Oceans (*Talley*, 2013). The dynamics of this cell appear to have been very active in the geological past, especially in the context of abrupt climate change, for both past (*Knutti et al.*, 2004) and immediate future (*Srokosz and Bryden*, 2015). Notably, the Antarctic Intermediate Water (AAIW) extent appears to have implications for the NADW formation (*Pahnke and Zahn*, 2005). The second cell is associated with the formation of Antarctic Bottom Water (AABW) in the Antarctic zone of the Southern Ocean, today mainly in the Ross Sea and the Weddell Sea (Fig. 2.4). Both the NADW and AABW are of great importance in the export of carbon into the deep ocean, these two overturning cells are largely influenced by the Southern Ocean (*e.g.Marshall and Speer*, 2012).

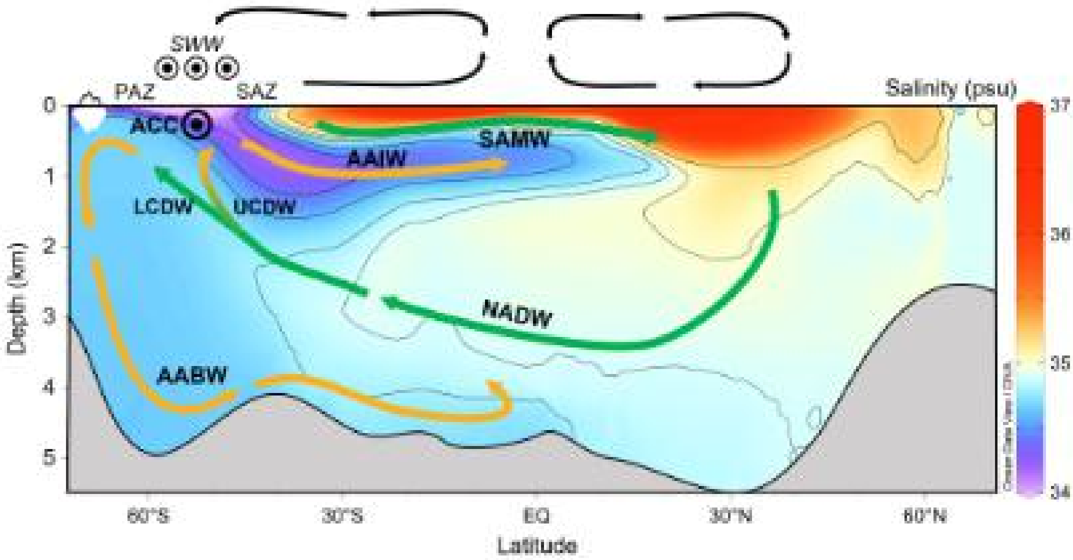

Figure 2.4: **Meridional overturning schematic for the Atlantic Ocean following *Talley* [2013].** The green arrows represent the North Atlantic Deep Water (NADW) cell feeding into the Lower Circumpolar Deep Water (LCDW) in the Polar Antarctic Zone (PAZ). The orange arrows represent the Antarctic Bottom Water (AABW) cell, feeding into the Upper Circumpolar Deep Water (UCDW). Upwelling occurs in the Southern Ocean in response to the Ekman Divergence across the Antarctic Circumpolar Current (ACC). Subantarctic Mode Water (SAMW) and Antarctic Intermediate Water (AAIW) are subdued in the Subantarctic Zone (SAZ).

Southern Ocean

The Southern Ocean is broadly considered as the ocean surrounding the Antarctic Continent. Figure 2.5 highlights the centrality of the Southern Ocean in the global ocean circulation (*Meredith*, 2019). Uninterrupted by landmasses, the Southern Ocean's unique geometry links the ocean circulation of the Pacific, Atlantic, and Indian Oceans, and as discussed above, mixing and spreading water masses into the major basins.

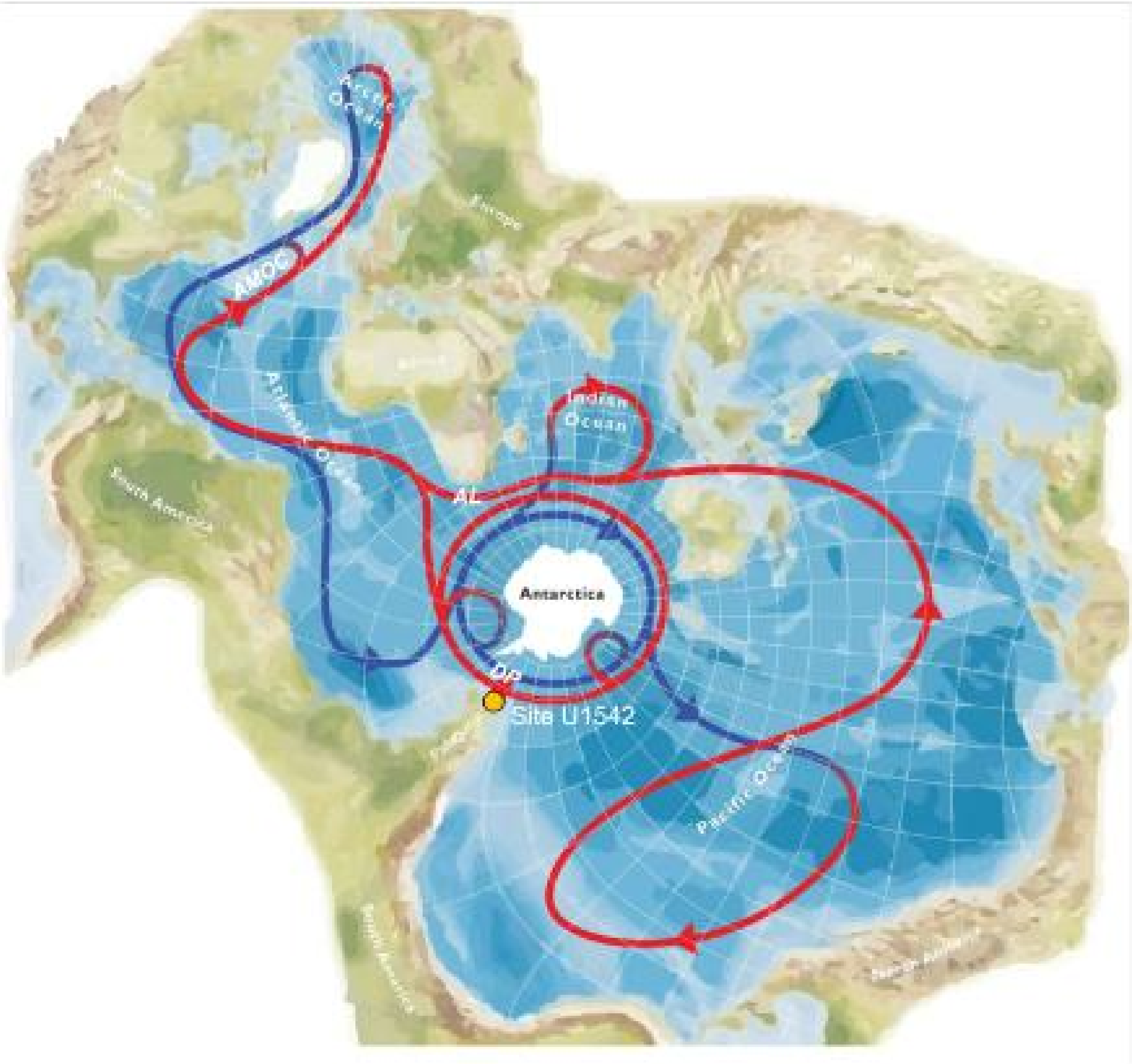

Figure 2.5: **Spilhaus's projection of the Global Ocean circulation, modified from *Meredith* [2019].** AMOC = Atlantic Meridional Overturning Circulation, AL = Agulhas Leakage, DP = Drake Passage.

The Southern Ocean's major feature is the ACC, the world's largest current system, flowing eastward and transporting more than 100 million cubic meters of water per second (*Meredith*, 2019; *Rintoul*, 2018). Predominantly driven by the Southern Westerly Winds (SWW) - a constant eastbound wind - the ACC is also significantly influenced by buoyancy forces from heat and freshwater inputs affecting its density structure (*Rintoul*, 2018). Reaching abyssal depths, the ACC connects deep, intermediate, and shallow ocean circulations (*Talley*, 2013). The oceanic fronts associated with the ACC also influence the formation of intermediate water masses and deep-water upwelling (*Chapman et al.*, 2020; *Orsi et al.*, 1995; *Rintoul*, 2018).

The Subantarctic Southern Ocean serves as a bridge between Antarctica and lower latitudes, with atmosphere-ocean interactions. The Southern Ocean's overturning circulation exchanges carbon dioxide, biological nutrients, and other properties between the deep ocean and the surface layer, significantly impacting climate and biogeochemical cycles.

The glacial Southern Ocean is thought to exert a predominant influence on the global carbon cycle through changes in ocean biogeochemistry and circulation. For instance, the ocean's biological carbon pump, involving the production of organic carbon by phytoplankton in the surface ocean and its sinking, sequesters CO_2 in the deep ocean, thereby lowering atmospheric CO_2 levels (*Ai et al.*, 2020). However, phytoplankton growth is currently limited by iron and/or light in the Southern Ocean. Consequently, the nutrients and CO_2 brought to the surface by upwelling from the deeper ocean are not fully consumed, resulting in CO_2 outgassing from the ocean to the atmosphere, or simply a "leak" in the Southern Ocean's biological pump (*Ai et al.*, 2020). During the glacial period, this Southern Ocean leak may have been stemmed by several mechanisms, such as an increased stratification (*Sigman et al.*, 2021) or the iron fertilization hypothesis (*Martin*, 1990). An increased export of dust during glacial periods (*Lamy et al.*, 2014; *Martínez-Garcia et al.*, 2011; *Weis et al.*, 2024) would have stimulated the net primary production and carbon sequestration by supplying soluble iron (Fe) to the Fe-deficient Southern Ocean, contributing to a more-complete consumption of upwelled carbon and nutrients during ice ages.

Southeast Pacific, a unique setting of the Patagonian ice sheet and the Drake Passage

Southern South America is a major dust source in the Southern Hemisphere, exporting dust to the Southern South Atlantic (*Martinez-Garcia et al.*, 2014), Antarctica (*Basile et al.*, 1997; *Grousset et al.*, 1992; *Lunt and Valdes*, 2001; *Sugden et al.*, 2009) and the Central South Pacific (*Struve et al.*, 2020). As the only landmass intersecting the core of the westerlies belt at latitudes between 49 and 53°S, Patagonia monitors the dynamics of the SWW (*e.g.*, *Lamy et al.*, 2010). A more complete overview of Patagonia's climate is provided in the introduction of Chapter 6. The southern tip of America is also the major barrier of the ACC, and together with the Antarctic Peninsula, the Drake Passage acts as a "bottleneck" for the ACC. At the southern Chilean margin, the coastal Cap Horn Current marks the northern limit of the ACC that crosses the Drake Passage throughflow (see section 3.2 for further details). Moreover, increased terrigenous sediment input from the Andean hinterland makes this region ideal for high-resolution sedimentary archives. A review of paleoclimate records from the Holocene and the last glacial period in southern Patagonia is provided by *Kilian and Lamy* [2012]. Among remarkable sedimentary records of the last glacial period, we can include the northern Ocean Drilling Project Site 1233 (*Kaiser et al.*, 2005; *Lamy et al.*, 2004), the central coring site MR16-09 PC03 (*Hagemann et al.*, 2024) and the southern location MD07-3128 (*Caniupán et al.*, 2011; *Lamy et al.*, 2015). Further offshore in the southern southeast Pacific, stratigraphically longer but lower temporal resolution deep-sea sediment records include GeoB3327-5 and PS75/034-2 (*Ho et al.*, 2012; *Tapia et al.*, 2021). Until the 2016 Polarstern Expedition PS97, the Drake Passage lacked significant sediment records. This expedition yielded high-resolution records such as PS97/085-3 covering the last glacial-interglacial cycle (*Wu et al.*, 2021) and longer Pleistocene records such as the 1.3 Myr proxy records from core PS97/093-2 (*Toyos et al.*, 2020). These records highlight a common challenge in geological archives: high-resolution records typically cover limited periods, while those extending further back often lack high resolution. This limitation can only be overcome by IODP drilling at continental sites. The present thesis therefore focuses on Site 1541 at the southern Chilean margin allowing resolution of millennial-scale subantarctic Southern Ocean and PIS changes across the past 800,000 years.

Chapter 3

Material, the sedimentary archive Site U1542

3.1 The International Ocean Discovery Program Site U1542

This thesis focuses on paleoclimatic and paleoceanographic reconstructions based on the composite sediment record drilled at U1542 during International Ocean Discovery Program (IODP) Expedition 383 (DYNAPACC) in June 2019 (*Lamy et al.*, 2021). Site U1542 (52°42.29'S, 75°35.77' W) is located 50 km off the Chilean margin, on the continental slope west-northwest of the western entrance of the Strait of Magellan. Four holes, from holes U1542A to U1542D, were drilled at Site U1542 using the full-length advanced piston corer (APC) system. The composite record used in this thesis is constructed from the four holes, providing a continuous spliced sequence, established through stratigraphic correlation using magnetic susceptibility and colour reflectance b* data from the Section Half Multisensor Logger.

3.2 Oceanography

Located at a water depth of 1,101 meters, Site U1542 lies at the lower boundary between the Pacific Deep Water (PDW) and the Antarctic Intermediate Water (AAIW) masses (Fig. 3.1). PDW in the Southeast Pacific is characterized by high nutrient content and low oxygen, while the AAIW, found approximately between 500 and 1200 meters depth, is distinguished by low temperatures (3 - 7°C), low salinity (∼34.3 per mil) and high oxygen content (Fig. 3.1). AAIW forms under the effect of the Ekman spiral between the Polar and the Subantarctic Zone, and their migration affects the dynamics of the AAIW (*Rintoul*, 2018). Its dynamic, in turn, impacts the North Atlantic Deep-Water stability and thus influences the Meridional Overturning Circulation (*Pahnke et al.*, 2008). Furthermore, these intermediate waters are significant as an anthropogenic CO_2 sink and play a major role in global ocean oxygenation (*Sabine et al.*, 2004).

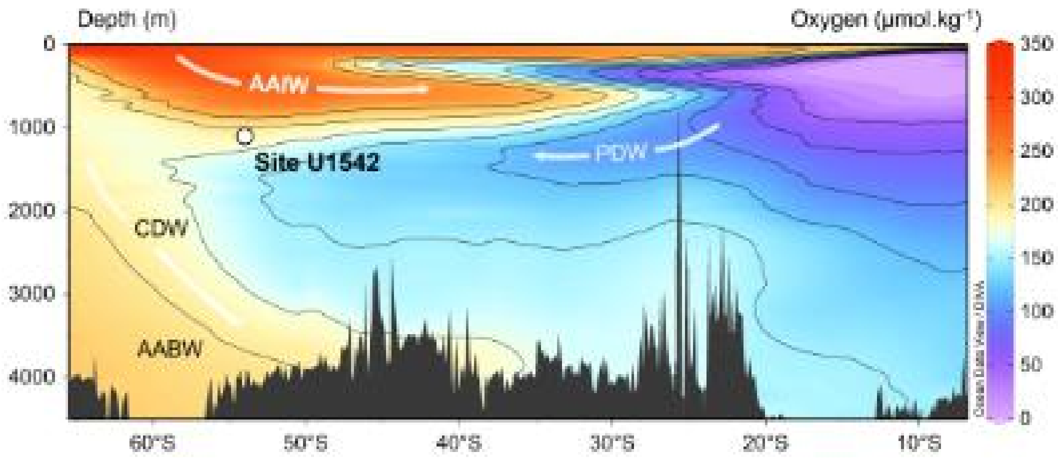

Figure 3.1: **Latitudinal oxygen transect at 90°E.** Oxygen data are from World Ocean Database. Bathymetry is derived from GEBCO 2014 with 6x6min at global resolution.

The upper ocean circulation at Site U1542 is driven by the coastal Cap Horn Current (CHC). The CHC origins from the ACC where it impinges on the Chilean margin (between 40°S and 45°S) into an equatorward branch, the Humboldt Current, and a southward branch, the CHC (Fig. 3.2). Evidence from surface buoy trajectories shows that when a drifter reaches the coastal region at ∼44°S, it is advected southward into the CHC and returns to the ACC two months later (*Chaigneau and Pizarro*, 2005). This observation is further confirmed by *Zheng et al.* [2023], from satellite altimetry (1993–2021, 400 m meters depth) and 2 ocean models, one free-running and one data-assimilating. This study indicates that the CHC acts as an inter-basin conduit, drawing relatively cold and fresh subantarctic surface water from the South Pacific, and injecting it into the South Atlantic. The Sediments below the CHC have been addressed by several surface sediments studies (*e.g.*, *Vollmar et al.*, 2022; *Wu et al.*, 2019). The only paleo record of the CHC (*Lamy et al.*, 2015) suggests that the water masses of CHC are advected through into the DP during both interglacials and glacials but the intensity is reduced during glacial period. The similar glacial reduction observed within the CHC (site MD07-3128) and in the northern DP (site MR0806) further implies that the CHC is connected to the subantarctic area of the DP. Ultimately, *Lamy et al.* [2015] highlight the ideal location of the CHC for paleo-studies, as the Drake Passage is known for its unwelcoming conditions, facing strong winds and waves, rendering any coring and drilling operation difficult.

Due to its strategic location, Site U1542 (very close to site MD07-3128) is ideally suited for a detailed study of the dynamics of the AAIW, the variation of the northernmost part of the ACC (*i.e.*, CHC) entering the Drake Passage, and to study the land-sea interactions including changes in the extent of the PIS along the southern Chilean continental margin (*Lamy et al.*, 2021).

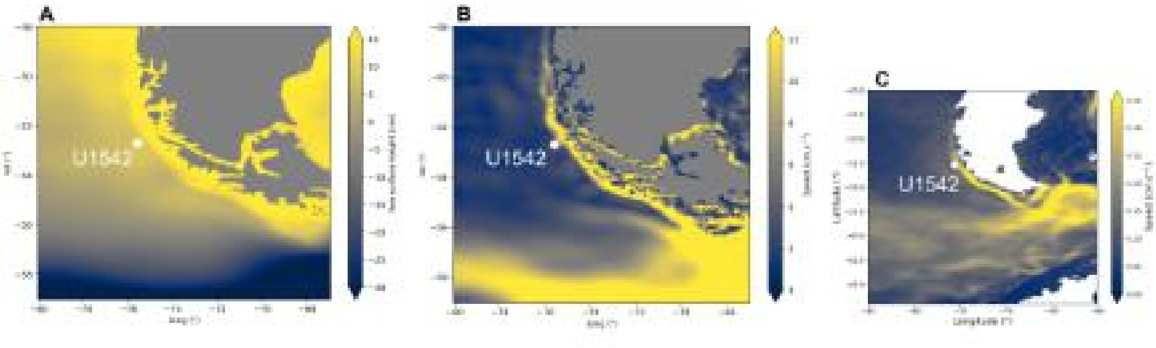

Figure 3.2: **NEMO time-mean (1958-2015) (A) sea surface height and (B) vertical-averaged (0-400 m) current speed (C). Mean ocean surface speed (1993-2022) from CMEMS altimetry data.** The acceleration of flow speed near the Chilean margin is the Cap Horn Current, flowing southward. Modified from *Zheng et al.*, 2023.

3.3 Sedimentology

The ∼249 m spliced sedimentary sequence recovered at Site U1542 sits on the upper slope of the Chilean continental margin, within a relatively small-scale sediment depocenter ("sediment drift"). The depositional environment at Site U1542 is of siliciclastic nature. The sedimentary sequence is dominated by a sand-bearing clayey silt to silty clay, representing the main lithology of the archive. This sequence exhibits meter-scale variations in color between gray and grayish olive, with occasional visually observed drop stones. Additionally, a second minor unit of light greenish-gray to light gray foraminifer-rich nannofossil ooze is interspersed within the main unit. These color changes largely parallel variations in grain size and biogeochemistry indices introduced in this thesis. $CaCO_3$ contents vary between ∼1 and 12 wt % for the main unit and between ∼30 and 55 wt % in the second unit. Biogenic silica and organic matter contents range from 0.3 to 0.8 wt % and from 1 to 4 wt %, respectively. TOC/TN ranges are low, suggesting a predominance of marine-derived organic matter. Diatoms and radiolarians are rare throughout the sediment succession, silicoflagellates are absent, nannofossils are few to barren, benthic and planktonic foraminifers are abundant, and ostracods are sparsely present in some intervals. The facies observed are interpreted as a mixture of turbidite-contourite depositional system largely influenced by the relative proximity of the PIS.

3.4 Construction of the composite Chilean margin record

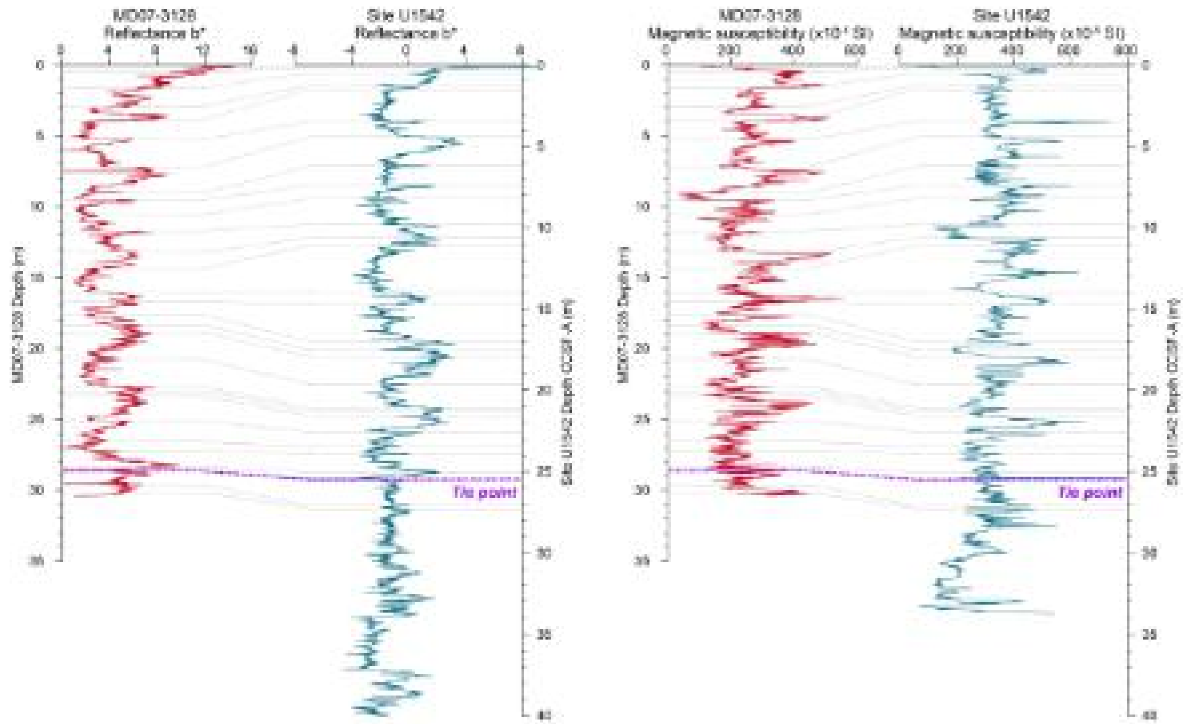

Figure 3.3: **magnetic susceptibility and reflectance b* of MD07-3128 (*Kissel*, 2007) compared with the respective proxies for Site U1542 (*Lamy et al.*, 2021.).** The dashed lines with arrows are used to indicate correlative features within the respective records. Differences in the depths are attributed to coring artefacts in the upper part, stretched in the Marion-Dufresne (MD) cores, or destroyed in the drilled site.

The pre-cruise site survey piston-core MD07-3128 (∼30 m long), located approximately 2 nautical miles north of Site U1542, provides excellent high-resolution palaeoceanographic records over the past 65 kyr (*Caniupán et al.*, 2011; *Lamy et al.*, 2015). As measurements on MD07-3128 previously published offer higher resolution for XRF and alkenones-derived SST compared to Site U1542, I developed a composite Chilean margin record consisting of MD07-3128 for the upper part and Site 1542 for the deeper part, used in Chapter 5.

Chapter 4

Biomarkers

This chapter aims to describe the proxies (*i.e.*, indicators of past climatic conditions) utilized in this thesis to investigate the questions outlined in the introduction. Organic molecules or compounds preserved in the geological record are key for environmental investigations in different domains of the Earth Sciences, providing insights into past climate conditions. Environmental changes influence living organisms, which may produce specific chemical compounds in response to these variations. The relationship between these compounds - called biological markers or simply biomarkers - and environmental parameters provides an excellent tool for paleoclimate studies.

In this thesis, we focus on three lipid-based proxies due to their simultaneous retrieval routine using organic geochemical methods, which streamlines multi-proxy comparisons and saves time. The first two proxies consist of long carbon chains: ***n*-alkanes** and **alkenones**. The third proxy is a complex molecule known as Glycerol Dialkyl Glycerol Tetraethers **GDGTs**.

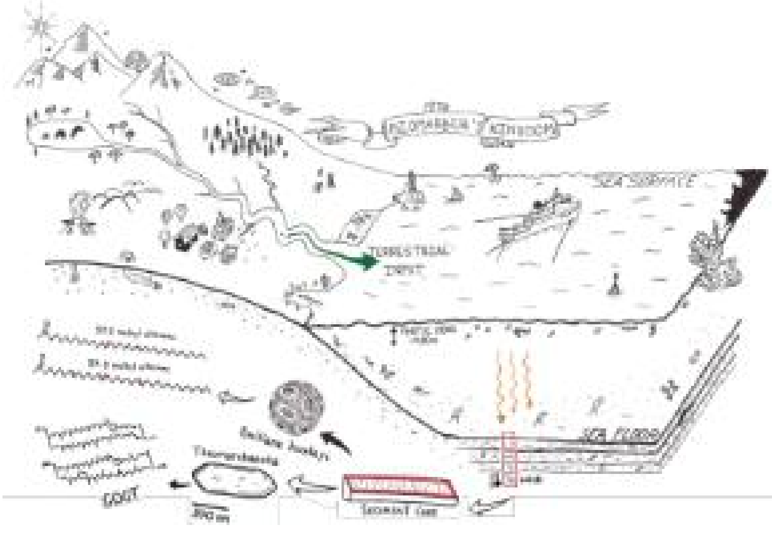

Figure 4.1: **The biomarkers kingdom.**

4.1 *n*-Alkanes

n-Alkanes are simple, straight chain hydrocarbons (CH_3 $(CH_2)_n$ CH_3), commonly found in sediments, with a marked odd-over-even carbon-number predominance. Short-chain (C_{15} - C_{17} - C_{19}) *n*-alkanes are produced by algae and offer insights into marine productivity (*Volkman*, 2006). Long chain (C_{25} to C_{33}) *n*-alkanes, synthesized as part of the epicuticular leaf wax of terrestrial plants, are widely recognizable and used terrestrial plant biomarkers (*Eglinton and Eglinton*, 2008), with a research history stretching back almost a century (*Chibnall et al.*, 1934).

They are often transported over long distances by water as well as by wind, where long-chain *n*-alkanes serve as indicators of aeolian land-plant derived organic matter. For instance, in the Southern Ocean, *n*-alkanes act as dust proxy in sediment cores, where their signal co-varies with iron and CO_2 concentrations over glacial/interglacial cycles (*Lamy et al.*, 2014; *Martinez-Garcia et al.*, 2014; *Martínez-Garcia et al.*, 2011).

The Average Chain Length of *n*-alkanes (ACL) describes the average number of carbon atoms per molecule based on the abundance of odd-carbon-numbered higher plant*n*-alkanes (*Poynter and Eglinton*, 1990). The distribution of chain length is highly variable within plant groups, and variations in the abundances of *n*-alkane chain lengths partly reflect changes in the environmental conditions experienced by plants, such as temperature and aridity. For instance, a high ACL most likely indicates the expansion of grassland (C4 plant; *Rommerskirchen et al.*, 2006), while a decrease in ACL likely reflects aridification and a sparser vegetation cover (*Sepúlveda et al.*, 2009).

$ACL_{23-35} = \sum [i.Xi]/ \sum [Xi]$, where X is abundance and i ranges from *n*-C_{23} to *n*-C_{35}.

Predominantly biosynthesized in odd carbon numbers, even-numbered *n*-alkanes are formed by the loss of a single carbon, potentially due to the degradation of organic matter in the sediment. The Carbon Preference Index (CPI), measuring the strength of odd-over-even predominance, is widely used to assess the degree of preservation of the organic matter (OM) in the sediment, with CPI decreasing with OM degradation (*Eglinton and Eglinton*, 2008).

$CPI_{23-33} = 0.5 \text{ x} \sum (C_{23-33})/(C_{24-32}) + 0.5 \text{ x} \sum (C_{23-33})/(C_{26-34})$

A complete and comprehensive review of*n*-alkanes has been written by *Eglinton and Eglinton* [2008]

4.2 Alkenones

Alkenones are long-chain (C_{37} - C_{39}) unsaturated methyl and ethyl *n*-ketones with two to four double bonds, produced by a few unicellular coccolithophorid species of the class Prymnesiophyceae (*Brassell et al.*, 1986). The ubiquitous *Emiliana Huxleyi* and the more regional Gephyrocapsa oceanica are marine haptophyte algae in the order Isochrysidales living in the upper surface of the ocean and have been considered as the exclusive producers of di-unsaturated ($C_{37:2}$) and tri-unsaturated ($C_{37:3}$) alkenones (*Wang et al.*, 2021). Notably, the degree of unsaturation determined by the number of double bonds, is inversely proportional to the temperature of the algae's growth environment (*Brassell et al.*, 1986; *Müller et al.*, 1998). Their exceptional diagenetic stability has enabled them to produce alkenones-based sea surface temperature and productivity records covering tens of millions of years of Earth's history (*Brassell and Dumitrescu*, 2004; *Wang et al.*, 2021). Alkenone paleothermometry is a very powerful tool for the understanding of the climatic evolution of the oceans, strengthened by the comparison with other palaeoceanographic proxies (*Ho et al.*, 2013).

Since the original observation of *Marlowe et al.* [1984] and the pioneering work of *Brassell et al.* [1986] and *Prahl and Wakeham* [1987], the alkenone unsaturation ketone index ($U^{k'}_{37}$ expressed as the ratio $C_{37:2}/(C_{37:2} + C_{37:3})$) is considered among the most powerful organic proxies for Sea Surface Temperature (SST) climate reconstruction, used on a nearly global basis (*Herbert et al.*, 2016; *Rosell-Melé et al.*, 2001). The $U^{k'}_{37}$ has been calibrated against algal culture in laboratory experiments and measurements taken in modern ocean environments, such as global core-top calibrations (*Müller et al.*, 1998; *Prahl and Wakeham*, 1987). This thesis uses the calibration of *Prahl et al.* [1988] (SST $= (U^{k'}_{37} - 0.039)\ /(0.034)$), probably the most used calibration in paleotemperature reconstructions, allowing direct comparison with other studies.

Worth noticing, lateral transport of alkenones (*i.e.*, advection) during the deposition through the water column could explain the discrepancy between core-top measurements and modern values (*Ausín et al.*, 2022; *Mollenhauer et al.*, 2005). While regional bias in seasonal production occurs, modern measurements support the use of the $U^{k'}_{37}$ SST proxy as a close approximation to mean annual SST (*Herbert et al.*, 2016; *Müller et al.*, 1998). Besides, $U^{k'}_{37}$ estimates become scattered in polar waters below ∼5°C and in the lower latitudes oceans above 28 °C (*Herbert et al.*, 2016).

The occurrence of tetra-unsaturated alkenone ($C_{37:4}$), produced by the group 2i Isochrysidales, is usually restricted in mid-to-high latitude oceans and coastal areas (*Wang et al.*, 2021). The relative abundance of $C_{37:4}$ ($\%C_{37:4}$) in both particulate matter and sediments of the Southern Ocean shows no trend with SST, and its consideration merely leads to an increase in the U^{k}_{37} index (that includes $C_{37:4}$) scattering (*Müller et al.*, 1998; *Sikes et al.*, 1997). Its relevance to paleoclimate has often been challenged (*Rosell-Melé*, 1998; *Wang et al.*, 2021), although it is associated with salinity changes in high latitude records (*Rosell-Melé*, 1998), or with surface advection of iceberg-bearing water masses (*Bard et al.*, 2000), and shows a significant positive correlation with annual mean sea ice concentration (*Wang et al.*, 2021). This relationship led several studies to use the relative abundance of $C_{37:4}$ (*i.e.*, $\%C_{37:4}$) as a tracer of low sea surface salinity from polar and subpolar water mass distribution in high latitudes sediment records (*Martínez-Garcia et al.*, 2010; *McClymont et al.*, 2008).

A complete and comprehensive review of alkenones has been written by *Herbert* [2003] and more recently by *Ho et al.* [2013].

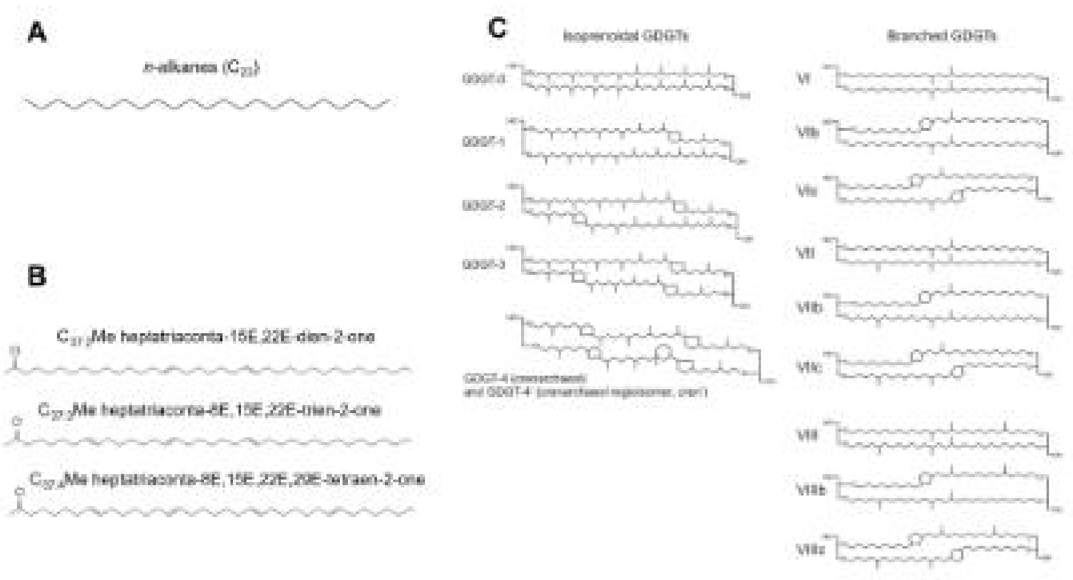

Figure 4.2: **Molecular structure and standard IUPAC names** of (A) n-alkanes, (B) C_{37} alkenones and (C) GDGTs (modified from *Kaiser et al.* [2015]).

4.3 Glycerol Diakyl Glycerol Tetraethers

Glycerol dialkyl glycerol tetraether lipids (subsequently shortened GDGTs) are membrane lipids synthesized by a wide variety of archaea and bacteria and originate from both continental and marine realms. These lipids biomarkers have garnered particular attention since the XXIst century as they occur ubiquitously in a wide range of environments and are preserved in sediments older than 140 Ma (*Schouten et al.*, 2013a).

Terrestrial branched GDGTs (brGDGT) originate from unknown heterotrophic bacteria that can be found in soils and peats, thereby associated with terrigenous input into the sediment. Consisting of n-alkyl chains with 0 to 2 cyclopentane moieties and 4 to 6 branches with methyl groups, the cyclisation ratio of branched tetraethers (CBT') increases with the pH of soils, while the Methylation index of Branched Tetraethers (MBT') covaries with the mean annual air temperature (MAT) (*Weijers et al.*, 2007).

Marine isoprenoid GDGTs (isoGDGT), included Crenarchaeol and its regioisomer (Cren'), are biosynthesized by ammonia-oxiding archea *Thaumarchaeota* (previously known as Group I Crenarchaeota), ubiquitous in all latitudes of the global ocean (*Ho et al.*, 2014), and more abundant deeper in the water column than in surface waters, hence reflecting subsurface water settings (*Huguet et al.*, 2007). The number of cyclopentane moieties of these archaeal GDGT lipids is linearly correlated with the mean annual growth temperature (*Ho et al.*, 2014; *Schouten et al.*, 2013a). Based on this relationship, the TEX_{86} (TetraEther indeX of tetraethers consisting of 86 carbon atoms) is a proxy for sub-sea surface temperature (subSST) derived from the distribution of archaeal isoGDGT (*Schouten et al.*, 2002). Their exceptional diagenetic stability has enabled production of TEX_{86}-based subSST records back to the Cretaceous and Jurassic (*Jenkyns et al.*, 2012). Notwithstanding, core-top calibration studies have identified discrepancies in sedimentary GDGT distributions between cooler (sub)polar oceans (SST <15 °C) and warmer tropical oceans (SST >15 °C). Consequently, separate calibrations have been proposed for the reconstruction of cold (TEX_{86}^{L}) and warm (TEX_{86}^{H}) sub-SST (*Kim et al.*, 2010). In the case of Site U1542, a comparison between different proxies' distributions suggests that TEX_{86}^{L} is more suitable for temperature reconstructions in the Southeast Pacific (Fig. 4.4).

The relative ratio between the abundance of Crenarchaeol (marine) and brGDGT (terrigenous), the Branched vs. Isoprenoid Tetraether (BIT) index, is a commonly used and powerful indicator of magnitude of terrestrial organic matter input into the marine realm (*Hopmans et al.*, 2004, Fig. 4.3). BIT values can range from 0.01 in open marine sediments to 1 in some soils (*Schouten et al.*, 2013b, and references cited therein). A complete and comprehensive review of GDGTs has been written by *Schouten et al.* [2013b].

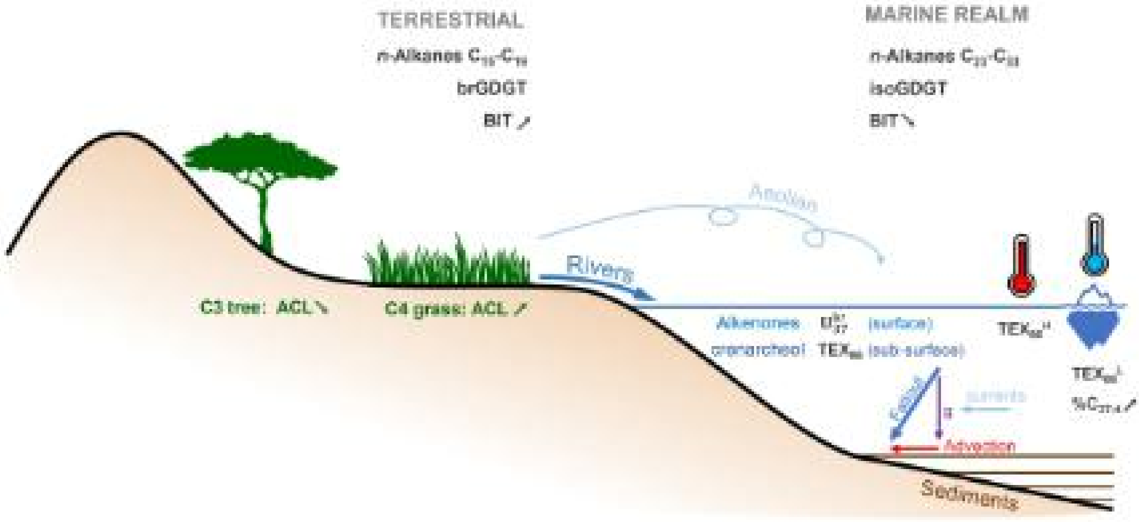

Figure 4.3: **Environmental location of the biomarers introduced in this study and their corresponding indices**

4.4 Paleotemperature

Both paleothermometry methods, the $U_{37}^{k'}$ and U_{37}^{k} index based on coccolithophores-derived alkenones and the TEX_{86} index based on *thaumarcheota*-derived GDGT have been used in numerous studies in the Southeast Pacific (*Caniupán et al.*, 2011; *Hagemann et al.*, 2022, 2024; *Kaiser et al.*, 2005). These SST proxies complement foraminifer- and diatom-based SST reconstruction but represent different depths. It is well-established that the alkenones-based reconstruction represents the surface (≤25 m) of the oceans. However, due to the unknown depth origin and uncertain source organism of *Thaumarchaeota*, along with the discrepancy between TEX_{86}^{L} and TEX_{86}^{H}, and the lack of an important database of records comparable with Site U1542, the choices of using alkenones as a main SST proxy at Site U1542 is preferred. Furthermore, the relatively shallow depth (1,101 m) of Site U1542 bypasses potential issues related to long-distance lateral transport, which is thought to affect isoprenoid GDGTs less than alkenones (*Mollenhauer et al.*, 2007).

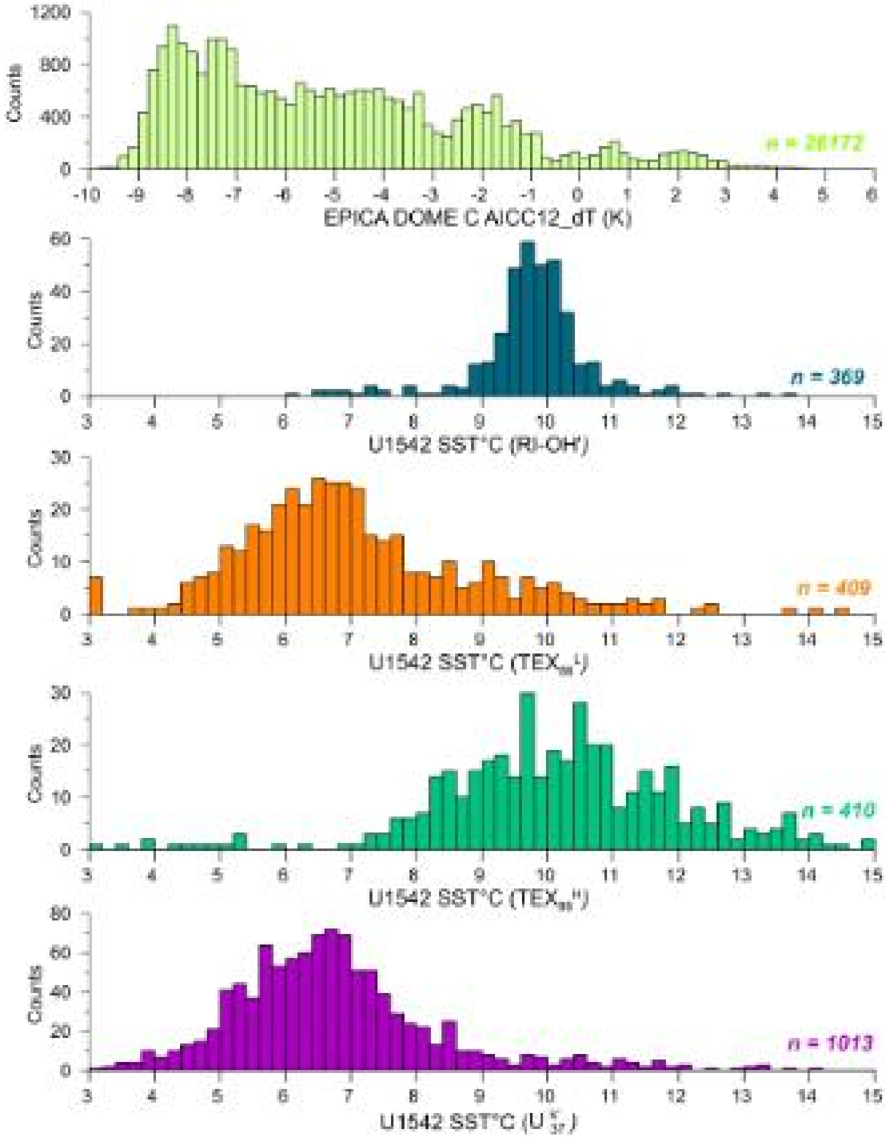

Figure 4.4: **Sorting of biomarker-derived temperature values from the different indices measured at Site U1542.** The range of atmospheric temperature recorded at Epica Dome C (light green) varies from -9.5 to 4°C. This range is more than sea surface temperature reconstructed at Site U1542. the TEX_{86}^{L} temperatures display a range similar to the $U_{37}^{k'}$ (purple), from 3 to 14°C, while temperatures using TEX_{86}^{H} (green) and RI-OH' (blue) index display warmer temperatures. The RI-OH' index present the less variability, concentrated between 9 and 11°C.

4.5 Sampling strategy, preparation, and methods

Biomarker analyses at Site U1542 were performed at Alfred Wegener Institute Bremerhaven. A total of 1100 samples of 10 cc volume each (5 g) from the bulk sediment were taken in January 2020 during the Expedition 383 sampling party at the IODP Gulf Coast Repository (College Station, USA) for our purpose. The initial sampling strategy consisted of a 30 cm interval between each sample, and 10 cm during periods of lower sedimentation rate to obtain a sub-millennial resolution, based on the preliminary shipboard age model. Subsequently to age model refinement, additional samples have been selected, resulting in about 1300 samples investigated in this project.

After the reception in Bremerhaven, samples were immediately freeze-dried, preferred for sediments used for alkenone analysis because air-drying (commonly used for samples before microfossil analysis) is thought to lead to significant loss of alkenones and potentially bias the temperature estimation (*McClymont et al.*, 2007).

Several extraction methods were applied in this work, ultrasonication and the Accelerated Solvent Extractor (Dionex ASE-350, Fig. 4.5). As there is no evidence of extraction method-induced bias in index values, the ASE method was selected; faster, using less solvent and extracting higher compound concentration per sediment weight.

5 g of homogenized freeze-dried sediment were heated at 100 °C for 5 min followed by 3 cycles of 5 min in static phase with solvent (Dichloromethane:Methanol, v:v, 9:1) in high pressure (1500 psi). Internal standards (squalane, C_{36} n-alkane, C_{46}-GDGT) added before extraction served for quantification purposes. The resulting total lipid extract is composed of a large suite of biomarkers derived from various organisms. To have purer samples for better quantification, the total lipid extracts were partitioned into different fractions through silica gel chromatography.

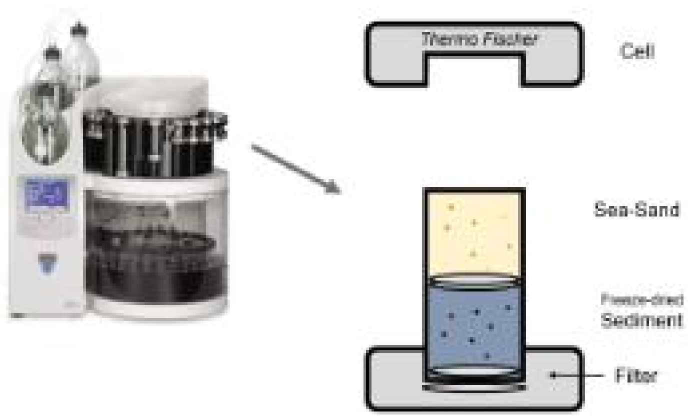

Figure 4.5: **ASE 350 (thermofisher) and detailled view of cells filed for total lipid extract.**

After extraction, the total lipid extracts were separated into three fractions by silica gel chromatography prepared from Pasteur pipettes. The organic compounds move through the silica column at different rates depending on their affinity to the solvents (mobile phase) compared to the column (stationary phase). There is higher affinity between silica and polar compounds, hence the less polar n-alkanes elute through the columns before, together with Hexan. The second fraction following contains the alkenones, eluted with Dichloromethane. The third fraction elutes using a solvent mixture of Dichloromethane and Methanol (1:1) to finally recover the more polar GDGTs. The GDGTs fraction is subsequently filtered with Millex Hydrophobic Fluoropore filter (PTFE) in Hexane:Isopropanol (99:1) solvent before analyses. This path is resumed in figure 4.6.

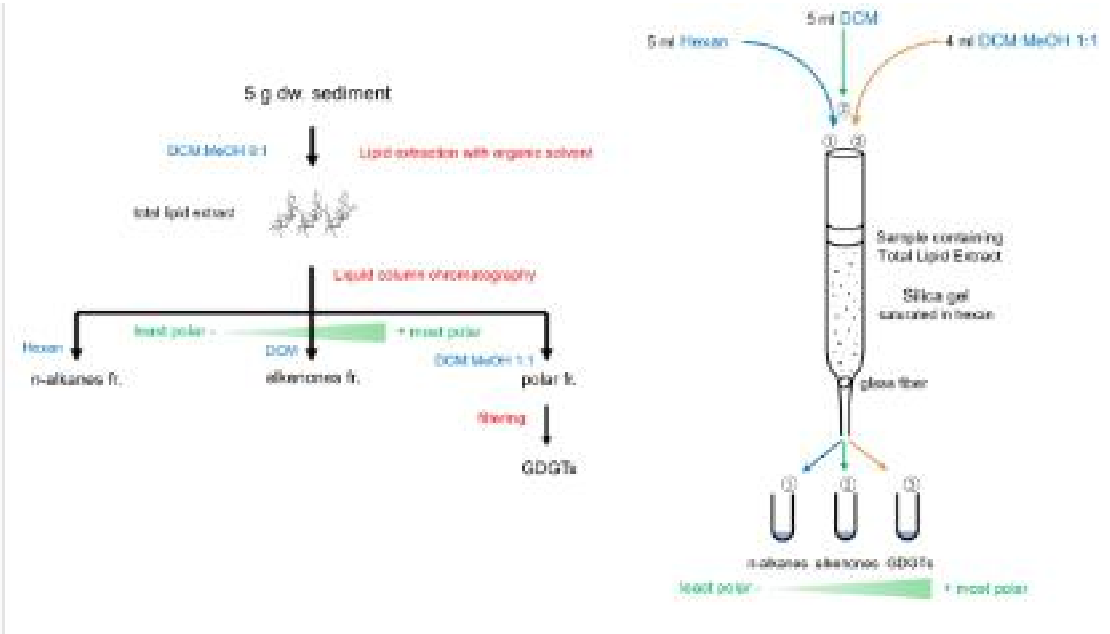

Figure 4.6: **Path of different steps to extract and separate the fractions of biomarkers** from the bulk sediment (left). Schematic of silica column chromatography to separate a mixture of organic compounds (right).

Once ready, the identification of the different compounds was achieved through comparison of the chromatographic relative retention times of the target compounds with standards.n-Alkanes fraction was measured with a HP6890 gas chromatographer fitted to a flame ionization detector (GC-FID), using Helium as a carrier as. Chromatographic separation of the organic compound was achieved using a Varian VF-1ms capillary column of 80 m length, 0.25 mm internal diameter and 0.25 μm film thickness. The oven temperature was programmed to be held at 80 °C for 1 minute, then increased at 40 °C/minute to 300 °C and held for 60 minutes.

Alkenones were analysed by gas chromatography on an Agilent 7890 fitted with a flame ionization detector using an Agilent VF-200 ms capillary column (60 m length, 250 μm diameter, 0.25 μm film thickness). The oven temperature was programmed to be held at 50 °C for 2 min, then increased at 20 °C/min to 255 °C, at 3 °C/min to 300 °C, at 10 °C/min until 320 °C and held for 10 min. The identification of alkenones was achieved by comparing chromatographic retention times of the samples with those of a laboratory *Emiliania huxleyi* culture extract that was routinely used as a working standard to control data quality

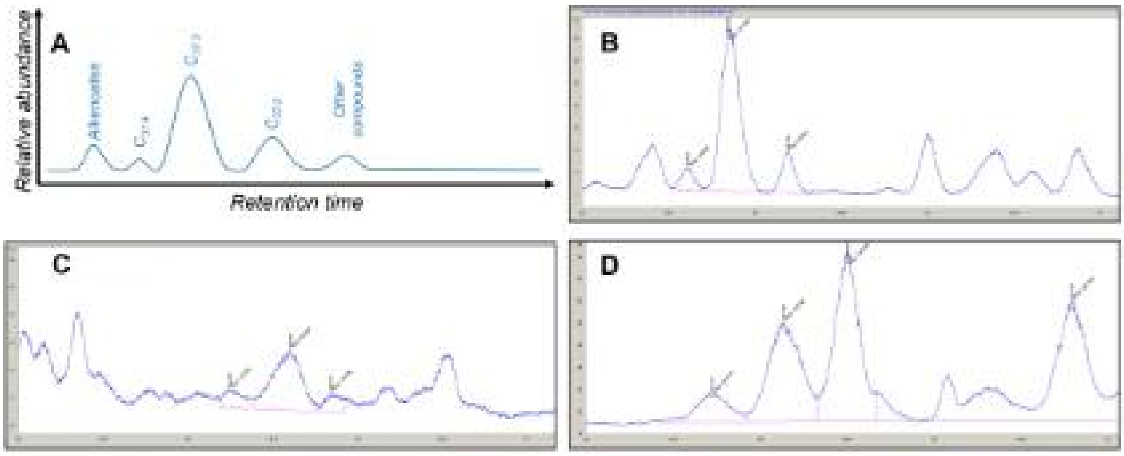

Figure 4.7: **Chromatograms of DCM (alkenones) fractions of lipids extracts.** (A), schematic chromatogram with relative appearance of different compounds. (B) Clean sample of cold glacial period ($C_{37:3} > C_{37:2}$). (C) dirty and unreliable samples appearing when the separation process was not successfull . (D) Clean sample of interglacial period ($C_{37:3} < C_{37:2}$).

The reproducibility of the procedure was evaluated using a homogeneous sediment standard, extracted with every batch of samples. The relative analytical errors in the quantification of alkenone concentrations were below 6%. The reproducibility of alkenone temperatures for replicate samples (n = 25) of a homogeneous marine sediment lab standard run during the project is better than ±0.2°C at the 95% confidence level.

GDGTs fractions, due to the relatively high-molecular-weight GDGTs, is not adequate for analysing using classic gas chromatography. GDGTs were analysed on an Agilent 1260 Infinity II ultrahigh-performance liquid chromatography-mass spectrometry (UHPLC-MS) system, consisting of a G1712B binary pump, a G7129A vial sampler with integrated sample thermostat, a G7116A multicolumn thermostat, and a G6125C single quadrupole mass spectrometer with an atmospheric pressure chemical ionization

(APCI) ion source. Chromatographic separation (including 5-and 6-Methyl isomers of brGDGTs) of the GDGTs was achieved by coupling two UPLC silica columns (Waters Acquity BEH HILIC, 2.1 × 150 mm, 1.7 μm) with a 2.1 × 5 mm pre-column as in *Hopmans et al.* [2016], but with the following chromatographic modifications: Mobile phases A and B consisted of n-hexane: chloroform (99:1, v/v) and n-hexane: 2-propanol: chloroform (89:10:1, v/v/v), respectively. The flow rate was set to 0.4 ml/min and the columns were heated to 50 °C, resulting in a maximum backpressure of 425 bar. Sample aliquots of 20 μl were injected with isocratic elution for 20 minutes using 86% A and 14% B, followed by a gradient to 30% A and 70% B within the next 20 min. After this, the mobile phase was set to 100% B, and the column was rinsed for 13 min, followed by a 7 min re-equilibration time with 86% A and 14% B before the next sample analysis. The total run time was 60 min. GDGTs were detected using positive ion APCI-MS and selective ion monitoring (SIM) of (M + H)+ ions (*Schouten et al.*, 2007) with the following settings: nebulizer pressure 50 psi, vaporizer and drying gas temperature 350 °C, drying gas flow 5 L/min. The capillary voltage was 4 kV and the corona current +5 μA. The detector was set for the following SIM ions: m/z 744 (C_{46} standard), m/z 1302.3 (GDGT-0), m/z 1300.3 (GDGT-1), m/z 1298.3 (GDGT-2), m/z 1296.3 (GDGT-3), m/z 1292.3 (crenarchaeol and crenarchaeol isomer), m/z 1022 (GDGT-Ia), m/z 1020 (GDGT-Ib), m/z 1018 (GDGT-Ic), m/z 1036 (GDGT-IIa and IIa'), m/z 1034 (GDGT-IIb and IIb'), m/z 1032 (GDGT-IIc and IIc'), m/z 1050 (GDGT-IIIa and IIIa'), m/z 1048 (GDGT-IIIb and IIIb'), m/z 1046 (GDGT-IIIc and IIIc'). The resulting scan/dwell time was 66ms.

Chapter 5

Persistent interhemispheric link of the Antarctic Circumpolar Current millennial-scale oscillations over the last 800 kyr

In revision at Nature Communications

Vincent Rigalleau, Frank Lamy, Nicoletta Ruggieri, Henrik Sadatzki, Helge W. Arz, Stephen Barker, Lester Lembke-Jene, Antje Wegwerth, Gregor Knorr, Igor M. Venancio, Tainã M. L. Pinho, Ralf Tiedemann & Gisela Winckler

5.1 Abstract

Millennial-scale variations in the strength and position of the Antarctic Circumpolar Current (ACC) exert considerable impact on the global meridional overturning circulation, heat transport and the ocean carbon cycle. However, we still lack a deeper mechanistic understanding of these variations, due to the scarcity of sediment records covering multiple glacial-interglacial cycles with millennial-scale resolution. Here we present high-resolution current strength and sea surface temperature (SST) records covering the past 790,000 years from the Cape Horn Current, the northern branch of the ACC, flowing along the Southern Chilean Margin towards the Drake Passage. The records document persisting millennial-scale climate variability throughout all Late Pleistocene glacial stages with stronger ACC flow and warmer SST coinciding with Antarctic warm inter-

vals. These Southern Hemisphere changes are linked to North Atlantic millennial-scale fluctuations, plausibly involving changes in Drake Passage throughflow and the Atlantic thermohaline circulation. The millennial-scale changes in ACC strength and SST are likely associated with rates of atmospheric CO_2 changes, suggesting a mechanistic link through the Southern Ocean carbon cycle.

5.2 Introduction

The last glacial period (71-11.7 thousand years ago, ka) exhibited pronounced millennial-scale (~1 to 10 kyr) variability in ocean circulation and global climate widely described in Greenland ice cores (*Dansgaard et al.*, 1993), speleothems records (*Cheng et al.*, 2016), and marine sediment cores (*Arz et al.*, 1998; *Bond et al.*, 1993; *Kanfoush et al.*, 2000; *Lamy et al.*, 2015; *McManus et al.*, 1999). In the Southern Hemisphere, the counterparts to these northern abrupt warming (so-called Dansgaard-Oeschger events; DO events) are known as the Antarctic Isotope Maxima (AIM) and exhibit more gradual, smaller-amplitude changes (*Blunier et al.*, 1998; *EPICA Community Members*, 2006). For this glacial millennial-scale climate variability, the concept of a bipolar seesaw was established, describing a thermal asynchrony between both hemispheres related to the dynamics of the global ocean overturning circulation (*Barker et al.*, 2009; *Blunier and Brook*, 2001; *Blunier et al.*, 1998; *Stocker*, 1998). Beyond the last glacial cycle and the stratigraphic range covered by Greenland ice-cores, sediment records documenting millennial-scale climatic changes across several glacial cycles are mostly restricted to the Northern Hemisphere (NH) (*Barker et al.*, 2019; *Cheng et al.*, 2016; *Hodell et al.*, 2008, 2023; *Martrat et al.*, 2007; *McManus et al.*, 1999; *Sun et al.*, 2021) in comparison to few Southern Hemisphere records (*Jouzel et al.*, 2007; *Pahnke et al.*, 2003).

The Antarctic Circumpolar Current (ACC), located in the Southern Ocean between 40° and 60°S is the largest current system on Earth. It is driven by atmospheric forcing, the Southern Westerly Winds (SWW)(*Toggweiler et al.*, 2006), bathymetry and ocean density gradients originating from surface, intermediate and deep ocean temperature, and salinity changes (*Rintoul*, 2018). Connecting the Atlantic, Pacific, and Indian Ocean basins, the ACC responds to global climate variability and interlinks the various shallow to deeper southern water masses *Marshall and Speer*, 2012; *Rintoul*, 2018), thereby regulating the exchange with the global deep ocean (*Rintoul*, 2018; *Toggweiler et al.*, 2006). The ACC is a crucial component in the global carbon budget (*Marshall and Speer*, 2012) and exerts a major influence on the global uptake of anthropogenic heat and carbon dioxide (*Sabine et al.*, 2004). The major bathymetric constriction of the ACC occurs at the Drake Passage (DP). Complementing the so-called warm-water route that connects the Indian and Atlantic oceans (*i.e.*, Agulhas current), the cold-water route (*i.e.*, DP) connects the Pacific and Atlantic oceans. Various model studies have proposed that the Southern Ocean, particularly the DP throughflow together with the Agulhas current (*Knorr and Lohmann*, 2003), exerts a strong influence on the Atlantic Meridional Overturning Circulation (AMOC).

Over the last glacial period, significant millennial-scale fluctuations in DP throughflow (*Wu et al.*, 2021) and in the Agulhas current (*Beal et al.*, 2011) have been observed and their instability at millennial timescales has been suggested as a possible trigger for DO events (*Buizert and Schmittner*, 2015; *Oka et al.*, 2021). However, the remote location of the Southern Ocean has resulted in relatively fewer paleo-studies compared to other oceanic regions. Consequently, knowledge about the presence and recurrence of such Southern Hemisphere millennial-scale oscillations in earlier parts of the Earth's Quaternary history is limited. Obtaining a more comprehensive picture of the dynamics of abrupt changes in the Southern Ocean is crucial to understand its role within the climate system.

Here, we present high-resolution Pleistocene sedimentological and geochemical records obtained from International Ocean Discovery Program (IODP) Site U1542 (52°42.29'S, 75°35.77' W; 1,101m water depth, Fig. 5.1) (*Lamy et al.*, 2021). The site is located approximately 30 nautical miles off the Chilean coast in the southward flowing Cape Horn Current (CHC). We focus on reconstructions of sea surface temperature (SST) using the alkenone palaeothermometry (*e.g.*, *Caniupán et al.*, 2011; *Ho*, 2012; *Kaiser et al.*, 2005; *Martrat et al.*, 2007) and near bottom current strength based the zirconium to rubidium ratio (Zr/Rb) calibrated with sortable silt data (*Lamy et al.*, 2015; *McCave et al.*, 1995; *Toyos et al.*, 2020; *Wu et al.*, 2021). Both SST and current strength reconstructions have been successfully applied in that region. Our study extends the existing sediment records from the nearby Calypso piston coring site MD07-3128 that reach back to ~60 ka (*Caniupán et al.*, 2011; *Lamy et al.*, 2015, 2021). Together, these records enable us to explore the orbital and millennial scale climate variability of the subantarctic ACC at the entrance of the DP across the Late Pleistocene in an unprecedented detail, notably relevant for understanding contemporary trends under anthropogenic forcing (*Shi et al.*, 2021).

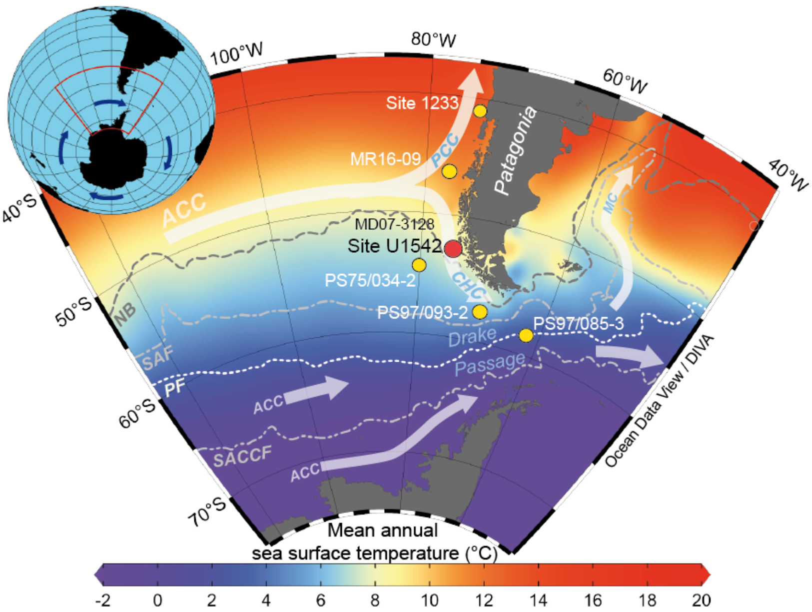

Figure 5.1: **Regional modern ocean hydrography and location of cores discussed in the study.** Map of the Drake Passage (DP) region with mean annual sea surface temperature (World Ocean Atlas 2018). White transparent arrows are schematic representations of major currents; the Antarctic Circumpolar Current (ACC), the Cap Horn Current (CHC), the Peru Chilean Current (PCC) and the Malvinas Current (MC). Altimetry-derived ACC fronts (*Park et al.*, 2019); Northern Boundary (NB), Subantarctic Front (SAF), Polar Front (PF), Southern ACC front (SACCF). Maps created in Ocean Data View

5.3 Results

SST and ACC strength reconstruction from current-controlled deposits

The 249m-long composite record covers the past 790 kyr (see methods for details on the age model), with an average sedimentation rate of ~30 cm/kyr. During glacial times, enhanced hinterland discharge contributed to an increased supply of terrigenous sediment, resulting in a bulk accumulation rate up to 5 times higher compared to interglacial periods, consistent with earlier records from the region (*Kaiser et al.*, 2005).

We obtained alkenone-based SSTs from 929 samples at an average temporal resolution of ~700 years. Holocene SSTs reach up to ~11.5°C during the Holocene Climate Optimum, and gradually decreased toward cooler values, reaching ~9.6°C during the late Holocene, *i.e.* ~1.5°C above the modern mean annual SST in this region. This offset can be attributed to an previously observed seasonal bias of alkenone SSTs of ~1° C versus the annual mean SST at the southern Chilean margin (*Hagemann et al.*, 2022). Over the past 790 kyr, the reconstructed SST range at Site U1542 (Fig. 5.2) varies from ∼3°C during the Last Glacial Maximum (LGM; sensu lato 18–28 ka), Marine Isotope Stage (MIS) 11b (386 ka) and MIS 7d (275 ka) to more than 12°C, during MIS 9e, MIS 7e and MIS 5e. The mean glacial to interglacial temperature difference at glacial terminations is ∼6°C from 0 to 430 ka and ∼4°C before 430 ka. The transition into glacial periods is marked by a strong and abrupt cooling, with temperatures dropping by ∼7°C. We observe exceptionally high-amplitude SST variability of ∼1-3°C at the millennial timescale during glacial periods, consistently persistent across all eight glacial periods recorded at Site U1542.

Site U1542 and MD07-3128 are both located underneath the CHC and variations in SSTs are plausibly linked to changes in the strength of this current, which flows along the Chilean continental margin towards the Drake Passage. As the subantarctic surface water of the ACC impinges on the Chilean margin, a minor part bifurcates (between 40°S and 45°S) into an equatorward branch, the Humboldt Current, while the major part deviates into the southward branch, the CHC (Fig. 5.1). This narrow current of ∼100–150-km width along the Chilean margin is therefore the northernmost branch of the ACC entering the DP (Fig. 5.1) (*Chaigneau and Pizarro*, 2005). Oscillations in the CHC strength constitute a substantial fraction of subantarctic DP throughflow variability (*Lamy et al.*, 2015). As the CHC strength largely represents the northern, subantarctic ACC entering the DP, we will subsequently refer to it as CHC/ACC strength.

To assess the relationship between our SST record and the strength of the CHC/ACC, we reconstructed the near-bottom current speed (see methods; Fig. 10.4, 10.5) (*McCave et al.*, 1995). The calculated flow speeds depend on the sensitivity of the grain size to the bottom-current flow speed that may partly depend on local conditions such as bathymetry and seafloor morphology. Considering that Site U1542 is located on the continental slope and contains a sedimentary sequence consisting mostly of siliciclastic sediments, we expect only limited ice-rafted debris impact, potentially during full glacial conditions when the Patagonian ice sheet reached its maximum extent (*Davies et al.*, 2020). In current-controlled deposits such as the sediment drift where Site U1542 is located (*Lamy et al.*, 2021), the accumulation is relatively rapid and ice-rafted supply has little effect on sortable silt (SS) (*McCave et al.*, 2017). Furthermore, *Lamy et al.* [2015] demonstrated that the deposition of ice-rafted debris at our location shows fluctuations that are independent of SS and fine-sand contents. Additionally, changes in SS and the weight percentage of the SS component are positively correlated, providing strong evidence for primarily current-controlled grain size changes within the silt fraction (*McCave et al.*, 2014). Therefore, the use of Zr/Rb coupled with SS measurements has proven to be a reliable indicator of bottom current speed on the Chilean margin (*Lamy et al.*, 2015), in the DP (*Toyos et al.*, 2020; *Wu et al.*, 2021), and in the Scotia Sea (*McCave et al.*, 2014).

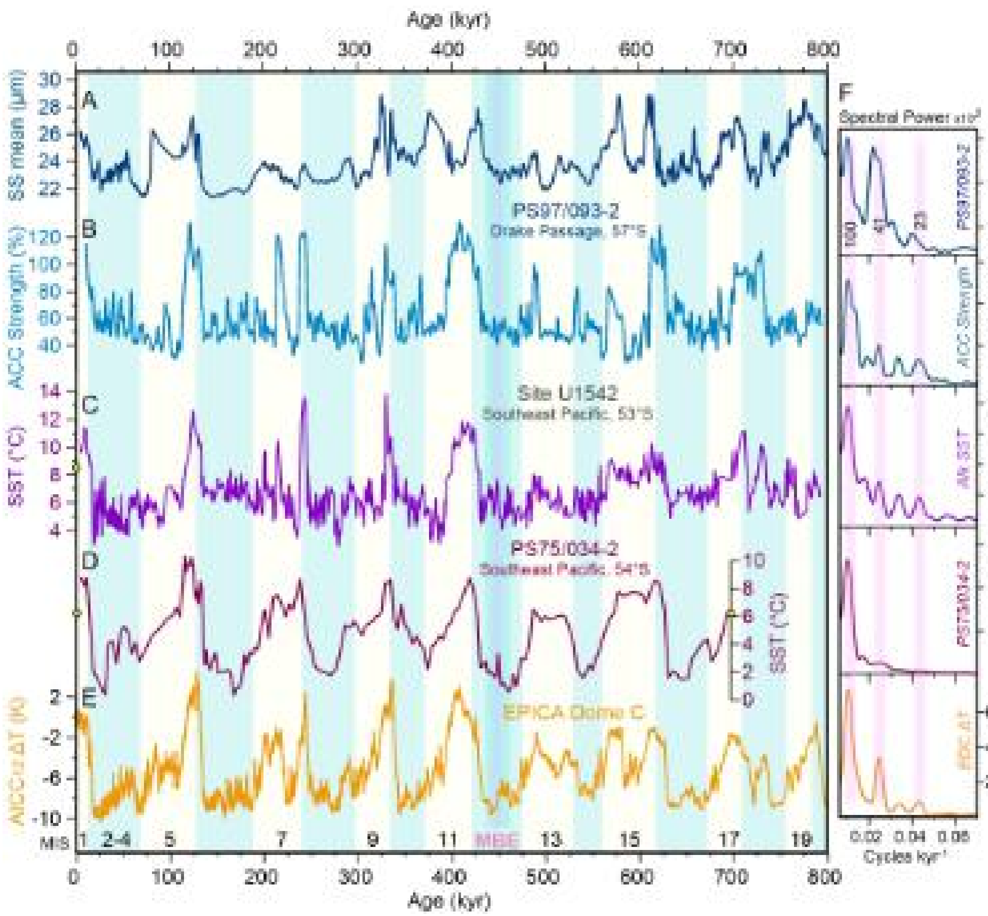

Figure 5.2: **Long-term, orbital-scale variability of SST and ACC Strength in the Southeast Pacific, and their respective spectral analyses.** (A) Sortable silt record from sediment core PS97/093-2 representing ACC strength changes at entrance of the Drake Passage (*Toyos et al.*, 2020), (B) ACC strength and (C) alkenone-derived SST from Site U1542, yellow dot indicates the modern SST at the core location), (D) alkenone-derived SST from PS75/034-2 (*Ho et al.*, 2012), (E) Antarctic ice core EDC temperature record (*Jouzel et al.*, 2007) on the AICC2012 age model (*Bazin et al.*, 2013), and (F) spectral power of (A) to (E). Timing and nomenclature of Marine Isotope Stages (MIS) follow (*Lisiecki and Raymo*, 2005). MBE correspond to the Mid-Bruhnes Event.

The early stage of most interglacial periods (MIS 15, 11, 9, 7 & 5) presents a consistent ACC strength (mean sortable silt = 38.6 μm; current speed = 45 cm/s, see methods) (McCave, Thornalley, et Hall 2017), reaching ~50-52 cm/s at their maxima, corresponding to 120% of the interglacial mean (Fig. 5.2B). MIS 17 and 13 present relatively slower flow speeds than the other interglacials (42 cm/s max.). During all glacial periods, the flow strength is reduced to ∼16-20 cm/s on average, translating to ∼50-60% weakening from mean interglacial values (45 cm/s, Fig. 5.2B). This reduction is substantially larger than previous Pleistocene estimates at the entrance of DP (6 to 16% reduction, Fig. 5.2A) (*Toyos et al.*, 2020), but in line with estimates of 40 to 50% reduction in the CHC (*Lamy et al.*, 2015) and in the central DP at the Polar Front during the last glacial period (*Wu et al.*, 2021). The ACC strength reconstruction also exhibits pronounced millennial-scale variability corresponding to ∼15 cm/s fluctuation (from ∼30% to ∼70% of IG values). Similar to the SST record, the millennial scale variability in ACC strength persist in all glacial stages. Altogether, our SST and ACC strength reconstructions from Site U1542 underline the exceptional palaeoceanographic sensitivity at the Chilean margin and provide a unique opportunity to explore in detail the millennial-scale changes of the ACC during G/IG cycles.

790,000 years of millennial-scale events

We used a thresholding approach to distinguish the occurrence of climatic events from the variability of the signal. A Southern Hemisphere event is defined in our record by an abrupt ACC strengthening (103 events identified in total) or SST warming (103 events) (see method, Fig. 5; 10.8). We classified each event by defining two categories based on their amplitudes (Fig. 10.9). We identified 66 major SST events characterized by a warming exceeding 1.6°C and 51 major ACC strengthening events displaying a strengthening greater than ∼10 cm/s. Not all strengthening events in the ACC necessarily are associated with a warming event in SST, as SST events tend to link only the stronger ACC events. These differences might be due to different millennial-scale sensitivities and thresholds for SST and ACC strength changes related to various atmospheric and oceanic forcings. The identification of a millennial-scale event in both SST and ACC strength records, particularly for major events, serves as a robust indicator of climate dynamics that can be related to both oceanic and atmospheric circulation. For instance, during the last glacial period, we consistently observe a major reacceleration of flow strength (increasing from 50% to 80% of the interglacial mean) coupled with a temperature rise of approximately 2 to 3°C toward all major AIM events (*i.e.*, AIM 17, 12, 8 and 4). We found 41 (31 related to millennial-scale events) events monitoring an ACC acceleration concomitant with SST warming within a timeframe shorter than 1 ka. Among these, 17 events present a warming preceding an ACC acceleration, while 5 events show simultaneous occurrences of ACC acceleration and SST warming.

Millennial-scale SST and ACC strength events are amplified during mid-glacial periods, respectively between 4 to 6°C and 35 to 55 % of IG strength (Fig. 5.3A, B), coinciding with periods characterized by an intermediate state of ice sheet volume (Fig. 5.2) (*Jouzel et al.*, 2007). This suggests that the ACC exhibited an enhanced sensitivity to climate oscillations during an intermediate climate state (*i.e.*, transitional periods leading to full glacial conditions) or that events are larger during these periods, consistent with findings from northern hemisphere records (*Barker et al.*, 2019; *Hodell et al.*, 2023; *McManus et al.*, 1999; *Sun et al.*, 2021). For both SST and ACC strength record, the recurrence of the millennial-scale climate events is essentially constant along the record, supported by the positive relashionship between number of event and the duration of each period (Fig. 5.3C, D). This imply that the frequency of events is rather constant, even though the magnitude varies with background climate. Moreover, the frequency of millennial-scale events recorded at Site U1542 seems to follow a stochastic pattern, lacking any discernible cyclic behavior (Fig. 10.7). On the other hand, the magnitude of the events appears to be slighty larger when the duration of the MIS is longer, as supported by the variance of the filtered signal (Fig. 5.3E, F). For instance, the recurrence of events does not change with the Mid-Brunhes Transition (MBT) (*Jansen et al.*, 1986) (59 ACC and 64 SST events over the last 430 kyr), but we observe more majors events (30 ACC and 44 SST major events), when the duration of the associated glacial period increases. This implies that the magnitude of millennial-scale events varies in accordance with background climate and that the MBT affects climate variability from orbital to millennial timescales. In contrast, the amplitude of millennial-scale events are smaller during warmer periods, consistent with the relative stability observed during extended interglacial periods in the Northern Hemisphere (*Hodell et al.*, 2023; *McManus et al.*, 1999; *Sun et al.*, 2021).

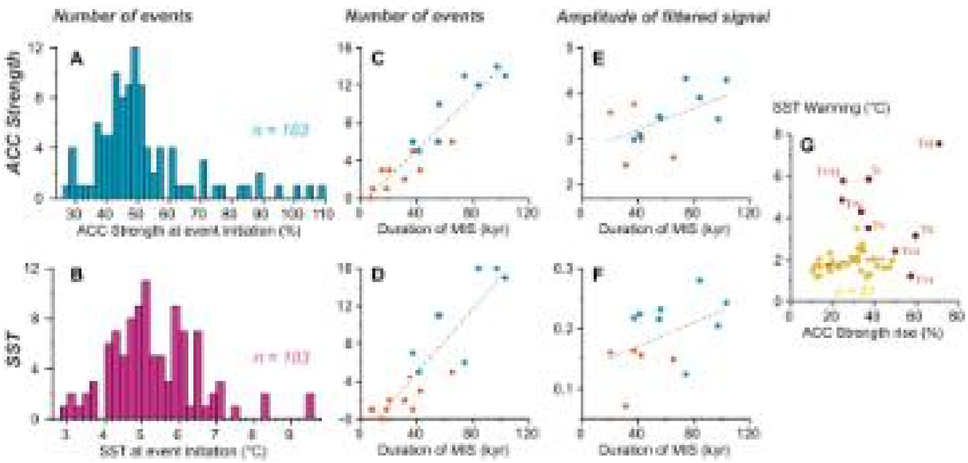

Figure 5.3: **Distribution of millennial-scale events.** (A, B) Distribution of millennial-scale events recorded at Site U1542 according to the condition at the initiation, (C, D) number of events in each MIS and (E, F) amplitude of the filtered SST and ACC strength for each MIS. (G) is the relation between SST warming millennial-scale event occurring synchronous with ACC strengthening millennial-scale events in less than 1 kyr (yellow dots). Red dots indicate SST warming and ACC strengthening at the glacial terminations. Interglacial periods are represented in red and glacial periods are represented in blue. The amplitude is defined by the standard deviation of the filtered (<7 kyr) SST and ACC strength signals. Label numbers indicates MIS.

5.4 Discussion

Sensitivity of the Southeast Pacific to orbital and millennial-scale climate oscillations

At orbital timescales over the past 790 kyr, our reconstructed SST variations at the southern Chilean margin largely follow the atmospheric temperature record of the Antarctic ice core EDC (*Jouzel et al.*, 2007) and the open Southeast Pacific SST recorded at PS75/034-2 (Fig. 5.2C-E) (*Ho et al.*, 2012). On average, the G/IG temperature amplitude varies from 5 to 7°C, slightly smaller compared to the 8°C changes recorded at EDC, but similar to PS75/034-2. However, we observe a ∼2°C SST difference in temperature between Site U1542 and core PS75/034-2, located about 350 km southwest from Site U1542 (Fig. 5.1). This offset can be explained by the influence of the southward CHC, which transports comparatively warmer water masses, thus explaining the higher temperature recorded at Site U1542 versus core PS75/034-2.

Our record presents a predominant spectral power in the eccentricity (100-kyr) band during the Pleistocene. Small amplitude spectral peaks occur at the obliquity (41-kyr) and precessional (23-19-kyr) bands (Fig. 5.2F). Though overall spectral power at the common orbital cyclicities is comparable between the Site U1542 SST records and the Antarctic temperature record, a direct comparison of the records reveals substantial differences at several time intervals. Importantly, we observe a prolonged warming trend throughout MIS 12 (+1°C between early glaciation to termination), MIS 10 (+2°C), and MIS 6 (+2°C). We observe a comparable trend in the PS75/34-2 record where the alkenone-SSTs show a persistent warming trend throughout MIS 12, 10, and 6. A Southern Ocean warming has been observed during the last glacial period and MIS 6a, likely initiated by changes in insolation (Pahnke et Sachs 2006) and more recently in the western Indian Ocean during glacial intervals over past 1.2 Ma (*Nuber et al.*, 2023). This decoupling between mid (Southern Ocean) and high (Antarctica) southern latitudes likely resulted in an increase of the meridional thermal gradient, which potentially increased the supply of moisture to the poles, promoting continued ice sheet growth during MIS 10 and MIS 6 (*Pahnke and Zahn*, 2005). However, this feature is probably not a prerequisite for the ice sheet growth, as no mid-to-high latitude decoupling is observed during MIS 8 and MIS 2. Furthermore, no clear similar trends are monitored by other mid-latitude austral records, in the South Atlantic (*e.g.*, ODP 1090) (*Martínez-Garcia et al.*, 2010) and Southwest Pacific (*e.g.*, MD97-2120) (*Pahnke et al.*, 2003).

On G/IG timescales, changes in the strength of the ACC are synchronous with SST variability (Fig. 5.2B, C). Enhanced flow speeds coincide with warmer periods, while reduced flow speeds coincide with colder periods, implying a close coupling between near-bottom current velocity and SST (Fig. 10.4). The ACC strength-temperature coupling prevailed during the last 800 ka, as supported by a strong ACC strength observed in the DP (*Toyos et al.*, 2020) and during warm periods in the Southeast Pacific (*Ho et al.*, 2012). This relationship extends also to shorter timescales, suggesting a direct connection between Southern Hemisphere temperature fluctuations and ACC strength on both orbital and millennial timescales (Fig. 5.3G). These findings support the idea that a reduction in the strength of DP throughflow is linked to the northward shift of Southern Ocean frontal systems during glacial times (*Lamy et al.*, 2015; *Toyos et al.*, 2020; *Wu et al.*, 2021). In the DP, geostrophic current velocities are highest in the vicinity of the Subantarctic and Polar Fronts (*Koenig et al.*, 2014), and the movement of the fronts (*i.e.*, latitudinal shifts) is linked to temperature changes (*Rintoul*, 2018). Using a grain-size based ACC strength record from sediment core PS97/85, located in the DP at the Polar Front, Wu et al. (S. Wu et al. 2021) found a notable correspondence between millennial-scale peaks in ACC strength and major winter sea ice retreat in the DP. This sea ice retreat is coupled with SWW strengthening and southward shifts, acting as a positive feedback mechanism that amplifies millennial-scale changes in ACC strength

(*Toggweiler et al.*, 2006; *Wu et al.*, 2021).

This amplification of millennial-scale variability manifests as exceptionally high-amplitude SST variability observed in two records from the Chilean margin, ODP site 1233 and core MR16-09PC03 (Fig. 5.4) (*Hagemann et al.*, 2024; *Kaiser et al.*, 2005). These records together with that from Site U1542 exhibit consistency in timing and amplitude, ranging from ∼2-3°C during the last glacial period, comparable to atmospheric temperature reconstructions from the Antarctic ice cores (∼2°C), with higher values during specific periods, such as the LGM (*EPICA community members*, 2004). Located north of Site U1542 (between ∼41°S and 53°S, Fig. 5.1), these sites suggest that the northward deflection of the ACC into the Humboldt Current (*i.e.*, the South Pacific Gyre) records these substantial millennial-scale changes and support the idea of SWW shifts as a primary driver of changes recorded at Site U1542 (*Lamy et al.*, 2015).

A persistent interhemispheric teleconnection

Over the last glacial period, SST records from the Southeast Pacific region have been shown to reveal an 'Antarctic timing' of millennial-scale temperature patterns (*Anderson et al.*, 2021; *Caniupán et al.*, 2011; *Lamy et al.*, 2004). Millennial-scale climate events at Site U1542 are found to be contemporaneous with AIM events (*EPICA Community Members*, 2006) (Fig. 5.4). Additionally, our temperature record is consistent in timing and amplitude with a mid-depth record from the Southwestern Pacific, spanning the past three glacial cycles (Fig. 5.5F; (*Pahnke et al.*, 2003). The Mg/Ca ratio in foraminifera as a sub-surface temperatures proxy and the synchronous $\delta^{13}C_b$ values (*Pahnke and Zahn*, 2005), as an intermediate water mass composition proxy, shows contemporaneous millennial scale oscillations with our alkenone-derived SST and the ACC strength. This suggests that the variability recorded in both records represents surface to mid-depth oscillations of the wider subantarctic Southern Ocean. Throughout the last glacial period, the timing of our millennial-scale climate events coincides with the sediment core PS97/85 (Fig. 5.4D; *Wu et al.*, 2021). This record further reveals that the ACC accelerated during Antarctic warming events, in parallel with the weakening of the AMOC during Heinrich Stadials (*Barker et al.*, 2009) in the Northern Hemisphere (NH), as indicated by high $^{231}Pa/^{230}Th$ ratios (Fig. 5.4C)(*Henry et al.*, 2016).

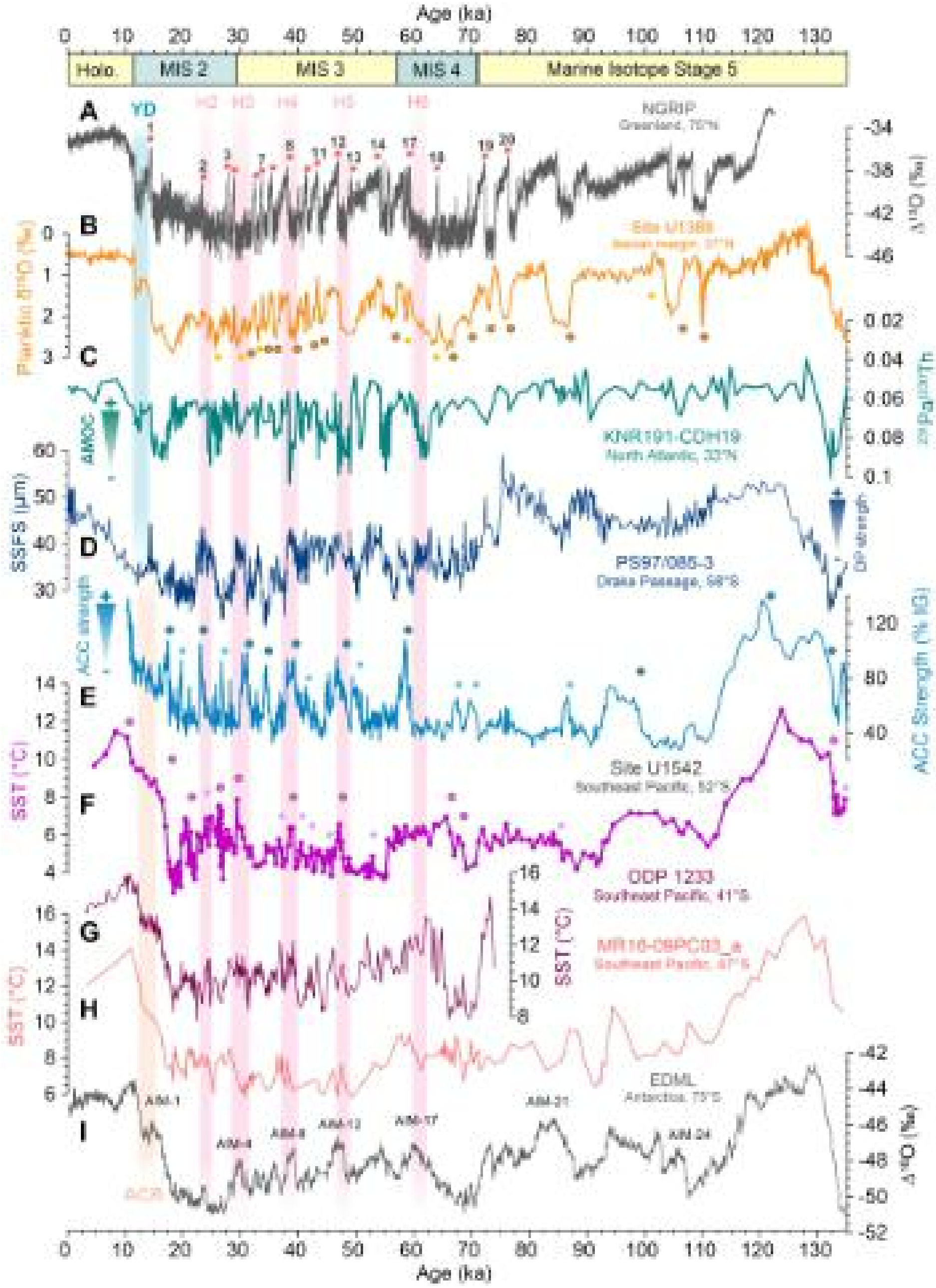

Figure 5.4: **Interhemispheric linkages during the last Glacial Period.** (A) Greenland climate reconstruction (EPICA Community Members 2006; North Greenland Ice Core Project members 2004) recording millennial-scales abrupt events, called D-O events (red dots), (B) planktic δ^{18}O from North Atlantic (*Hodell et al.*, 2023), taken as proxy for SST changes, (C) compilation of Pa/Th as a proxy for AMOC strength (*Henry et al.*, 2016), (D) grain size based strength of DP throughflow reconstruction (*Wu et al.*, 2021), (E) ACC strength, (F) SST at Site U1542, (G) SST from ODP Site 1233 (*Lamy et al.*, 2015), (H) SST from MR16-09PC03 (*Hagemann et al.*, 2024), (I) Antarctic climate reconstruction at EDML site (*EPICA Community Members*, 2006), YD; Younger Dryas, ACR; Antarctic Cold Reversal, H; Henrich events, AIM; Antarctic Isotopic Maxima, MIS; Marine Isotope Stage.

To robustly assess interhemispheric connections across the past 800 kyr, we identified major events at Site U1385 (located at the Iberian margin in the North Atlantic) (*Hodell et al.*, 2023), and within the synthetic Greenland climate reconstruction (*Barker et al.*, 2011), both high-resolution records spanning our study period. The planktic δ^{18}O signal from Site U1385 primarily reflects surface temperature conditions, synchronous with the appearance of DO events in Greenland and, therefore, is an indicator of NH millennial-scale surface water changes. By applying the same thresholding approach used for Site U1542, we identified 110 NH stadial events (69 major events) at Site U1385 over the past 800 kyr, consistent with the findings of *Hodell et al.* [2023]. According to the bipolar seesaw concept (*Blunier and Brook*, 2001), northern stadial events are expected to be associated with ACC strengthening event and SST warming in the Southern Hemisphere, as observed during the last glacial period (Fig. 5.4D) (*Wu et al.*, 2021). To mitigate the impact of age model uncertainties between the two locations, we have chosen to employ a non-overlapping moving window of 10 kyr (*Hodell et al.*, 2023) to evaluate the interhemispheric relation of millennial-scale events occurrence (Fig. 10.6) This approach is thought to maintain the fundamental pattern regardless of the chosen start time. The analysis (Fig. 10.6) reveals similarities between both records in the number of events per 10 kyr, with the highest occurrence observed during glacial periods and terminations, and indicating that the temporal concentration of DO events observed during the last glacial period is unique when compared to the Late Pleistocene. Several studies have suggested that a prolonged intermediate climate state, such as MIS 3, provides favorable conditions for high amplitude DO-type variability (*Barker et al.*, 2011; *Hodell et al.*, 2023). During full glacial boundary conditions (*e.g.*, LGM), NH records suggest relatively stable climate with reduced millennial-scale variability during these periods (*McManus et al.*, 1999). However, our records demonstrate significant millennial-scale oscillations during MIS 10, 8, and 2 at periods of enhanced global ice volume (Fig. 10.6). This interhemispheric disparity likely arises from the enhanced local sensitivity, notably with the Patagonian Ice Sheet that reached the continental shelf edge at their maxima (*Davies et al.*, 2020). For instance, during the LGM, records from the Chilean margin and DP depict higher amplitude millennial-scale events (Fig. 5.4D-H) compared to NH records (Fig. 5.4A-C)

In both sediment records from Site U1542 and U1385, we observe an intensification of SST and δ^{18}O planktic millennial-scale events subsequent to the MBT (Fig. 10.6), consistent with the observation that the recurrence of millennial events increases together with the extended duration of glacial periods. This suggests that the MBT, induced by changes in insolation (*Yin*, 2013), not only amplified the G/IG signal (*Jansen et al.*, 1986), but also impacted the climate on the millennial timescale.

At Site U1385, a notable out-of-phase relationship between benthic and planktic oxygen isotopes representing within a single record a southern signal in deep waters versus a northern signal in surface waters, respectively, has been documented (*Shackleton*, 2000 This out-of-phase pattern aligns with Antarctic and Greenland climate records, respectively, and illustrates the bipolar seesaw mechanism, extended over the mid-to-late Pleistocene (*Hodell et al.*, 2023; *Margari et al.*, 2010).

We find millennial-scale features of SST and ACC strength at Site U1542 matching the North Atlantic record, within age model uncertainties between the sites. For instance, during the penultimate glacial period, SST and ACC strength millennial climate events at Site U1542 are in phase with benthic δ^{18}O fluctuations observed in the Iberian margin sediment core (referred to as AIM6i to AIM6vi,between 180 et 155 ka) (*Margari et al.*, 2010), themselves synchronous with AIM events (Fig. 5.5, 10.12). Expanding upon these observations, we find that several major surface warming and ACC strengthening episodes recorded at Site U1542 can be associated with negative benthic δ^{13}C incursions in the North Atlantic at Site U1308 (Fig. 5.5B, 10.12), and/or increased ice-rafted debris (IRD) concentrations at ODP 983 (Fig. 5.5A, 10.12): both parameters associated with a reduced AMOC during these events (*Barker et al.*, 2019; *Hodell et al.*, 2023). This suggests that these important variations of the DP, that have been linked to AMOC instability over the last glacial cycle (*Wu et al.*, 2021), persisted over the past 800 kyr. Furthermore, this one-to-one relationship reinforces previous findings highlighting strong interhemispheric climate linkages on orbital and millennial time scales (*Knorr and Lohmann*, 2003; *Oka et al.*, 2021).

In addition to these oceanic mechanisms for interhemispheric climate linkages related to the bipolar seesaw, important atmospheric connections have been proposed to operate, at least for the last glacial cycle. For example, strong millennial-scale SST warming during Heinrich event 1 at Southeast Pacific Site 1233 has been linked to southward displacement and/or strengthening of the SWW induced by the southward shift of the Intertropical Convergence Zone (*Chiang*, 2009). This atmospheric interhemispheric bridge would plausibly affect both SSTs and ACC strength, although we acknowledge that the ACC flow is affected by forcing other than wind, such as the buoyancy forcing effect and eddy activity (*Munday et al.*, 2013), which can regulate ACC flow strength.

Studies of anthropogenic climate change using both models and observations detect an acceleration of zonally averaged zonal flow on the northern flank of the ACC and identify anthropogenic ocean warming as the dominant driver (*Shi et al.*, 2021). This reinforces the fundamental physical relationship between SST and ACC speeds that form the baseline of this study. Moreover, considering the widely anticipated weakening of the AMOC in response to anthropogenic warming (*Bakker et al.*, 2016; *Weijer et al.*, 2020), state of the-art climate models seem to reinforce the teleconnection between Southern Ocean conditions and circulation in the North Atlantic.

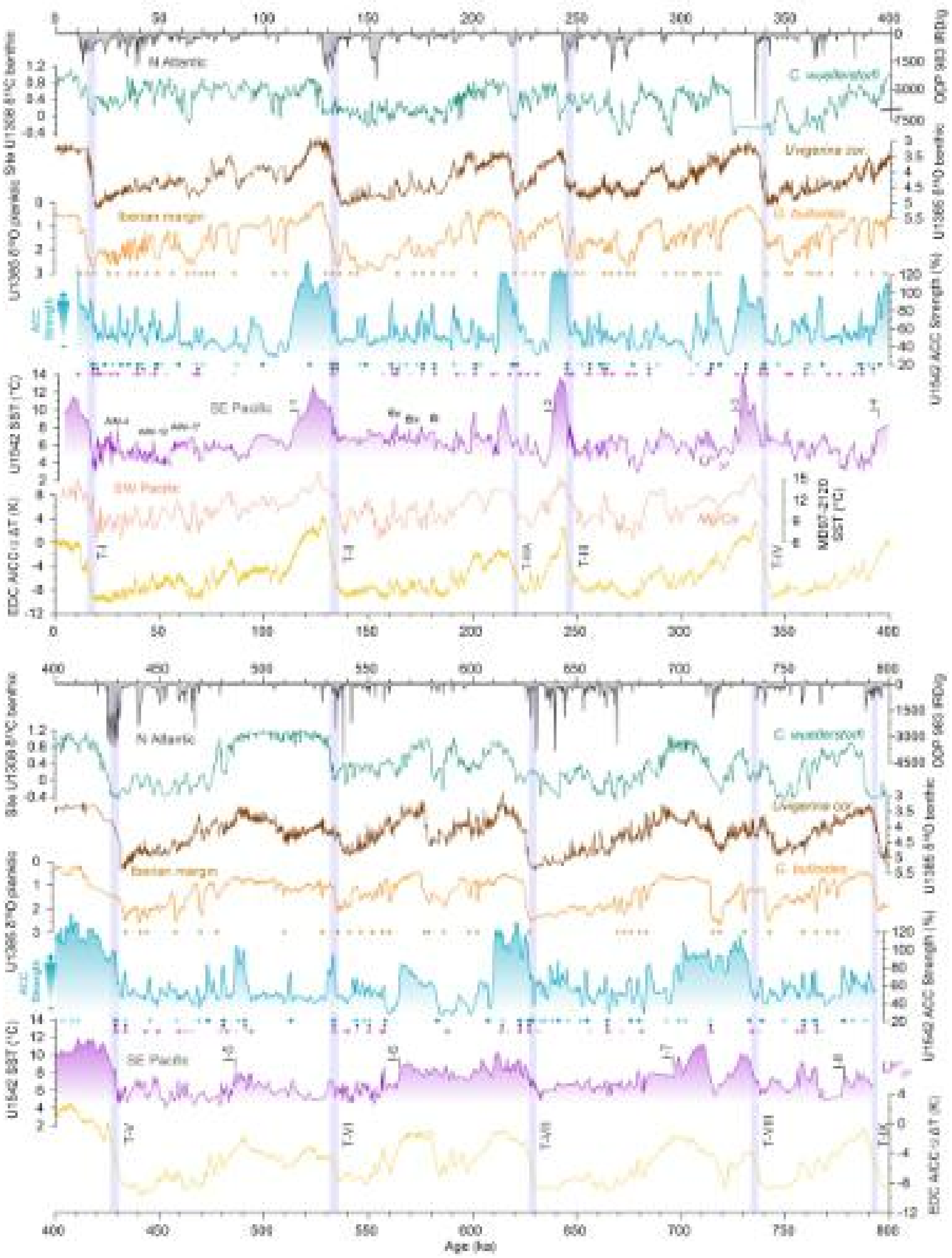

Figure 5.5: **Interhemispheric millennial-scale reconstruction of the ACC strength and SST.** (A) Ice-rafted debris at ODP Site 983 (*Barker et al.* 2019), (B) benthic δ^{13}C from Site U1308 indicating mixing ratio between northern and southern sourced waters (*Hodell et al.*, 2008), (C) planktic δ^{18}O from Site U1385 (*Hodell et al.*, 2023) taken as proxy for SST changes, (D) ACC strength and (E) SST from Site U1542 (this study), (F) Mg/Ca-derived SST from the Southwest Pacific (*Pahnke et al.*, 2003), and (G) Antarctic ice core EDC temperature record (*Jouzel et al.*, 2007) on the AICC2012 age model (*Bazin et al.*, 2013). Purple, blue and orange dots respectively represent SST, ACC and stadial events recorded from Site U1542 and Site U1385. Timing and nomenclature of isotopic stage follow (*Lisiecki and Raymo*, 2005). Vertical purple bars and roman numerals indicate glacial terminations.

Role of ACC in CO_2 exchanges

To evaluate the role of ACC strength variability in driving atmospheric carbon dioxide (CO_2) variability, we compare our ACC strength reconstruction with the rate of atmospheric CO_2 changes, smoothed over a 2 kyr period (Fig. 5.6) (*Barker et al.*, 2019). 31 (10 related to glacial terminations) millennial-scale CO_2 increase events can be associated with millennial ACC strengthening events within 7 kyr windows (Fig. 5.6A, B, S13), suggesting a direct link between changes in glacial ACC flow and shifts in global atmospheric CO_2 concentrations. Moreover, the relative changes in flow strength appear to be positively correlated to the amplitude of CO_2 variations (Fig. 10.13). For instance, during glacial terminations, the increase of 60 to 80 ppmv (Fig. 5.6C), corresponds to a 50 to 80% acceleration in ACC flow. At millennial timescales, we observe reduced but discernible variability. For instance, during the 6i event (∼178 ka), a 40% increase in ACC strength corresponds to 15 ppmv rise, and during AIM-17 (∼60 ka), a 35% ACC increase corresponds to 30 ppmv rise. In total, 21 millennial-scale ACC strengthening events (from 28% to 60%) can be associated with atmospheric CO_2 release events (from 5 ppmv to ∼30 ppmv), showing a linear correlation (Fig. 10.13).

The Southern Ocean modulates the exchange of CO_2 between the deep sea and the atmosphere (*Rintoul*, 2018; *Toggweiler et al.*, 2006). The latitudinal shifts of westerlies exert control over the balance between the organic carbon pump, which sequesters carbon into the deep ocean through the sinking of organic carbon from the surface ocean (*Gottschalk et al.*, 2016; *Sigman et al.*, 2021) and the release of CO_2 from ventilation of deep water upwelling in response to surface ocean stratification (*Anderson et al.*, 2009; *Bakker et al.*, 2016; *Skinner et al.*, 2010). The mechanistic relationship between surface ocean conditions and atmospheric CO_2 changes is closely tied to shifts in the SWW, a major driver of CO_2 upwelling (*Anderson et al.*, 2009), and therefore the ACC strength (*Lamy et al.*, 2015; *Wu et al.*, 2021). *Ahn and Brook* [2008] and more recently (*Barker et al.* [2019]) have observed a relative shoaling in the North Atlantic deepwater formation as well as an increase in IRD deposits in the North Atlantic during phases of rising CO_2 (Fig. 5.5A), possibly initiated by freshwater input. An AMOC disturbance induces a change in the meridional heat transport resulting in heat being retained in the Southern Hemisphere, which can then melt sea ice (*Skinner et al.*, 2010) and/or cause a southward migration of the Intertropical Convergence Zone (*Anderson and Carr*, 2010). This can result in a strengthening and southward displacement of the SWW, enhancing ACC strength, decreasing Southern Ocean stratification, promoting ventilation, and consequently, increasing atmospheric CO_2 levels. Our results confirm and extend the role of the millennial-scale northern ACC/CHC reacceleration in enhancing the exchange between surface and deep water in the Southern Ocean and the corresponding release of CO_2 (*Anderson and Carr*, 2010; *Anderson et al.*, 2009; *Skinner et al.*, 2010).

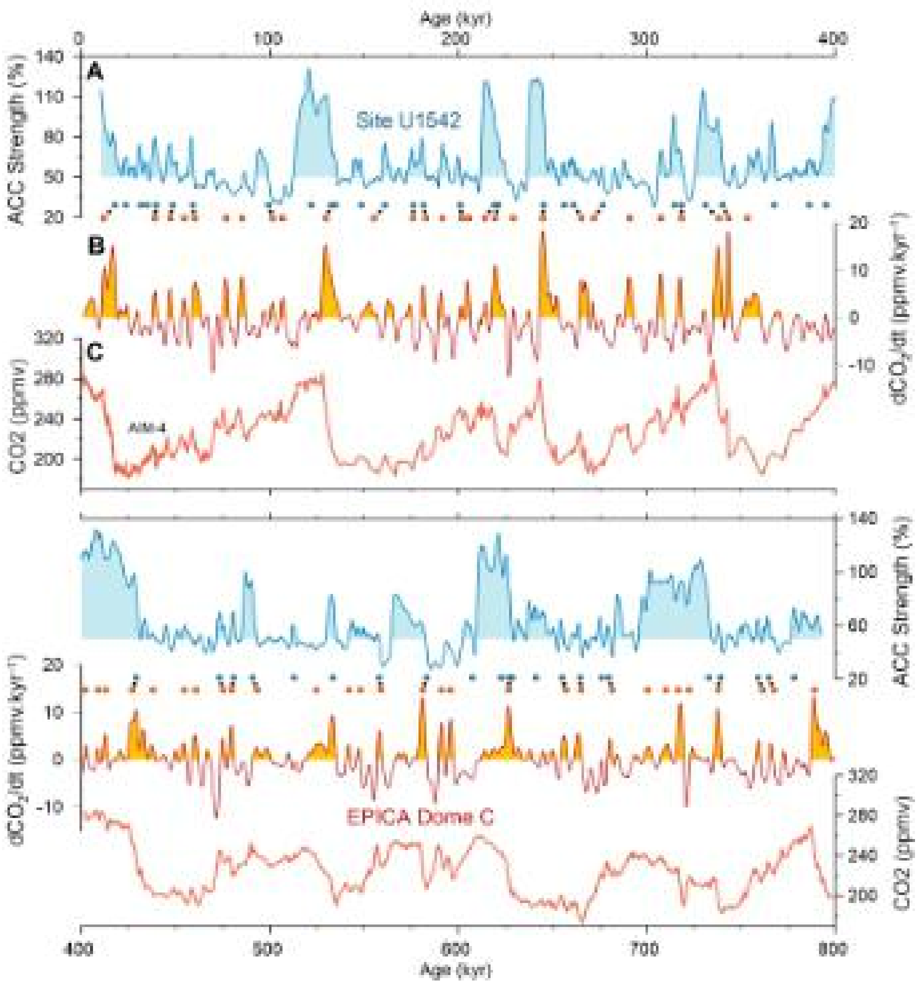

Figure 5.6: **Rate of atmospheric CO_2 changes and Antarctic circumpolar conditions during the Pleistocene.** (A) ACC strength from Site U1542, (B) Rate of atmospheric CO_2 changes ($\delta CO_2/\delta t$) from (*Barker et al.*, 2019) based on (C) atmospheric CO_2 concentrations from the EDC ice core, (*Bereiter et al.*, 2015). Blue dots indicate major ACC strengthening events, yellow dots indicate CO_2 increase events and black dots indicate association ($n = 31$) between both events in less than 7 kyr.

During each glacial inception, a reduction in SWW wind-driven upwelling, marked by the abrupt drop in the ACC strength record (up to 80% reduction during Inception 6, 3, 2 and 1; Fig. 5.6A) may have reduced exchange of water from the deep ocean to the surface, thus contributing to the storage of carbon in the deep ocean and the reduction of atmospheric CO_2 (*Sigman et al.*, 2021). Other mechanisms, such as dust-borne iron fertilization (*Martin*, 1990), SST and salinity changes (*Köhler et al.*, 2005) also contributed to the continuing and gradual drawdown of CO_2 (Fig. 5.6C) throughout the glacial stage by enhancing the efficiency of the global ocean's biological pump (*Martinez-Garcia et al.*, 2014; *Sigman et al.*, 2021).

Site U1542, located underneath the palaeoceanographically sensitive Cape-Horn current, provides unprecedented insights into the millennial-scale ACC variability over the past 790 kyr in the Southeast Pacific. Coupled ACC strength and SST changes provide compelling evidence that millennial-scale variability previously documented for the last glacial cycle persisted over the past 790 kyr. Our findings reveal that the amplitude of the millennial-scale events directly correlate with the duration of the glacial stages. In line with evidence from other Southern Ocean records, this variability is representative of the broader Southern Hemisphere. Despite age model uncertainties, a comparison with Northern Hemisphere records indicates that the interhemispheric dynamics observed during the last glacial period have persisted over the Late Pleistocene. Periods of climate instability in one hemisphere align with those in the other hemisphere. Moreover, our findings shed light on the impact of the DP throughflow on Atlantic circulation on millennial timescales, and the significant role played by the ACC promoting inter-basin water mass exchange in the Southern Ocean that can influence CO_2 exchanges. Notably, these findings align with contemporary observations of a warming and accelerated Southern Ocean (*Shi et al.*, 2020) in conjunction with AMOC weakening (*Srokosz and Bryden*, 2015) under anthropogenic forcing of the climate.

5.5 Material & Methods

Sediment record

We analyzed a Pleistocene sediment record recovered during International Ocean Discovery Program (IODP) Expedition 383 Site U1542 (*Lamy et al.*, 2021). Positioned in the Southeast Pacific at 52°42.29'S, 75°35.77' W, IODP Site U1542 is situated approximately 30 nautical miles west of the entrance to the Strait of Magellan, at a water depth of 1,101 meters (Fig. 5.1). The site sits at the upper slope of the Chile continental margin, within a relatively small-scale sediment depocenter ("sediment drift"). The nearly continuous, undisturbed, 249-meter-long sedimentary sequence recovered at Site U1542 covers the past 790,000 years with sedimentation rates that exceed 30 cm/kyr. The glacial sedimentary sequence is primarily constituted of siliciclastic sediments with low carbonate contents (∼1–12 wt% $CaCO_3$), and biogenic silica contents ranging from 1 to 4 wt%. Interglacials are characterized by sandy foraminiferal ooze (∼30–55 wt% $CaCO_3$) deposited during warm interglacial periods (*Lamy et al.*, 2021). From an oceanographical perspective, Site U1542 is situated beneath the southward-flowing Cape-Horn Current, a northern branch of the Antarctic Circumpolar Current that extends towards the Drake Passage. Additionally, it is located at the lower limit of Antarctic Intermediate Waters (AAIW), close to or within the major modern AAIW formation.

Southern Chilean Margin composite record

We combine the sedimentary record from Site U1542 with the published records from nearby located Calypso piston core, MD07-3128. The U1542 'pre-site survey' sediment core MD07-3128 (30.33 m) was recovered in 2007, at 52°39.57'S, 75°33.97'W (1,032 m water depth), situated only ∼5 nautical miles from U1542 during the IMAGES (International Marine Past Global Changes Studies) XV-MD159-Pachiderme cruise on board R/V Marion Dufresne. Given the availability of several high-resolution multi-proxy records for MD07-3128 (*Caniupán et al.*, 2011; *Lamy et al.*, 2015), we chose to incorporate the approximately 65 kyr of MD07-3128 sediment core data into the corresponding section of the Site U1542 sediment record, in order to build a composite sequence with very high resolution in the last glacial period. To achieve this, we aligned the bottom of MD07-3128 with the corresponding age in Site U1542, using reflectance b* records from both cores and alkenone-derived SST and XRF Zr/Rb serving as controls (Fig. 10.2). The tie point was identified at 28.63m (56.88 ka, (*Anderson et al.*, 2021) in MD07-3128 and at 25.47 CCSF-A (m) in U1542. Due to the observed persistent temperature offset in alkenone-derived SST between the two records, attributed to the use of a different gas chromatographer column type for the MD07-3128 core, we applied a correction of + 1.44°C to the MD07-3128 SST data from *Caniupán et al.* [2011] (Fig. 10.2). This correction is derived from the repeated measurement of a reference alkenone standard using both chromatography columns employed for the two sedimentary records. We note that this correction does not change the amplitude between G/IG and millennial-scale shift of SST. Furthermore, a discrepancy in XRF ratio Zr/Rb values between Site U1542 and MD07-3128 has been observed. Considering that XRF measurements may exhibit variability across different laboratories, we employed here a simple linear regression between both records to assess the drift between devices. The regression equation (ValueU1542 = 0.6779*ValueMD07-3128 + 0.1836) was utilized to align MD07-3128 values to the same scale as Site U1542 values.

Age model

The stratigraphy of MD07-3128 is well-constrained by 13 Accelerated Mass Spectrometry 14C AMS age from mixed planktonic foraminifera, along with the identification of the Laschamp paleomagnetic excursion (*Anderson et al.*, 2021; *Caniupán et al.*, 2011; *Lamy et al.*, 2015). For Site U1542 in the time interval 65-800 ka, we tuned glacial terminations and inceptions based on the XRF Ca/counts from Site U1542 to the Antarctic ice core EDC temperature record (*Jouzel et al.*, 2007) on the AICC2012 age model (Fig. 10.3) (*Bazin et al.*, 2013), which was primarily realized onboard during IODP Expedition 383. At millennial time-scales, we aligned our benthic foraminiferal (*G. uvigerina*) oxygen isotope (δ^{18}O) record with the EDC temperature record. As Site U1542 is located at a relatively shallow depth, several periods exhibit strong variability, with a relatively subdued G/IG variability in the benthic record. For instance, MIS 13 and 7 are not evident in the XRF Ca or benthic $\delta^{18}O$ record. To address this, we added additional tuning points using our SST reconstruction with reference to the Antarctic ice core. For each tie point, the proxy used can be found in figure 10.3. All tuning were performed using AnalySeries (*Paillard et al.*, 1996).

Stable oxygen analysis on benthic foraminifera

Foraminiferal stable oxygen ($\delta^{18}O$) measurements were performed on samples of each 2 shells of the infaunal benthic foraminifera *G. uvigerina peregrina* from core Site U1542. The samples were wet-sieved using a 125 μm mesh, oven-dried at 50°C and then stored in glass vials. *G. uvigerina peregrina* from the sediment fraction larger than 250 μm were handpicked under a binocular microscope every 20 cm. Isotopic analyses were performed on a Thermo Scientific MAT 253 mass spectrometer with an automated Kiel IV Carbonate Preparation Device at AWI. External reproducibility of $\delta^{18}O$ measurements based on an internal laboratory standard (Solnhofen limestone) measured over a 1-year period together with the samples was better than 0.08‰ for $\delta^{18}O$. Isotope data has been converted to the delta notation. The isotope values were calibrated versus IAEA603 and are given in per mil (‰) relative to the V-PDB (Vienna Pee Dee Belemnite) standard.

Biomarkers analysis

For the determination of alkenones at Site U1542, about 5 g of freeze-dried and homogenized sediment samples were extracted by accelerated solvent extraction (ASE 350, Dionex) with a mixture of dichloromethane and methanol (DCM:MeOH, 9:1, v/v) at Alfred Wegener Institute Bremerhaven. The resulting total lipid extract was further separated into three fractions through column chromatography with silica gel as the stationary phase. *n*-alkanes were eluted with Hexane (5 ml), alkenones were separated using DCM (5 ml), and glycerol dialkyls glycerol tetraethers (GDGTs) were eluted with DCM: MeOH (1:1; 4 ml). The first and third fractions (*i.e.*, *n*-alkanes and GDGTs, respectively) were stored for subsequent investigations. Internal standards (squalane, hexatriacontane, C_{46}-GDGT) added before extraction served for quantification purposes. Alkenones were analysed by gas chromatography on an Agilent 7890 fitted with a flame ionization detector using an Agilent VF-200 ms capillary column (60 m length, 250 μm diameter, 0.25 μm film thickness). The oven temperature was programmed to be held at 50 °C for 2 min, then increased at 20 °C/min to 255 °C, at 3 °C/min to 300 °C, at 10 °C/min until 320 °C and held for 10 min. The identification of alkenones was achieved by comparing chromatographic retention times of the samples with those of a laboratory *Emiliania huxleyi* culture extract that was routinely used as a working standard to control data quality. The reproducibility of the procedure was evaluated using a homogeneous sediment standard extracted simultaneously with our samples. To convert $U_{37}^{k'}$ values (expressed as the ratio of $C_{37:2}$ /($C_{37:2}$ + $C_{37:3}$)), into an estimation of SST, we applied here the calibration of *Prahl et al.* [1988] (SST = ($U_{37}^{k'}$ –0.039) /(0.034)), widely used in paleotemperature reconstructions. Analytical precision based on replicate analyses of the culture extract was 0.23°C (n = 29). Most data sets used $U_{37}^{k'}$, except for the PS75/34-2 record that use U_{37}^{k}, as no G/IG variability is observed before 430 ka (*Ho et al.*, 2012).

X-Ray Fluorescence

The high-resolution X-ray fluorescence (XRF) scanning measurements at Site U1542 were conducted using an Avaatech (non-destructive) XRF Core Scanner at Texas A&M University. The scanning was performed at intervals of 3 cm (area 10 x 12 mm, downcore x cross-core) across the core in three runs 10kV (Tube current 0.16 mA, live time 6s, no filter), 30kV (1.25 mA, 6s, Pd-thick filter) and 50kV (0.75 mA, 10s, Cu filter).

Current speed reconstruction

To assess changes in near-bottom flow speed, we employed the sortable silt (SS) proxy. SS is widely used to assess variations in near-bottom flow speed in deep-sea sediments. This sedimentological parameter operates on the principle that a coarser mean size reflects stronger near-bottom flow, through selective deposition and winnowing (*McCave et al.*, 1995). This proxy exhibits a strong correlation with modern variability in the Drake Passage area (*Wu et al.*, 2021). For the grain-size analysis, the terrigenous fraction was isolated from 5g of freeze-dried bulk sediment by treating each sample with 5 ml H_2O_2 (35%), 5 ml HCl (10%) and 5 ml NaOH (6%) while being heated, to remove organic matter, carbonate and biogenic silica. The samples were rinsed and centrifuged until reaching a neutral pH between each step. Immediately prior to measurements, $Na_4P_2O_7$ - $10H_2O$ (sodium pyrophosphate) was added to the leached material and the samples were sonicated for 30s, to avoid aggregations. Grain-size analyses were carried out with a Mastersizer 3000 (Malvern Panalytical) at the Leibniz Institute for Baltic Sea Research Warnemünde (IOW). To investigate whether the sediments were subject to significant bottom current sorting, the mean sortable silt grain-size (SS; geometric mean of the 10 – 63 μm silt fraction) and the sortable silt percentage (SS%, defined as the 10–63 μm fraction relative to the <63 μm fraction) were calculated after *McCave et al.* [1995] utilizing the software GRADISTATv9.1 (*Blott and Pye*, 2001). Several studies suggested that changes in the element compositions of fine-grained sediments, particularly the zirconium/rubidium (Zr/Rb) count ratio, hold significant potential as a tracer for grain-size variations of marine sediments, providing valuable insights into current strength(*McCave et al.*, 1995). Recently, the logarithmic Zr/Rb ratio derived from XRF core scanning has been utilized as a proxy for reconstructing millennial-scale variability in near-bottom flow speed in the Drake Passage (*Lamy et al.*, 2015; *Toyos et al.*, 2020; *Wu et al.*, 2021) and in the Southern Ocean (*Wu et al.*, 2020). To apply the (Zr/Rb) proxy to our record, we correlated SS and ln(Zr/Rb), obtaining a tight linear-positive correlation (SS = 16.18 x ln(Zr/Rb) + 12.88, $r2 = 0.76$, $n = 94$, Fig. 10.5). For a continuous resolution along the record, we resampled at 100-year intervals, subsequently 0.6 kyr smooth, broadly following the resolution of alkenones SST reconstruction. This running mean window has also the advantage of being close to the smoothing window selected by *Barker et al.* [2011] to predict abrupt events, providing a reasonable compromise between noise reduction and signal fidelity. We calibrated the ultra-high resolution (~100 years on average) XRF measurements with grain size analyses, thereafter getting a current speed reconstruction by using the calibration of SS for the Scotia-Weddell Sea region (SS = 0.59U + 12.23) (*McCave et al.*, 2017) (Fig. 10.5).

Spectral analyses and filtering

To identify periodic components in the spectrum of the U1542 record, spectral analyses were performed using the Blackman-Tukey spectral power estimator, implemented in the Analyseries software. Prior to analysis, linear trends were removed, and values were normalized. The frequency scale was resampled from 0 to 0.1 with a step of 0.0002. A Bartlett window was applied, and the bandwidth was approximately set to 0.005. Prior to analysis, our record was evenly sampled at 200 years. In consideration of the lower resolution of PS75/34-2, the record was evenly sampled at 1 ka, and the frequency scale step was adjusted to 0.0005. To remove the long-term insolation-driven signal from our record (Milankovitch periodicity), a high-pass Finite Impulse Response (FIR) filter was applied using the PAST software, which uses the Parks-McClellan algorithm. A cut-off at 7 kyr was selected, consistent with several previous studies (5 kyr in *Pahnke et al.* [2003], 7 kyr in *Barker et al.* [2011]). The filtered result emphasizes millennial-scale variability and is thought to remove the background climate evolution on G-IG timescales.

Characterization of the millennial scale events

To identify millennial scale events in the records, we used a thresholding approach, following *Barker et al.* [2011] to predict the occurrence of Dansgaard-Oeschger (DO) events. We identify events using minima in the first-time differential of the 600 years mean signal giving similar results from the filtered signal (*i.e.*, < 7 kyr to exclude long-term insolation driven signal) of ACC strength and SST record (Fig. 10.8). This approach is thought to avoid any subjectivity in the detection of millennial-scale events (*Hodell et al.*, 2023). Each event is therefore defined by an abrupt ACC strengthening or SST warming. The empirical choice of the threshold underscored the importance of maintaining a balanced approach. An overly sensitive threshold could indeed prevent the distinction between environmental changes in the record and variations introduced by analytical and calibration uncertainties in the alkenone-SST and bottom-current estimates. On the other hand, a threshold that is too insensitive might omit important events, potentially leading to a biased representation of Pleistocene millennial-scale changes. We selected a threshold with the goal of effectively distinguishing between event magnitudes chosen to ensure that the number of events fell within the range of DO events observed over the last glacial period and in accordance with estimations for the northern hemisphere records. Ultimately the threshold selected was set higher than the standard deviation of the data to only capture climatic events, minimizing the inclusion of noise or non-climatic variations in the sedimentary record. Subsequently, we identified major events by separating in two population each event in function of their respective amplitude (Fig. 10.9). Each amplitude is defined by the difference between the minima before each event (on a 1 kyr average) and the maxima after each event (on a 1 kyr average) (Fig. 10.8).

Acknowledgments

We thank the captain, crew, and scientific party of R/V JOIDES *Resolution* for their support during International Ocean Discovery Program (IODP) Expedition 383 'Dynamics of Pacific Antarctic Circumpolar Current (DYNAPACC)'. We acknowledge funding by the AWI Helmholtz-Zentrum for Polar- und Meeresforschung through institutional research program 'Changing Earth – Sustaining Our Future' through the PhD program INSPIRES. The authors are grateful to N.Beech that greatly assisted in improving the English of the manuscript, to Nils Plonkas and to the IOW-IODP project DFG Priority Programme 527 grant SESPOD (AR 367/16-1).

Author contributions

V.R. and F.L. conceived the study. V.R. conducted the analysis and drafted the manuscript. V.R., N.R. and H.S. conducted alkenones measurements. H.W.A provided sortable silt measurements. L.L.J and I.M.V conducted the isotope measurements. V.R, F.L, L.L.J and H.W.A constructed the age model. All authors contributed to the scientific discussion, reviewed and contributed to the text of the manuscript.

Chapter 6

Patagonian Ice-Sheet dynamic controlled by local sea surface temperature

To be submitted

Vincent Rigalleau, Frank Lamy, Helge W. Arz, Julia Hagemann, Nicoletta Ruggieri, Antje Wegwerth, Henrik Sadatzki & Ralf Tiedemann

6.1 Abstract

Past changes in the extent of the Patagonian ice sheet (PIS) played a critical role in paleoclimate at global and regional scales. The PIS affects sea level changes and albedo, impacts sediment supply to the continental margin, and influences the availability of sediments in the Patagonian outwash plains which impacted dust generation and thus indirectly iron fertilization in the Southern Ocean. Traditionally, the maximum geographic extent of the ice sheet is mainly determined through geomorphological mapping of continental moraine sequences often absolutely dated through radionuclides. Unfortunately, older glaciations are mostly eroded by more recent glacial advances, resulting in an incomplete picture of past glaciations from terrestrial archives. In this study, we use the sediment record from International Ocean Discovery Program (IODP) Site U1542 on the Chilean margin (∼53°S) to investigate PIS changes back in time. We use ice-rafted debris and terrigenous sediment accumulation rates, together with terrestrial biomarkers to reconstruct the history of the PIS over the past 790,000 years. This study

presents the first detailed, continuous reconstruction of the PIS covering the middle and late Pleistocene. The timing of enhanced terrestrial sediment deposition overall corresponds to the age and extent of Patagonian moraines and mirrors dust records from Antarctic ice cores and deep-ocean sediment cores from the South Atlantic. The close connection between PIS and dust input to the Southern Ocean emphasizes its role in the global carbon budget. Our PIS records highlight the crucial role of sea temperature in controlling PIS growth. Additionally, the sediment discharge to the Chilean margin is controlled by sea level changes allowing the advance of the PIS to the continental margin and strengthening sediment supply during sea level lowstands.

6.2 Introduction

A significant fraction of past variations in atmospheric carbon dioxide concentrations (CO_2) during the Earth's most recent period are connected to changes in the supply of dust to the Southern Ocean (*Lambert et al.*, 2008; *Lamy et al.*, 2014; *Martínez-Garcia et al.*, 2011). This dust-climate coupling supports the iron fertilization hypothesis, according to which the windblown dust, carrying soluble iron (Fe) to the Fe-deficient Southern Ocean, may have stimulated the net primary production and carbon sequestration, thereby contributing to atmospheric CO_2 drawdown during ice ages (*Martin*, 1990). Recent data and model-based estimates indicate that iron fertilization enhances glacial Southern Ocean biological productivity by one-third (*Weis et al.*, 2024), consistent with estimates of a contribution of ~25 ppm to the glacial CO_2 drawdown. Southern South America (here referred to Patagonia) plays a fundamental role in this process, as it serves as the primary dust source to the Southern Hemisphere, exporting dust to the Southern South Atlantic (*Martinez-Garcia et al.*, 2014), to Antarctica (*Basile et al.*, 1997; *Grousset et al.*, 1992; *Lunt and Valdes*, 2001; *Sugden et al.*, 2009), and potentially even around the globe to the Central South Pacific (*Struve et al.*, 2020). The Southern Andean region in Patagonia is the only mountain barrier intersecting the core of the Southern Westerly Wind belt (SWW) at latitudes between 49 and 53°S, hence facing windy and rainy climatic conditions and strong lee-side acceleration and dry climates east of the Andes. In this area, variations in the extent of the PIS during Quaternary glaciations, serve as a major fine-grained sediment producer, including a high proportion of Fe-rich dust-size particles released in the outwash plains (*Sugden et al.*, 2009).

Despite the importance of the PIS for regional and global climate, the more detailed reconstruction of PIS dynamics over multiple glacial cycles is not well constrained. This is mainly because the most recent glacial advance during the Last Glacial Maximum (LGM) eroded and overprinted archives of previous glaciations. Consequently, land-based information on older glacial cycles is inherently incomplete (*Hein et al.*, 2017; *Mendelová et al.*, 2020; *Peltier et al.*, 2021). Therefore, our knowledge of past changes in PIS volume and its geographic extent relies on indirect methods, mainly through continental ice-derived sedimentary sequences on land (*e.g.*, radionuclide-dated moraines; *e.g.*, PATICE; *Davies et al.*, 2020). Moreover, glacial advances in older than LGM deposits are difficult to date accurately, thus preventing a precise correlation of the timing of successive PIS advances with the marine isotope stratigraphy framework (*Lisiecki and Raymo*, 2005). In the marine realm, due to high sedimentation rates on the continental shelf edge and slope, so far examined marine sediment sequences including their PIS signal are likewise only restricted to the last glacial period (*Caniupán et al.*, 2011; *Hagemann et al.*, 2024; *Kaiser et al.*, 2005; *Kilian and Lamy*, 2012). The reconstruction of the PIS and more broadly mid-latitude ice-sheet extent during Quaternary glaciations is nevertheless crucial because former ice sheets did not simply react passively to glacial/interglacial variability. Instead, they played a dynamic role by amplifying, pacing, and driving local to global climate changes, participating in sea level changes, albedo effect, and sediment production (*Clark et al.*, 1999). Also, the interhemispheric teleconnections between Southern Hemisphere mid-latitude glacier development and Northern Hemisphere alpine glacier and ice sheet dynamics are crucial for understanding the paleoclimatic forcing of Quaternary glaciations at orbital and millennial time-scales (*Darvill et al.*, 2016; *Denton et al.*, 2022; *Mercer*, 1984; *Oerlemans*, 2005; *Schaefer et al.*, 2006).

Paleoclimatic reconstructions since the last glacial period show that Patagonia was a highly sensitive region to environmental and climate change (*Davies et al.*, 2020; *Euler and Ninnemann*, 2010; *Kilian and Lamy*, 2012; *Lamy et al.*, 2004). The maritime location of the ice sheet along the Chilean margin establishes a close connection with atmospheric and oceanic circulation in the southeast Pacific and the northernmost reaches of the Antarctic Circumpolar Current (ACC; *Hagemann et al.*, 2024; *Kaplan et al.*, 2008; *Peltier et al.*, 2021. Latitudinal shifts and variations in the intensity of the SWW belt strongly influence the supply of moisture to the Southern Andes, thereby controlling precipitation that affects the extent of Patagonian glaciers. These changes also impact vegetation, erosion, and subsequent fluvial sediment input (*e.g.*, *Davies et al.*, 2020; *Kilian and Lamy*, 2012; *Peltier et al.*, 2021; *Sepúlveda et al.*, 2009). Additionally, the sea surface temperature (SST) of the Southeast Pacific is closely linked to the dynamics of the ACC and the SWW and significantly influences the PIS extent (*Denton et al.*, 2022; *Mercer*, 1984). More generally, the coherent chronology of glaciations in the New Zealand Alps and Patagonia suggests common orbital-scale forcing mechanisms that involve large-scale atmosphere changes (*Darvill et al.*, 2016; *Denton et al.*, 2010, 2022; *Kaplan et al.*, 2008; *Peltier et al.*, 2021). For instance, it has been suggested that the expansion of Southern Hemisphere ice sheets depends on the local summer duration (*Huybers and

Denton, 2008). Moreover, southern mid-latitude glaciers advanced contemporaneously with cold Antarctic stadials (*Darvill et al.*, 2016; *García et al.*, 2018; *Hagemann et al.*, 2024; *Shulmeister et al.*, 2019).

Despite limited preservation of pre-LGM moraine systems, various studies shed light on the timing of glacier advances since the so-called Great Patagonian Glaciation around 1.2 million years ago (*Hein et al.*, 2017). For example, evidence for Rio Corcovado glacier (45°S) expansion has been noted for MIS 8 and MIS 6 (*Leger et al.*, 2023). While there is a solid grasp of the most recent glaciation and deglaciation in Patagonia, earlier glaciations remain less documented. Extended sediment records are primarily found on the continental margin north of the rather limited northernmost PIS off central Chile (ODP Site 1234; *e.g.*, *Barth et al.*, 2018; *Heusser et al.*, 1999) and further offshore in the southern section of the southeast Pacific (GeoB3327-5 and PS75/034-2; *Ho et al.*, 2012; *Tapia et al.*, 2021). These more offshore records are at the western limit of the range of terrigenous sediment input from South America and their significance in reconstructing long-term PIS variations is limited. However, reconstructing the evolution of the former PIS over multiple glacial/interglacial variability would offer unique insights into past terrestrial cryosphere dynamics related to orbital changes in the southern mid and high latitudes.

Here we report terrestrial sediment flux records from western Patagonia to the southeast Pacific based on a composite sediment record from International Ocean Discovery Program (IODP) Site U1542 (52°42.29'S, 75°35.77' W; 1,101m water depth, Fig. 6.1), drilled at the Chilean margin during the IODP Expedition 383 onboard R/V JOIDES *Resolution*. We have investigated with high temporal resolution the 253 m-long sediment sequence representing the continuous sedimentation history throughout the last 790 kyr (*Rigalleau et al.*, In review). To reconstruct changes in the PIS western extent, we follow a comparable multi-proxy approach as recently used to document PIS changes at the southern Chilean margin further north at ∼45°S (*Hagemann et al.*, 2024). This approach includes the accumulation rates of terrigenous leaf wax biomarkers synthesized by land plants (*i.e.*, *n*-alkanes) and terrestrial bacteria (*i.e.*, branched Glycerol Dialkyls Glycerol Tetraethers) which provide us information on continental vegetation (*Eglinton and Eglinton*, 2008) in combination with various terrigenous sedimentary proxies, such as ice-rafted debris (IRD) and major element composition (*i.e.*, titanium (Ti) and iron (Fe)), reflecting siliciclastic input from Andean rocks.

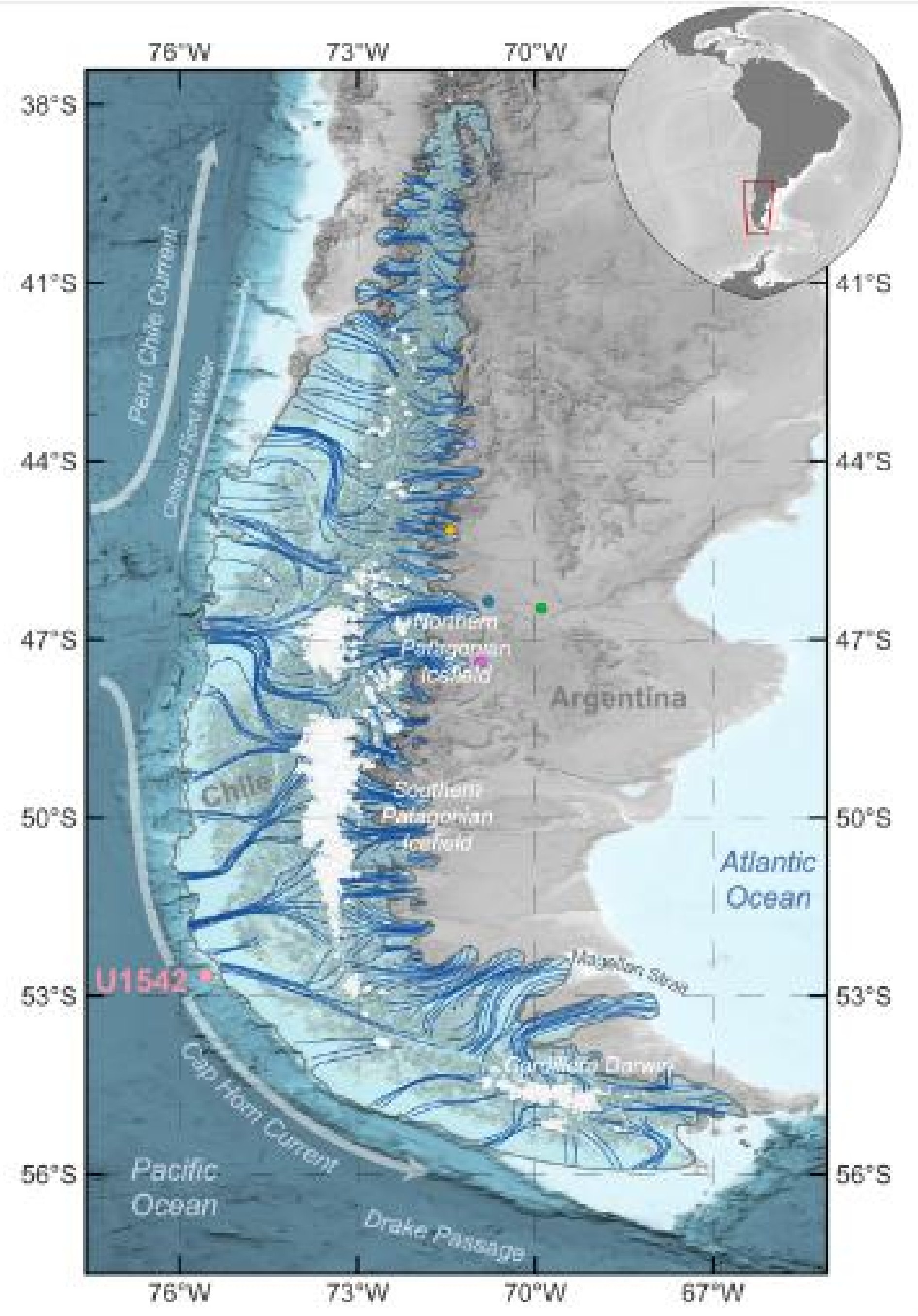

Figure 6.1: **Location of Site U1542, Patagonian and oceanographic settings.** The modern Patagonian icefields (in white), Patagonian Ice Sheet (in light blue transparent) extent and ice flow (blue lines) at 35 ka reconstructed from *Davies et al.* [2020]. The white arrows represent the northward bifurcation (Peru-Chile Current) and the southward bifurcation (Cap Horn Current) of the Antarctic Circumpolar Current. Dots indicates location of moraines advances, corresponding to Fig 6.6. Map realised with QGIS, Global map with ODV. Ocean Data View: https://odv.awi.de/

6.3 Study area

Marine realm: the Chilean margin

The ACC connects the Pacific, Indian, and Atlantic Ocean basins and plays a crucial role in the global circulation of the world's oceans and in regulating climate (*Rintoul*, 2018). The major bathymetric constriction of the ACC occurs at the Drake Passage (DP). The Southern Ocean, particularly the DP throughflow together with the Agulhas current (*Beal et al.*, 2011) exerts a strong influence on the Atlantic Meridional Overturning Circulation (*e.g.*, *Oka et al.*, 2021). When the ACC impinges the southern tip of South America, it bifurcates into the southward-flowing and coastal Cap Horn Current. Site U1542, situated underneath the CHC, is situated approximately 30 nautical miles west of the entrance to the Strait of Magellan, at a water depth of 1,101 meters. The site sits at the upper slope of the Chilean continental margin, within a relatively small-scale sediment depocenter ("sediment drift"). At the location of Site U1542, sea surface temperature averages ∼9.6°C.

Modern Patagonian icefields: legacy of the PIS and largest mid-latitude ice system

Patagonia is the meridional region in South America that extends from about 40°S at the southernmost section of the Andes down to the austral tip of the continent, Tierra del Fuego (55°S). This high mountain chain of the Andes is the major barrier of the SWW, and the western (Chilean) Patagonia is a 50 to 150 km wide intricated strip of land and fjords between the Pacific coast and the Andean crest that rises to 2500 m at these latitudes. As a natural obstacle, rainfall amounts strongly differ on both sides of the Andes. On the windward side along the Pacific coast, the luv effect of the Andes leads to hyperhumid conditions constantly windswept by the strong SWW. At the eastern (Argentinian) lee-side of the mountains, the outwash plains are characterized by arid and highly evaporative conditions (*Garreaud et al.*, 2013).

Nowadays, the Patagonian icefields represent the largest continental ice masses in the mid-latitudes (*Warren and Sugden*, 1993). They are divided into three main glacier systems, the Northern and Southern icefields (46°-52°S) and the Darwin Mountain ice field in Tierra del Fuego (54°-55°S) (Fig. 6.1). In this high mountain setting, the glacial erosion processes control the overall glaciofluvial sediment flux (*Hebbeln et al.*, 2007) with rapid glacial erosion at altitudes near the snowline (*Jaeger and Koppes*, 2016). Particularly sensible to climate changes, the PIS is, after the Greenland and Alaska region, the largest contributor to global sea rise (*Zemp et al.*, 2019), contributing 1.2-1.5 meters to global sea level rise (*Davies et al.*, 2020; *Hulton et al.*, 2002) since the LGM.

During this period, the icefields expanded to form the extensive PIS, which covered the entire Andean part of southern South America, spanning approximately 38°S to 56°S (*Davies et al.*, 2020).

The geographic maximum eastward extent of the LGM-PIS is well-constrained by continental ice-derived sedimentary sequences on land such as radionuclide-dated moraines (*e.g.*, *Darvill et al.*, 2016; *Davies et al.*, 2020; *García et al.*, 2018; *Kaplan et al.*, 2008; *Peltier et al.*, 2021). Because lake basins have been covered by glaciers, the few lacustrine records mostly start after the ice retreat between 17 and 14 ka BP (*e.g.*, *Lamy et al.*, 2010), with exceptions found in records from the non-glaciated Laguna Potrok Aike, extending back to approximately 50 ka BP (*e.g.* *Lisé-Pronovost et al.*, 2013; *Recasens et al.*, 2012). Though less is known on the Pacific-ward extent of the PIS, the glaciers, at their maxima, most likely reached the continental shelf edge and terminated in iceberg-calving fronts. This resulted in stratigraphically complex deposits on the continental shelf, that destroyed the glacial records formed from previous glaciations (*Jaeger and Koppes*, 2016). It is hypothesized that at its maximum expansion, the ice sheet likely extended close to the shelf break, relatively close to our upper continental slope Site U1542. Consequently, an important meltwater influence on surface water salinities and possibly also on SST at our site is thus expected (*Caniupán et al.*, 2011).

6.4 Material & Methods

The sediment sequence consists of sand-bearing clayey silt to silty clay that represents the main lithology. This unit reveals meter-scale variations in color between gray and grayish olive, with occasional visually observed drop stones. This unit is interspersed by a second minor and thin unit of olive-to-yellow foraminifera ooze. These color changes largely parallel the variations in grain size and geochemistry. $CaCO_3$ contents vary between ~1 and 12 wt % for the clayey silt/silty clay unit and between ~30 and 55 wt % for the foraminifera ooze unit. Biogenic silica and organic matter contents range from 0.3 to 0.8 wt % and from 1 to 4 wt %, respectively. The nearly continuous, undisturbed, 249-meter-long sedimentary sequence recovered at Site U1542 covers the past 790,000 years with sedimentation rates that exceed 30 $cm.kyr^{-1}$.

Chronology

The age model of Site U1542 follows *Rigalleau et al.* [In review]. Briefly, it is based on the upper part (0 - 65 ka) by tuning the color reflectance record (b*) of the U1542 composite record to the b*record of core MD07-3128 recovered in the vicinity of site U1542 and covering the past ∼65 kyr. The stratigraphy of MD07-3128 is well-constrained by 13 accelerated mass spectrometry (^{14}C AMS) dating from mixed planktonic foraminifera, along with the identification of the Laschamp paleomagnetic excursion (*Anderson et al.*, 2021; *Caniupán et al.*, 2011; *Lamy et al.*, 2015). For the Site U1542 record, in the time interval 65 - 790 kyr, glacial terminations, and inceptions defined from XRF Ca count records (reflecting biogenic carbonate occurring during interglacials) were tuned to the Antarctic EDC temperature record (*Jouzel et al.*, 2007) on the Antarctic ice core chronology (AICC2012) age model (*Bazin et al.*, 2013). Within the glacial periods, the benthic foraminiferal (*G. uvigerina*) oxygen isotope (δ^{18}O) record was aligned with the EDC temperature record. As Site U1542 is located at a relatively shallow water depth of 1,101 m, several periods exhibit strong variability, with a relatively subdued G/IG variability in the benthic record. For instance, MIS 13 and 7 are not evident in the XRF Ca or benthic δ^{18}O record. To address this, additional tuning points using our SST reconstruction to the Antarctic ice core temperature record were added (*Rigalleau et al.*, In review).

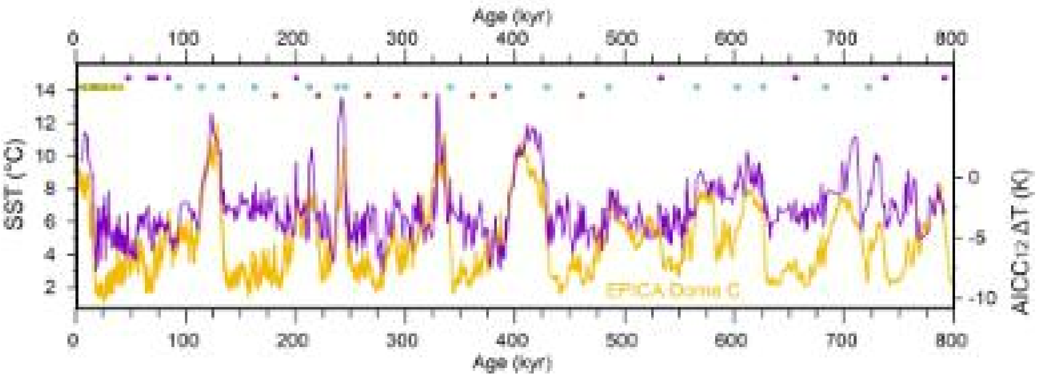

Figure 6.2: **Age model developed by *Rigalleau et al.* [In review].** Alkenones SST fit with the antarctic ice core temperature reconstructions. Dots indicates tie points.

X-Ray Fluorescence

The high-resolution bulk intensity of major elements from X-ray fluorescence (XRF) scanning measurement at Site U1542 was measured with an Avaatech energy-dispersive X-ray fluorescence analyzer at Texas A&M University. Scanning was done every 3 cm steps (area 10 x 12 mm, down-core x cross-core) along the entire length of the composite core in three runs 10 kV (Tube current 0.16 mA, live time 6s, no filter), 30 kV (1.25 mA, 6s, Pd-thick filter) and 50 kV (0.75 mA, 10s, Cu filter) to obtain reliable intensities (counts per second) of major elements (*i.e.*, Al, Si, S, Ti and Fe reflecting siliciclastic input from Andean rocks). Major elements used in this study were calibrated performing simple regressions based on the correlation of geochemical results and the XRF intensity signals of the regarded elements.

Ice Rafted Debris

Ice rafted debris (IRD) counts are presented as the concentration of lithic grains defined as the number of grains with diameters greater than ~0.5 mm. IRD was considered as the total number of lithogenic/terrigenous grains counted on the carbonate-free fraction, assuming that coarser-grained terrigenous sediment, supposed to be IRD, can only reach the core location through iceberg transport. IRD observations were part of the sediment visual core description and provided an account of the presence and abundance record of IRD. Processed X-ray images were used to estimate IRD abundance per X-ray image. Each image integrates 12 cm of core, and the IRD concentration was obtained for the central depth of the image. IRD appears as dark gray to black very dense defined particles in the X-ray images and were counted as particles larger than ~0.5 mm. In the scans, the density differences within the sediment become visible, which makes it possible to observe and analyze sediment structures and solid rock components interpreted as IRD. Additionally, the simple moving average was used to reduce the effects of local variations, artificial clusters, and background noise within the signal of the IRD. Scans of the bottom of a segment as well as strongly disturbed sections were not used in the counting process. IRD MAR was determined by counting detrital mineral grains in the >0.5 mm sediment fraction and multiplication by apparent bulk MAR, derived from estimates of dry bulk density and the linear sedimentation rate.

Biomarkers

For the determination of biomarkers at Site U1542, about 5 g of freeze-dried and homogenized sediment samples were extracted by accelerated solvent extraction (ASE 350, Dionex) with a mixture of dichloromethane and methanol (DCM:MeOH, 9:1, v/v) at Alfred Wegener Institute Bremerhaven. The resulting total lipid extract was further separated into 3 fractions through column chromatography with silica gel as the stationary phase. *n*-alkanes were eluted with Hexane (5 ml), alkenones were separated using DCM (5 ml), and Glycerol Dialkyls Glycerol Tetraethers (GDGTs) were eluted with DCM:MeOH (1:1; 4 ml). Internal standards (squalane, C_{36} *n*-alkane, C_{46}-GDGT) were added before extraction and served for quantification purposes.

n-alkanes ($n_{C23+25+27+29+31+33}$) were analysed by gas chromatography on a Hewlett-Packard HP7890 fitted with a flame ionization detector using an Agilent VF-200 ms capillary column (80 m length, 0.25 mm diameter, 0.25 mm film thickness). The oven temperature was programmed to be held at 80ºC for 1 minute, then increased at 40ºC/minute to 300ºC and held for 60 minutes.

The n-alkanes were identified by comparing the retention times to an external standard mixture (n-alkanes ranging from C_{17}-C_{36}). The n-alkanes concentration ($ng.g^{-1}$, dry weight sample) was determined based on the internal standard n-hexatriacontane (C_{36}).

Biomarkers-derived indices

The average chain length (ACL) was defined by the formula Eq. (1) (*Cochran et al.*, 1990) and the carbon preference index (CPI) was calculated using Eq. (2) (*Marzi et al.*, 1993).

(1) $ACL_{23-35} = \sum [i.Xi] / \sum [Xi]$, where X is abundance and i ranges from n-C_{23} to n-C_{35}.

(2) $CPI_{23-33} = 0.5 \text{ x } \sum (C_{23-33})/(C_{24-32}) + 0.5 \text{ x } \sum (C_{23-33})/(C_{26-34})$

The ACL index for the most abundant n-alkane length indicates the source of leaf wax production, where higher terrestrial plants (*i.e.*, vascular plants) are dominated by long-chain n-alkanes with more than 25 carbon atoms, whereas bacteria and algae contain mainly shorter chains less than 25 carbon atoms. The CPI is the odd-to-even predominance of the hydrocarbons. It indicates the degree of degradation of the organic matter (OM), where a lower (higher) value indicates further degraded (preserved) material.

Terrestrial anaerobic bacteria, abundant in soils and peats produce a class of compounds called branched (br) GDGTs ($GDGT_I$ - $GDGT_{III}$; reviewed in *Schouten et al.* 2013a). Marine archaea (*Thaumarchaeota*; *Brochier-Armanet et al.* 2008), on the other hand, synthesize isoprenoid (iso) GDGTs in the water column, with the iso$GDGT_0$ and the isoGDGT crenarchaeol being the most abundant (*Schouten et al.*, 2013a). The relative abundance (ratio) of these two compounds, the Branched vs. Isoprenoid Tetraether (BIT) index, is a commonly used proxy to reconstruct the magnitude of terrestrial OM input to the marine realm (*Hopmans et al.*, 2004).

$$\text{BIT index} = (GDGT_I + GDGT_{II} + GDGT_{III}) / (\text{Crenarchaeol} + GDGT_I + GDGT_{II} + GDGT_{II})$$

Estimation of the mass accumulation rate

Mass accumulation rate (MAR) was calculated by multiplying the concentration of the compounds ($ng.g^{-1}$ sed.), by the dry bulk density (DBD) ($g.cm^{-3}$), and the sedimentation rate ($m.kyr^{-1}$), according to the following formula:

$$MAR = SR \times DBD \times [\text{compounds}]$$

The DBD was estimated for each XRF measurement interval from the γ-ray attenuation (GRA) density measurements performed all along the sediment core onboard

JOIDES *Resolution*, therefore following the standard procedure of IODP (*Lamy et al.*, 2021). The terrigenous MAR (tMAR in g.cm^{-2}.kyr^{-1}) is defined by:

tMAR = SR × DBD × [1-carbonate content]

The carbonate content is calculated from the relative abundance of Ca through XRF measurements calibrated against geochemical composition measurements all along the record (n = 43) from ICP-OES using a Thermo iCAP 7300 Duo (Thermo Fisher Scientific) at the Leibniz Institute for Baltic Research Warnemünde (IOW).

6.5 Results

Siliciclastic components

The tMARs at Site U1542 (Fig. 6.3F) are less than 10 g.cm^{-2}.kyr^{-1} during interglacial, except for MIS 13 where the tMAR reaches 28 g.cm^{-2}.kyr^{-1}. It abruptly increases to more than 80 g.cm^{-2}.kyr^{-1} during glacial periods until 150 g.cm^{-2}.kyr^{-1} during MIS 14. But it reaches a much higher value during the LGM to 550 g.cm^{-2}.kyr^{-1}. Major elements are dominated by the Al (1.3 to 9 %), Fe (1.1 to 4.8 %), K (0.5 to 2.2 %), and Ti (0.1 to 0.5 %) reflecting siliciclastic input from Andean source rocks. Major terrigenous element concentrations are generally constant during each glacial period, suggesting that the source of the sediment did not change over the past 790 kyr.

IRD counts from the fraction >0.5 mm (Fig. 6.3D) vary from barren counts during interglacial periods to an average of 1000 during glacial periods. A maximum of counts appears at MIS 6 with more than 2000 IRD counts recorded. The IRD counts present an increasing trend throughout MIS 8 and MIS 2, and decreasing values are observed during MIS 10 and MIS 6. Glacial periods before the Mid Bruhnes Transition (*i.e.*, MIS 12/11) do not show a clear trend, mainly due to their relatively short duration. If IRD is mostly found during glacial periods, several IRD clasts can be found during most of the warm phases except MIS 11.

Organic Biomarkers

The long-chain *n*-alkane mass accumulation rate (*n*-alkane MAR) record at Site U1542 (Fig. 6.3C) generally documents low values (0.05 to 0.1 mg.m^{-2}.yr^{-1}) during interglacials compared to much higher values during glacial periods (reaching from 0.2 mg.m^{-2}.yr^{-1} during MIS 18 to to 1.5 mg.m^{-2}.yr^{-1} during MIS 14 and MIS 2). Glacial MIS 6, 8, 10, and 12 show similar *n*-alkane MAR, between 0.2 and 0.4 mg.m^{-2}.yr^{-1}. Generally, *n*-alkane MARs gradually decrease into glacial periods and show abrupt increases at glacial terminations.

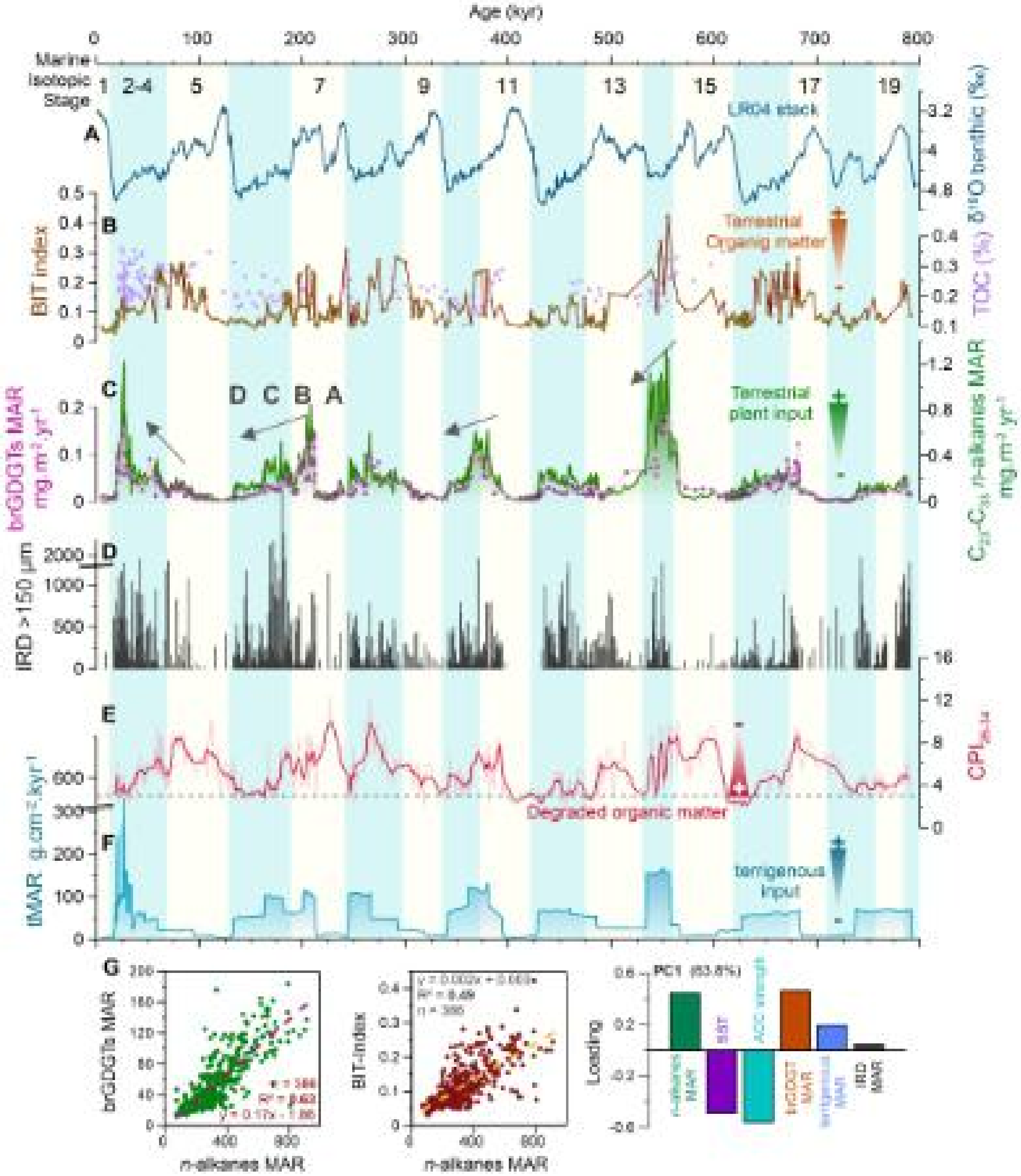

Figure 6.3: **Terrestrial proxies at Site U1542 used in this study.** (A), Benthic foraminifera oxygen isotope stack (Lisiecki et Raymo 2005). (B), BIT-Index and TOC. (C), *n*-alkanes and brGDGTs mass accumulation rates. (D), counts of Ice-rafted debris >0.5 mm. (E), Carbon Preference Index. (F), terrigenous mass accumulation rate. (G), scatter plot showing linear correlation between terrigenous biomarkers MAR and indices and Principal component analyse of proxies at Site U1542

The ACL values across the record range from 27.9 to 29.5 (ACL_{25-33}= 28.7), which is a typical characteristic of leaf waxes from higher land plants (*Eglinton and Eglinton*, 2008). Although the values show little variability, they demonstrate long-term changes along the Pleistocene. The CPI is an indicator of degradation/thermal maturity of the OM (*Bray and Evans*, 1961). The distribution of *n*-alkanes presents a strong odd carbon number predominance (Fig. 6.3E; CPI_{26-34}, ranges from 2 to 12) suggesting relatively fresh OM, especially in the early part of the glacial cycle. The contribution from reworked OM via storage in the fjord system is considered to be minor here and is concentrated in the glacial periods, where its geochemical signature corresponds to that of *n*-alkanes in mature OM. Their distribution presents relatively low CPI values of <3 during the glacials.

The MAR record of brGDGTs largely parallels the *n*-alkane MAR record (Fig. 6.6G). Low brGDGTs MAR occur during interglacials (0 to 0.05 $mg.m^{-2}.yr^{-1}$) and higher values during glacial periods (0.05 $mg.m^{-2}.yr^{-1}$ during MIS 12 and up to 0.16 $mg.m^{-2}.yr^{-1}$ during MIS 14, late MIS 7 and MIS 2). The BIT-index (Fig. 6.3B) presents minimum values during interglacials (<0.1), typically found in open marine environments (*Hopmans et al.*, 2004). It varies between 0.2 and 0.3 during glacial periods and higher values (>0.25) are reached at a certain point in every glacial period suggesting a predominant terrestrial input. MIS 12 is the glacial period presenting the lowest values and maximum values are reached during MIS 14 (0.42).

6.6 Discussion

We combine the different proxy records to discuss changes in the terrigenous supply to the Southeast Pacific continental margin at Site U1542. We focus on the interpretation of the IRD, biomarker, and terrigenous sediment input records as indicators of terrestrial transfer processes (*i.e.*, source-to-sink) from the Andes, across the Chilean fjords to our Chilean continental slope Site 1542 located ∼50 nm offshore (Fig. 6.1). This combination of organic and inorganic proxies enables the reconstruction of the PIS dynamics over the past ∼800 kyr.

Terrigenous input changes at Site U1542

Marine records of IRD are widely regarded as indicative of iceberg discharge into the marine environment and provide a nearly continuous signal of ice-sheet dynamics and variability (*Bond et al.*, 1992). In the Southern Ocean, IRD records from the Scotia Sea are primarily related to the deglacial instability of the Antarctic ice sheets (*Weber et al.*, 2014) as the ice shelf becomes unstable with deglacial warming and sea-level rise. On the other hand, more distal records often show IRD maxima in glacial intervals which may reflect enhanced iceberg production at the Antarctic shelf-break and the

SST-controlled survivability of icebergs along varying trajectories. This has been for example demonstrated in the South Atlantic where a shift in iceberg trajectories during glacial periods can result in a considerable redistribution of freshwater in the Southern Ocean affecting large-scale thermohaline ocean circulation (*Starr et al.*, 2021).

Owing to its proximity to the PIS, IRD at Site U1542 are primarily attributed to advances of PIS glaciers during glacials (*Caniupán et al.*, 2011). A negligible portion might originate from Antarctic icebergs as modern iceberg tracks rarely reach our study area (*Rackow et al.*, 2017) which potentially explains the presence of outsized clasts during several warm phases such as MIS 9, 5, and 1.

To support the IRD record, the biomarker-based records can be used to reconstruct the former ice sheet dynamics. In Site U1542 setting, the terrestrial biomarkers likely originate from the southern Andes. Throughout the record, n-alkanes and brGDGTs MARs show similar patterns (Fig. 6.3C) and are linearly correlated with the BIT index (Fig. 6.3G). This positive correlation among the biomarkers, *i.e.*, an increase in n-alkane MAR corresponds to higher ACL values, higher brGDGT concentrations, and high BIT-Index values (Fig. 6.3), clearly indicates that the biomarkers used in this study originate from terrestrial organic matter transported into the marine environment. These results also confirm that the mass accumulation rate of brGDGTs can be applied in marine sediment records to characterize terrestrial OM, as proposed by several studies *Hopmans et al.*, 2004; *Kim et al.*, 2006).The terrestrial origin of biomarkers at Site U1542 is further supported by the observed correlation between n-alkanes and the inorganic proxies (*i.e.*, time and IRD), confirming the variability in n-alkanes MAR measured at Site U1542 as a proxy for fluctuations of the PIS as previously demonstrated *Caniupán et al.*, 2011; *Hagemann et al.*, 2024; *Kilian and Lamy*, 2012). Moreover, Site U1542, located at the western entrance of the Magellan Strait, is ideal due to its proximity to a convergence area of the former PIS ice flow, encompassing a vast drainage basin (Fig. 6.1) (*Davies et al.*, 2020).

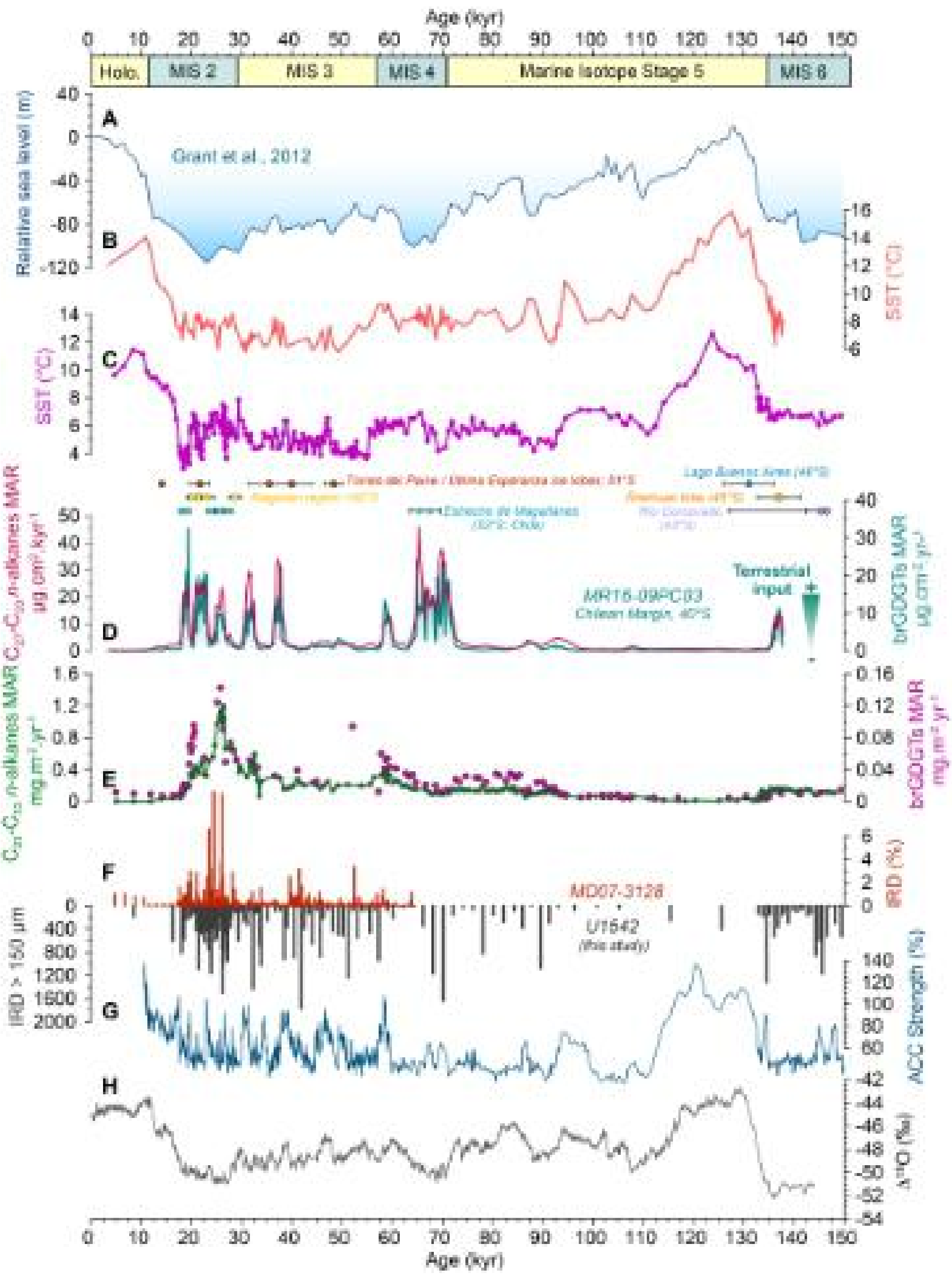

Figure 6.4: **Millennial-scale fluctuations of the Patagonian Ice sheet during the last Glacial cycle.** (A), Relative sea level (*Spratt and Lisiecki*, 2016). (B), Sea surface temperature from core MR16-09 PC03 at ~46°S (*Hagemann et al.*, 2024). (C), Sea surface temperature from Site U1542 composite record at ~53°S (*Rigalleau et al.*, In review). (D), *n*-alkanes and brGDGTs mass accumulation rates from core MR16-09 PC03, and (E) from Site U1542 composite record. (F), Ice rafted debris from the same location MD07-3128 (%) (*Caniupán et al.*, 2011) and from Site U1542 record (counts). (G), ANtarctic Circumpolar Current reconstruction at the Cape Horn Current from Site U1542 (*Rigalleau et al.*, In review). (H), Oxygen isotope reconstruction from Antarctic ice cores. This figure also displays a compilation of eastward Patagonian Ice sheet advances from ^{10}Be surface exposure ages (different refs. in text).

Patagonian ice sheet advances on Glacial/Interglacial variability

Marine sediment records documenting PIS advances rather focus on the last glacial period (*e.g.*, *Hagemann et al.*, 2024; *Kilian and Lamy*, 2012). *Hagemann et al.* [2024] described of the first continuous millennial-scale fluctuations of the western PIS spanning the last glacial period extending into MIS 6 using a sediment core located on the Pacific side at ∼46°S (Fig. 6.4B, D). They have documented three major PIS advance periods with terrigenous input phases (TIP) during MIS 6 (135 - 140 ka), late MIS 5 (∼85 - 95 ka), MIS 4 (∼60 - 70 ka) and late MIS 3 to MIS 2 (∼18 - 40 ka), occurring during sea-level low stands when the western Patagonian ice sheet covered most of the Chilean fjords. This study demonstrates that a source-to-sink study based on terrestrial biomarkers carried out on open marine sediment cores is suitable for reconstructing the fluctuations of the western margin of the PIS. Such TIPs were defined by an increase in organic (*i.e.*, MAR *n*-alkanes, MAR brGDGTs) and inorganic (*i.e.*, MAR Fe and IRD) terrestrial components (*Hagemann et al.*, 2024) and can also be identified in Site U1542 record. They generally occur together with glacial sea-level low stands (Fig. 6.4A). The terrigenous discharge increases at 35 ka, in the middle of MIS 3, shortly after the increase initiated in the central-western PIS at ∼38 ka (*Hagemann et al.*, 2024). The terrestrial input starts to decline at 25 ka, most likely related to the initiation of the reduction of PIS (*Davies et al.*, 2020), followed by a second decline at around 18 ka, synchronous with the northern retreat. Smaller *n*-alkanes MAR input is recorded at Site U1542 during MIS 4, although the presence of an outsized class of IRD supports a PIS advance. The input during MIS 4 may be hidden by the strong input during MIS 2, which is 10 times higher than described by *Hagemann et al.* [2024]. Furthermore, most of the IRD recorded at Site U1542 over the last glacial period are occurring during, during colder Antarctic temperatures, and weaker ACC (Fig. 6.4; *Rigalleau et al.*, In review). The PIS deglaciation started at 35 ka, and the retreating ice lost its connection to the shelf region between ∼11 - 25 ka (*Davies et al.*, 2020; *Sugden et al.*, 2009). This latter timing corresponds broadly with a decrease of the IRD recorded at Site U1542 and in the nearby sediment record MD07-3128 (*Caniupán et al.*, 2011) to its absence around 18 ka.

The SWW are source of heavy precipitation on the western side of the Andes (*Garreaud et al.*, 2013), leading to significant hinterland discharge from rivers and glaciers (*Kaiser et al.*, 2005). The observed decrease in mass accumulation rates of all terrestrial proxies during the interglacials could potentially be explained by a reduced fluviatile runoff resulting from decreased precipitation. However, the similarity between conditions in interglacial periods and the modern climate, including the Holocene, indicates important precipitation in southern Patagonia (*Garreaud et al.*, 2013). Hence, precipitation changes cannot most likely explain the threshold-like glacial/interglacial behavior. Furthermore, although the modern Patagonian ice fields are presently strongly reduced compared to the LGM extent, glaciomarine sedimentation may still play a role during the Holocene and previous interglacials. For instance, cosmogenic evidence on moraines supports an eastward extended PIS during the interglacials MIS 15 (*Hein et al.*, 2011), MIS 11 (*Tobal et al.*, 2021) and MIS 5 (*Mendelová et al.*, 2020). However, these periods exhibit low accumulation rates ($\sim$3 cm.kyr^{-1}; Fig. 6.5F) at Site U1542, suggesting that most of the terrigenous sediments appear to have been retained within the southern Chilean fjord system, analogous to conditions observed during the Holocene (*Hagemann et al.*, 2024; *Sepúlveda et al.*, 2009).

Former ice sheets are difficult to constrain in a linear source-to-sink fjord system (*Jaeger and Koppes*, 2016). To isolate the climatic signal of the advance/retreat of the PIS, it is necessary to account for transfer mechanisms from ice-proximal (fjord) to ice-distal (open ocean) sites that may partially disturb and delay the signal, *e.g.*, mass redistribution, gravity flows, ice rafting, and ocean circulation (*Jaeger and Koppes*, 2016). For instance, during peak interglacial conditions (Fig. 6.5A), *i.e.*, sea-level highstand and retreated PIS, an important part of the terrigenous sediments transported from Patagonia by rivers may remain trapped within the over-deepened Chilean fjords (*Sepúlveda et al.*, 2009). These periods are marked by low tMAR, reduced MAR *n*-alkanes, and brGDGTs, as well as lower BIT index and IRD (Fig. 6.3C, D, F), and a prevalence of biogenic sedimentation outweighs terrestrial sedimentation. This is indicated by high interglacial carbonate concentrations, characteristic of open ocean sediment (*Caniupán et al.*, 2011). In addition, as Site U1542 is located on the Chilean margin, underneath the strong Cap Horn Current (*Chaigneau and Pizarro*, 2005), the few terrigenous sediment that reach the open ocean may be transported by the Cap Horn Current toward the Drake Passage, 60% stronger during interglacial periods (*Lamy et al.*, 2015; *Rigalleau et al.*, In review).

On the contrary, during glacial conditions (Fig 3B-C), *i.e.*, sea-level low stand and advanced PIS, high increases in tMAR, with large amounts of glaciogenic sediments suggest a favored and direct seaward transfer of sediment reaching the continental slope. During full glacial conditions (Fig. 6.5D), the PIS most likely covered most of the hinterland and approached the Pacific continental shelf (*Caniupán et al.*, 2011; *Davies et al.*, 2020; *Hagemann et al.*, 2024), as decline in vegetation is implied by low pollen productivity (*Montade et al.*, 2013). This suggests that the high *n*-alkanes MAR deposited during full glacial conditions is remobilized material likely stored in the fjords.

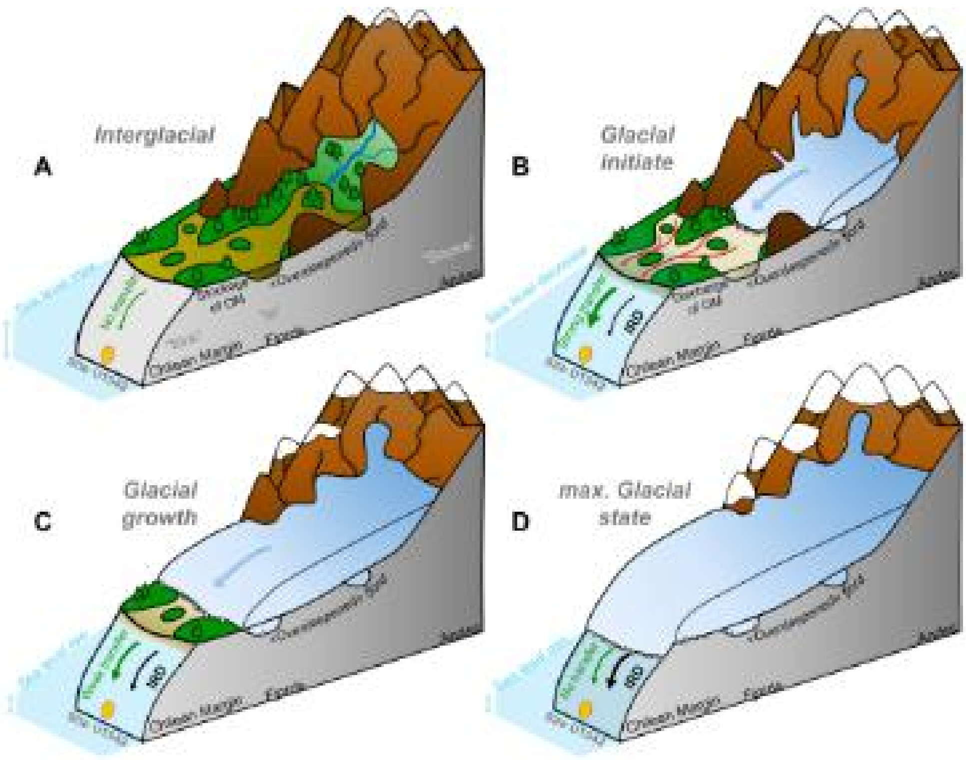

Figure 6.5: **Schematic representation of source to sink transfer in the Chilean margin (West Patagonia) during a complete glacial interglacial cycle.** The different stages of the glacial cycles correspond to figure 6.5. Note the eustatic evolution function of the global-ice-sheet volume.

Patagonian ice sheet advances on multiple glacial cycles

Based on moraine dating, *Darvill et al.* [2016] derived synchronous glacier advances in the Southern Alps of New Zealand and Patagonia during the last 110 kyr (especially during MIS 2), indicating a South Pacific-wide pattern. Moreover, the resulting Pacific-wide advances correlate well with the phases of a western extended Patagonian ice sheet (*Hagemann et al.*, 2024). To assess whether this correlation between sediment flux changes and moraine advances persisted in previous glacials, we compiled published ^{10}Be surface exposure ages indicating a significant advance of the PIS (Fig. 6.4) before the last glacial period (Fig. 7c).

Records of the PIS extent beyond the last glacial-interglacial cycle are limited and are mainly based on the dating of terrestrial moraine deposits on the eastern side of the Andes. One of the earliest recorded moraines is located in the Lago Pueyrredón valley, dating back approximately 600 ka (*Hein et al.*, 2011). This advance is associated with MIS 16 (620 - 675 ka; *Lisiecki and Raymo*, 2005), one of the coldest glacial stages (*Jouzel et al.*, 2007) of the last 800 kyr, which is characterized by a strong global sea level low stand (*Spratt and Lisiecki*, 2016) and low atmospheric CO_2 concentrations (*Siegenthaler et al.*, 2005). Notably, records from Antarctica exhibit a significant dust peak at 630 ka (>10 mg.m^{-2}.yr^{-1}; *Lambert et al.*, 2008). This suggests a large dust deflation in Patagonian dust source areas during MIS 16, considering it as the main source of dust in the Antarctica core (*Delmonte et al.*, 2004). This observation contrasts with the low tMAR at Site U1542, which does not suggest a significant PIS extension towards the Pacific in comparison with other glacial stages.

However, our records show the most pronounced PIS in more recent glacials, especially during MIS 8 and 6. During MIS 8, the maximum input of terrigenous material at Site U1542 was in the middle of the glacial stage, around 270 ka (Fig. 6.6B, C). This maximum advance corresponds in timing with moraine advance at ∼45°S dated at 267 ka at the Ñirehuao glacier lobe (*Peltier et al.*, 2023), the Hatcher moraines at Lago Pueyrredón (∼47.5°S; 260 ka; *Hein et al.*, 2009) and the Rio Corcovado glacier (∼43°S; 257 ka; *Leger et al.*, 2023). During MIS 6, the maximum tMARs at Site U1542 occur early in the glacial stage, at about 210 ka (Fig. 6.6B), corresponding to low dust flux in Antarctica. However, two advances have been observed at 219 ka and 210 ka at the Lago Buenos Aires (∼46°S; *Tobal et al.*, 2021). Our records document a decreasing trend in the terrestrial MARs throughout MIS 6, contrasting with dated advances based on moraines on land. For instance, two large advances of Ñirehuao glacier (∼45°S) are reported at 153 ka and 137 ka (*Peltier et al.* 2023), occurring during the coldest and dustiest periods of MIS 6 in Antarctica. The authors of this study propose a direct association between the extent of PIS extent and dust availability for transport by the westerlies to Antarctica (*Peltier et al.*, 2023), a relationship previously suggested to impact the Antarctic dust deposition during the last glacial period (*Sugden et al.*, 2009).

The *n*-alkanes (Fig. 6.6B) and IRD MAR (Fig. 6.6C) records from Site U1542 present similarities with the dust ice core record from EPICA Dome C in Antarctica (Fig. 6.6E; *Lambert et al.*, 2008) and *n*-alkanes flux record from ODP Site 1090 in the South Atlantic (Fig. 6.6F; *Martínez-Garcia et al.*, 2011), exception made with MIS 6. These dust compounds, eroded from outwash plains and soils by winds, are transported in the organic fraction of eolian dust eastward over the South Atlantic (*Martínez-Garcia et al.*, 2011; *Simoneit et al.*, 1977), and the Antarctic continent (*Basile et al.*, 1997; *Grousset et al.*, 1992; *Lunt and Valdes*, 2001; *Sugden et al.*, 2009). Both records from EPICA Dome C (dust) and ODP 1090 (*n*-alkanes) mirror each other, representing successive eastward PIS advances. Supporting this observation, the maximum dust MARs correspond with glaciers advances from moraines, particularly during MIS 8 and late 6 (Fig. 6.6D). The *n*-alkanes record from site U1542 display comparable orbital timescales changes, but diverges at several periods, notably during MIS 6 and MIS 10, where a decrease in *n*-alkanes MAR is observed, while both Atlantic and Antarctic sectors record a continuous increase in n-alkanes and dust, suggesting an active eastern PIS producing dust-size sediment in the outwash plains.

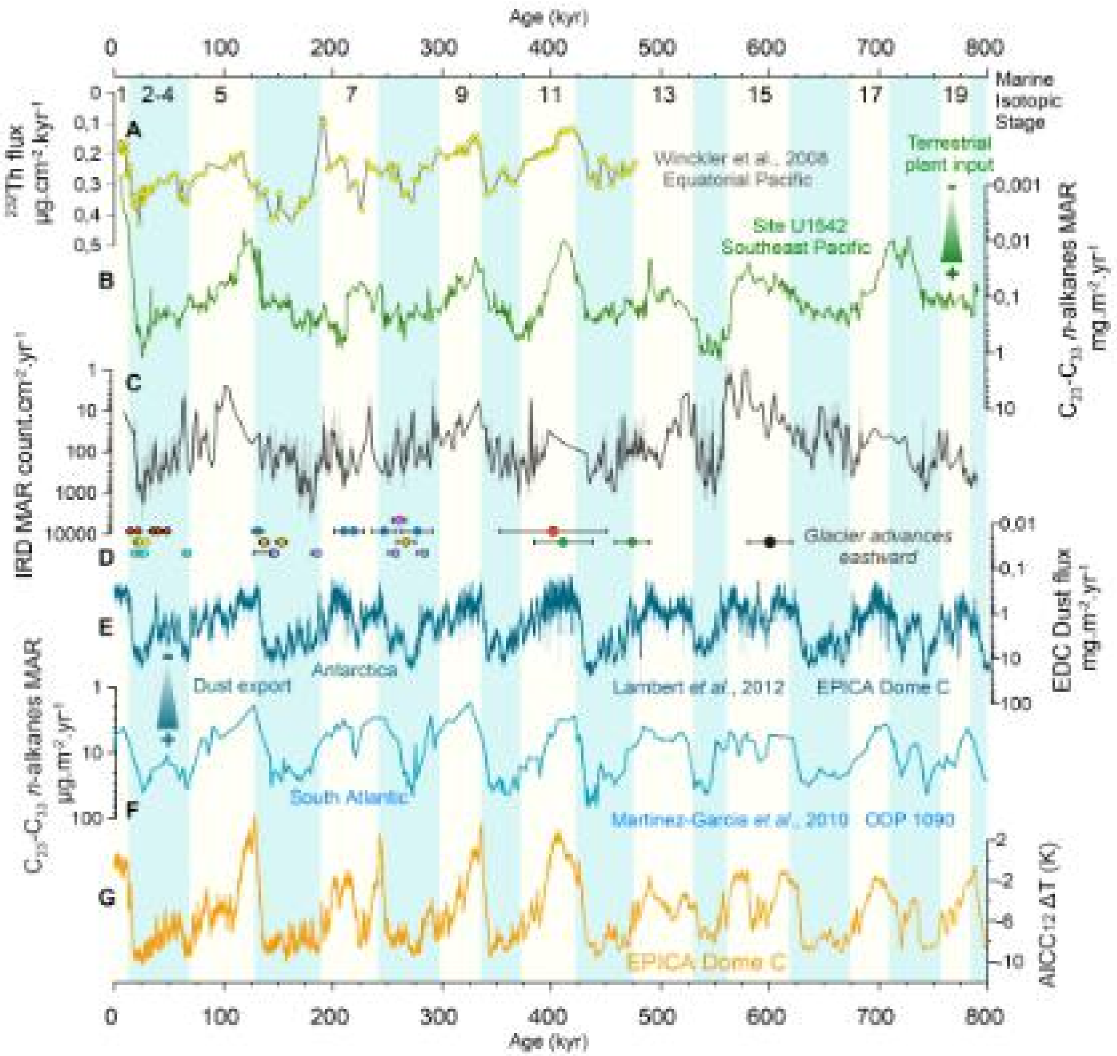

Figure 6.6: **Long-term variability of Patagonian terrigenous export in the Pacific and Southern hemisphere.** (A), ^{232}Th fluxes from TTN013-PC72 core in the central equatorial Pacific (*Winckler et al.*, 2008). (B), n-alkanes mass accumulation rates from Site U1542 composite record. (C), Ice rafted debris mass accumulation rates from Site U1542 composite record. (D), compilation of eastward Patagonian Ice sheet advances from ^{10}Be surface exposure ages (different refs. in text). (E) Dust fluxes record from EPICA Dome C (EDC) ice core (*Lambert et al.*, 2012). (F), n-alkanes mass accumulation in the south Atlantic, from ODP1090 record (*Martínez-Garcia et al.*, 2011). (G), Antarctic temperature record from EDC ice core (*Jouzel et al.*, 2007)

This discrepancy between the records likely suggests an asymmetry between the western PIS (Site U1542) and the eastern PIS (EDC, ODP 1090, and moraines advances) during MIS 10 and 6. An equatorial Pacific dust flux record (Fig. 6.6A; *Winckler et al.*, 2008), likely sourced from northern South America (*Nakai et al.*, 1993), corroborates this observation by indicating an increase from middle to late MIS 6, as Site U1542. These observations of the PIS dynamic recorded at Site U1542 confirm the significant role of the PIS as a major sediment producer. However, this comparison also suggests that the PIS did not evolve uniformly between the east and west over the past glacial/interglacial changes (*Davies et al.*, 2020; *Mendelová et al.*, 2020) or that processes influencing dust production, uptake, transport, and deposition are not always linearly linked to the extent of the PIS.

An ocean-temperature-controlled ice sheet

Being the first continuous record of PIS extent spanning multiple glacial and interglacial phases, Site U1542 records allow us to better constrain the orbital scale dynamics of the PIS and related ocean-atmosphere forcings. Across glacial-interglacial variability, *n*-alkanes MAR (Fig. 6.7D) and IRD MAR (Fig. 6.7F) closely covary with SST at Site U1542 (Fig. 6.7E; *Rigalleau et al.*, In review).

Over the last glacial period (MIS 2-4), glacial discharge exhibits a constant increase, reaching its peak during the LGM, while a gradual 2°C cooling is observed throughout the last glacial period. A similar pattern is observed in MIS 8, where an increase in *n*-alkanes and IRD MAR aligns with the 2 - 3°C cooling observed in SSTs, supporting the notion of a growing PIS during a global cooling phase and global ice sheet growth (*Jouzel et al.*, 2007; *Lisiecki and Raymo*, 2005). Accordingly, the long-term decrease of the *n*-alkanes and IRD MAR observed during MIS 10 (380 to 340 ka) and 6 (220 to 140 ka) is contemporaneous with a warming in the southeast Pacific SST record (*Rigalleau et al.*, In review). It suggests a PIS retreat in response to a warming in the Southeast Pacific, at a time when Earth's climate tends to cool with global ice-sheet growth (*Lisiecki and Raymo*, 2005).

Therefore, it implies that the extent of the western Patagonian glaciers is strongly controlled by subantarctic SST variations in the southeast Pacific. The link between glacier's dynamic response rapidly to ocean forcing can be explained as glacier extent in midlatitudes being influenced by the local air temperature (*Castillo-Llarena et al.*, 2023; *Greuell and Böhm*, 1998; *Oerlemans*, 2005), while the near-surface air temperature is directly coupled with SST (*Feng et al.*, 2018). Thus, the SST in the Southeast Pacific influences the air temperature that controls the glacier extent. This relationship between the extent of ice sheet in response to ocean forcing has also been observed in higher latitudes, for the LGM-Antarctic ice sheet (*Golledge et al.*, 2012).

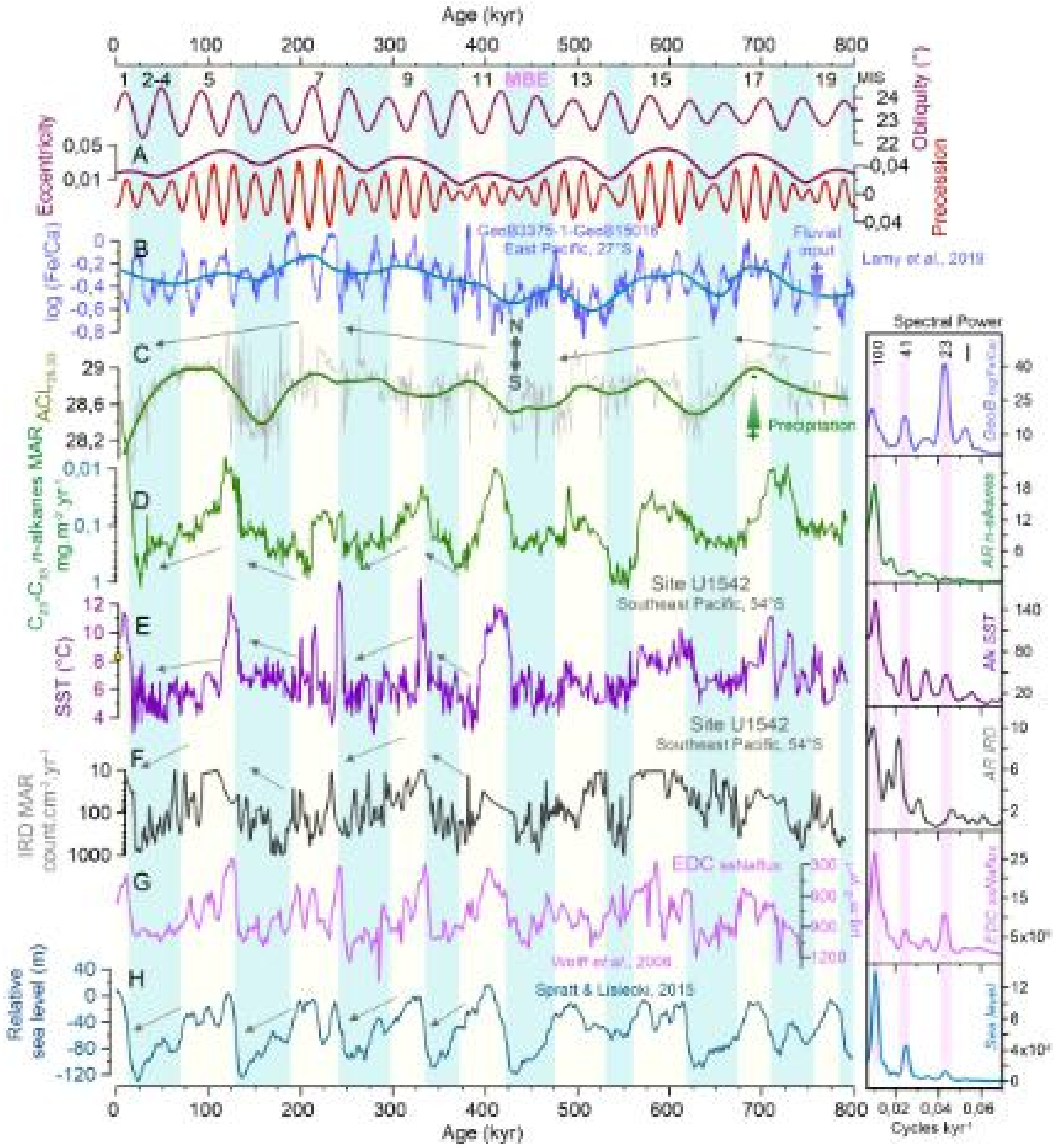

Figure 6.7: **Orbital control of the Patagonian Ice sheet fluctuations.** (A), Astronomical changes in obliquity, eccentricity, and precession (*Berger*, 1978). (B), n-alkanes average chain length from Site U1542 (54°S). (C), log (Fe/Ca) record documenting changes in fluvial sediment input at 27°S. (D), n-alkanes mass accumulation rates from Site U1542 composite record. (E), Sea surface temperature from Site U1542 (*Rigalleau et al.*, In review). (F), Ice rafted debris mass accumulation rates from Site U1542 composite record. (G), ssNa flux from EDC ice core taken as a quantitative winter ice extent (*Wolff et al.*, 2006). (H), relative sea level reconstruction (*Spratt and Lisiecki*, 2016). (I), respective spectral analyses of the main records displayed.

Role of the Westerlies

Over the last glacial period, the coinciding timing between the New Zealand Southern Alps and Patagonian glaciers advances suggests common orbital-scale forcing mechanisms involving coupled shifts in the Southern Ocean oceanic fronts and the large-scale atmospheric patterns, such as latitudinal displacements of the SWW (*Darvill et al.*, 2016; *Denton et al.*, 2010, 2022; *Kohfeld et al.*, 2013; *Mercer and Sutter*, 1982). Beyond temperature control, the latitudinal shift and/or contraction and expansion of the SWW play a crucial role in controlling precipitation including moisture and snowfall over the Patagonian Andes. This precipitation influences the accumulation that drives the extent and retreat of the western PIS (*Hagemann et al.*, 2024) in addition to temperature.

The ACL_{25-33} of leaf waxes (Fig. 6.7B) can be used to evaluate changes in plant physiology due to variations in humidity in extratropical climate (44°S; *Sepúlveda et al.*, 2009). For instance, humid/cold conditions are less favorable for evaporation and water loss in plants and longer-chain compounds provide better protection from evaporative water loss from the leaves (*Sachse et al.*, 2006). We observe a slight decrease in the length chain compound from 700 ka to 500 ka, followed by a long-term increase in ACL_{25-33} index from 500 ka to 200 ka and a relatively strong decrease since the last 100 kyr, which we attribute to a shift in vegetation accounting for the change in precipitation.

A long record of precipitation related to changes in the SWW comes from the Fe/Ca ratio on the subtropical (27°S) Chilean margin record (Fig. 6.7C), reconstructing precipitation related to the subtropical jet of the SWW (*Lamy et al.*, 2019). The opposite long-term trends between the Fe/Ca record from GeoB3375 and the leaf wax record at Site U1542 suggest latitudinal shifts in the SSWs because. The long period of increase in the length of ACL from 500 ka to 200 ka suggests a reduction in precipitations in the southern Andes. Conversely, the long-term increase in the Fe/Ca ratio at the same period suggests an increase of fluvial input in the northern Andes. The combination of these two records implies therefore a northward displacement of the SSW rain belt likely to be linked with the eccentricity orbital parameters that increase during the same period. The eccentricity modulates precession by increasing the amplitude of the signal at this period (Fig. 6.7A), hence inducing a northward shift in the Intertropical Convergence Zone (*Chiang*, 2009) that may displace the SSW rain belt northward. Despite the significant role of the SWW in shaping the western Patagonian landscape, the PIS reconstruction from Site U1542 exhibits dissimilarities when compared to the subtropical jet precipitation record (*Lamy et al.*, 2019), which is mainly driven by precession (~19-23-kyr cycles), as shown in figure 6I. The log n-alkanes MAR record is predominantly characterized by the eccentricity orbital band (~100-kyr cycles; Fig. 6.7I), common in records covering the last million years (*Cheng et al.*, 2016). We suggest that the obliquity orbital band (∼40-kyr cycles) and the precession band are missing due to the source-to-sink fjord system which is controlled by the sea-level stand, primarily showing a 100-kyr cycle. This, coupled with the predominance of the 100 kyr cycle in the SST record (*Rigalleau et al.*, In review), possibly mute the presence of the other orbital frequencies. Therefore, although precipitation changes could potentially be precession-paced, it is not shown, as sediment source-to-sink transfer from the hinterland to the open ocean is also controlled by relative sea level. For instance, the sea salt sodium (ssNa) flux curve from EPICA Dome C (Fig. 6.7G), among other parameters such as cyclones (*Lamy et al.*, 2019), may be taken as a reliable quantitative winter ice extent (*Wolff et al.*, 2006). There is a very close relationship between ssNa flux and SST throughout the last 740 kyr, with cold temperatures corresponding to higher ssNa (Fig. 6.7E, G). The spectral power of ssNa flux is dominated by the eccentricity band, but also monitors the precession cycle in the signal (Fig. 6.7I). The ocean-atmosphere changes related to the winter sea ice extent may link paleoclimate changes between the middle and higher latitudes and the winter ice extent. A northward winter-sea ice extent is coupled with a northward shift of both Southern Ocean fronts and SWW. This this may influence the advances of the southern mid-latitude glaciers (*Peltier et al.*, 2023; *Putnam et al.*, 2010).

As IRD MAR at Site U1542, produced by the PIS instabilities is thus related to SST changes, massive IRD discharge does not necessarily imply extremely cold temperatures (Fig. 6.6E, F). For instance, the early MIS 6 corresponds to the highest concentration of IRD (>0.5 mm) in the record at a period of relative mid-temperature (6°C). This suggests a strong instability of the PIS at this period, marked by a decoupling between a warming observed in the southeast Pacific during global climate cooling (*Rigalleau et al.*, In review). This instability echoes the Antarctic ice sheet during the last deglaciation, characterized by strong iceberg discharge in the Iceberg Alley (*Weber et al.*, 2014). The spectral power of the IRD record stands out in comparison with spectral power from the other records and reveals a prominent obliquity band along the eccentricity band (Fig. 6.7I). In latitudes higher than 60°, changes in obliquity have a greater effect on insolation (*Raymo and Huybers*, 2008). For instance, the changes in the West Antarctic ice sheet have been paced by obliquity since the Pliocene (*Naish et al.*, 2009; *Ohneiser et al.*, 2023). This suggests a high latitude imprint of the dynamic of the PIS, a pacing not recorded in the n-alkanes MAR record. Recently, *Peltier et al.* [2023] further found that the timing of glacial culminations in mid-latitude Patagonia (45°S) tends to correspond with times when Antarctic winter sea ice is expansive and both obliquity and eccentricity are at minima. Although the iceberg discharge in this source-to-sink fjord system (Fig. 6.5) is likely less impacted by sea level changes compared to the n-alkanes MAR record that may remain in the over-deepened fjords, the presence of obliquity in the IRD MAR spectral power aligns with the sea level spectral power which also underlines the importance of Patagonian ice sheet and more broadly cryosphere in controlling the sea level (*Ohneiser et al.*, 2023).

MIS14, a link between East-Antarctic Ice-sheet collapse and Patagonia?

The highest flux of *n*-alkanes appears during MIS 14, *i.e.* ca. 2 to 3 times higher than the average fluxes during glacial periods recorded at Site U1542. Only the LGM shows similarly high fluxes, with outstanding *n*-alkanes and IRD MAR.

Terrestrials, marine, and ice core records from both hemispheres show that MIS14 was an exceptional glacial stage for the Pleistocene period (*Hao et al.*, 2015). The Antarctic temperature and atmospheric carbon dioxide concentrations anomaly were significantly lower than in the other glacial periods (*Bereiter et al.*, 2015; *Howe and Piotrowski*, 2017; *Jouzel et al.*, 2007). The relative sea level was relatively high (*Spratt and Lisiecki*, 2016), which may benefit from a direct transfer from the fjord to the continental slope.

In the Northern Hemisphere, a prolonged climatic optimum during MIS 15 - 13 interval is suggested, supported by a limited mountain glaciers advance in the Lake Baikal region (*Prokopenko et al.*, 2002) and stadial-like arboreal vegetation in NE Greece (Fig. 6.8A; *Tzedakis et al.*, 2006). More recently, (*Hao et al.* [2015]) highlight a strong inter-hemispheric asymmetry in MIS 14 with a severe cold interval in Southern Hemisphere records, in comparison with Northern Hemisphere records. They suggest a southern inception of glaciation because MIS 14 is also characterized by a later trough in solar radiation early in the glacial cycle (*Hao et al.*, 2015; *Hughes and Gibbard*, 2018). Our PIS reconstruction favors this observation with the IRD fluxes and the *n*-alkanes fluxes together with the highest value of the BIT index reached during MIS14 (Fig. 6.8E), both implying strong terrestrial discharges, hence suggesting extended PIS at this period. Contrary to this observation of the PIS, several Southern Hemisphere suggest that MIS 14 was warm, included in the long 'lukewarm' interglacial system. For instance, the Antarctic dust signal is much weaker than for any other glacial cycles (Fig. 6.8G; *Lambert et al.*, 2008), a maximum Agulhas leakage occurs during MIS14, reflecting an unusually warm period (*Rackebrandt et al.*, 2011), which may have been linked with a to enhanced freshwater input to the Southern Ocean due to the collapse of the West Antarctic Ice Shield during this period (*Hillenbrand et al.*, 2009). At Site U1542, the alkenone-based SST reconstruction shows relatively warm temperatures and termination VI presents a very low G/IG amplitude (Fig. 6.8D). Warm southeast Pacific SST may influence the supply of moisture to the Southern Andes, essential in the growth of ice sheets, although the intensity of the southern westerly wind belt is not prominent at this period (Fig. 6.8B, C).

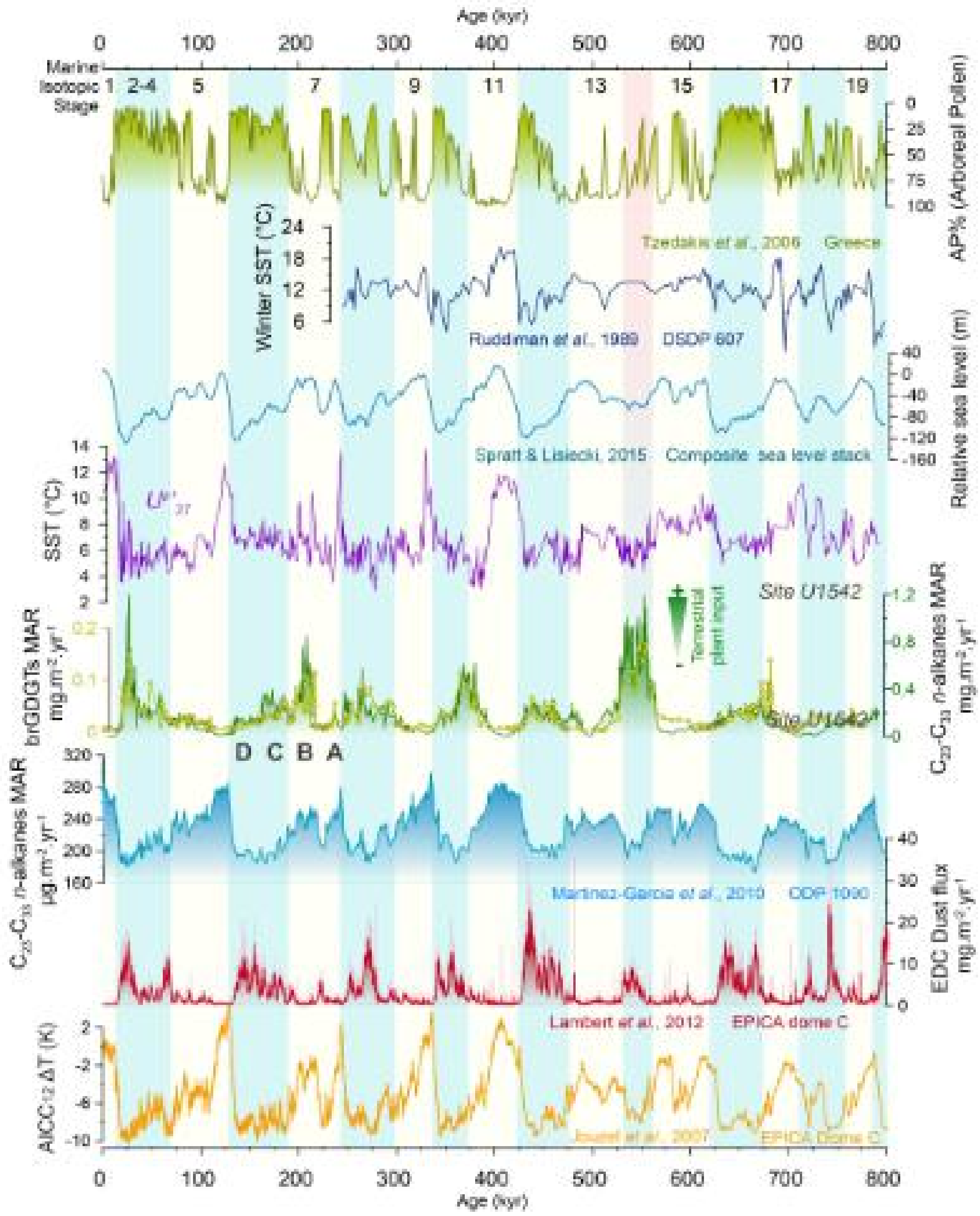

Figure 6.8: **Hemispheric discrepancy during MIS 14.** (A), Arboreal pollen from Tenaghi Philippon (*Tzedakis et al.*, 2006). (B), Winter sea surface temperature from North Atlantic (*Ruddiman et al.*, 1989). (C), relative sea level reconstruction (*Spratt and Lisiecki*, 2016). (D), n-alkanes and brGDGT mass accumulation rates from Site U1542 composite record. (E), n-alkanes mass accumulation in the south Atlantic, from ODP1090 record (*Martínez-Garcia et al.*, 2011). (F), Dust fluxes record from EPICA Dome C (EDC) ice core (*Lambert et al.*, 2008). (G), ssNa flux from EDC ice core taken as a quantitative winter ice extent (*Wolff et al.*, 2006). (H), Antarctic temperature record from EDC ice core (*Jouzel et al.*, 2007). North Hemisphere records presents relatively warm MIS 14, suggesting the "long system MIS 15-13" in the NH. In contrary, Southern records suggests extensive PIS during MIS 14.

One could argue that the sedimentation rate, which strongly affects the MAR values, during MIS 14 (1 m.kyr^{-1}), twice higher than other glacial stages (0.5 - 0.6 m.kyr^{-1} on average) could potentially be influenced by sediment processes not directly related to climate. On the Chilean slope, characterized by complex tectonics involving Antarctica, South America, and Scotia plates, the presence of a small-scale sediment depocenter ("sediment drift") in the sequence is partly related to contourite deposition. This active convergent plate margin is further conducive region for the generation of large-scale turbidity currents (*Bernhardt et al.*, 2017). However, although a relatively small-scale sediment drift has been identified at the upper continental slope near the location of Site U1542, no turbidite-like deposit is present in the sedimentary sequence (*Lamy et al.*, 2021), which cannot explain the high terrigenous discharge during MIS 14.

6.7 Conclusions

This study uses inorganic proxies such as IRD and terrigenous MAR, as well as terrestrial biomarkers accumulation rates (*i.e.*, *n*-alkanes MAR, brGDGTs MAR, BIT index) to reconstruct the PIS dynamics over the past eight glacial/interglacial cycles from the sedimentary archive IODP Site U1542 retrieved on the southern Chilean margin at the entrance of the Magellan Strait. The records allow a continuous reconstruction of the timing and magnitude of PIS discharges throughout the last 790 kyr, yielding detailed insight into the impact of Late Pleistocene glaciations onto the Southern Hemisphere midlatitudes and their relationship with orbital changes. The following conclusions can be drawn:

The sedimentary record from Site U1542, comprising terrestrial biomarkers along with IRD and XRF data, provides a unique and uninterrupted view of PIS dynamics across several glacial cycles. The timing of terrestrial sediment deposition is generally in agreement with the incomplete record from Patagonian moraines. The glacial-interglacial pattern observed mirrors dust records from Antarctic ice cores (*i.e.*, EPICA Dome C) and deep-ocean sediment cores (*i.e.*, ODP site 1090) dominated by Patagonian sources, which imply a close connection between PIS and global climate dynamic, emphasizing its role in the global carbon budget.

Rather than following the global "sawtooth" character of ice-age cycles, with gradual build-up and rapid collapse of ice sheets (*Cheng et al.*, 2016), the western PIS exhibits two major retreat periods during a period of global ice sheet expansion, during MIS 10 and 6. This retreat coincides with the SST warming observed in the southeast Pacific, highlighting the crucial role of SST in controlling the extent of the PIS. The similarities to the sea level reconstruction, rather than precession-driven westerlies, suggest sea level as the primary control in the sediment transfer toward the Chilean slope. Additionally, the presence of obliquity in the spectral signal of the IRD record points to high-latitude Antarctic ice sheet control.

The high accumulation rates observed during the warm MIS 14 suggest an extended ice sheet during this period, contradicting expectations of reduced cryosphere conditions during the ‘lukewarm’ interglacial. The discrepancy raises the possibility of sediment drift in the sedimentary record, warranting further investigation.

Chapter 7

Polar water retreat during the Mid-Brunhes climate transition

In preparation

Vincent Rigalleau, Nicoletta Ruggieri, Henrik Sadatzki, Oliver Esper & Frank Lamy

7.1 Abstract

Past climate variability across the past one million years is characterized by a succession of glacial and interglacial intervals, primarily dominated by ∼100 kyr cycles. The amplitude of these cycles strongly increased at ∼430 ka when interglacials became globally warmer during the Mid-Brunhes Climate Transition (MBT). The Southern Ocean is thought to play a strong role in the exchange of atmospheric CO_2 with the ocean and the storage of CO_2 in deep water masses. The release and storage of CO_2 in the Southern Ocean strongly correlates with the large orbital-scale atmosphere-ocean changes after the Mid-Pleistocene Transition between ∼1250 and ∼700 ka. In this study, we investigated the Southern Ocean surface water distribution using the percentage of tetra-unsaturated C_{37} alkenones ($\%C_{37:4}$). We show that $\%C_{37:4}$ is a robust indicator of the equatorward extension of polar surface waters. Our records from the Southern Ocean compared to published North Pacific data, indicate a poleward retreat of polar water masses throughout Marine Isotope Stage (MIS 12) in both hemispheres. This retreat likely contributed to the unusually warm temperatures during this period. Moreover, we find a period of less equatorward extended polar water during MIS 10, consequently to the exceptionally warm interglacial MIS 11. Ultimately, the more recent glacial-interglacial cycles

exhibit similarities to cycles before the MBT, favoring the idea of an event rather than a transition.

7.2 Introduction

Over the last 800 thousand years (kyr), the Earth's climate has been characterized by a 100-kyr-paced glacial/interglacial (G/IG) cycle (*Jouzel et al.*, 2007). *Jansen et al.* [1986] initially reported a climatic event in the middle of the Brunhes Chronozone (approximately 430 kyr ago, ka), associated with an increase in the amplitude of G/IG cycles (*Ao et al.*, 2020; *Cheng et al.*, 2016; *Jansen et al.*, 1986; *Jouzel et al.*, 2007). This Mid-Brunhes Event (MBE), led to warmer interglacials (*Jouzel et al.*, 2007), with higher concentrations of atmospheric CO_2 (*Lüthi et al.*, 2008) and greater G/IG-amplitude in $\delta^{18}O$ measurements in deep-sea records of benthic foraminifera, inferring reduced ice volume and/or warmer deep-ocean temperatures (*Lisiecki and Raymo*, 2005) compared to earlier interglacials within the last 800 kyr.

More recently, the idea of a succession of changes rather than a singular 'event' has been proposed, termed the Mid-Brunhes Transition (MBT) (*Ao et al.*, 2020; *Yin*, 2013). Various factors likely contributed to the MBT, including changes in monsoon strength (*Ao et al.*, 2020), dynamics related to ice sheets, and the carbon cycle during Marine Isotope Stage (MIS) 14 and MIS 13 (*Barth et al.*, 2018). Additionally, variations in the insolation impacting Southern Ocean (SO) ventilation and deep-ocean temperature (*Yin*, 2013), likely contributed to increased atmospheric CO_2 concentrations during the MBT (*Ao et al.*, 2020). Since the SO plays a critical role in the carbon cycle by sequestering and releasing CO_2 (*Sigman et al.*, 2021), a key question regarding the origin of the MBT likely pertains to changes in the behavior of the SO G/IG variability. This study aims to explore the evolution of SO water masses across the MBT to better quantify its role during this climatic transition.

For this purpose, we investigate the potential of an alkenone-based proxy as a polar water tracer. Ubiquitous cocolithophirodeae (*e.g., Emiliana huxleyi*) produce di-, tri-, and tetra-unsaturated methyl alkenones ($C_{37:2}$, $C_{37:3}$, and $C_{37:4}$), whose relative abundance is primarily influenced by the temperature at which they grow, making them valuable proxies for past sea surface temperatures (*Brassell et al.*, 1986; *Prahl and Wakeham*, 1987). Specifically, the alkenone unsaturation index $U^{k'}_{37}$, defined as $C_{37:2}/(C_{37:2} + C_{37:3})$ is one of the most powerful tools for climate reconstruction. Unlike the di- and tri-unsaturated C_{37} alkenones, the temperature response of the tetra-unsaturated C_{37} alkenone is less certain (*Sikes and Sicre*, 2002) and it was likely associated with salinity changes in high latitude records (*Rosell-Melé et al.*, 2002), or with surface advection of iceberg-bearing water masses (*Bard et al.*, 2000). More recently, the relative abundance of $C_{37:4}$ (*i.e.*, $\%C_{37:4}$) produced by the group 2i Isochrysidales, has shown a significant positive correlation with annual mean sea ice concentration (*Wang et al.*, 2021). These relationships have led several studies to use $\%C_{37:4}$ as a tracer of low sea surface salinity from polar and subpolar water masses in high latitudes sediment records (*Martínez-Garcia et al.*, 2010; *McClymont et al.*, 2008), a topic further explored in this study.

Here, the surface ocean circulation in the central and eastern Southern Pacific Ocean across the MBT is investigated. We present new $\%C_{37:4}$ from two International Ocean Drilling Program (IODP) sites covering the past 800 kyr: the central South Pacific (CSP) Site U1541 and eastern South Pacific (ESP) Site U1542. By comparing these new results together with a compilation of published studies from the South Atlantic, Southeast Pacific, and North Pacific, we further investigate the role of polar water mass changes and frontal shifts during the MBT.

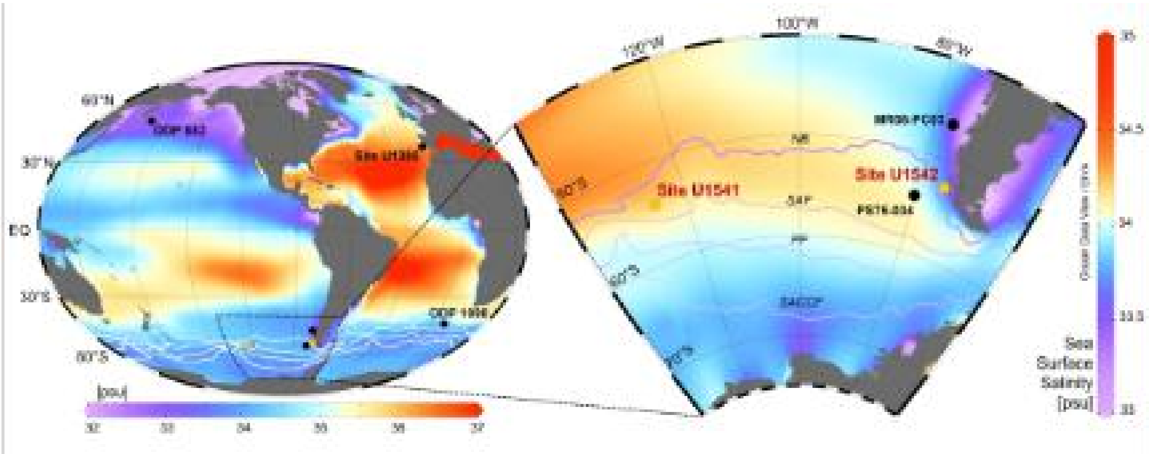

Figure 7.1: **Modern sea surface salinity and location of cores introduced in this study.** Sea surface salinity originates from World Ocean Atlas 2018. Line indicates southern oceanic frontal system described by *Park et al.* [2019]. NB = Northern Boundary, SAF = Subantarctic Front, PF = Polar Front and SACCF = Southern Antarctic Circumpolar Current Front. Maps created in Ocean Data View: https://odv.awi.de/

7.3 Study Area

One of the most prominent oceanographic features of the Southern Ocean is a system of deep-reaching oceanic fronts, which is associated with upward shoaling of density surfaces towards the south, upwelling of deep waters, the formation of intermediate water masses, and steep upper ocean gradients (*Orsi et al.*, 1995; *Park et al.*, 2019). Through this linkage of the shallow and deep ocean, the Southern Ocean plays a critical role in the carbon cycle and changes in atmospheric CO_2 (*Rintoul*, 2018). The main fronts are, from North to South, the Subantarctic Front (SAF), the Antarctic Polar Front (PF), and the Southern-ACC Front (SACCF). The northern Subantarctic Front (SAF) represents the core of the Antarctic Circumpolar Current (ACC) flow and less prominently at the Northern Boundary (NB) front and the Polar Front (PF). The Polar Frontal Zone (PFZ), encompassed by the SAF and PF, is the core of the formation of the Antarctic Intermediate Water masses (AAIW, *Rintoul*, 2018). During glacial periods, the fronts shifted equatorward (*e.g.*, *Civel-Mazens et al.*, 2021) reducing surface/deep exchange affecting CO_2 storage (*Sigman et al.*, 2021), and the ACC was reduced in the Pacific sector (*Lamy et al.*, 2015, 2024). Under modern conditions, Site U1541 and U1542 are located North of the SAF in the Subantarctic Zone (SAZ), close to the NB (Fig. 7.1). The modern salinity at Site U1541 is higher (∼34.2 psu) than Site U1542 (∼33.6 psu; Fig. 7.1)

7.4 Material & Methods

The methodological strategy of this work relies on the combination of existing records coupled with two new $\%C_{37:4}$ records from Sites U1541 and. This biogeochemical indicator is further compared with diatom-derived winter sea ice from two marine sediment cores located in the South Atlantic, ODP 1093 and ODP 1094 (*Kunz-Pirrung et al.*, 2002; *Schneider-Mor et al.*, 2005).

Sediments

Site U1541 and U1542 have been drilled during Expedition 383 onboard (R/V) JOIDES Resolution and therefore described in the Proceeding of IODP 383 expedition (*Lamy et al.*, 2021).

Site U1541 (54°12.76'S, 125°25.54'W) is located in the CSP on the western flank of the southernmost East Pacific Ridge at a water depth of ∼3600 m. The sediment record at Site 1541 extends to ∼145-m composite depth and provides a continuous pelagic sedimentary sequence covering the Pliocene and Pleistocene (*Lamy et al.*, 2024). The age model is based on benthic foraminiferal stable oxygen-isotope stratigraphy (*Middleton et al.*, 2023) and orbital tuning (*Lamy et al.*, 2024). The sedimentary sequence of Site U1541 includes four lithofacies: carbonate-bearing to carbonate-rich diatom ooze, diatom-bearing to diatom-rich nannofossil/calcareous ooze, nearly pure nannofossil ooze, and clay-bearing to clayey biogenic ooze (*Lamy et al.*, 2021).

Site U1542 is located in the SEP (52°42.29'S, 75°35.77' W) and 50 km offshore from the Chilean margin in the continental slope at 1,101 m water depth. Site U1542 provides a continuous sediment (*Lamy et al.*, 2021). The age model is based on benthic foraminiferal (*G. uvigerina*) oxygen isotope (δ^{18}O) combined with tuning of the X-ray fluorescence Core Scanner derived Ca-counts record to the Antarctic ice core EDC temperature record (*Rigalleau et al.*, In review). The U1542 sediment record reaches back to ∼780 kyr. The sedimentary sequence of Site U1542 is primarily constituted of siliciclastic sediments with low carbonate contents (∼1–12 wt% $CaCO_3$), and biogenic silica contents ranging from 1 to 4 wt%. Lithofacies of sandy foraminiferal ooze (∼30–55 wt% $CaCO_3$) characterize interglacial periods.

Biomarkers

Biomarker analyses at Site U1541 and Site U1542 were performed at Alfred Wegener Institute Bremerhaven and previously described in *Rigalleau et al.* [In review]. Briefly, to recover the total lipid extract, an Accelerated Solvent Extractor 350 was used. 5g of homogenized freeze-dried sediment, was heated at 100°C for 5 min followed by 3 cycles of 5 min with solvent (Dichloromethane:Methanol, v:v, 9:1) static in the cell containing the sediment. The total lipid extract was subsequently separated into three fractions using silica columns prepared from Pasteur pipettes. The first fraction was eluted using Hexane to recover *n*-alkanes. The second fraction was eluted using Dichloromethane to recover alkenones. The third fraction was eluted using a solvent mixture of Dichloromethane and Methanol (1:1) to recover Glycerol Dialkyls Glycerol Tetraethers (GDGTs). First and third (*i.e.*, *n*-alkanes and GDGTs, respectively) fractions are not used in this study. Alkenones were measured using a Gas chromatographer (Hewlett-Packard HP7890) fitted to a Flame Ionization Detector (GC-FID) using Helium as carrier gas. Samples were vaporized and led through a capillary column.

Diatoms reconstruction techniques

The diatom-derived Winter Sea Ice (WSI) reconstructions from ODP Site 1093 (49°59'S, 5°52'E) and Site 1094 (53°10.8'S, 5°7.8'E) were obtained using transfer functions developed by (*Esper and Gersonde*, 2014a,b). As the diatom reconstruction techniques are not the scope of this study, the methodology is not detailed here. Briefly, for WSI concentration estimates, the MAT from (*Hutson*, 1980) was applied. Statistical details and background of the methods and their performance at different application levels and in comparison with other estimation methods are presented in (*Esper and Gersonde*, 2014a,b). A more complete description can be found in (*Benz et al.*, 2016). The counting method and first WSI estimation at ODP 1093 can be found in *Schneider-Mor et al.*

[2005]. The counting method and first WSI estimation at ODP 1094 can be found in *Kunz-Pirrung et al.* [2002].

7.5 Results & Discussion

%$C_{37:4}$ as a polar water mass proxy

At both Site U1541 and Site U1542 the %$C_{37:4}$ show large fluctuations with generally higher values (∼15-20%) during colder periods and lower values (<5%) during warm periods (Fig. 7.2). In the CSP, $C_{37:4}$ alkenones exhibit their highest abundance (up to 20%) during glacial Marine Isotope Stages (MIS) 18, 16, 14, 12 and 8. At Site U1542, the highest %$C_{37:4}$ (up to 18 %) is found during MIS 18.

The interpretation of %$C_{37:4}$ as a tracer fro inferring variations in the meridional extent of polar and subpolar conditions through time is based of the few previously available studies in high latitudes sediment records (*Bendle et al.*, 2005; *Martínez-Garcia et al.*, 2010; *McClymont et al.*, 2008) and is further explored in this study. In the pelagic Southern Ocean, the %$C_{37:4}$ increases in the vicinity of the PF slightly north of the winter sea-ice margin.

The slightly lower %$C_{37:4}$ at Site U1542 may be attributed to its location north of the NB (Fig. 7.1; *Park et al.*, 2019), whereas Site U1541 is located southward of the NB. Both SAZ records present strong similarities, in terms of variability and abundance, with a South Atlantic record, ODP 1090, located in the SAZ (Fig. 7.2; *Martínez-Garcia et al.*, 2010). Closer to the SAF in the Southeast Pacific, the open eastern South Pacific sediment record PS75/034-2 exhibits as well higher abundance of %$C_{37:4}$ (up to 25%) compared to the more coastal U1542 record (Fig. 7.2; *Ho et al.*, 2012).

There is dissension on whether $C_{37:4}$ alkenones originate from salinity changes related to meltwater input or water mass changes. It has been demonstrated that %$C_{37:4}$ shows a positive correlation with ice-rafted debris (IRD), as meltwater bears icebergs (*Bard et al.*, 2000; *Seki et al.*, 2005). On the Chilean margin where Site U1542 is located (Fig. 7.2B, C), if both proxies covary with glacial/interglacial variability, *i.e.*, with lower values during warm periods and higher values during the glacial cold periods when the Patagonian Ice sheet was expended. However, both records also exhibit discrepancies, with, for instance, high $C_{37:4}$ abundance around 600, 515, and 110 ka, while no IRD are found at these periods. Thus, IRD likely reflects a more local component of the Patagonian glaciers, whereas $C_{37:4}$ alkenones might mirror the presence of Southern Ocean waters. *Hagemann et al.* [2024] found substantially elevated values of %$C_{37:4}$ in a marine record located on the western flank of the Chilean margin during all terrigenous input phases associated to temperature minima, inferring a meltwater origin from ice discharge, which reduces offshore salinities.

A thin layer (<30 m) of low salinity (<33.5 psu) (*Strub et al.*, 2019) is known as Chilean Fjord Water flows northward from the fjord region within ~200 km off the coast (*Strub et al.*, 2019; *Tapia et al.*, 2021). However, Site U1542 is located south of the pathway of Chilean Fjord Water, thus less influenced by this water mass. Instead, it is more affected by the open ocean water masses of the ACC, which explains the relatively low Patagonian freshwater signal at Site U1542 and its similarity in signal and abundance to offshore records. This contradicts the previously hypothesized origin of $C_{37:4}$ alkenones from the nearby MD07-3128 sediment record, advocating a Patagonian ice-sheet influence of the signal (*Caniupán et al.*, 2011). Taken together, the available evidence suggests that the algae from the group 2i Isochrysidales, which produce the $C_{37:4}$ (*Wang et al.*, 2021), are poorly influenced by meltwater from the continental glaciers (in this case, Patagonian), as the coastal records U1542 exhibit similar variability and abundance (up to 20%) to the offshore records (Fig. 7.2). Therefore, the increase in $\%C_{37:4}$ due to Patagonian freshwater seems to be negligible compared to the influence of polar water from the Southern Ocean. The low salinity along Chile likely only affects the area further north where polar water masses are less present and the influence of the PIS on surface water salinity becomes more important (*Hagemann et al.*, 2024). Taken together, the strong similarities between U1541, U1542, PS75/034-2, and ODP 1090 suggest that the $\%C_{37:4}$ is a robust tracer for inferring variations in the meridional extent of polar and subpolar conditions through time, rather than solely serving as a proxy for freshwater or sea ice.

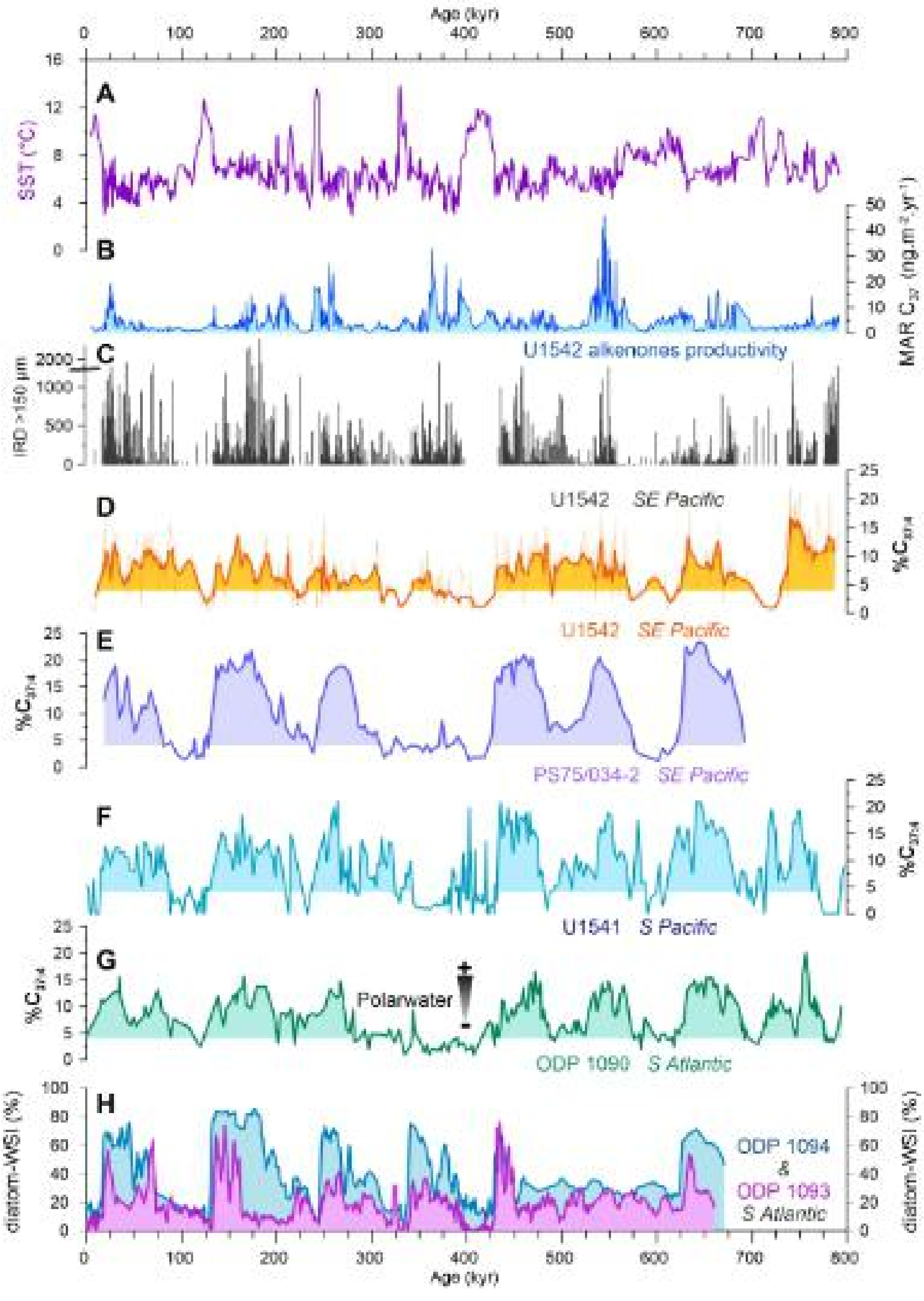

Figure 7.2: **Sea surface proxies reconstructing the Southern Ocean variability.** (A) Alkenones-derived sea surface temperature, (B) alkenones-derived marine productivity, and (C) Ice-rafted debris at Site U1542. (D) $\%C_{37:4}$ from Site U1542, (E) from PS75/034-2 (*Ho et al.*, 2012, (F) from Site U1541, and (G) from ODP Site 1090 (*Martínez-Garcia et al.*, 2010 (H) Diatom-derived winter sea ice extent from ODP Site 1093 and ODP Site 1094. The percentage of $C_{37:4}$ among C_{37} alkenones is defined by $\%C_{37:4} = 100x[C_{37:4}]/[\ C_{37:2} + C_{37:3} + C_{37:4}]$ with quantities based on the chromatographic peak areas.

%$C_{37:4}$ and diatom-derived sea ice reconstruction

It has also been suggested that during the glacial periods, elevated %$C_{37:4}$ likely results from increased seasonal sea ice persisting into summer and melting, thereby providing cold freshwater to the surface ocean during the haptophyte algae growing season in summer (*Seki et al.*, 2005).

To determine if $C_{37:4}$ is an indicator of sea ice, we compare the abundance of $C_{37:4}$ to Winter Sea Ice (WSI) reconstruction, derived from a transfer function on diatom assemblages (*Benz et al.*, 2016; *Esper and Gersonde*, 2014a,b). This relationship between diatoms-derived sea ice and the relative abundance of $C_{37:4}$ has been previously suggested (*Horikawa et al.*, 2015). As diatom-derived sea ice reconstructions are rare, we compare our findings with two available records from the South Atlantic, ODP 1093 and ODP 1094 located respectively near the PF and near the modern winter sea ice boundary (*Comiso*, 2003). These, along with the subantarctic record at ODP Site 1090 (*Gersonde et al.*, 1999), form a cross-frontal transect in the Atlantic SO: In general, the %WSI records from both ODP Site 1093 (Fig. 7.2G) and ODP Site 1094 (Fig. 7.2H) show clear similarities in relative changes. The ODP Site 1094 WSI record ranges from 20% during warm periods to 100% WSI during glacial periods while the ODP Site 1093 WSI record varies from 0% to 80% WSI, consistent with its location at lower latitude near the modern APF, hence less influenced by the Antarctic Sea ice. The relative changes in both WSI records largely covary with the %$C_{37:4}$ record at ODP Site 1090, showing similar glacial/interglacial variability. However, several periods of extended sea ice are not associated with %$C_{37:4}$ increases at ODP Site 1090 even when considering age model uncertainties into account. This suggests that diatom-derived sea ice extent and the latitudinal extent of polar water derived from $C_{37:4}$ abundance are not necessarily in agreement, as the first one is representative of winter sea ice and alkenones production reflects mostly an annual mean signal (*Hagemann et al.*, 2022), implying a seasonal discrepancy between both proxies. However, ODP Site 1090 is located relatively far north in the SAZ, and thus is most likely not affected by winter sea ice even during glacial periods.

Southern Ocean pacing of latitudinal extent polar water masses

The orbital-scale variations in the relative abundance of $C_{37:4}$ from sites in the Central South Pacific (Site U1541), Southeast Pacific (Site U1542 and PS75/034-2; *Ho et al.*, 2012), and South Atlantic (ODP 1090; *Martínez-Garcia et al.*, 2010), all situated in the subantarctic SO, show a similar pattern. The signal variability of %$C_{37:4}$, expressed as the standard deviation (σ), is high at Site U1541 ($\sigma = 5.3$), as the site is located near the East Pacific Rise, where modern latitudinal shifts of oceanic fronts are bathymetry locked

(*Lamy et al.*, 2024). Similarly, the highly variable PS75/034-2 ($\sigma = 6.9$), located at the entrance of the Drake Passage, the bottleneck of the ACC where fronts are gathered, experiences notable gradient changes associated with rapid shifts of oceanic fronts. In contrast, Site U1542, located underneath the relatively warm Cap Horn Current (Fig. 7.1; *Park et al.*, 2019), shows lower variability ($\sigma = 3.9$), similar to ODP 1090 ($\sigma = 4.2$), located farther North from the SAF in the South Atlantic, where polar fronts are more scattered. This indicates a consistent latitudinal pattern in the contraction and the extent of polar water into the modern SAZ of the Southern Ocean, with variability in polar water masses contingent upon their proximity to the Southern Ocean fronts.

Thereafter, given the consistency in abundance and variability among these records, we aim to reconstruct the surface ocean circulation within the SAZ over the past 800 kyr using a SO stack compiling the records from Site U1541, U1542, ODP 1090, and PS75/034-2. This SO stack documents a significant G/I variability where glacial stages are associated with lower $\%C_{37:4}$ values and interglacial stages exhibit higher $\%C_{37:4}$ values. The transitions between these states are abrupt, indicating a rapid retreat and advance of polar water masses, likely due to the locations of the sites close to the fronts where gradients are supposed to be high. However, retreat from glacial to interglacial conditions shows a more gradual trend from 550 to 500 ka and becomes more pronounced from 480 to 435 ka.

Frontal dynamic during the Mid-Brunhes Transition

The SO stack reveals a reorganization of polar water mass dynamics during a key period of the Late Pleistocene known as the MBT (*Jansen et al.*, 1986). Glacial cycles preceding the MBT (430 - 800 ka) show variability ranging from 5% during MIS 15 to over 15% during MIS 18, 16, 14, and 12. During MIS 14, the SO stack suggests relatively cold conditions and a northward extent of the Polar Front, contrasting with the concept of a prolongated “Lukewarm” MIS 15 – 13 interglacial system (*Jaccard et al.*, 2013). The cold SO conditions during MIS 14 coincide with the occurrence of giant diatom deposits in the subtropical South Atlantic at ca. 530 ka, suggesting the advection of colder waters of southern origin northward and supporting high $\%C_{37:4}$ values (*Romero and Schmieder*, 2006).

Ao et al. [2020] suggested a two-stage process starting around ∼500 ka (MBT-1), characterized by enhanced warming of Northern Hemisphere continents, limited warming in the Southern Hemisphere, and an associated intensification and more extensive northward swings of the Intertropical Convergence Zone (*Ao et al.*, 2020). The SO stack corroborates this, showing extended equatorward expansion of polar waters during this period, characterized by high ($\%C_{37:4} < 5\%$) values for an interglacial period. The second stage of the Mid-Brunhes Climate Transition (MBT-2) suggested by *Ao et al.* [2020] around ∼400 ka, indicates a global transition towards increased interglacial warmth linked to rising atmospheric CO_2 concentrations, alongside reduced ice volume starting at MIS 11.

The SO stack indicates a substantial and continuous retreat of polar water masses, depicted by a decrease in $\%C_{37:4}$ from more than 15% throughout MIS 12 to values below 3% at MIS 11, indicating the absence of polar water. The MBT-2 period shows prolonged polar water retreat in the SO between 480 and 435 ka, reaching 0% during MIS 11. This phase is further characterized by the highest carbonate concentration during the Pleistocene (*Lamy et al.*, 2021; *Saavedra-Pellitero et al.*, 2017a; *Toyos et al.*, 2020), and the "IRD-free period" between 432 and 395 ka in the Subantarctic South Atlantic (*Hodell et al.*, 2003).

In the Northern Hemisphere, the $C_{37:4}$ record of ODP Site 882 spans the timeframe of this study. Located in the sub-Arctic Pacific at 50°N, (*Martínez-Garcia et al.*, 2010; *McClymont et al.*, 2008), this offshore record not only shows a similar abundance of $C_{37:4}$ (2 - 25%) but also presents similar G/IG variability ($\sigma = 5.7$) as the SO records. This underlines a parallel latitudinal expansion of Arctic and Subantarctic water masses distribution across glacial cycles and suggests an interhemispheric coupling.

The polar water retreat initiated in the early part of MIS 12 aligns with the onset of deep ventilation towards the MIS 12/11 transition, contributing to the release of CO_2 into the atmosphere. The Southern Ocean modulates the exchange of CO_2 between the deep sea and the atmosphere (*Rintoul*, 2018), by promoting the ventilation of deep water through upwelling in response to a strengthening of deep circulation and decreasing Southern Ocean stratification (*Sigman et al.*, 2021; *Skinner et al.*, 2010). This reduction in stratification is linked to a southward migration of the SO fronts, likely driven by an intensification and southward displacement of the SWW (*Anderson et al.*, 2009). MIS 12 also corresponds to a dust increase in the Southern Hemisphere (*Barth et al.*, 2018), further supporting the potential strengthening and southward displacement of the SWW. Following the glacial inception at the end of MIS 11, no increase of $\%C_{37:4}$ is observable in the stack. The period of polar water retreat during the outstanding MIS 11 extends until MIS 9c, at around 325 ka. The absence of $C_{37:4}$ (<5%) is unique for a glacial period over the last 800 kyr and implies a poleward position of the SO fronts (Fig. 7.3C), as well as for the subpolar North Pacific (Fig. 7.3B). Given that this unique configuration follows MIS 11, it is likely that the MBT profoundly influenced the configuration of the frontal system. The absence of polar water during MIS 10 further suggests a delay in the response of mid-to-high latitude front systems after an exceptionally long and warm interglacial period.

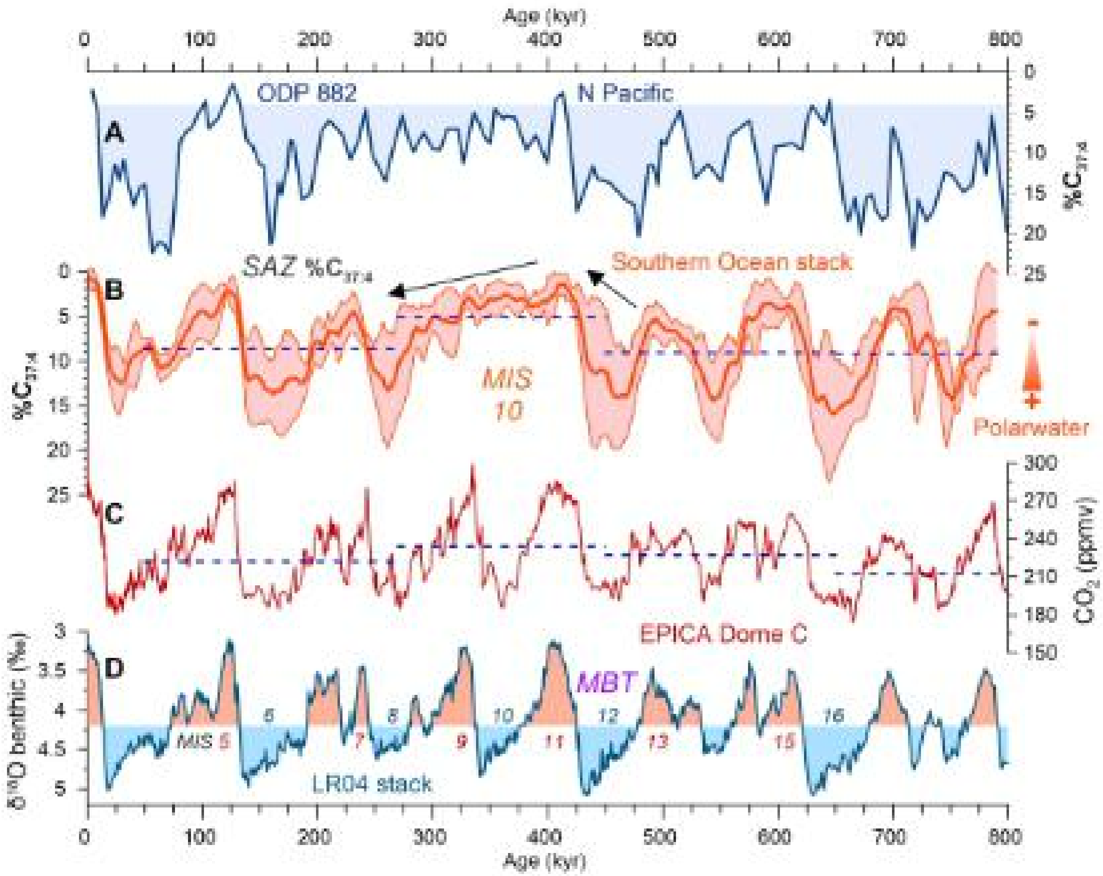

Figure 7.3: **Pleistocene fluctuation of polar water masses across the Mid-Brunhes climate transition.** (A) %$C_{37:4}$ from Site 882 (*Martínez-Garcia et al.*, 2010 (B) Southern Ocean stack representing latitudinal extension of polar waters near the Northern boundary (NB). (C) Atmospheric CO_2 concentration from Antarctic ice core (*Bereiter et al.*, 2015 (D) LR04 stack (*Lisiecki and Raymo*, 2005

Compared to other glacial periods, MIS 12 and particularly MIS 10 stand out as cold with enhanced productivity (*Bard and Rickaby*, 2009). Along the Chilean margin, underneath the Humboldt current (*Tapia et al.*, 2021) and the Cap Horn Current at Site U1542, MIS 10 is characterized by a notably high coccolithophoridae production (Fig. 7.2A; *Saavedra-Pellitero et al.*, 2017b). This significant production of 2i Isochrysidales taxa may have 'diluted' the signal of the 2i Isochrysidales taxa, thereby reducing the relative abundance of $C_{37:4}$, explaining the lower values during MIS 10. However, MIS 14 and MIS 2-4 show relatively high production, yet display a high abundance of $C_{37:4}$. Thus, a 'dilution' effect cannot fully account for the low abundance during MIS 10. A possible near-extinction of the taxa producing the $C_{37:4}$ during MIS 11 could justify the absence of $C_{37:4}$ during MIS 10, and slowly (during 100 to 120 kyr) reappearing to reach pre-MIS 11 values. However, a significant abundance of $C_{37:4}$ during MIS 10 in the

Iberian margin record suggests that freshwater taxa were not impacted by the reduction in population during MIS 11 (*Rodrigues et al.*, 2017). Furthermore, the North Pacific record ODP Site 882 also indicates a retreat during MIS 12 and the prolongated absence of %$C_{37:4}$, making it challenging to conceive a quasi-extinction of the 2i Isochrysidales taxa in both hemispheres. Ultimately, the high coccolithophoridae productivity during MIS 10 likely supported a retreated polar water rather than taxa extinction.

Thereafter, a persistent equatorward expansion of polar water is indicated by gradual increases of %$C_{37:4}$, reaching glacial values (>15%) around MIS 8. In the North Pacific, MIS 8 is also characterized by a relatively low abundance in $C_{37:4}$ (<10%) compared to other glacials. *Yin* [2013] stated that during the post-MBE interglacials (*i.e.*, MIS 9, 7, 5, and 1), the Southern Ocean surface was less salty, and warmer (*Schaefer et al.*, 2006), and had reduced sea ice extent (*Wolff et al.*, 2006), with the APF located farther south (*Kemp et al.*, 2010). However, this observation is not prominently reflected in the SO stack, as post-MBT interglacials only slightly exhibit lower values, ranging from 2 to 5%. This minimal change is likely related to the polar front location, as salinity exerts reduced influence on the abundance of $C_{37:4}$. Additionally, consistent %$C_{37:4}$ (~12 – 15%) throughout the SO record does not suggest more intense or prolonged glaciations post-MBE (*Kemp et al.*, 2010).

7.6 Conclusions

In this study, we used the %$C_{37:4}$, a relatively uncommon proxy, to infer latitudinal shifts of the SO frontal system over the past 800 kyr. Contrary to IRD and diatom-derived winter sea ice records, %$C_{37:4}$ does not indicate salinity/freshwater input or sea ice presence in the SAF. Instead, the strong correlation among records from the Central South Pacific, Southeast Pacific, and South Atlantic implies that %$C_{37:4}$ functions as its own proxy, providing a robust indicator of surface frontal shifts and the extension of polar water masses. Compiled into a Southern Ocean stack, elevated contents of $C_{37:4}$ during glacials and lower values during interglacials mirror the contraction and expansion of Antarctic polar water and north-south shifts of the SO frontal system across glacial-interglacial cycles. Early polar water retreats throughout MIS 12 and a poleward position of polar water during MIS 10 in both hemispheres suggest a crucial role of mid-latitude surface water mass evolution during the Mid-Brunhes Climate Transition toward more pronounced glacial and interglacial conditions. Furthermore, the robust correspondence between records in both hemispheres indicates a reduced metabolic disparity among coccolithophorids endemic to Arctic, Antarctic, or coastal water masses (*Schulz et al.*, 2000). The two-stage MBT proposed by *Ao et al.* [2020] can be applied here, although the two main events occurring during MIS 12 and 10, with MIS 11 serving as a key period. Moreover, the absence of notable change in the G/IG regime suggests that the MBT did not profoundly impact the surface circulation of high latitudes. However, the early retreat of polar water during MIS 12 and its absence during MIS 10, centered around the MBT and MIS 11, implies a major role of northern and southern polar water in shaping this transition. Nonetheless, it is evident that a comprehensive assessment of polar water mass extent requires high-resolution reconstructions of deep-water temperatures and other proxies spanning the MBT.

Chapter 8

Concluding remarks and outlook

In this PhD thesis, I focused on reconstructing past climatic variability in the Southeast Pacific since the Late Pleistocene and the end of the Mid Pleistocene Transition using the sedimentary archive IODP Site U1542. Matured by 50 years of scientific ocean drilling (*Becker et al.*, 2019), Site U1542 provides an unprecedented high-resolution view of the climate in the Southern Hemisphere over the past 790,000 years (Figure 8.1).

Strategically located on the southern Chilean margin at a depth of 1,101 meters, Site U1542 records ocean-atmosphere-cryosphere interactions and teleconnections. The site sits underneath the Cape Horn Current, the northernmost branch of the ACC that flows into the Drake Passage (*Zheng et al.*, 2023). Variations in the strength of the Cape Horn Current indicate past changes in the strength of the Antarctic Circumpolar Current, the world's strongest current(*Lamy et al.*, 2015). Moreover, the oceanic fronts converge in the Drake Passage, and strong latitudinal gradients can be observed in the area. Thus, it is a suitable location to reconstruct meridional fluctuations of surface waters. Additionally, this mid-latitude southern (54°S) record is situated in the southern westerly wind belt, a predominant driver of the ACC. The terrigenous sediment input on the Chilean margin significantly increases during glacial periods due to contributions from the Andean hinterland. Therefore, changes in terrestrial proxies on the Chilean margin indicate advances and/or instabilities of the Patagonian ice sheet.

The overarching goal of this thesis was to better constrain orbital to millennial-scale variations in the Southern Ocean by producing millennial-scale resolved records at Site U1542 using biomarkers proxies (*i.e.*, *n*-alkanes, alkenones, and GDGTs). In addition, by analysing inorganic proxies such as grain size, XRF, terrigenous elements concentrations, and ice-rafted debris (IRD), several conclusions emerge. Chapter 5 explores the close coupling between alkenone-derived SST and bottom current reconstruction at Site

U1542, examining variability from orbital to millennial scales. Comparing Site U1542 with a planktic $\delta^{18}O$ North Atlantic record reveals a strong interhemispheric teleconnection, emphasizing the role of oceanic circulation in millennial-scale variability. Furthermore, the reconstruction of the ACC strength highlights the Southern Ocean's influence in promoting deep-sea ventilation that influences the release of CO_2 into the atmosphere. Chapter 6 investigates variations in the terrigenous fraction and terrestrial biomarkers of Site U1542 to reconstruct changes in the PIS over multiple glacial cycles. This unprecedented detailed picture reveals that PIS growth is largely controlled by SST in the Southeast Pacific, with sea level variations driving sediment transfer from the PIS towards the Chilean margin. Chapter 7 focuses on the percentage of tetra-unsaturated ketone ($\%C_{37:4}$) in Site U1542 sediments as a tracer for polar water masses. This record is included in a Southern Ocean-wide $\%C_{37:4}$ stack, showing a polar water retreat during the early Mid Brunhes Transition (450 to 410 ka), followed by a prolonged period of retreated polar water (410 to 300 ka). This suggests a rearrangement of Southern Ocean circulation during the Mid-Brunhes Transition. Altogether, the records produced for this thesis provide new insights into global climate over the past million years.

The peculiar location of Site U1542 may partially disturb or bias different records. Situated at a relatively shallow depth (1,101 meters), Site U1542 offers several advantages, such as reduced particulate residence time in the water column and minimized biomarker advection. However, this complicates the benthic foraminifera oxygen isotope record most commonly used to establish age model correlations. The glacial-interglacial variability in the benthic isotope record is relatively subdued, while strong variability is observed at millennial timescales. Terrigenous input may also influence oceanic proxies such as alkenones. *Caniupán et al.* [2011] suggested that a warming trend observed during the LGM originated from meltwater and icebergs from the PIS, which likely reached the continental margin at this time (*Davies et al.*, 2020). Accordingly, Site U1542 exhibits strong variability in alkenone and bottom current strength records during peak glacial periods, potentially due to terrestrial overprint. The TEX_{86} proxy is not further interpreted in this thesis, as it shows high variability when the BIT index is high, in other words, at times of high terrigenous input (*Hagemann et al.*, 2024). Offshore sediment records, on the other hand, potentially provide a clearer view of larger-scale palaeoceanographic changes (*e.g.*, core PS75/34 located ∼200 nm offshore (*Ho et al.*, 2012). However, these records are rare due to confounding deep-ocean processes, such as carbonate dissolution. Additionally, the absence of terrigenous input reduces sedimentation rates, which may enshroud the millennial-scale signal, and little is known about millennial-scale variability in the pelagic Southern Ocean.

The IODP 383 expedition drilled six sites in the Southern Pacific. As Site U1542 presented in this thesis, the high-resolution Site U1539 from the central South Pacific could substantially enhance our understanding of sub-orbital climate variations and potential tipping points in the pelagic Southern Ocean as well as their link to the marine carbon cycle and Antarctic ice-sheet stability. The unique location of Site U1539 is characterised by unusually high sedimentation rates (~10-50 cm/kyr), providing high-resolution pelagic sediment close to the subantarctic front and close to the influence of the opal belt. These sediments are capable of resolving millennial-scale climate variations over the past ~1.4 Myr therefore extending Site U1542 beyond the mysterious Mid-Pleistocene Transition. Moreover, this time interval corresponds to the planned European Beyond EPICA – oldest ice project (*Fischer et al.*, 2013), and the Site U1539 records might develop into a marine counterpart of the prolongated Antarctic ice-core expected in the near future.

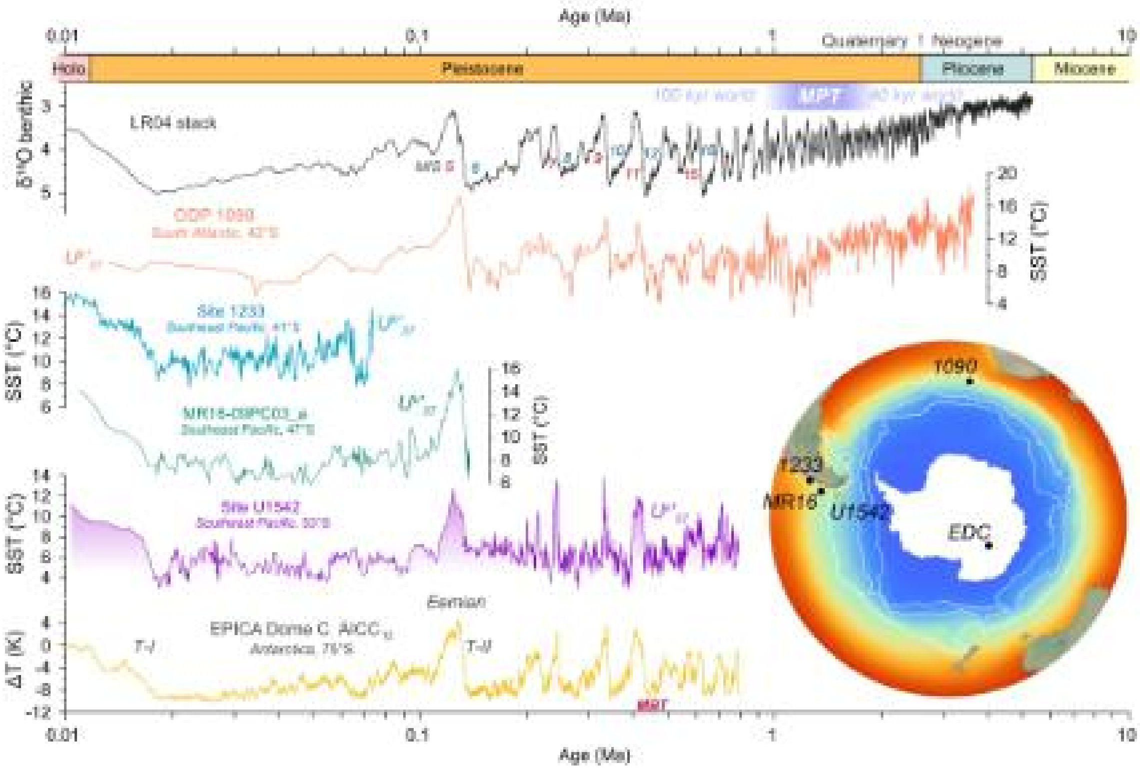

Figure 8.1: **The last 8 Millions years of Earth's History on a logarithmic scale.** Sea Surface Temperature reconstruction at Site U1542 among remarkable similar records in the Southern Hemisphere. A southern millennial-scale resolved record covering multiple glacial cycle is unprecedented in the scientific community. LR04 stack after *Lisiecki and Raymo* [2005], ODP 1090 (*Martínez-Garcia et al.*, 2010), Site 1233 (*Kaiser et al.*, 2005), MR16 (*Hagemann et al.*, 2024), EDC (*Jouzel et al.*, 2007)

Chapter 9

Declaration of Authors' Contribution

The initial proposal for this thesis consisted of producing a millennial-scale (>1000 samples) resolved biomarker record at Site U1542 in its entirety. Vincent Rigalleau performed all biomarkers laboratory work, from extraction and measurements to peak integration (>1300 samples plus replicates) under the supervision of Nicoletta Ruggieri at Alfred Wegener Institute for Polar and Marine Research in Bremerhaven (AWI). The exception was the GDGT measurements, which were performed by Jens Hefter, and the $C_{37:4}$ measurements at Site U1541 were performed by Henrik Sadatzki.

Lester Lembke Jene and Igor M. Venancio carried out the stable isotope measurements at the Alfred Wegener Institute for Polar and Marine Research in Bremerhaven and Universidade Federal Fluminense, respectively. X-ray Fluorescence major element records for Site U1542 were conducted by Expedition 383 scientists and co-workers as well as the IODP staff at the Texas A&M University in College Station, USA. The age model was developed equally by Vincent Rigalleau, Frank Lamy, and Helge W. Arz, building on the preliminary shipboard age model.

IRD counts and XRF calibration at Site U1542 measurements were performed by Nils Ponka and Clemens as part of their master's thesis at the Leibniz Institute for Baltic Sea Research in Warnemünde (IOW), issued from the collaboration between AWI and the IOW with the group of Helge W. Arz, co-investigator of the drilling proposal and sedimentologist on Expedition 383.

Vincent Rigalleau and Frank Lamy designed the three lines of research (Chapters 5, 6, and 7). The entire thesis including the three main chapters was written by Vincent Rigalleau, with all authors providing comments and feedback on the manuscripts.

Chapter 10

Appendix: Supplementary figures for Chapter 5

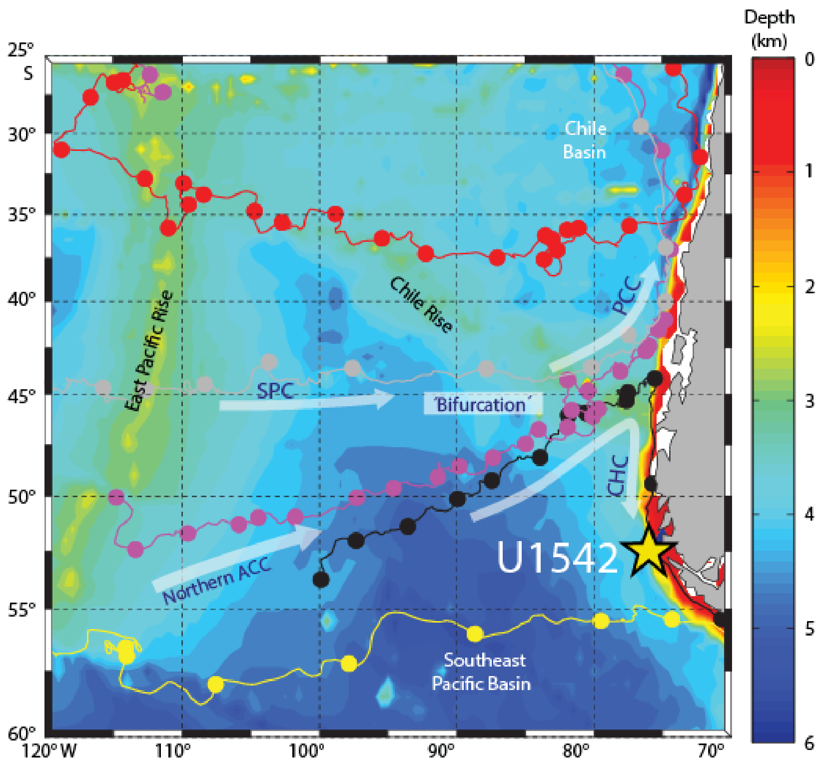

Figure 10.1: Surface circulation in the Southeast Pacific with examples of surface buoy trajectories (each 30-day position is marked by a circle) indicating northeast flow of northern ACC water after crossing the East Pacific Rise. When the ACC impinges the Chilean coast, it bifurcates (at about 45°S) with northward flowing water in the Peru Chilean Current (PCC) and southward flow in the Cap Horn Current (CHC) toward the Drake Passage. Eastward drifting buoys follow the South Pacific Current (SPC). Modified from(*Chaigneau and Pizarro*, 2005; *Lamy et al.*, 2015, 2021).

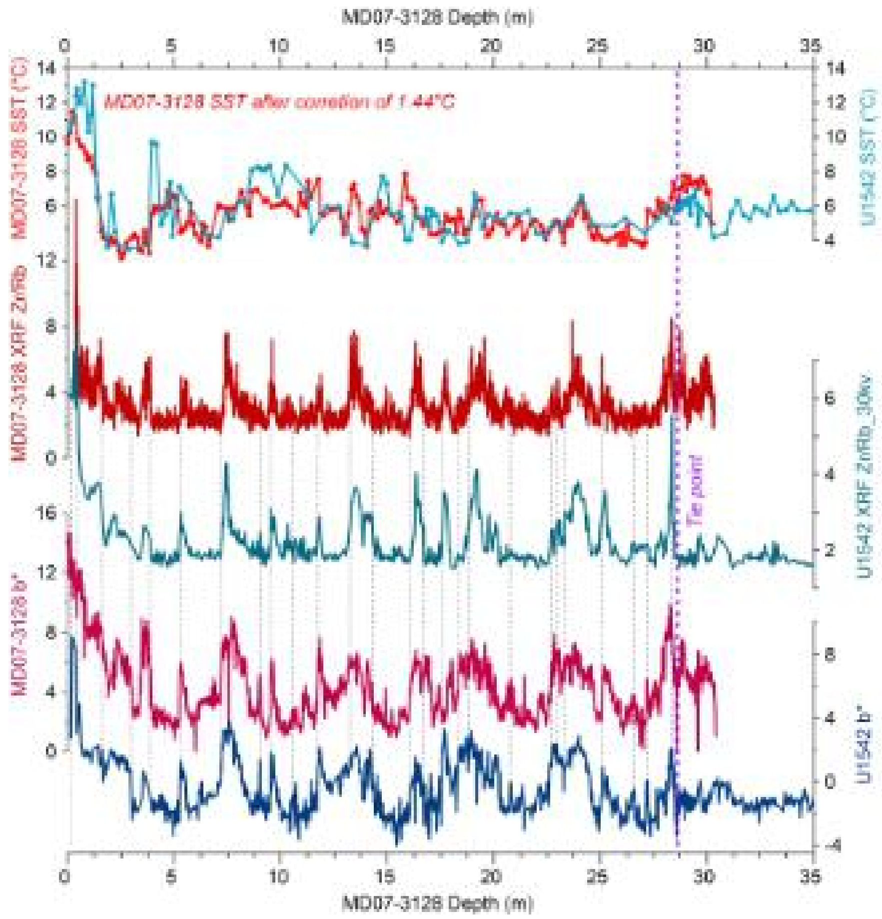

Figure 10.2: The appending of U1542 (blue) to the bottom of MD07-3128 (red). SST, XRF Zr/Rb and b* are the main proxies used to correlate the two records. b* was mainly used to correlate both records with control of XRF Zr/Rb ratio. Correlation made with AnalySeries (*Paillard et al.*, 1996).

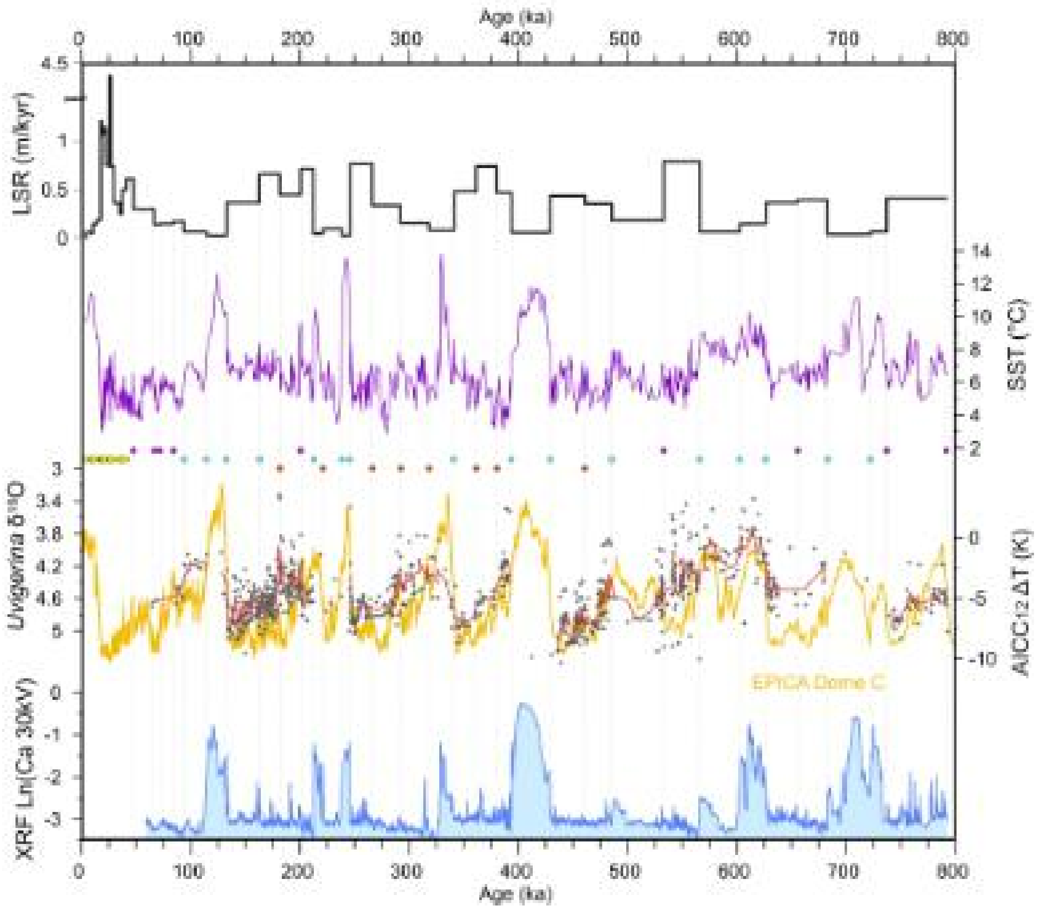

Figure 10.3: Chronology and constraint for the age model construction for Site U1542. From top to bottom, resulting linear sedimentation rate (LSR), sea surface temperature reconstruction form Site U1542, δ^{18}O record from *uvigerina* (benthic) foraminifera isotopes, Antarctic ice core EPICA Dome C temperature record (*Jouzel et al.*, 2007) on the AICC2012 age model(*Bazin et al.*, 2013) and XRF-derived ln(Ca) from Site U1542. The target used was the Antarctic ice core temperature record. The orbital correlation at glacial/interglacial boundary was performed using ln(Ca) (blue dots). As several transitions were not well marked in the ln(Ca) record, alkenones-derived SST (purple dots) was used. Subsequently, δ^{18}O record was used to align our records with Antarctic isotope maxima (pink dots). The first 60 kyr, based on MD07-3128 are based on the latest age model from *Anderson et al.* [2021].

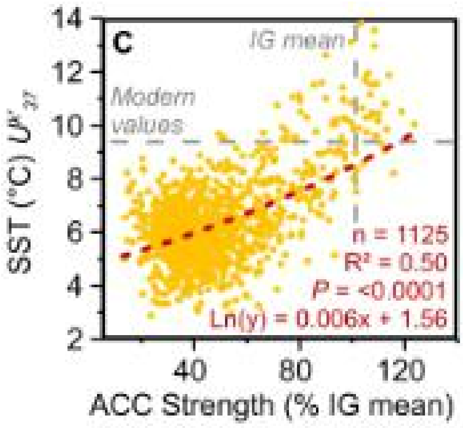

Figure 10.4: Relation between the two main proxies from Site U1542 used in this study. Correlation between ACC strength and alkenones-derived SST.

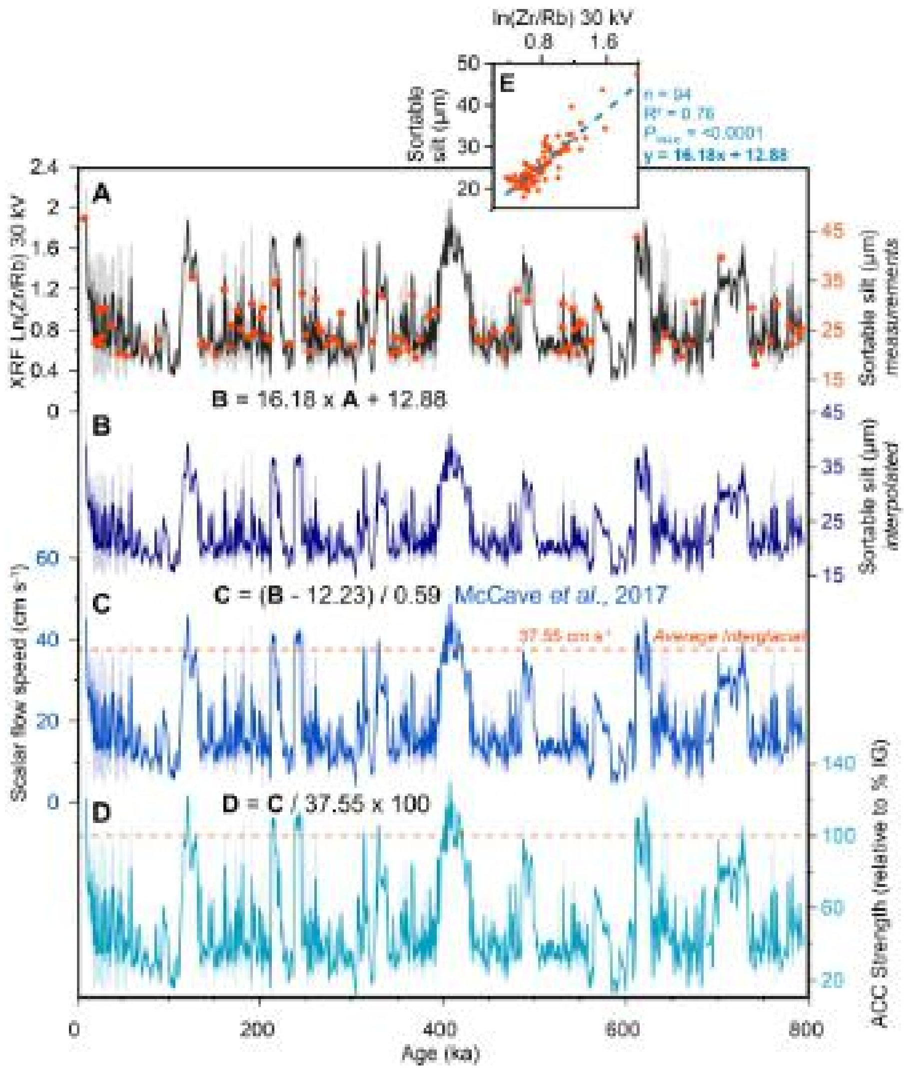

Figure 10.5: Path of different steps to reconstruct the ACC strength proxy relative to the full IG mean. (A) XRF-derived ln (Zr/Rb) (black) with the 94 sortable silt measurements along the record (orange dots). (B) Sortable silts (SS) interpolated using the linear regression SS = 16.18 x ln(Zr/Rb) + 12.88. (C) Scalar flow speed derived from (B) using McCave calibration (*McCave et al.*, 2014). (D) Scalar flow speed related to full interglacial mean value expressed as a percentage.

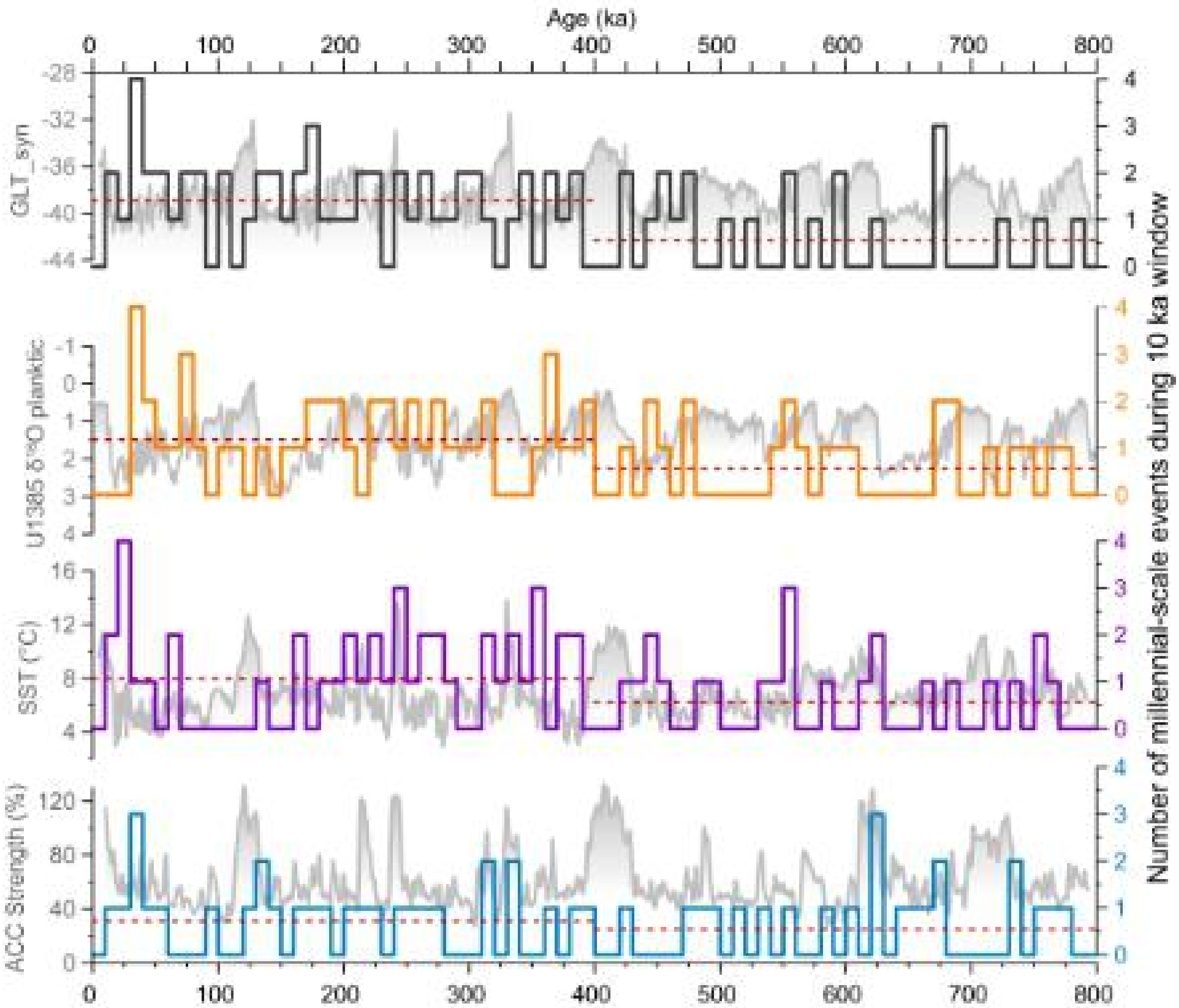

Figure 10.6: The number of major DO events in the synthetic reconstruction of Greenland climate (*Barker et al.*, 2011)(black), stadial event at Site U1385 (*Hodell et al.*, 2023) (orange) and the number of SST warming (purple) and ACC strengthening (blue) events at Site U1542 in non-overlapping windows of 10 ka duration. In grey their respective original data. Dashed line represents the number of events per 10 kyr on a 400-kyr average, broadly corresponding to the Mid Brunhes Transition.To mitigate the impact of age model uncertainties between the two locations, we have chosen to employ a non-overlapping moving window of 10 kyr to evaluate the interhemispheric relation of millennial-scale events occurrence (Fig. 9.6) This approach is thought to maintain the fundamental pattern regardless of the chosen start time.

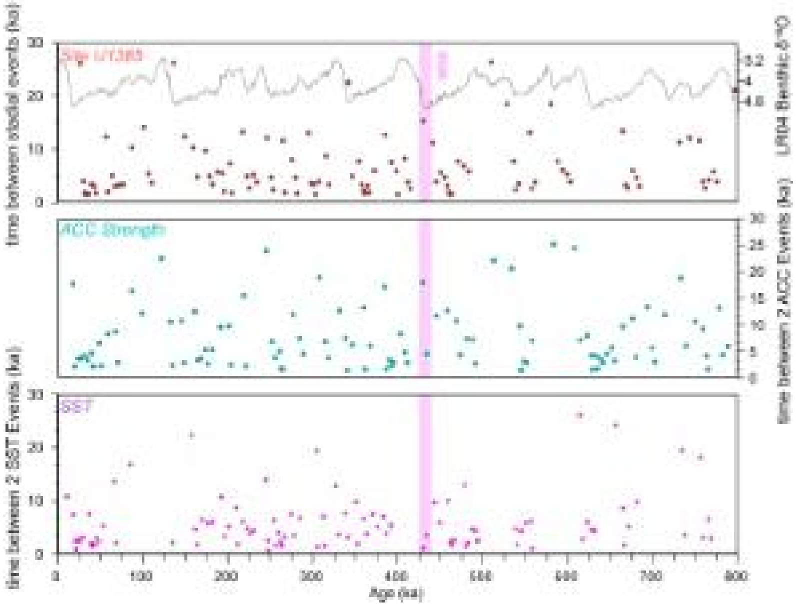

Figure 10.7: Recurrence of millennial-scale strengthening and warming events during glacial periods. Time is the difference between an event and the previous one.

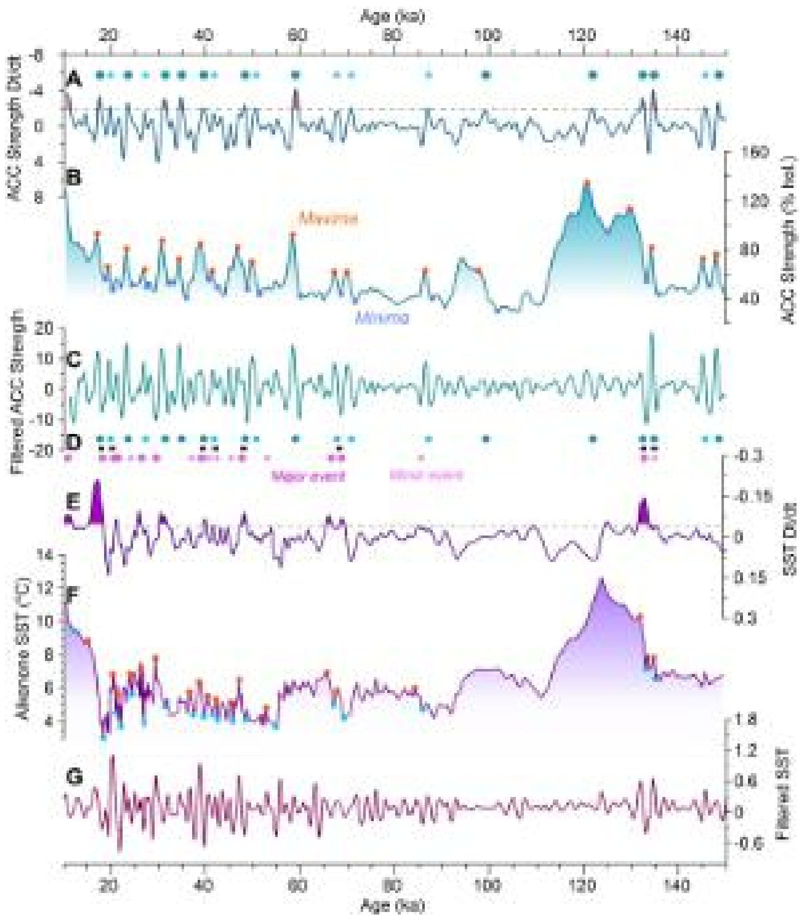

Figure 10.8: Visualization of different steps to identify millennial-scale climatic events. The selection threshold was applied to the minima of the first differential (A and D). The resulting curve is similar to the filtered signal (C and F). Removal of orbital-timescale variability of the original signal (B and E) is achieved by subtracting a 7 kyr high-pass filter using a FIR filter (Finite Impulse Response).

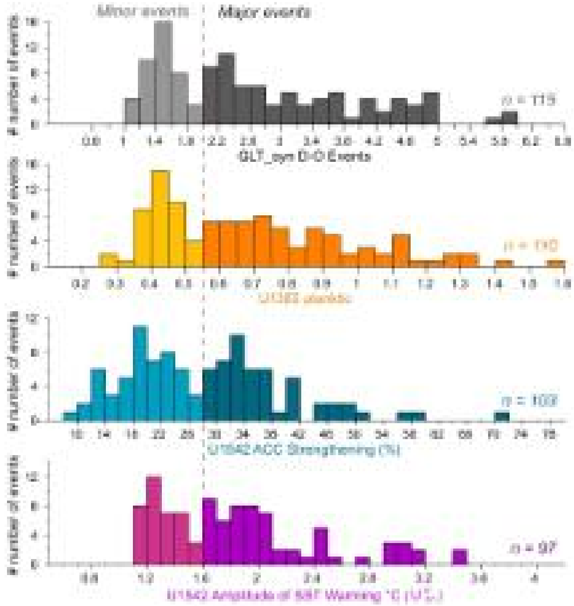

Figure 10.9: Sorting predicted Dansgaard-Oeschger events (grey) from the synthetic Greenland reconstruction (*Barker et al.*, 2011), stadial events (orange) recorded at Site U1385 (*Hodell et al.*, 2023), SST events (purple) and ACC strength events (blue) recorded at Site U1542 according to their respective amplitude.

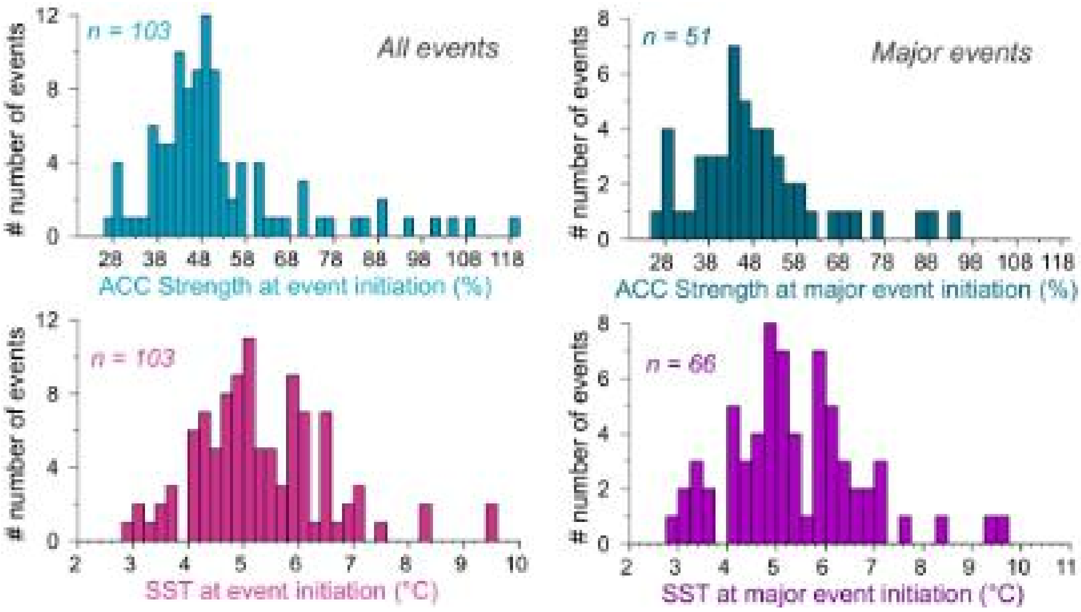

Figure 10.10: Distribution of SST (red and purple) and ACC strength (light and dark blue) millennial-scale events recorded at Site U1542 according to the condition at the initiation. All events are considered on the left panels and only the major events are considered on the right panel.

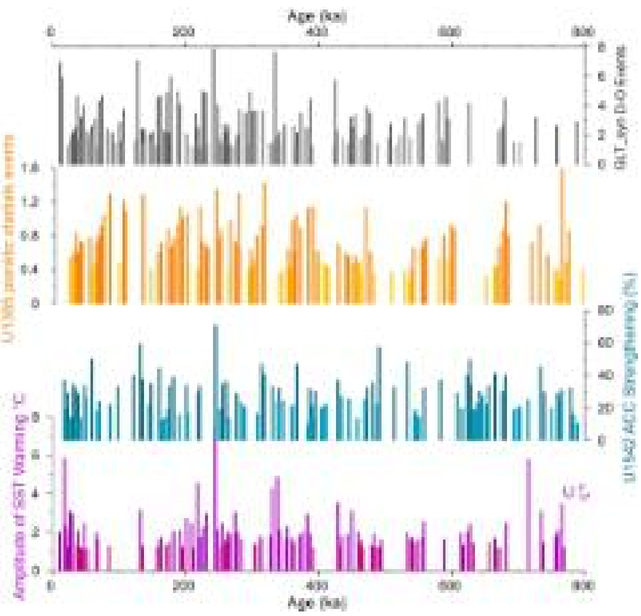

Figure 10.11: Amplitude of SST events (purple), ACC strength events (blue) recorded at Site U1542, stadial events (orange) recorded at Site U1385 (*Hodell et al.*, 2023) and predicted Dansgaard-Oeschger events (grey) the synthetic Greenland reconstruction (*Barker et al.*, 2011) on age scale (kyr). Colors corresponds with Figs 9.9 and 9.10.

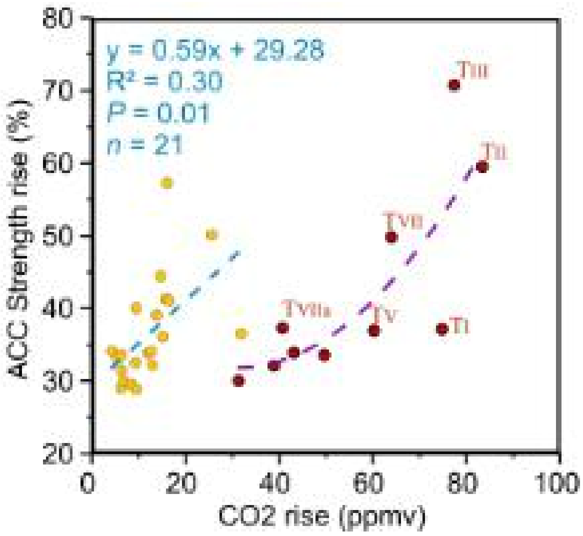

Figure 10.12: Relation between magnitude (%) of the ACC events with rise of CO_2 (ppmv) observed. We associated 31 Major ACC strengthening events with CO_2 rise in less than 7 kyr over the past 790 kyr. 15 events present a CO_2 rise before an ACC strengthening, 15 events present a CO_2 rise after an ACC strengthening, and 1 event present a synchronous CO_2 rise and ACC strengthening. Among these 31 events, 10 (red dots) are associated with terminations and are removed from the linear correlation. Associated events are shown in Figure 6 by black dots.

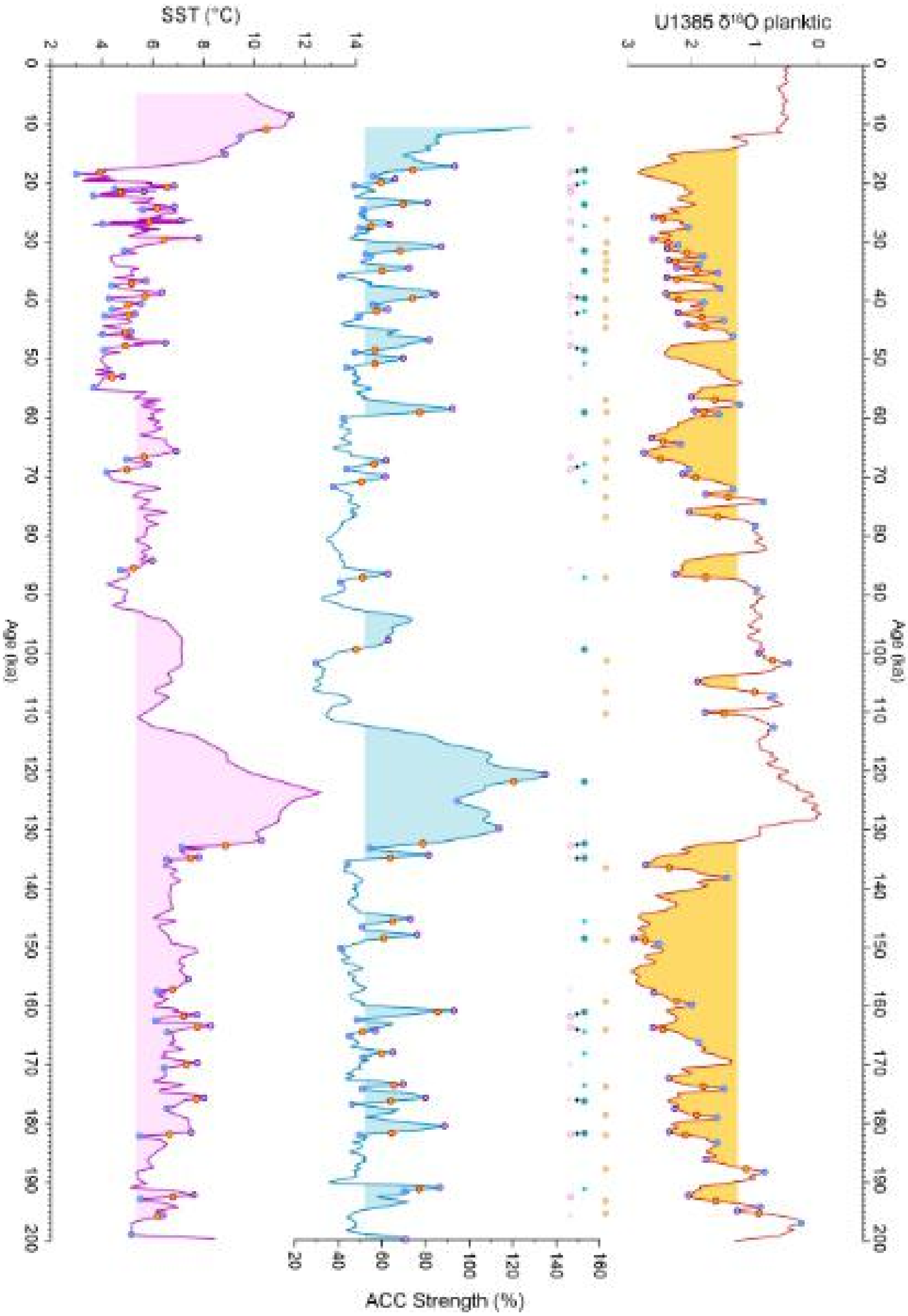

U1385 δ18O planktic
SST (°C)
ACC Strength (%)
Age (ka)

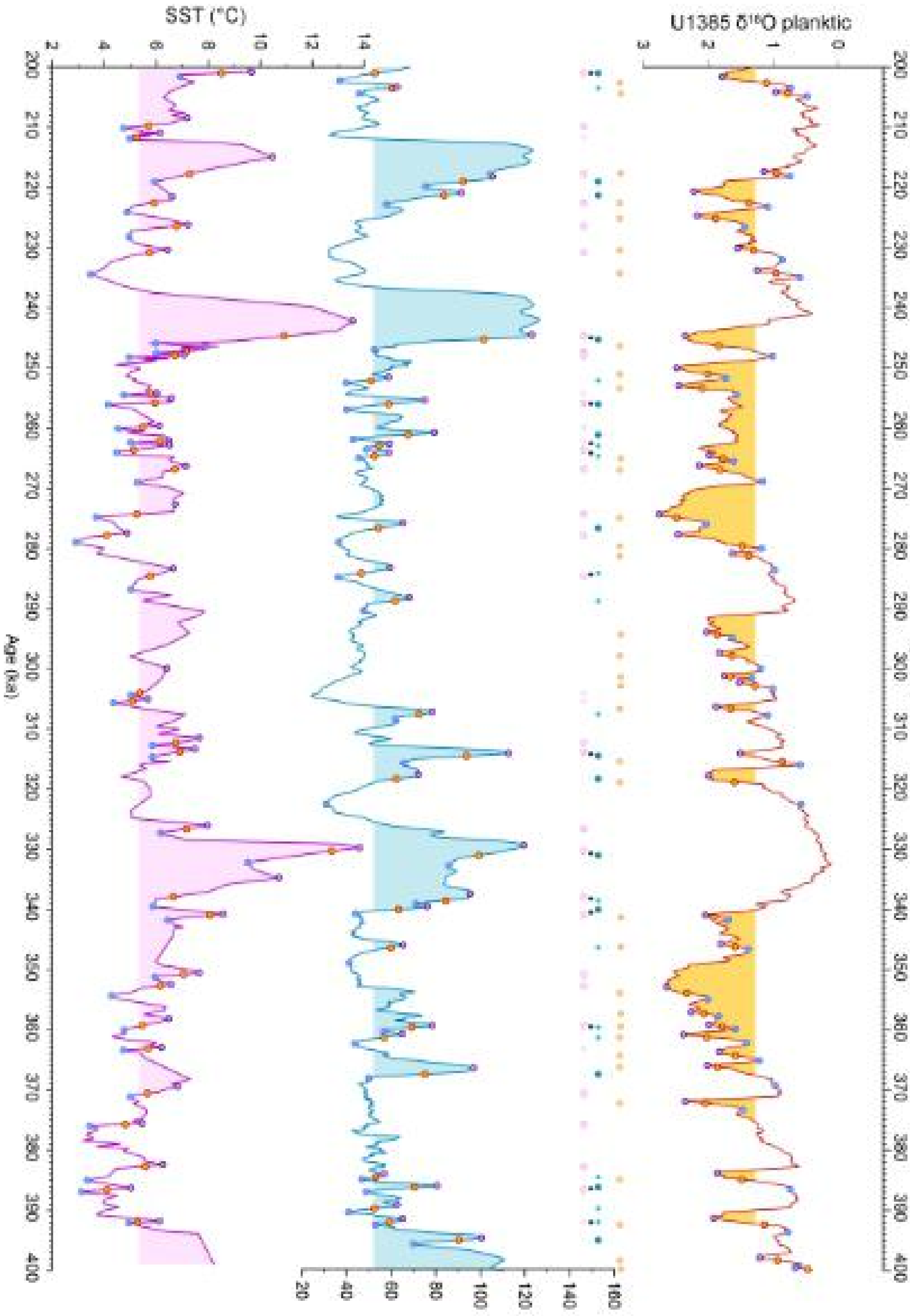
U1385 δ18O planktic
SST (°C)
ACC Strength (%)
Age (ka)

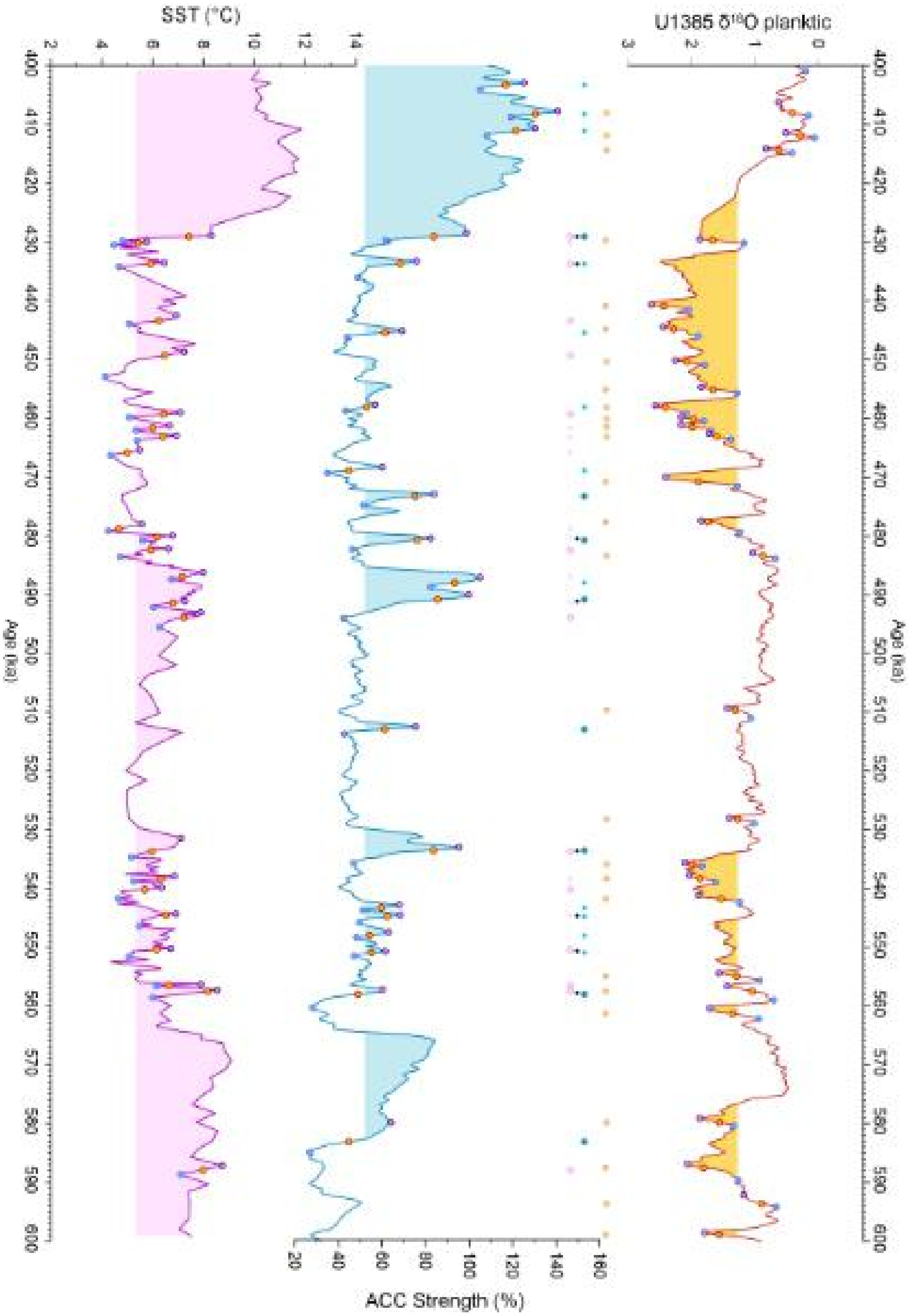
U1385 δ18O planktic
SST (°C)
ACC Strength (%)
Age (ka)

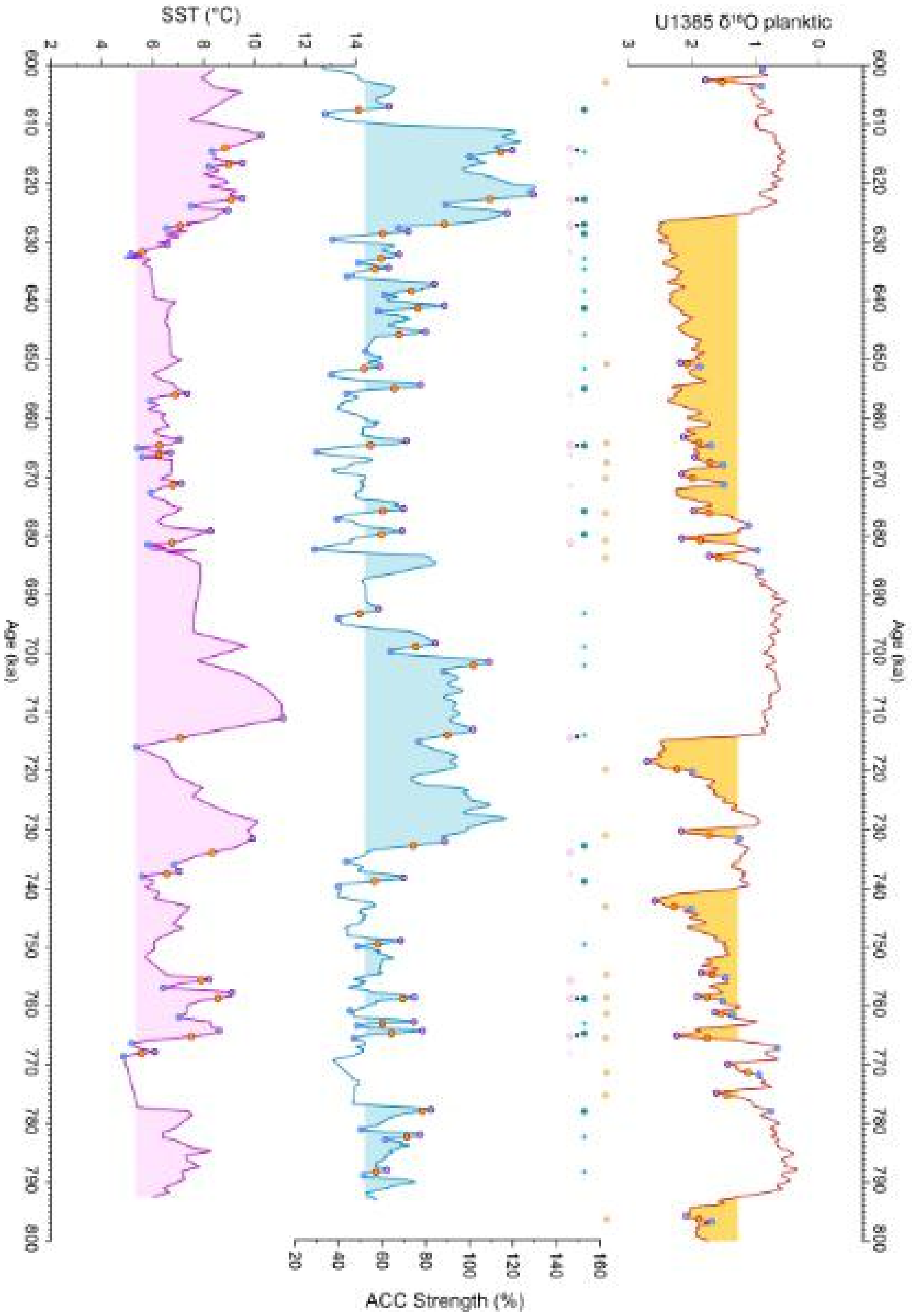

Figure 10.13: details of the interhemispheric teleconnection

Bibliography

Agassiz, L., J. Bettannier, and H. Nicolet (1840), *Études sur les glaciers*, vol. 1840, Aux frais de l'auteur, Neuchâtel. 1

Ahn, J., and E. J. Brook (2008), Atmospheric CO2 and Climate on Millennial Time Scales During the Last Glacial Period, *Science*, *322*(5898), 83–85, doi:10.1126/science.1160832, publisher: American Association for the Advancement of Science. 2.1, 5.4

Ai, X. E., A. S. Studer, D. M. Sigman, A. Martínez-García, F. Fripiat, L. M. Thöle, E. Michel, J. Gottschalk, L. Arnold, S. Moretti, M. Schmitt, S. Oleynik, S. L. Jaccard, and G. H. Haug (2020), Southern Ocean upwelling, Earth's obliquity, and glacial-interglacial atmospheric CO $_2$ change, *Science*, *370*(6522), 1348–1352, doi:10.1126/science.abd2115. 2.2

Anderson, H., J. Pedro, H. Bostock, Z. Chase, and T. Noble (2021), Compiled Southern Ocean sea surface temperatures correlate with Antarctic Isotope Maxima, *Quaternary Science Reviews*, *255*, 106,821, doi:10.1016/j.quascirev.2021.106821. 5.4, 5.5, 6.4, 10.3

Anderson, R. F., and M.-E. Carr (2010), Uncorking the Southern Ocean's Vintage CO2, *Science*, *328*(5982), 1117–1118, doi:10.1126/science.1190765, publisher: American Association for the Advancement of Science. 5.4

Anderson, R. F., S. Ali, L. I. Bradtmiller, S. H. H. Nielsen, M. Q. Fleisher, B. E. Anderson, and L. H. Burckle (2009), Wind-Driven Upwelling in the Southern Ocean and the Deglacial Rise in Atmospheric CO2, *Science*, *323*(5920), 1443–1448, doi:10.1126/science.1167441, publisher: American Association for the Advancement of Science. 5.4, 7.5

Ao, H., E. J. Rohling, C. Stringer, A. P. Roberts, M. J. Dekkers, G. Dupont-Nivet, J. Yu, Q. Liu, P. Zhang, Z. Liu, X. Ma, W. Zhou, Z. Jin, G. Xiao, H. Wang, Q. Sun, P. Yang, X. Peng, Z. Shi, X. Qiang, and Z. An (2020), Two-stage mid-Brunhes climate transition and mid-Pleistocene human diversification, *Earth-Science Reviews*, *210*, 103,354, doi:https://doi.org/10.1016/j.earscirev.2020.103354. 7.2, 7.5, 7.6

Arz, H. W., J. Pätzold, and G. Wefer (1998), Correlated Millennial-Scale Changes in Surface Hydrography and Terrigenous Sediment Yield Inferred from Last-Glacial Marine Deposits off Northeastern Brazil, *Quaternary Research*, *50*(2), 157–166, doi:10.1006/qres.1998.1992. 1, 5.2

Ausín, B., N. Haghipour, E. Bruni, and T. Eglinton (2022), The influence of lateral transport on sedimentary alkenone paleoproxy signals, *Biogeosciences*, *19*(3), 613–627, doi:10.5194/bg-19-613-2022. 4.2

Bakker, P., A. Schmittner, J. T. M. Lenaerts, A. Abe-Ouchi, D. Bi, M. R. van den Broeke, W.-L. Chan, A. Hu, R. L. Beadling, S. J. Marsland, S. H. Mernild, O. A. Saenko, D. Swingedouw, A. Sullivan, and J. Yin (2016), Fate of the Atlantic Meridional Overturning Circulation: Strong decline under continued warming and Greenland melting, *Geophysical Research Letters*, *43*(23), 12,252–12,260, doi:10.1002/2016GL070457, _eprint: https://onlinelibrary.wiley.com/doi/pdf/10.1002/2016GL070457. 5.4, 5.4

Bard, E., and R. E. M. Rickaby (2009), Migration of the subtropical front as a modulator of glacial climate, *Nature*, *460*(7253), 380–383, doi:10.1038/nature08189, publisher: Nature Publishing Group. 1, 7.5

Bard, E., F. Rostek, J.-L. Turon, and S. Gendreau (2000), Hydrological Impact of Heinrich Events in the Subtropical Northeast Atlantic, *Science*, *289*(5483), 1321–1324, doi:10.1126/science.289.5483.1321, publisher: American Association for the Advancement of Science. 1, 4.2, 7.2, 7.5

Barker, S., P. Diz, M. J. Vautravers, J. Pike, G. Knorr, I. R. Hall, and W. S. Broecker (2009), Interhemispheric Atlantic seesaw response during the last deglaciation, *Nature*, *457*(7233), 1097–1102, doi:10.1038/nature07770. 5.2, 5.4

Barker, S., G. Knorr, R. L. Edwards, F. Parrenin, A. E. Putnam, L. C. Skinner, E. Wolff, and M. Ziegler (2011), 800,000 Years of Abrupt Climate Variability, *Science*, *334*(6054), 347–351, doi:10.1126/science.1203580, publisher: American Association for the Advancement of Science. 1, 5.4, 5.5, 10.6, 10.9, 10.11

Barker, S., G. Knorr, S. Conn, S. Lordsmith, D. Newman, and D. Thornalley (2019), Early Interglacial Legacy of Deglacial Climate Instability, *Paleoceanography and Paleoclimatology*, *34*(8), 1455–1475, doi:10.1029/2019PA003661, publisher: John Wiley & Sons, Ltd. 5.2, 5.3, 5.4, 5.5, 5.4, 5.6

Barth, A. M., P. U. Clark, N. S. Bill, F. He, and N. G. Pisias (2018), Climate evolution across the Mid-Brunhes Transition, *Climate of the Past*, *14*(12), 2071–2087, doi:10.5194/cp-14-2071-2018, publisher: Copernicus GmbH. 6.2, 7.2, 7.5

Basile, I., F. E. Grousset, M. Revel, J. R. Petit, P. E. Biscaye, and N. I. Barkov (1997), Patagonian origin of glacial dust deposited in East Antarctica (Vostok and Dome C) during glacial stages 2, 4 and 6, *Earth and Planetary Science Letters*, *146*(3), 573–589, doi:https://doi.org/10.1016/S0012-821X(96)00255-5. 2.2, 6.2, 6.6

Bazin, L., A. Landais, B. Lemieux-Dudon, H. Toyé Mahamadou Kele, D. Veres, F. Parrenin, P. Martinerie, C. Ritz, E. Capron, V. Lipenkov, M.-F. Loutre, D. Raynaud, B. Vinther, A. Svensson, S. O. Rasmussen, M. Severi, T. Blunier, M. Leuenberger, H. Fischer, V. Masson-Delmotte, J. Chappellaz, and E. Wolff (2013), An optimized multi-proxy, multi-site Antarctic ice and gas orbital chronology (AICC2012): 120–800 ka, *Climate of the Past*, *9*(4), 1715–1731, doi:10.5194/cp-9-1715-2013. 5.2, 5.5, 5.5, 6.4, 10.3

Beal, L. M., W. P. M. De Ruijter, A. Biastoch, R. Zahn, M. Cronin, J. Hermes, J. Lutjeharms, G. Quartly, T. Tozuka, S. Baker-Yeboah, T. Bornman, P. Cipollini, H. Dijkstra, I. Hall, W. Park, F. Peeters, P. Penven, H. Ridderinkhof, J. Zinke, and SCOR/WCRP/IAPSO Working Group 136 (2011), On the role of the Agulhas system in ocean circulation and climate, *Nature*, *472*(7344), 429–436, doi:10.1038/nature09983. 1, 5.2, 6.3

Becker, K., J. Austin, N. Exon, S. Humphris, M. Kastner, J. McKenzie, K. Miller, K. Suyehiro, and A. Taira (2019), Fifty Years of Scientific Ocean Drilling, *Oceanography*, *32*(1), 17–21, doi:10.5670/oceanog.2019.110. 8

Bendle, J., A. Rosell-Melé, and P. Ziveri (2005), Variability of unusual distributions of alkenones in the surface waters of the Nordic seas, *Paleoceanography*, *20*(2), doi:10.1029/2004PA001025, _eprint: https://onlinelibrary.wiley.com/doi/pdf/10.1029/2004PA001025. 7.5

Benz, V., O. Esper, R. Gersonde, F. Lamy, and R. Tiedemann (2016), Last Glacial Maximum sea surface temperature and sea-ice extent in the Pacific sector of the Southern Ocean, *Quaternary Science Reviews*, *146*, 216–237, doi:10.1016/j.quascirev.2016.06.006. 7.4, 7.5

Bereiter, B., S. Eggleston, J. Schmitt, C. Nehrbass-Ahles, T. F. Stocker, H. Fischer, S. Kipfstuhl, and J. Chappellaz (2015), Revision of the EPICA Dome C CO2 record from 800 to 600kyr before present, *Geophysical Research Letters*, *42*(2), 542–549, doi:10.1002/2014GL061957, publisher: John Wiley & Sons, Ltd. 5.6, 6.6, 7.3

Berger, A. (1978), Long-term variations of caloric insolation resulting from the earth's orbital elements, *Quaternary Research*, *9*(2), 139–167, doi:https://doi.org/10.1016/0033-5894(78)90064-9. 6.7

Berger, A., and M. F. Loutre (1991), Insolation values for the climate of the last 10 million years, *Quaternary Science Reviews*, *10*(4), 297–317, doi:https://doi.org/10.1016/0277-3791(91)90033-Q. 2.1

Berger, A., M. F. Loutre, and J. Laskar (1992), Stability of the Astronomical Frequencies Over the Earth's History for Paleoclimate Studies, *Science*, *255*(5044), 560–566, doi:10.1126/science.255.5044.560, publisher: American Association for the Advancement of Science. 2.1

Bernhardt, A., W. Schwanghart, D. Hebbeln, J.-B. W. Stuut, and M. R. Strecker (2017), Immediate propagation of deglacial environmental change to deep-marine turbidite systems along the Chile convergent margin, *Earth and Planetary Science Letters*, *473*, 190–204, doi:10.1016/j.epsl.2017.05.017. 6.6

Blott, S. J., and K. Pye (2001), GRADISTAT: a grain size distribution and statistics package for the analysis of unconsolidated sediments, *Earth Surface Processes and Landforms*, *26*(11), 1237–1248, doi:10.1002/esp.261, _eprint: https://onlinelibrary.wiley.com/doi/pdf/10.1002/esp.261. 5.5

Blunier, T., and E. J. Brook (2001), Timing of Millennial-Scale Climate Change in Antarctica and Greenland During the Last Glacial Period, *Science*, *291*(5501), 109–112, doi:10.1126/science.291.5501.109, publisher: American Association for the Advancement of Science. 5.2, 5.4

Blunier, T., J. Chappellaz, J. Schwander, A. Dällenbach, B. Stauffer, T. F. Stocker, D. Raynaud, J. Jouzel, H. B. Clausen, C. U. Hammer, and S. J. Johnsen (1998), Asynchrony of Antarctic and Greenland climate change during the last glacial period, *Nature*, *394*(6695), 739–743, doi:10.1038/29447, number: 6695 Publisher: Nature Publishing Group. 1, 2.1, 5.2

Bond, G., H. Heinrich, W. Broecker, L. Labeyrie, J. McManus, J. Andrews, S. Huon, R. Jantschik, S. Clasen, C. Simet, K. Tedesco, M. Klas, G. Bonani, and S. Ivy (1992), Evidence for massive discharges of icebergs into the North Atlantic ocean during the last glacial period, *Nature*, *360*(6401), 245–249, doi:10.1038/360245a0. 6.6

Bond, G., W. Broecker, S. Johnsen, J. McManus, L. Labeyrie, J. Jouzel, and G. Bonani (1993), Correlations between climate records from North Atlantic sediments and Greenland ice, *Nature*, *365*(6442), 143–147, doi:10.1038/365143a0. 1, 5.2

Bond, G., W. Showers, M. Cheseby, R. Lotti, P. Almasi, P. deMenocal, P. Priore, H. Cullen, I. Hajdas, and G. Bonani (1997), A Pervasive Millennial-Scale Cycle in

North Atlantic Holocene and Glacial Climates, *Science*, *278*(5341), 1257–1266, doi: 10.1126/science.278.5341.1257, publisher: American Association for the Advancement of Science. 1

Bond, G., B. Kromer, J. Beer, R. Muscheler, M. N. Evans, W. Showers, S. Hoffmann, R. Lotti-Bond, I. Hajdas, and G. Bonani (2001), Persistent Solar Influence on North Atlantic Climate During the Holocene, *Science*, *294*(5549), 2130–2136, doi:10.1126/science.1065680, publisher: American Association for the Advancement of Science. (document), 1

Brassell, S. C., and M. Dumitrescu (2004), Recognition of alkenones in a lower Aptian porcellanite from the west-central Pacific, *Organic Geochemistry*, *35*(2), 181–188, doi: 10.1016/j.orggeochem.2003.09.003. 4.2

Brassell, S. C., G. Eglinton, I. T. Marlowe, U. Pflaumann, and M. Sarnthein (1986), Molecular stratigraphy: a new tool for climatic assessment, *Nature*, *320*(6058), 129–133, doi:10.1038/320129a0, number: 6058 Publisher: Nature Publishing Group. 4.2, 7.2

Bray, E. E., and E. D. Evans (1961), Distribution of n-paraffins as a clue to recognition of source beds, *Geochimica et Cosmochimica Acta*, *22*(1), 2–15, doi:https://doi.org/10.1016/0016-7037(61)90069-2. 6.5

Brochier-Armanet, C., B. Boussau, S. Gribaldo, and P. Forterre (2008), Mesophilic Crenarchaeota: proposal for a third archaeal phylum, the Thaumarchaeota, *Nature Reviews. Microbiology*, *6*(3), 245–252, doi:10.1038/nrmicro1852. 6.4

Broecker, W. S. (1991), The Great Ocean Conveyor, *Oceanography*, *4*(2), 79–89, publisher: Oceanography Society. 2.2

Brovkin, V., A. Ganopolski, D. Archer, and S. Rahmstorf (2007), Lowering of glacial atmospheric CO2 in response to changes in oceanic circulation and marine biogeochemistry, *Paleoceanography*, *22*(4), doi:10.1029/2006PA001380, _eprint: https://onlinelibrary.wiley.com/doi/pdf/10.1029/2006PA001380. 1

Buizert, C., and A. Schmittner (2015), Southern Ocean control of glacial AMOC stability and Dansgaard-Oeschger interstadial duration, *Paleoceanography*, *30*(12), 1595–1612, doi:https://doi.org/10.1002/2015PA002795, _eprint: https://agupubs.onlinelibrary.wiley.com/doi/pdf/10.1002/2015PA002795. 5.2

Caley, T., J. Giraudeau, B. Malaizé, L. Rossignol, and C. Pierre (2012), Agulhas leakage as a key process in the modes of Quaternary climate changes, *Proceedings of the National Academy of Sciences*, *109*(18), 6835–6839, doi:10.1073/pnas.1115545109, publisher: Proceedings of the National Academy of Sciences. 1

Caniupán, M., F. Lamy, C. B. Lange, J. Kaiser, H. Arz, R. Kilian, O. Baeza Urrea, C. Aracena, D. Hebbeln, C. Kissel, C. Laj, G. Mollenhauer, and R. Tiedemann (2011), Millennial-scale sea surface temperature and Patagonian Ice Sheet changes off southernmost Chile (53°S) over the past 60 kyr, *Paleoceanography*, *26*(3), doi:10.1029/2010PA002049, _eprint: https://onlinelibrary.wiley.com/doi/pdf/10.1029/2010PA002049. 2.2, 3.4, 4.4, 5.2, 5.4, 5.5, 6.2, 6.3, 6.4, 6.6, 6.4, 6.6, 7.5, 8

Castillo-Llarena, A., F. Retamal-Ramírez, J. Bernales, M. Jacques-Coper, and I. Rogozhina (2023), Climate and ice sheet dynamics in Patagonia during the Last Glacial Maximum, *preprint*, Ice Dynamics/Modelling only/Pleistocene, doi:10.5194/cp-2023-47. 6.6

Chaigneau, A., and O. Pizarro (2005), Surface circulation and fronts of the South Pacific Ocean, east of 120°W, *Geophysical Research Letters*, *32*(8), doi:10.1029/2004GL022070, publisher: John Wiley & Sons, Ltd. 3.2, 5.3, 6.6, 10.1

Chapman, C. C., M.-A. Lea, A. Meyer, J.-B. Sallée, and M. Hindell (2020), Defining Southern Ocean fronts and their influence on biological and physical processes in a changing climate, *Nature Climate Change*, *10*(3), 209–219, doi:10.1038/s41558-020-0705-4. 2.2

Cheng, H., R. L. Edwards, A. Sinha, C. Spötl, L. Yi, S. Chen, M. Kelly, G. Kathayat, X. Wang, X. Li, X. Kong, Y. Wang, Y. Ning, and H. Zhang (2016), The Asian monsoon over the past 640,000 years and ice age terminations, *Nature*, *534*(7609), 640–646, doi:10.1038/nature18591, number: 7609. 1, 2.1, 5.2, 6.6, 6.7, 7.2

Chiang, J. C. (2009), The Tropics in Paleoclimate, *Annual Review of Earth and Planetary Sciences*, *37*(1), 263–297, doi:10.1146/annurev.earth.031208.100217, _eprint: https://doi.org/10.1146/annurev.earth.031208.100217. 5.4, 6.6

Chibnall, A. C., S. H. Piper, A. Pollard, E. F. Williams, and P. N. Sahai (1934), The constitution of the primary alcohols, fatty acids and paraffins present in plant and insect waxes, *Biochemical Journal*, *28*(6), 2189, publisher: Portland Press Ltd. 4.1

Civel-Mazens, M., X. Crosta, G. Cortese, E. Michel, A. Mazaud, O. Ther, M. Ikehara, and T. Itaki (2021), Antarctic Polar Front migrations in the Kerguelen Plateau region, Southern Ocean, over the past 360 kyrs, *Global and Planetary Change*, *202*, 103,526, doi:10.1016/j.gloplacha.2021.103526. 7.3

Clark, P. U., R. B. Alley, and D. Pollard (1999), Northern Hemisphere Ice-Sheet Influences on Global Climate Change, *Science*, *286*(5442), 1104–1111, doi:10.1126/science.286.5442.1104. 1, 6.2

Clark, P. U., N. G. Pisias, T. F. Stocker, and A. J. Weaver (2002), The role of the thermohaline circulation in abrupt climate change, *Nature*, *415*(6874), 863–869, doi: 10.1038/415863a, publisher: Nature Publishing Group. 1

Cochran, J., D. Stow, and et al. (Eds.) (1990), *Proceedings of the Ocean Drilling Program, 116 Scientific Results*, *Proceedings of the Ocean Drilling Program*, vol. 116, Ocean Drilling Program, doi:10.2973/odp.proc.sr.116.1990. 6.4

Comiso, J. C. (2003), Large-scale Characteristics and Variability of the Global Sea Ice Cover, in *Sea Ice*, pp. 112–142, John Wiley & Sons, Ltd, doi:10.1002/9780470757161.ch4, section: 4 _eprint: https://onlinelibrary.wiley.com/doi/pdf/10.1002/9780470757161.ch4. 7.5

Dansgaard, W., S. J. Johnsen, H. B. Clausen, D. Dahl-Jensen, N. S. Gundestrup, C. U. Hammer, C. S. Hvidberg, J. P. Steffensen, A. E. Sveinbjörnsdottir, J. Jouzel, and G. Bond (1993), Evidence for general instability of past climate from a 250-kyr ice-core record, *Nature*, *364*(6434), 218–220, doi:10.1038/364218a0. 1, 5.2

Darvill, C. M., M. J. Bentley, C. R. Stokes, and J. Shulmeister (2016), The timing and cause of glacial advances in the southern mid-latitudes during the last glacial cycle based on a synthesis of exposure ages from Patagonia and New Zealand, *Quaternary Science Reviews*, *149*, 200–214, doi:10.1016/j.quascirev.2016.07.024. 6.2, 6.3, 6.6, 6.6

Davies, B. J., C. M. Darvill, H. Lovell, J. M. Bendle, J. A. Dowdeswell, D. Fabel, J.-L. García, A. Geiger, N. F. Glasser, D. M. Gheorghiu, S. Harrison, A. S. Hein, M. R. Kaplan, J. R. Martin, M. Mendelova, A. Palmer, M. Pelto, Rodés, E. A. Sagredo, R. K. Smedley, J. L. Smellie, and V. R. Thorndycraft (2020), The evolution of the Patagonian Ice Sheet from 35 ka to the present day (PATICE), *Earth-Science Reviews*, *204*, 103,152, doi:10.1016/j.earscirev.2020.103152. 5.3, 5.4, 6.2, 6.1, 6.3, 6.6, 6.6, 6.6, 8

Delmonte, B., I. Basile-Doelsch, J. R. Petit, V. Maggi, M. Revel-Rolland, A. Michard, E. Jagoutz, and F. Grousset (2004), Comparing the Epica and Vostok dust records during the last 220,000 years: stratigraphical correlation and provenance in glacial periods, *Earth-Science Reviews*, *66*(1), 63–87, doi:10.1016/j.earscirev.2003.10.004. 6.6

Denton, G. H., R. F. Anderson, J. R. Toggweiler, R. L. Edwards, J. M. Schaefer, and A. E. Putnam (2010), The Last Glacial Termination, *Science*, *328*(5986), 1652–1656, doi:10.1126/science.1184119, publisher: American Association for the Advancement of Science. 6.2, 6.6

Denton, G. H., S. Toucanne, A. E. Putnam, D. J. Barrell, and J. L. Russell (2022), Heinrich summers, *Quaternary Science Reviews*, *295*, 107,750, doi:10.1016/j.quascirev.2022.107750. 6.2, 6.6

Eglinton, T. I., and G. Eglinton (2008), Molecular proxies for paleoclimatology, *Earth and Planetary Science Letters*, *275*(1), 1–16, doi:10.1016/j.epsl.2008.07.012. 1, 4.1, 6.2, 6.5

Emiliani, C. (1955), Pleistocene Temperatures, *The Journal of Geology*, *63*(6), 538–578, doi:10.1086/626295, _eprint: https://doi.org/10.1086/626295. 1, 2.1

EPICA community members (2004), Eight glacial cycles from an Antarctic ice core, *Nature*, *429*(6992), 623–628, doi:10.1038/nature02599. 5.4

EPICA Community Members (2006), One-to-one coupling of glacial climate variability in Greenland and Antarctica, *Nature*, *444*(7116), 195–198, doi:10.1038/nature05301. 1, 2.1, 5.2, 5.4, 5.4

Esper, O., and R. Gersonde (2014a), New tools for the reconstruction of Pleistocene Antarctic sea ice, *Palaeogeography, Palaeoclimatology, Palaeoecology*, *399*, 260–283, doi:10.1016/j.palaeo.2014.01.019. 7.4, 7.5

Esper, O., and R. Gersonde (2014b), Quaternary surface water temperature estimations: New diatom transfer functions for the Southern Ocean, *Palaeogeography, Palaeoclimatology, Palaeoecology*, *414*, 1–19, doi:10.1016/j.palaeo.2014.08.008. 7.4, 7.5

Euler, C., and U. S. Ninnemann (2010), Climate and Antarctic Intermediate Water coupling during the late Holocene, *Geology*, *38*(7), 647–650, doi:10.1130/G30902.1. 1, 6.2

Fagan, B. (2019), *The Little Ice Age: How Climate Made History 1300-1850*, Hachette UK, google-Books-ID: hZuZDwAAQBAJ. (document)

Feng, X., K. Haines, and E. de Boisséson (2018), Coupling of surface air and sea surface temperatures in the CERA-20C reanalysis, *Quarterly Journal of the Royal Meteorological Society*, *144*(710), 195–207, doi:10.1002/qj.3194, _eprint: https://onlinelibrary.wiley.com/doi/pdf/10.1002/qj.3194. 6.6

Fischer, H., J. Severinghaus, E. Brook, E. Wolff, M. Albert, O. Alemany, R. Arthern, C. Bentley, D. Blankenship, J. Chappellaz, T. Creyts, D. Dahl-Jensen, M. Dinn, M. Frezzotti, S. Fujita, H. Gallee, R. Hindmarsh, D. Hudspeth, G. Jugie, K. Kawamura, V. Lipenkov, H. Miller, R. Mulvaney, F. Parrenin, F. Pattyn, C. Ritz, J. Schwander, D. Steinhage, T. van Ommen, and F. Wilhelms (2013), Where to find 1.5 million yr old ice for the IPICS "Oldest-Ice" ice core, *Climate of the Past*, *9*(6), 2489–2505, doi:10.5194/cp-9-2489-2013, publisher: Copernicus GmbH. 8

Ganopolski, A., and S. Rahmstorf (2001), Rapid changes of glacial climate simulated in a coupled climate model, *Nature*, *409*(6817), 153–158, doi:10.1038/35051500, publisher: Nature Publishing Group. 1

García, J.-L., A. S. Hein, S. A. Binnie, G. A. Gómez, M. A. González, and T. J. Dunai (2018), The MIS 3 maximum of the Torres del Paine and Última Esperanza ice lobes in Patagonia and the pacing of southern mountain glaciation, *Quaternary Science Reviews*, *185*, 9–26, doi:10.1016/j.quascirev.2018.01.013. 6.2, 6.3

Garreaud, R., P. Lopez, M. Minvielle, and M. Rojas (2013), Large-Scale Control on the Patagonian Climate, *Journal of Climate*, *26*(1), 215–230, doi:10.1175/JCLI-D-12-00001.1. 6.3, 6.6

Gersonde, R., D. A. Hodell, and P. Blum (1999), Leg 177 summary: southern ocean paleoceanography, in *Proc. Ocean Drill. Program Initial Rep*, vol. 177. 7.5

Gibbons, A. (1993), How the Akkadian Empire Was Hung Out to Dry, *Science*, *261*(5124), 985–985, doi:10.1126/science.261.5124.985, publisher: American Association for the Advancement of Science. (document)

Golledge, N. R., C. J. Fogwill, A. N. Mackintosh, and K. M. Buckley (2012), Dynamics of the last glacial maximum Antarctic ice-sheet and its response to ocean forcing, *Proceedings of the National Academy of Sciences*, *109*(40), 16,052–16,056, doi:10.1073/pnas.1205385109, publisher: Proceedings of the National Academy of Sciences. 6.6

Gottschalk, J., L. C. Skinner, J. Lippold, H. Vogel, N. Frank, S. L. Jaccard, and C. Waelbroeck (2016), Biological and physical controls in the Southern Ocean on past millennial-scale atmospheric CO2 changes, *Nature Communications*, *7*(1), 11,539, doi:10.1038/ncomms11539. 5.4

Greuell, W., and R. Böhm (1998), 2 m temperatures along melting mid-latitude glaciers, and implications for the sensitivity of the mass balance to variations in temperature, *Journal of Glaciology*, *44*(146), 9–20, doi:10.3189/S0022143000002306, edition: 2017/01/20 Publisher: Cambridge University Press. 6.6

Grousset, F. E., P. E. Biscaye, M. Revel, J.-R. Petit, K. Pye, S. Joussaume, and J. Jouzel (1992), Antarctic (Dome C) ice-core dust at 18 k.y. B.P.: Isotopic constraints on origins, *Earth and Planetary Science Letters*, *111*(1), 175–182, doi:https://doi.org/10.1016/0012-821X(92)90177-W. 2.2, 6.2, 6.6

Hagemann, J. R., L. Lembke-Jene, F. Lamy, M.-E. Vorrath, J. Kaiser, J. Müller, H. W. Arz, J. Hefter, A. Jaeschke, N. Ruggieri, and R. Tiedemann (2022), Upper ocean temperature characteristics in the subantarctic Southeast Pacific based on biomarker reconstructions, *EGUsphere*, *2022*, 1–32, doi:10.5194/egusphere-2022-1456. 4.4, 5.3, 7.5

Hagemann, J. R., F. Lamy, H. W. Arz, L. Lembke-Jene, A. Auderset, N. Harada, S. L. Ho, S. Iwasaki, J. Kaiser, C. B. Lange, M. Murayama, K. Nagashima, N. Nowaczyk, A. Martínez-García, and R. Tiedemann (2024), A marine record of Patagonian ice sheet changes over the past 140,000 years, *Proceedings of the National Academy of Sciences*, *121* (12), e2302983,121, doi:10.1073/pnas.2302983121, publisher: Proceedings of the National Academy of Sciences. 2.2, 4.4, 5.4, 5.4, 6.2, 6.6, 6.4, 6.6, 6.6, 6.6, 7.5, 8, 8.1

Hao, Q., L. Wang, F. Oldfield, and Z. Guo (2015), Extra-long interglacial in Northern Hemisphere during MISs 15-13 arising from limited extent of Arctic ice sheets in glacial MIS 14, *Scientific Reports*, *5* (1), 12,103, doi:10.1038/srep12103. 6.6

Hays, J. D., J. Imbrie, and N. J. Shackleton (1976), Variations in the Earth's Orbit: Pacemaker of the Ice Ages, *Science*, *194* (4270), 1121–1132, doi:10.1126/science.194.4270.1121, publisher: American Association for the Advancement of Science. 2.1, 2.1, 2.1

Hebbeln, D., F. Lamy, M. Mohtadi, and H. Echtler (2007), Tracing the impact of glacial-interglacial climate variability on erosion of the southern Andes, *Geology*, *35* (2), 131, doi:10.1130/G23243A.1. 6.3

Hein, A. S., N. R. J. Hulton, T. J. Dunai, C. Schnabel, M. R. Kaplan, M. Naylor, and S. Xu (2009), Middle Pleistocene glaciation in Patagonia dated by cosmogenic-nuclide measurements on outwash gravels, *Earth and Planetary Science Letters*, *286* (1), 184–197, doi:10.1016/j.epsl.2009.06.026. 6.6

Hein, A. S., T. J. Dunai, N. R. Hulton, and S. Xu (2011), Exposure dating outwash gravels to determine the age of the greatest Patagonian glaciations, *Geology*, *39* (2), 103–106, doi:10.1130/G31215.1. 6.6, 6.6

Hein, A. S., A. Cogez, C. M. Darvill, M. Mendelova, M. R. Kaplan, F. Herman, T. J. Dunai, K. Norton, S. Xu, M. Christl, and Rodés (2017), Regional mid-Pleistocene glaciation in central Patagonia, *Quaternary Science Reviews*, *164*, 77–94, doi:10.1016/j.quascirev.2017.03.023. 6.2

Henry, L. G., J. F. McManus, W. B. Curry, N. L. Roberts, A. M. Piotrowski, and L. D. Keigwin (2016), North Atlantic ocean circulation and abrupt climate change during the last glaciation, *Science*, *353* (6298), 470–474, doi:10.1126/science.aaf5529. 5.4, 5.4

Herbert, T. D. (2003), Alkenone Paleotemperature Determinations, *Treatise on Geochemistry*, *6*, 625, doi:10.1016/B0-08-043751-6/06115-6, aDS Bibcode: 2003TrGeo...6..391H. 4.2

Herbert, T. D., K. T. Lawrence, A. Tzanova, L. C. Peterson, R. Caballero-Gill, and C. S. Kelly (2016), Late Miocene global cooling and the rise of modern ecosystems, *Nature Geoscience*, *9*(11), 843–847, doi:10.1038/ngeo2813, publisher: Nature Publishing Group. 4.2

Heusser, L., C. Heusser, A. Kleczkowski, and S. Crowhurst (1999), A 50,000-yr Pollen Record from Chile of South American Millennial-Scale Climate Instability during the Last Glaciation, *Quaternary Research*, *52*(2), 154–158, doi:10.1006/qres.1999.2069. 6.2

Hillenbrand, C.-D., G. Kuhn, and T. Frederichs (2009), Record of a Mid-Pleistocene depositional anomaly in West Antarctic continental margin sediments: an indicator for ice-sheet collapse?, *Quaternary Science Reviews*, *28*(13-14), 1147–1159, doi:10.1016/j.quascirev.2008.12.010. 6.6

Ho, S. L. (2012), Reconstructing sea surface temperature in the South Pacific using organic proxies, accepted: 2020-03-09T14:42:26Z Publisher: Universität Bremen. 5.2

Ho, S. L., G. Mollenhauer, F. Lamy, A. Martínez-Garcia, M. Mohtadi, R. Gersonde, D. Hebbeln, S. Nunez-Ricardo, A. Rosell-Melé, and R. Tiedemann (2012), Sea surface temperature variability in the Pacific sector of the Southern Ocean over the past 700 kyr, *Paleoceanography*, *27*(4), doi:10.1029/2012PA002317, _eprint: https://onlinelibrary.wiley.com/doi/pdf/10.1029/2012PA002317. 2.2, 5.2, 5.4, 5.5, 6.2, 7.5, 7.2, 7.5, 8

Ho, S. L., B. Naafs, and F. Lamy (2013), PALEOCEANOGRAPHY, BIOLOGICAL PROXIES | Alkenone Paleothermometry Based on the Haptophyte Algae, in *Encyclopedia of Quaternary Science*, pp. 755–764, Elsevier, doi:10.1016/B978-0-444-53643-3.00278-8. 4.2

Ho, S. L., G. Mollenhauer, S. Fietz, A. Martínez-Garcia, F. Lamy, G. Rueda, K. Schipper, M. Méheust, A. Rosell-Melé, R. Stein, and R. Tiedemann (2014), Appraisal of TEX86 and TEX86L thermometries in subpolar and polar regions, *Geochimica et Cosmochimica Acta*, *131*, 213–226, doi:https://doi.org/10.1016/j.gca.2014.01.001. 4.3

Hodell, D. A., M. Brenner, J. H. Curtis, and T. Guilderson (2001), Solar Forcing of Drought Frequency in the Maya Lowlands, *Science*, *292*(5520), 1367–1370, doi:10.1126/science.1057759, publisher: American Association for the Advancement of Science. (document)

Hodell, D. A., S. L. Kanfoush, K. A. Venz, C. D. Charles, and F. J. Sierro (2003), The Mid-Brunhes Transition in Odp Sites 1089 and 1090 (Subantarctic South Atlantic), in *Earth's Climate and Orbital Eccentricity: The Marine Isotope Stage 11 Question*, pp. 113–129, American Geophysical Union (AGU), doi:10.1029/137GM09, _eprint: https://onlinelibrary.wiley.com/doi/pdf/10.1029/137GM09. 7.5

Hodell, D. A., J. E. T. Channell, J. H. Curtis, O. E. Romero, and U. Röhl (2008), Onset of "Hudson Strait" Heinrich events in the eastern North Atlantic at the end of the middle Pleistocene transition (640 ka)?, *Paleoceanography*, *23*(4), doi:10.1029/2008PA001591, publisher: John Wiley & Sons, Ltd. 5.2, 5.5

Hodell, D. A., S. J. Crowhurst, L. Lourens, V. Margari, J. Nicolson, J. E. Rolfe, L. C. Skinner, N. C. Thomas, P. C. Tzedakis, M. J. Mleneck-Vautravers, and E. W. Wolff (2023), A 1.5-million-year record of orbital and millennial climate variability in the North Atlantic, *Climate of the Past*, *19*(3), 607–636, doi:10.5194/cp-19-607-2023. 1, 5.2, 5.3, 5.4, 5.5, 5.5, 10.6, 10.9, 10.11

Hopmans, E. C., J. W. H. Weijers, E. Schefuß, L. Herfort, J. S. S. Damsté, and S. Schouten (2004), A novel proxy for terrestrial organic matter in sediments based on branched and isoprenoid tetraether lipids, *Earth and Planetary Science Letters*, *224*(1), 107–116, doi:https://doi.org/10.1016/j.epsl.2004.05.012. 4.3, 6.4, 6.5, 6.6

Hopmans, E. C., S. Schouten, and J. S. Sinninghe Damsté (2016), The effect of improved chromatography on GDGT-based palaeoproxies, *Organic Geochemistry*, *93*, 1–6, doi:10.1016/j.orggeochem.2015.12.006. 4.5

Horikawa, K., E. E. Martin, C. Basak, J. Onodera, O. Seki, T. Sakamoto, M. Ikehara, S. Sakai, and K. Kawamura (2015), Pliocene cooling enhanced by flow of low-salinity Bering Sea water to the Arctic Ocean, *Nature Communications*, *6*(1), 7587, doi:10.1038/ncomms8587, number: 1 Publisher: Nature Publishing Group. 1, 7.5

Howe, J. N. W., and A. M. Piotrowski (2017), Atlantic deep water provenance decoupled from atmospheric CO2 concentration during the lukewarm interglacials, *Nature Communications*, *8*(1), 2003, doi:10.1038/s41467-017-01939-w, number: 1 Publisher: Nature Publishing Group. 6.6

Hughes, P. D., and P. L. Gibbard (2018), Global glacier dynamics during 100 ka Pleistocene glacial cycles, *Quaternary Research*, *90*(1), 222–243, doi:10.1017/qua.2018.37. 6.6

Huguet, C., R. H. Smittenberg, W. Boer, J. S. S. Damste, and S. Schouten (2007), Twentieth century proxy records of temperature and soil organic matter input in the Drammensfjord, southern Norway, *Organic Geochemistry*, p. 12. 4.3

Hulton, N., R. Purves, R. McCulloch, D. Sugden, and M. Bentley (2002), The Last Glacial Maximum and deglaciation in southern South America, *EPILOG*, *21*(1), 233–241, doi:10.1016/S0277-3791(01)00103-2. 6.3

Hutson, W. H. (1980), The Agulhas Current During the Late Pleistocene: Analysis of Modern Faunal Analogs, *Science*, *207*(4426), 64–66, doi:10.1126/science.207.4426.64, publisher: American Association for the Advancement of Science. 7.4

Huybers, P., and G. Denton (2008), Antarctic temperature at orbital timescales controlled by local summer duration, *Nature Geoscience*, *1*(11), 787–792, doi:10.1038/ngeo311. 6.2

Huybers, P., and C. Wunsch (2005), Obliquity pacing of the late Pleistocene glacial terminations, *Nature*, *434*(7032), 491–494, doi:10.1038/nature03401. 2.1

Imbrie, J., and J. Z. Imbrie (1980), Modeling the Climatic Response to Orbital Variations, *Science*, *207*(4434), 943–953, doi:10.1126/science.207.4434.943. 2.1

Jaccard, S. L., C. T. Hayes, A. Martínez-García, D. A. Hodell, R. F. Anderson, D. M. Sigman, and G. H. Haug (2013), Two Modes of Change in Southern Ocean Productivity Over the Past Million Years, *Science*, *339*(6126), 1419–1423, doi:10.1126/science.1227545, publisher: American Association for the Advancement of Science. 7.5

Jaeger, J. M., and M. N. Koppes (2016), The role of the cryosphere in source-to-sink systems, *Earth-Science Reviews*, *153*, 43–76, doi:10.1016/j.earscirev.2015.09.011. 6.3, 6.6

Jansen, J. H. F., A. Kuijpers, and S. R. Troelstra (1986), A Mid-Brunhes Climatic Event: Long-Term Changes in Global Atmosphere and Ocean Circulation, *Science*, *232*(4750), 619–622, doi:10.1126/science.232.4750.619, publisher: American Association for the Advancement of Science. 2.1, 5.3, 5.4, 7.2, 7.5

Jenkyns, H. C., L. Schouten-Huibers, S. Schouten, and J. S. Sinninghe Damsté (2012), Warm Middle Jurassic–Early Cretaceous high-latitude sea-surface temperatures from the Southern Ocean, *Climate of the Past*, *8*(1), 215–226, doi:10.5194/cp-8-215-2012, publisher: Copernicus GmbH. 4.3

Jouzel, J., V. Masson-Delmotte, O. Cattani, G. Dreyfus, S. Falourd, G. Hoffmann, B. Minster, J. Nouet, J. M. Barnola, J. Chappellaz, H. Fischer, J. C. Gallet, S. Johnsen, M. Leuenberger, L. Loulergue, D. Luethi, H. Oerter, F. Parrenin, G. Raisbeck, D. Raynaud, A. Schilt, J. Schwander, E. Selmo, R. Souchez, R. Spahni, B. Stauffer, J. P. Steffensen, B. Stenni, T. F. Stocker, J. L. Tison, M. Werner, and E. W. Wolff (2007), Orbital and Millennial Antarctic Climate Variability over the Past 800,000 Years, *Science*, *317*(5839), 793–796, doi:10.1126/science.1141038. 1, 2.2, 2.1, 5.2, 5.2, 5.3, 5.4, 5.5, 5.5, 6.4, 6.6, 6.6, 6.6, 6.8, 7.2, 8.1, 10.3

Kaiser, J., F. Lamy, and D. Hebbeln (2005), A 70-kyr sea surface temperature record off southern Chile (Ocean Drilling Program Site 1233), *Paleoceanography*, *20*(4), doi:10.1029/2005PA001146, publisher: John Wiley & Sons, Ltd. 2.2, 4.4, 5.2, 5.3, 5.4, 6.2, 6.6, 8.1

Kaiser, J., S. Schouten, R. Kilian, H. W. Arz, F. Lamy, and J. S. Sinninghe Damsté (2015), Isoprenoid and branched GDGT-based proxies for surface sediments from marine, fjord and lake environments in Chile, *Organic Geochemistry*, *89-90*, 117–127, doi:10.1016/j.orggeochem.2015.10.007. 4.2

Kanfoush, S. L., D. A. Hodell, C. D. Charles, T. P. Guilderson, P. G. Mortyn, and U. S. Ninnemann (2000), Millennial-Scale Instability of the Antarctic Ice Sheet During the Last Glaciation, *Science*, *288*(5472), 1815–1819, doi:10.1126/science.288.5472.1815. 1, 5.2

Kaniewski, D., E. Paulissen, E. Van Campo, M. Al-Maqdissi, J. Bretschneider, and K. Van Lerberghe (2008), Middle East coastal ecosystem response to middle-to-late Holocene abrupt climate changes, *Proceedings of the National Academy of Sciences*, *105*(37), 13,941–13,946, doi:10.1073/pnas.0803533105, publisher: Proceedings of the National Academy of Sciences. (document)

Kaplan, M. R., C. J. Fogwill, D. E. Sugden, N. R. J. Hulton, P. W. Kubik, and S. P. H. T. Freeman (2008), Southern Patagonian glacial chronology for the Last Glacial period and implications for Southern Ocean climate, *Quaternary Science Reviews*, *27*(3), 284–294, doi:10.1016/j.quascirev.2007.09.013. 6.2, 6.3

Kemp, A. E. S., I. Grigorov, R. B. Pearce, and A. C. Naveira Garabato (2010), Migration of the Antarctic Polar Front through the mid-Pleistocene transition: evidence and climatic implications, *Quaternary Science Reviews*, *29*(17), 1993–2009, doi:10.1016/j.quascirev.2010.04.027. 7.5

Kilian, R., and F. Lamy (2012), A review of Glacial and Holocene paleoclimate records from southernmost Patagonia (49–55°S), *Quaternary Science Reviews*, *53*, 1–23, doi:10.1016/j.quascirev.2012.07.017. 2.2, 6.2, 6.6, 6.6

Kim, J.-H., S. Schouten, R. Buscail, W. Ludwig, J. Bonnin, J. S. Sinninghe Damsté, and F. Bourrin (2006), Origin and distribution of terrestrial organic matter in the NW Mediterranean (Gulf of Lions): Exploring the newly developed BIT index, *Geochemistry, Geophysics, Geosystems*, *7*(11), doi:10.1029/2006GC001306, _eprint: https://onlinelibrary.wiley.com/doi/pdf/10.1029/2006GC001306. 6.6

Kim, J.-H., J. v. d. Meer, S. Schouten, P. Helmke, V. Willmott, F. Sangiorgi, N. Koç, E. C. Hopmans, and J. S. S. Damsté (2010), New indices and calibrations derived from the distribution of crenarchaeal isoprenoid tetraether lipids: Implications for past sea surface temperature reconstructions, *Geochimica et Cosmochimica Acta*, *74*(16), 4639–4654, doi:https://doi.org/10.1016/j.gca.2010.05.027. 4.3

Kindler, P., M. Guillevic, M. Baumgartner, J. Schwander, A. Landais, and M. Leuenberger (2014), Temperature reconstruction from 10 to 120 kyr b2k from the NGRIP ice core, *Climate of the Past*, *10*(2), 887–902, doi:10.5194/cp-10-887-2014, publisher: Copernicus GmbH. 1

Kissel, C. (2007), Md159/pachiderme cruise, marion dufresne r/v. 3.3

Knorr, G., and G. Lohmann (2003), Southern Ocean origin for the resumption of Atlantic thermohaline circulation during deglaciation, *Nature*, *424*(6948), 532–536, doi:10.1038/nature01855. 1, 5.2, 5.4

Knutti, R., J. Flückiger, T. F. Stocker, and A. Timmermann (2004), Strong hemispheric coupling of glacial climate through freshwater discharge and ocean circulation, *Nature*, *430*(7002), 851–856, doi:10.1038/nature02786, publisher: Nature Publishing Group. 2.1, 2.2

Koenig, Z., C. Provost, R. Ferrari, N. Sennéchael, and M.-H. Rio (2014), Volume transport of the Antarctic Circumpolar Current: Production and validation of a 20 year long time series obtained from in situ and satellite observations, *Journal of Geophysical Research: Oceans*, *119*(8), 5407–5433, doi:10.1002/2014JC009966, _eprint: https://onlinelibrary.wiley.com/doi/pdf/10.1002/2014JC009966. 5.4

Kohfeld, K., R. Graham, A. de Boer, L. Sime, E. Wolff, C. Le Quéré, and L. Bopp (2013), Southern Hemisphere westerly wind changes during the Last Glacial Maximum: paleodata synthesis, *Quaternary Science Reviews*, *68*, 76–95, doi:10.1016/j.quascirev.2013.01.017. 6.6

Kunz-Pirrung, M., R. Gersonde, and D. A. Hodell (2002), Mid-Brunhes century-scale diatom sea surface temperature and sea ice records from the Atlantic sector of the Southern Ocean (ODP Leg 177, sites 1093, 1094 and core PS2089-2), *Palaeogeography, Palaeoclimatology, Palaeoecology*, *182*(3), 305–328, doi:10.1016/S0031-0182(01)00501-6. 7.4

Köhler, P., H. Fischer, G. Munhoven, and R. E. Zeebe (2005), Quantitative interpretation of atmospheric carbon records over the last glacial termination, *Global Biogeochemical Cycles*, *19*(4), doi:10.1029/2004GB002345, _eprint: https://onlinelibrary.wiley.com/doi/pdf/10.1029/2004GB002345. 5.4

Lambert, F., B. Delmonte, J. R. Petit, M. Bigler, P. R. Kaufmann, M. A. Hutterli, T. F. Stocker, U. Ruth, J. P. Steffensen, and V. Maggi (2008), Dust-climate couplings over the past 800,000 years from the EPICA Dome C ice core, *Nature*, *452*(7187), 616–619, doi:10.1038/nature06763. 6.2, 6.6, 6.6, 6.8

Lambert, F., M. Bigler, J. P. Steffensen, M. Hutterli, and H. Fischer (2012), Centennial mineral dust variability in high-resolution ice core data from Dome C, Antarctica, *Climate of the Past*, *8*(2), 609–623, doi:10.5194/cp-8-609-2012. 6.6

Lamy, F., J. Kaiser, U. Ninnemann, D. Hebbeln, H. W. Arz, and J. Stoner (2004), Antarctic Timing of Surface Water Changes off Chile and Patagonian Ice Sheet Response, *Science*, *304*(5679), 1959–1962, doi:10.1126/science.1097863, publisher: American Association for the Advancement of Science. 2.2, 5.4, 6.2

Lamy, F., R. Kilian, H. W. Arz, J.-P. Francois, J. Kaiser, M. Prange, and T. Steinke (2010), Holocene changes in the position and intensity of the southern westerly wind belt, *Nature Geoscience*, *3*(10), 695–699, doi:10.1038/ngeo959, number: 10 Publisher: Nature Publishing Group. 2.2, 6.3

Lamy, F., R. Gersonde, G. Winckler, O. Esper, A. Jaeschke, G. Kuhn, J. Ullermann, A. Martinez-Garcia, F. Lambert, and R. Kilian (2014), Increased Dust Deposition in the Pacific Southern Ocean During Glacial Periods, *Science*, *343*(6169), 403–407, doi:10.1126/science.1245424, publisher: American Association for the Advancement of Science. 2.2, 4.1, 6.2

Lamy, F., H. W. Arz, R. Kilian, C. B. Lange, L. Lembke-Jene, M. Wengler, J. Kaiser, O. Baeza-Urrea, I. R. Hall, N. Harada, and R. Tiedemann (2015), Glacial reduction and millennial-scale variations in Drake Passage throughflow, *Proceedings of the National Academy of Sciences*, *112*(44), 13,496–13,501, doi:10.1073/pnas.1509203112, publisher: Proceedings of the National Academy of Sciences. 1, 2.2, 3.2, 3.4, 5.2, 5.3, 5.3, 5.4, 5.4, 5.4, 5.5, 6.4, 6.6, 7.3, 8, 10.1

Lamy, F., J. C. H. Chiang, G. Martínez-Méndez, M. Thierens, H. W. Arz, J. Bosmans, D. Hebbeln, F. Lambert, L. Lembke-Jene, and J.-B. Stuut (2019), Precession modulation of the South Pacific westerly wind belt over the past million years, *Proceedings of the National Academy of Sciences*, *116*(47), 23,455–23,460, doi:10.1073/pnas.1905847116, publisher: Proceedings of the National Academy of Sciences. 1, 6.6

Lamy, F., G. Winckler, and C. Alvarez Zarikian (2021), *Volume 383: Dynamics of the Pacific Antarctic Circumpolar Current (DYNAPACC)*, *Proceedings of the International Ocean Discovery Program*, vol. 383, International Ocean Discovery Program, doi:10.14379/iodp.proc.383.2021. 1, 3.1, 3.2, 3.3, 5.2, 5.3, 5.5, 6.4, 6.6, 7.4, 7.5, 10.1

Lamy, F., G. Winckler, H. W. Arz, J. R. Farmer, J. Gottschalk, L. Lembke-Jene, J. L. Middleton, M. van der Does, R. Tiedemann, C. Alvarez Zarikian, C. Basak, A. Brombacher, L. Dumm, O. M. Esper, L. C. Herbert, S. Iwasaki, G. Kreps, V. J. Lawson, L. Lo, E. Malinverno, A. Martinez-Garcia, E. Michel, S. Moretti, C. M. Moy, A. C. Ravelo, C. R. Riesselman, M. Saavedra-Pellitero, H. Sadatzki, I. Seo, R. K. Singh, R. A. Smith, A. L. Souza, J. S. Stoner, M. Toyos, I. M. V. P. de Oliveira, S. Wan, S. Wu, and X. Zhao (2024), Five million years of Antarctic Circumpolar Current strength variability, *Nature*, *627*(8005), 789–796, doi:10.1038/s41586-024-07143-3, publisher: Nature Publishing Group. 7.3, 7.4, 7.5

Lang, N., and E. W. Wolff (2011), Interglacial and glacial variability from the last 800 ka in marine, ice and terrestrial archives, *Climate of the Past*, *7*(2), 361–380, doi:10.5194/cp-7-361-2011, publisher: Copernicus GmbH. 1

Laskar, J., P. Robutel, F. Joutel, M. Gastineau, A. C. M. Correia, and B. Levrard (2004), A long-term numerical solution for the insolation quantities of the Earth, *Astronomy & Astrophysics*, *428*(1), 261–285, doi:10.1051/0004-6361:20041335. 2.1, 2.1

Le Roy Ladurie, E. (2011), Révolutions, le déclic climatique, *25*(12), 22–22, doi:10.3917/gdsh.025.0022, place: Auxerre Publisher: Éditions Sciences Humaines. (document)

Leger, T. P. M., A. S. Hein, Rodés, R. G. Bingham, I. Schimmelpfennig, D. Fabel, P. Tapia, and ASTER Team (2023), A cosmogenic nuclide-derived chronology of pre-Last Glacial Cycle glaciations during MIS 8 and MIS 6 in northern Patagonia, *Climate of the Past*, *19*(1), 35–59, doi:10.5194/cp-19-35-2023. 6.2, 6.6

Li, C., and A. Born (2019), Coupled atmosphere-ice-ocean dynamics in Dansgaard-Oeschger events, *Quaternary Science Reviews*, *203*, 1–20, doi:10.1016/j.quascirev.2018.10.031. 1

Lisiecki, L. E., and M. E. Raymo (2005), A Pliocene-Pleistocene stack of 57 globally distributed benthic 18O records, *Paleoceanography*, *20*(1), doi:10.1029/2004PA001071, publisher: John Wiley & Sons, Ltd. 2.1, 5.2, 5.5, 6.2, 6.6, 6.6, 7.2, 7.3, 8.1

Lisé-Pronovost, A., G. St-Onge, C. Gogorza, T. Haberzettl, M. Preda, P. Kliem, P. Francus, and B. Zolitschka (2013), High-resolution paleomagnetic secular variations and relative paleointensity since the Late Pleistocene in southern South America, *Quaternary Science Reviews*, *71*, 91–108, doi:https://doi.org/10.1016/j.quascirev.2012.05.012. 6.3

Lunt, D. J., and P. J. Valdes (2001), Dust transport to Dome C, Antarctica, at the Last Glacial Maximum and present day, *Geophysical Research Letters*, *28*(2), 295–298, doi: 10.1029/2000GL012170, publisher: John Wiley & Sons, Ltd. 2.2, 6.2, 6.6

Lüthi, D., M. Le Floch, B. Bereiter, T. Blunier, J.-M. Barnola, U. Siegenthaler, D. Raynaud, J. Jouzel, H. Fischer, K. Kawamura, and T. F. Stocker (2008), High-resolution carbon dioxide concentration record 650,000–800,000 years before present, *Nature*, *453*(7193), 379–382, doi:10.1038/nature06949, publisher: Nature Publishing Group. 2.2, 2.1, 7.2

Margari, V., L. C. Skinner, P. C. Tzedakis, A. Ganopolski, M. Vautravers, and N. J. Shackleton (2010), The nature of millennial-scale climate variability during the past two glacial periods, *Nature Geoscience*, *3*(2), 127–131, doi:10.1038/ngeo740. 5.4

Marlowe, I., J. Green, A. Neal, S. Brassell, G. Eglinton, and P. Course (1984), Long chain (n-C37–C39) alkenones in the Prymnesiophyceae. Distribution of alkenones and other lipids and their taxonomic significance, *British Phycological Journal*, *19*(3), 203–216, doi:10.1080/00071618400650221, publisher: Taylor & Francis _eprint: https://doi.org/10.1080/00071618400650221. 4.2

Marshall, J., and K. Speer (2012), Closure of the meridional overturning circulation through Southern Ocean upwelling, *Nature Geoscience*, *5*(3), 171–180, doi:10.1038/ngeo1391. 1, 2.2, 5.2

Martin, J. H. (1990), Glacial-interglacial CO2 change: The Iron Hypothesis, *Paleoceanography*, *5*(1), 1–13, doi:10.1029/PA005i001p00001, _eprint: https://onlinelibrary.wiley.com/doi/pdf/10.1029/PA005i001p00001. 2.2, 5.4, 6.2

Martinez-Garcia, A., D. M. Sigman, H. Ren, R. F. Anderson, M. Straub, D. A. Hodell, S. L. Jaccard, T. I. Eglinton, and G. H. Haug (2014), Iron Fertilization of the Subantarctic Ocean During the Last Ice Age, *Science*, *343*(6177), 1347–1350, doi: 10.1126/science.1246848. 2.2, 4.1, 5.4, 6.2

Martrat, B., J. O. Grimalt, N. J. Shackleton, L. de Abreu, M. A. Hutterli, and T. F. Stocker (2007), Four Climate Cycles of Recurring Deep and Surface Water Destabilizations on the Iberian Margin, *Science*, *317*(5837), 502–507, doi:10.1126/science.1139994. 5.2

Martínez-Garcia, A., A. Rosell-Melé, E. L. McClymont, R. Gersonde, and G. H. Haug (2010), Subpolar Link to the Emergence of the Modern Equatorial Pacific Cold Tongue, *Science*, *328*(5985), 1550–1553, doi:10.1126/science.1184480, publisher: American Association for the Advancement of Science. 1, 4.2, 5.4, 7.2, 7.5, 7.2, 7.5, 7.3, 8.1

Martínez-Garcia, A., A. Rosell-Melé, S. L. Jaccard, W. Geibert, D. M. Sigman, and G. H. Haug (2011), Southern Ocean dust–climate coupling over the past four million years, *Nature*, *476*(7360), 312–315, doi:10.1038/nature10310. 2.2, 4.1, 6.2, 6.6, 6.6, 6.8

Marzi, R., B. E. Torkelson, and R. K. Olson (1993), A revised carbon preference index, *Organic Geochemistry*, *20*(8), 1303–1306, doi:https://doi.org/10.1016/0146-6380(93)90016-5. 6.4

McCave, I., D. Thornalley, and I. Hall (2017), Relation of sortable silt grain-size to deep-sea current speeds: Calibration of the 'Mud Current Meter', *Deep Sea Research Part I: Oceanographic Research Papers*, *127*, 1–12, doi:10.1016/j.dsr.2017.07.003. 5.3, 5.5

McCave, I. N., B. Manighetti, and S. G. Robinson (1995), Sortable silt and fine sediment size/composition slicing: Parameters for palaeocurrent speed and palaeoceanography, *Paleoceanography*, *10*(3), 593–610, doi:10.1029/94PA03039. (document), 5.2, 5.3, 5.5

McCave, I. N., S. J. Crowhurst, G. Kuhn, C.-D. Hillenbrand, and M. P. Meredith (2014), Minimal change in Antarctic Circumpolar Current flow speed between the last glacial and Holocene, *Nature Geoscience*, *7*(2), 113–116, doi:10.1038/ngeo2037. 5.3, 10.5

McClymont, E. L., A. Martínez-Garcia, and A. Rosell-Melé (2007), Benefits of freeze-drying sediments for the analysis of total chlorins and alkenone concentrations in marine sediments, *Organic Geochemistry*, *38*(6), 1002–1007, doi:10.1016/j.orggeochem.2007.01.006. 4.5

McClymont, E. L., A. Rosell-Melé, G. H. Haug, and J. M. Lloyd (2008), Expansion of subarctic water masses in the North Atlantic and Pacific oceans and implications for mid-Pleistocene ice sheet growth, *Paleoceanography*, *23*(4), doi:10.1029/2008PA001622, _eprint: https://onlinelibrary.wiley.com/doi/pdf/10.1029/2008PA001622. 1, 4.2, 7.2, 7.5, 7.5

McManus, J. F., D. W. Oppo, and J. L. Cullen (1999), A 0.5-Million-Year Record of Millennial-Scale Climate Variability in the North Atlantic, *Science*, *283*(5404), 971–975, doi:10.1126/science.283.5404.971, publisher: American Association for the Advancement of Science. 5.2, 5.3, 5.4

Mendelová, M., A. S. Hein, Rodés, and S. Xu (2020), Extensive mountain glaciation in central Patagonia during Marine Isotope Stage 5, *Quaternary Science Reviews*, *227*, 105,996, doi:10.1016/j.quascirev.2019.105996. 6.2, 6.6, 6.6

Mercer, J. H. (1984), Simultaneous climatic change in both hemispheres and similar bipolar interglacial warming: Evidence and implications, *Washington DC American Geo-*

physical Union Geophysical Monograph Series, *29*, 307–313, doi:10.1029/GM029p0307. 6.2

Mercer, J. H., and J. F. Sutter (1982), Late miocene—earliest pliocene glaciation in southern Argentina: implications for global ice-sheet history, *Palaeogeography, Palaeoclimatology, Palaeoecology*, *38*(3), 185–206, doi:10.1016/0031-0182(82)90003-7. 6.6

Meredith, M. P. (2019), The global importance of the Southern Ocean and the key role of its freshwater cycle, *Ocean Challenge*, *23*(2), 27–32, number: 2 Publisher: Challenger Society for Marine Science. 2.2, 2.5, 2.2

Middleton, J. L., J. Gottschalk, G. Winckler, J. Hanley, C. Knudson, J. R. Farmer, F. Lamy, L. E. Lisiecki, and the Expedition 383 Scientists (2023), Evaluating manual versus automated benthic foraminiferal δ^{18}O alignment techniques for developing chronostratigraphies in marine sediment records, *EGUsphere*, pp. 1–46, doi:10.5194/egusphere-2023-2906, publisher: Copernicus GmbH. 7.4

Milankovitch, M. K. (1941), Kanon der Erdbestrahlung und seine Anwendung auf das Eiszeitenproblem, *Royal Serbian Academy Special Publication*, *133*, 1–633, publisher: Israel Program for Sceientific Translation, U. S. Department of Commerce. 2.1

Mollenhauer, G., M. Kienast, F. Lamy, H. Meggers, R. R. Schneider, J. M. Hayes, and T. I. Eglinton (2005), An evaluation of 14C age relationships between co-occurring foraminifera, alkenones, and total organic carbon in continental margin sediments, *Paleoceanography*, *20*(1), doi:10.1029/2004PA001103, publisher: John Wiley & Sons, Ltd. 4.2

Mollenhauer, G., M. Inthorn, T. Vogt, M. Zabel, J. S. Sinninghe Damsté, and T. I. Eglinton (2007), Aging of marine organic matter during cross-shelf lateral transport in the Benguela upwelling system revealed by compound-specific radiocarbon dating, *Geochemistry, Geophysics, Geosystems*, *8*(9), doi:10.1029/2007GC001603, _eprint: https://onlinelibrary.wiley.com/doi/pdf/10.1029/2007GC001603. 4.4

Montade, V., N. Combourieu Nebout, C. Kissel, S. G. Haberle, G. Siani, and E. Michel (2013), Vegetation and climate changes during the last 22,000 yr from a marine core near Taitao Peninsula, southern Chile, *Palaeogeography, Palaeoclimatology, Palaeoecology*, *369*, 335–348, doi:10.1016/j.palaeo.2012.11.001. 6.6

Munday, D. R., H. L. Johnson, and D. P. Marshall (2013), Eddy Saturation of Equilibrated Circumpolar Currents, *Journal of Physical Oceanography*, *43*(3), 507–532, doi:10.1175/JPO-D-12-095.1, publisher: American Meteorological Society Section: Journal of Physical Oceanography. 5.4

Müller, P. J., G. Kirst, G. Ruhland, I. von Storch, and A. Rosell-Melé (1998), Calibration of the alkenone paleotemperature index U37K based on core-tops from the eastern South Atlantic and the global ocean (60°N-60°S), *Geochimica et Cosmochimica Acta*, *62*(10), 1757–1772, doi:10.1016/S0016-7037(98)00097-0. 4.2

Naish, T., R. Powell, R. Levy, G. Wilson, R. Scherer, F. Talarico, L. Krissek, F. Niessen, M. Pompilio, T. Wilson, L. Carter, R. DeConto, P. Huybers, R. McKay, D. Pollard, J. Ross, D. Winter, P. Barrett, G. Browne, R. Cody, E. Cowan, J. Crampton, G. Dunbar, N. Dunbar, F. Florindo, C. Gebhardt, I. Graham, M. Hannah, D. Hansaraj, D. Harwood, D. Helling, S. Henrys, L. Hinnov, G. Kuhn, P. Kyle, A. Läufer, P. Maffioli, D. Magens, K. Mandernack, W. McIntosh, C. Millan, R. Morin, C. Ohneiser, T. Paulsen, D. Persico, I. Raine, J. Reed, C. Riesselman, L. Sagnotti, D. Schmitt, C. Sjunneskog, P. Strong, M. Taviani, S. Vogel, T. Wilch, and T. Williams (2009), Obliquity-paced Pliocene West Antarctic ice sheet oscillations, *Nature*, *458*(7236), 322–328, doi:10.1038/nature07867, number: 7236 Publisher: Nature Publishing Group. 6.6

Nakai, S., A. N. Halliday, and D. K. Rea (1993), Provenance of dust in the Pacific Ocean, *Earth and Planetary Science Letters*, *119*(1), 143–157, doi:10.1016/0012-821X(93)90012-X. 6.6

Nuber, S., J. W. B. Rae, X. Zhang, M. B. Andersen, M. D. Dumont, H. T. Mithan, Y. Sun, B. de Boer, I. R. Hall, and S. Barker (2023), Indian Ocean salinity build-up primes deglacial ocean circulation recovery, *Nature*, *617*(7960), 306–311, doi:10.1038/s41586-023-05866-3, number: 7960 Publisher: Nature Publishing Group. 1, 5.4

Obrochta, S. P., H. Miyahara, Y. Yokoyama, and T. J. Crowley (2012), A re-examination of evidence for the North Atlantic "1500-year cycle" at Site 609, *Quaternary Science Reviews*, *55*, 23–33, doi:10.1016/j.quascirev.2012.08.008. 1

Oerlemans, J. (2005), Extracting a Climate Signal from 169 Glacier Records, *Science*, *308*(5722), 675–677, doi:10.1126/science.1107046, publisher: American Association for the Advancement of Science. 6.2, 6.6

Ohneiser, C., C. L. Hulbe, C. Beltran, C. R. Riesselman, C. M. Moy, D. B. Condon, and R. A. Worthington (2023), West Antarctic ice volume variability paced by obliquity until 400,000 years ago, *Nature Geoscience*, *16*(1), 44–49, doi:10.1038/s41561-022-01088-w, number: 1 Publisher: Nature Publishing Group. 6.6

Oka, A., A. Abe-Ouchi, S. Sherriff-Tadano, Y. Yokoyama, K. Kawamura, and H. Hasumi (2021), Glacial mode shift of the Atlantic meridional overturning circulation by warming over the Southern Ocean, *Communications Earth & Environment*, *2*(1), 169, doi:10.1038/s43247-021-00226-3. 1, 5.2, 5.4, 6.3

Orsi, A. H., T. Whitworth, and W. D. Nowlin (1995), On the meridional extent and fronts of the Antarctic Circumpolar Current, *Deep Sea Research Part I: Oceanographic Research Papers*, *42*(5), 641–673, doi:10.1016/0967-0637(95)00021-W. 2.2, 7.3

Pahnke, K., and R. Zahn (2005), Southern Hemisphere Water Mass Conversion Linked with North Atlantic Climate Variability, *Science*, *307*(5716), 1741–1746, doi:10.1126/science.1102163. 2.2, 5.4

Pahnke, K., R. Zahn, H. Elderfield, and M. Schulz (2003), 340,000-Year Centennial-Scale Marine Record of Southern Hemisphere Climatic Oscillation, *Science*, *301*(5635), 948–952, doi:10.1126/science.1084451, number: 5635. 5.2, 5.4, 5.5, 5.5

Pahnke, K., S. L. Goldstein, and S. R. Hemming (2008), Abrupt changes in Antarctic Intermediate Water circulation over the past 25,000 years, *Nature Geoscience*, *1*(12), 870–874, doi:10.1038/ngeo360. 3.2

Paillard, D., L. Labeyrie, and P. Yiou (1996), Macintosh Program performs time-series analysis, *EOS Transactions*, *77*(39), 379–379, doi:10.1029/96EO00259. 5.5, 10.2

Park, Y.-H., T. Park, T.-W. Kim, S.-H. Lee, C.-S. Hong, J.-H. Lee, M.-H. Rio, M.-I. Pujol, M. Ballarotta, I. Durand, and C. Provost (2019), Observations of the Antarctic Circumpolar Current Over the Udintsev Fracture Zone, the Narrowest Choke Point in the Southern Ocean, *Journal of Geophysical Research: Oceans*, *124*(7), 4511–4528, doi:10.1029/2019JC015024, _eprint: https://onlinelibrary.wiley.com/doi/pdf/10.1029/2019JC015024. 5.1, 7.1, 7.3, 7.5, 7.5

Paul, A., and M. Schulz (2002), Holocene Climate Variability on Centennial-to-Millennial Time Scales: 2. Internal and Forced Oscillations as Possible Causes, in *Climate Development and History of the North Atlantic Realm*, edited by G. Wefer, W. H. Berger, K.-E. Behre, and E. Jansen, pp. 55–73, Springer, Berlin, Heidelberg, doi:10.1007/978-3-662-04965-5_5. 1

Peltier, C., M. R. Kaplan, S. D. Birkel, R. L. Soteres, E. A. Sagredo, J. C. Aravena, J. Araos, P. I. Moreno, R. Schwartz, and J. M. Schaefer (2021), The large MIS 4 and long MIS 2 glacier maxima on the southern tip of South America, *Quaternary Science Reviews*, *262*, 106,858, doi:10.1016/j.quascirev.2021.106858. 6.2, 6.3

Peltier, C., M. R. Kaplan, E. A. Sagredo, P. I. Moreno, J. Araos, S. D. Birkel, R. Villa-Martínez, R. Schwartz, S. A. Reynhout, and J. M. Schaefer (2023), The last two glacial cycles in central Patagonia: A precise record from the Ñirehuao glacier lobe, *Quaternary Science Reviews*, *304*, 107,873, doi:10.1016/j.quascirev.2022.107873. 6.6, 6.6

Petersen, S. V., D. P. Schrag, and P. U. Clark (2013), A new mechanism for Dansgaard-Oeschger cycles, *Paleoceanography*, *28*(1), 24–30, doi:10.1029/2012PA002364, _eprint: https://onlinelibrary.wiley.com/doi/pdf/10.1029/2012PA002364. 1

Poynter, J., and G. Eglinton (1990), (Table 4) UK37 index and alkane characteristics of ODP Hole 116-717C, PANGAEA, doi:10.1594/PANGAEA.756550, type: data set. 4.1

Prahl, F. G., and S. G. Wakeham (1987), Calibration of unsaturation patterns in long-chain ketone compositions for palaeotemperature assessment, *Nature*, *330*(6146), 367–369, doi:10.1038/330367a0, number: 6146. 4.2, 7.2

Prahl, F. G., L. A. Muehlhausen, and D. L. Zahnle (1988), Further evaluation of long-chain alkenones as indicators of paleoceanographic conditions, *Geochimica et Cosmochimica Acta*, *52*(9), 2303–2310, doi:10.1016/0016-7037(88)90132-9. 4.2, 5.5

Prokopenko, A. A., D. F. Williams, M. I. Kuzmin, E. B. Karabanov, G. K. Khursevich, and J. A. Peck (2002), Muted climate variations in continental Siberia during the mid-Pleistocene epoch, *Nature*, *418*(6893), 65–68, doi:10.1038/nature00886. 6.6

Putnam, A. E., J. M. Schaefer, D. J. A. Barrell, M. Vandergoes, G. H. Denton, M. R. Kaplan, R. C. Finkel, R. Schwartz, B. M. Goehring, and S. E. Kelley (2010), In situ cosmogenic 10Be production-rate calibration from the Southern Alps, New Zealand, *Quaternary Geochronology*, *5*(4), 392–409, doi:10.1016/j.quageo.2009.12.001. 6.6

Rackebrandt, N., H. Kuhnert, J. Groeneveld, and T. Bickert (2011), Persisting maximum Agulhas leakage during MIS 14 indicated by massive Ethmodiscus oozes in the subtropical South Atlantic, *Paleoceanography*, *26*(3), doi:https://doi.org/10.1029/2010PA001990, _eprint: https://agupubs.onlinelibrary.wiley.com/doi/pdf/10.1029/2010PA001990. 6.6

Rackow, T., C. Wesche, R. Timmermann, H. H. Hellmer, S. Juricke, and T. Jung (2017), A simulation of small to giant Antarctic iceberg evolution: Differential impact on climatology estimates, *Journal of Geophysical Research: Oceans*, *122*(4), 3170–3190, doi:10.1002/2016JC012513, _eprint: https://onlinelibrary.wiley.com/doi/pdf/10.1002/2016JC012513. 6.6

Rahmstorf, S. (2002), Ocean circulation and climate during the past 120,000 years, *Nature*, *419*(6903), 207–214, doi:10.1038/nature01090, publisher: Nature Publishing Group. 1

Raymo, M. E., and P. Huybers (2008), Unlocking the mysteries of the ice ages, *Nature*, *451*(7176), 284–285, doi:10.1038/nature06589, number: 7176 Publisher: Nature Publishing Group. 6.6

Recasens, C., D. Ariztegui, C. Gebhardt, C. Gogorza, T. Haberzettl, A. Hahn, P. Kliem, A. Lisé-Pronovost, A. Lücke, N. Maidana, et al. (2012), New insights into paleoenvironmental changes in laguna potrok aike, southern patagonia, since the late pleistocene: the pasado multiproxy record, *The Holocene*, *22*(11), 1323–1335. 6.3

Rigalleau, V., F. Lamy, N. Ruggieri, H. Sadatzki, H. W. Arz, S. Barker, L. Lembke-Jene, A. Wegwerth, G. Knorr, I. M. Venancio, T. M. L. Pinho, R. Tiedemann, and G. Winckler (In review), Persistent interhemispheric link of the antarctic circumpolar current millennial-scale variability over the last 790 kyr. 6.2, 6.4, 6.2, 6.4, 6.6, 6.6, 6.7, 6.6, 7.4

Rintoul, S. R. (2018), The global influence of localized dynamics in the Southern Ocean, *Nature*, *558*(7709), 209–218, doi:10.1038/s41586-018-0182-3. 2.2, 3.2, 5.2, 5.4, 5.4, 6.3, 7.3, 7.5

Rodrigues, T., M. Alonso-García, D. A. Hodell, M. Rufino, F. Naughton, J. O. Grimalt, A. H. L. Voelker, and F. Abrantes (2017), A 1-Ma record of sea surface temperature and extreme cooling events in the North Atlantic: A perspective from the Iberian Margin, *Quaternary Science Reviews*, *172*, 118–130, doi:10.1016/j.quascirev.2017.07.004. 7.5

Romero, O., and F. Schmieder (2006), Occurrence of thick *Ethmodiscus* oozes associated with a terminal Mid-Pleistocene Transition event in the oligotrophic subtropical South Atlantic, *Palaeogeography, Palaeoclimatology, Palaeoecology*, *235*(4), 321–329, doi:10.1016/j.palaeo.2005.10.026. 7.5

Rommerskirchen, F., A. Plader, G. Eglinton, Y. Chikaraishi, and J. Rullkötter (2006), Chemotaxonomic significance of distribution and stable carbon isotopic composition of long-chain alkanes and alkan-1-ols in C4 grass waxes, *Organic Geochemistry*, *37*(10), 1303–1332, doi:10.1016/j.orggeochem.2005.12.013. 4.1

Rosell-Melé, A. (1998), Interhemispheric appraisal of the value of alkenone indices as temperature and salinity proxies in high-latitude locations, *Paleoceanography*, *13*(6), 694–703, doi:10.1029/98PA02355, _eprint: https://onlinelibrary.wiley.com/doi/pdf/10.1029/98PA02355. 4.2

Rosell-Melé, A., E. Bard, K. C. Emeis, J. O. Grimalt, P. Müller, R. Schneider, I. Bouloubassi, B. Epstein, K. Fahl, A. Fluegge, K. Freeman, M. GoñI, U. Güntner, D. Hartz, S. Hellebust, T. Herbert, M. Ikehara, R. Ishiwatari, K. Kawamura, F. Kenig, J. de Leeuw, S. Lehman, L. Mejanelle, N. Ohkouchi, R. D. Pancost, C. Pelejero, F. Prahl, J. Quinn, J. F. Rontani, F. Rostek, J. RullköTter, J. Sachs, T. Blanz, K. Sawada, D. Schulz-Bull, E. Sikes, C. Sonzogni, Y. Ternois, G. Versteegh, J. K.

Volkman, and S. Wakeham (2001), Precision of the current methods to measure the alkenone proxy U37K' and absolute alkenone abundance in sediments: Results of an interlaboratory comparison study, *Geochemistry, Geophysics, Geosystems*, *2*, 1046–28, doi:10.1029/2000GC000141, aDS Bibcode: 2001GGG.....2.1046R. 4.2

Rosell-Melé, A., E. Jansen, and M. Weinelt (2002), Appraisal of a molecular approach to infer variations in surface ocean freshwater inputs into the North Atlantic during the last glacial, *Global and Planetary Change*, *34* (3), 143–152, doi:10.1016/S0921-8181(02) 00111-X. 1, 7.2

Ruddiman, W. F. (2017), *Plows, plagues, and petroleum: how humans took control of climate*, Princeton University Press, iSBN: 9780691173214. (document)

Ruddiman, W. F., M. E. Raymo, D. G. Martinson, B. M. Clement, and J. Backman (1989), Pleistocene evolution: Northern hemisphere ice sheets and North Atlantic Ocean, *Paleoceanography*, *4* (4), 353–412, doi:10.1029/PA004i004p00353, _eprint: https://onlinelibrary.wiley.com/doi/pdf/10.1029/PA004i004p00353. 6.8

Saavedra-Pellitero, M., K.-H. Baumann, J. Ullermann, and F. Lamy (2017a), Marine Isotope Stage 11 in the Pacific sector of the Southern Ocean; a coccolithophore perspective, *Quaternary Science Reviews*, *158*, 1–14, doi:10.1016/j.quascirev.2016.12.020. 7.5

Saavedra-Pellitero, M., K.-H. Baumann, F. Lamy, and P. Köhler (2017b), Coccolithophore variability across Marine Isotope Stage 11 in the Pacific sector of the Southern Ocean and its potential impact on the carbon cycle: SO MIS 11 Coccolithophore Variability, *Paleoceanography*, *32* (8), 864–880, doi:10.1002/2017PA003156. 7.5

Sabine, C. L., R. A. Feely, N. Gruber, R. M. Key, K. Lee, J. L. Bullister, R. Wanninkhof, C. S. Wong, D. W. R. Wallace, B. Tilbrook, F. J. Millero, T.-H. Peng, A. Kozyr, T. Ono, and A. F. Rios (2004), The Oceanic Sink for Anthropogenic CO2, *Science*, *305* (5682), 367–371, doi:10.1126/science.1097403, publisher: American Association for the Advancement of Science. 3.2, 5.2

Sachse, D., J. Radke, and G. Gleixner (2006), D values of individual n-alkanes from terrestrial plants along a climatic gradient – Implications for the sedimentary biomarker record, *Organic Geochemistry*, *37* (4), 469–483, doi:10.1016/j.orggeochem.2005.12.003. 6.6

Schaefer, J. M., G. H. Denton, D. J. A. Barrell, S. Ivy-Ochs, P. W. Kubik, B. G. Andersen, F. M. Phillips, T. V. Lowell, and C. Schlüchter (2006), Near-Synchronous Interhemispheric Termination of the Last Glacial Maximum in Mid-Latitudes, *Science*, *312*(5779), 1510–1513, doi:10.1126/science.1122872, publisher: American Association for the Advancement of Science. 6.2, 7.5

Schneider-Mor, A., R. Yam, C. Bianchi, M. Kunz-Pirrung, R. Gersonde, and A. Shemesh (2005), Diatom stable isotopes, sea ice presence and sea surface temperature records of the past 640 ka in the Atlantic sector of the Southern Ocean, *Geophysical Research Letters*, *32*(10), doi:10.1029/2005GL022543, _eprint: https://onlinelibrary.wiley.com/doi/pdf/10.1029/2005GL022543. 7.4

Schouten, S., E. C. Hopmans, E. Schefuß, and J. S. S. Damsté (2002), Distributional variations in marine crenarchaeotal membrane lipids: a new tool for reconstructing ancient sea water temperatures?, *Earth and Planetary Science Letters*, *204*(1), 265–274, doi:https://doi.org/10.1016/S0012-821X(02)00979-2. 4.3

Schouten, S., C. Huguet, E. C. Hopmans, M. V. M. Kienhuis, and J. S. S. Damsté (2007), Analytical methodology for TEX86 paleothermometry by high-performance liquid chromatography/atmospheric pressure chemical ionization-mass spectrometry, *Analytical Chemistry*, *79*(7), 2940–2944, doi:10.1021/ac062339v. 4.5

Schouten, S., E. C. Hopmans, and J. S. Sinninghe Damsté (2013a), The organic geochemistry of glycerol dialkyl glycerol tetraether lipids: A review, *Organic Geochemistry*, *54*, 19–61, doi:10.1016/j.orggeochem.2012.09.006. 4.3, 6.4

Schouten, S., E. C. Hopmans, A. Rosell-Melé, A. Pearson, P. Adam, T. Bauersachs, E. Bard, S. M. Bernasconi, T. S. Bianchi, J. J. Brocks, L. T. Carlson, I. S. Castañeda, S. Derenne, A. D. Selver, K. Dutta, T. Eglinton, C. Fosse, V. Galy, K. Grice, K.-U. Hinrichs, Y. Huang, A. Huguet, C. Huguet, S. Hurley, A. Ingalls, G. Jia, B. Keely, C. Knappy, M. Kondo, S. Krishnan, S. Lincoln, J. Lipp, K. Mangelsdorf, A. Martínez-García, G. Ménot, A. Mets, G. Mollenhauer, N. Ohkouchi, J. Ossebaar, M. Pagani, R. D. Pancost, E. J. Pearson, F. Peterse, G.-J. Reichart, P. Schaeffer, G. Schmitt, L. Schwark, S. R. Shah, R. W. Smith, R. H. Smittenberg, R. E. Summons, Y. Takano, H. M. Talbot, K. W. R. Taylor, R. Tarozo, M. Uchida, B. E. van Dongen, B. A. S. Van Mooy, J. Wang, C. Warren, J. W. H. Weijers, J. P. Werne, M. Woltering, S. Xie, M. Yamamoto, H. Yang, C. L. Zhang, Y. Zhang, M. Zhao, and J. S. S. Damsté (2013b), An interlaboratory study of TEX $_{86}$ and BIT analysis of sediments, extracts, and standard mixtures: TEX $_{86}$ and BIT Index Round Robin, *Geochemistry, Geophysics, Geosystems*, *14*(12), 5263–5285, doi:10.1002/2013GC004904. 4.3

Schulz, H.-M., A. Schöner, and K.-C. Emeis (2000), Long-chain alkenone patterns in the Baltic sea—an ocean-freshwater transition, *Geochimica et Cosmochimica Acta*, *64*(3), 469–477, doi:10.1016/S0016-7037(99)00332-4. 7.6

Schulz, M., W. H. Berger, M. Sarnthein, and P. M. Grootes (1999), Amplitude variations of 1470-year climate oscillations during the last 100,000 years linked to fluctuations of continental ice mass, *Geophysical Research Letters*, *26*(22), 3385–3388, doi:10.1029/1999GL006069, _eprint: https://onlinelibrary.wiley.com/doi/pdf/10.1029/1999GL006069. 1

Seki, O., K. Kawamura, T. Sakamoto, M. Ikehara, T. Nakatsuka, and M. Wakatsuchi (2005), Decreased surface salinity in the Sea of Okhotsk during the last glacial period estimated from alkenones, *Geophysical Research Letters*, *32*(8), doi:10.1029/2004GL022177, _eprint: https://onlinelibrary.wiley.com/doi/pdf/10.1029/2004GL022177. 7.5, 7.5

Sepúlveda, J., S. Pantoja, K. A. Hughen, S. Bertrand, D. Figueroa, T. León, N. J. Drenzek, and C. Lange (2009), Late Holocene sea-surface temperature and precipitation variability in northern Patagonia, Chile (Jacaf Fjord, 44°S), *Quaternary Research*, *72*(3), 400–409, doi:10.1016/j.yqres.2009.06.010. 4.1, 6.2, 6.6, 6.6

Shackleton, N. J. (2000), The 100,000-Year Ice-Age Cycle Identified and Found to Lag Temperature, Carbon Dioxide, and Orbital Eccentricity, *Science*, *289*(5486), 1897–1902, doi:10.1126/science.289.5486.1897. 5.4

Shi, J.-R., L. D. Talley, S.-P. Xie, W. Liu, and S. T. Gille (2020), Effects of Buoyancy and Wind Forcing on Southern Ocean Climate Change, *Journal of Climate*, *33*(23), 10,003–10,020, doi:10.1175/JCLI-D-19-0877.1, place: Boston MA, USA Publisher: American Meteorological Society. 5.4

Shi, J.-R., L. D. Talley, S.-P. Xie, Q. Peng, and W. Liu (2021), Ocean warming and accelerating Southern Ocean zonal flow, *Nature Climate Change*, *11*(12), 1090–1097, doi:10.1038/s41558-021-01212-5. 5.2, 5.4

Shulmeister, J., G. D. Thackray, T. M. Rittenour, D. Fink, and N. R. Patton (2019), The timing and nature of the last glacial cycle in New Zealand, *Quaternary Science Reviews*, *206*, 1–20, doi:10.1016/j.quascirev.2018.12.020. 6.2

Siegenthaler, U., T. F. Stocker, E. Monnin, D. Lüthi, J. Schwander, B. Stauffer, D. Raynaud, J.-M. Barnola, H. Fischer, V. Masson-Delmotte, and J. Jouzel (2005), Stable Carbon Cycle Climate Relationship During the Late Pleistocene, *Science*, *310*(5752), 1313–1317, doi:10.1126/science.1120130, publisher: American Association for the Advancement of Science. 6.6

Sigman, D. M., F. Fripiat, A. S. Studer, P. C. Kemeny, A. Martínez-García, M. P. Hain, X. Ai, X. Wang, H. Ren, and G. H. Haug (2021), The Southern Ocean during the ice ages: A review of the Antarctic surface isolation hypothesis, with comparison to the North Pacific, *Quaternary Science Reviews*, *254*, 106,732, doi:10.1016/j.quascirev.2020.106732. 2.2, 5.4, 5.4, 7.2, 7.3, 7.5

Sikes, E. L., and M.-A. Sicre (2002), Relationship of the tetra-unsaturated C37 alkenone to salinity and temperature: Implications for paleoproxy applications, *Geochemistry, Geophysics, Geosystems*, *3*(11), 1–11, doi:10.1029/2002GC000345, _eprint: https://onlinelibrary.wiley.com/doi/pdf/10.1029/2002GC000345. 7.2

Sikes, E. L., J. K. Volkman, L. G. Robertson, and J.-J. Pichon (1997), Alkenones and alkenes in surface waters and sediments of the Southern Ocean: Implications for paleotemperature estimation in polar regions, *Geochimica et Cosmochimica Acta*, *61*(7), 1495–1505, doi:10.1016/S0016-7037(97)00017-3. 4.2

Simoneit, B. R. T., R. Chester, and G. Eglinton (1977), Biogenic lipids in particulates from the lower atmosphere over the eastern Atlantic, *Nature*, *267*(5613), 682–685, doi:10.1038/267682a0. 6.6

Skinner, L. C., S. Fallon, C. Waelbroeck, E. Michel, and S. Barker (2010), Ventilation of the Deep Southern Ocean and Deglacial CO2 Rise, *Science*, *328*(5982), 1147–1151, doi:10.1126/science.1183627, publisher: American Association for the Advancement of Science. 5.4, 7.5

Spratt, R. M., and L. E. Lisiecki (2016), A Late Pleistocene sea level stack, *Climate of the Past*, *12*(4), 1079–1092, doi:10.5194/cp-12-1079-2016, publisher: Copernicus GmbH. 6.4, 6.6, 6.7, 6.6, 6.8

Srokosz, M. A., and H. L. Bryden (2015), Observing the Atlantic Meridional Overturning Circulation yields a decade of inevitable surprises, *Science*, *348*(6241), 1255,575, doi:10.1126/science.1255575, publisher: American Association for the Advancement of Science. 2.2, 5.4

Starr, A., I. R. Hall, S. Barker, T. Rackow, X. Zhang, S. R. Hemming, H. J. L. van der Lubbe, G. Knorr, M. A. Berke, G. R. Bigg, A. Cartagena-Sierra, F. J. Jiménez-Espejo, X. Gong, J. Gruetzner, N. Lathika, L. J. LeVay, R. S. Robinson, and M. Ziegler (2021), Antarctic icebergs reorganize ocean circulation during Pleistocene glacials, *Nature*, *589*(7841), 236–241, doi:10.1038/s41586-020-03094-7, publisher: Nature Publishing Group. 6.6

Stocker, T. F. (1998), The Seesaw Effect, *Science*, *282*(5386), 61–62, doi:10.1126/science.282.5386.61, publisher: American Association for the Advancement of Science. 5.2

Strub, P. T., C. James, V. Montecino, J. A. Rutllant, and J. L. Blanco (2019), Ocean circulation along the southern Chile transition region (38°–46°S): Mean, seasonal and interannual variability, with a focus on 2014–2016, *Progress in Oceanography*, *172*, 159–198, doi:10.1016/j.pocean.2019.01.004. 7.5

Struve, T., K. Pahnke, F. Lamy, M. Wengler, P. Böning, and G. Winckler (2020), A circumpolar dust conveyor in the glacial Southern Ocean, *Nature Communications*, *11*(1), 5655, doi:10.1038/s41467-020-18858-y. 2.2, 6.2

Sugden, D. E., R. D. McCulloch, A. J.-M. Bory, and A. S. Hein (2009), Influence of Patagonian glaciers on Antarctic dust deposition during the last glacial period, *Nature Geoscience*, *2*(4), 281–285, doi:10.1038/ngeo474. 2.2, 6.2, 6.6, 6.6

Sun, Y., J. F. McManus, S. C. Clemens, X. Zhang, H. Vogel, D. A. Hodell, F. Guo, T. Wang, X. Liu, and Z. An (2021), Persistent orbital influence on millennial climate variability through the Pleistocene, *Nature Geoscience*, *14*(11), 812–818, doi:10.1038/s41561-021-00794-1. 5.2, 5.3

Talley, L. D. (2013), Closure of the Global Overturning Circulation Through the Indian, Pacific, and Southern Oceans: Schematics and Transports, *Oceanography*, *issue_volume*. 2.2, 2.4, 2.2

Tapia, R., S. L. Ho, S. Núñez-Ricardo, M. Marchant, F. Lamy, and D. Hebbeln (2021), Increased Marine Productivity in the Southern Humboldt Current System During MIS 2–4 and 10–11, *Paleoceanography and Paleoclimatology*, *36*(4), doi:10.1029/2020PA004066. 2.2, 6.2, 7.5, 7.5

Tobal, J. E., E. G. Morabito, C. M. Terrizzano, R. Zech, B. Colavitto, J. Struck, M. Christl, and M. C. Ghiglione (2021), Quaternary landscape evolution of patagonia at the Chilean Triple Junction: Climate and tectonic forcings, *Quaternary Science Reviews*, *261*, 106,960, doi:10.1016/j.quascirev.2021.106960. 6.6, 6.6

Toggweiler, J. R. (2008), Origin of the 100,000-year timescale in Antarctic temperatures and atmospheric CO2, *Paleoceanography*, *23*(2), doi:10.1029/2006PA001405, _eprint: https://onlinelibrary.wiley.com/doi/pdf/10.1029/2006PA001405. 2.1

Toggweiler, J. R., J. L. Russell, and S. R. Carson (2006), Midlatitude westerlies, atmospheric CO2, and climate change during the ice ages, *Paleoceanography*, *21*(2), doi:10.1029/2005PA001154, publisher: John Wiley & Sons, Ltd. 5.2, 5.4, 5.4

Toyos, M. H., F. Lamy, C. B. Lange, L. Lembke-Jene, M. Saavedra-Pellitero, O. Esper, and H. W. Arz (2020), Antarctic Circumpolar Current Dynamics at the Pacific Entrance to the Drake Passage Over the Past 1.3 Million Years, *Paleoceanography and Paleoclimatology*, *35*(7), doi:10.1029/2019PA003773. 2.2, 5.2, 5.3, 5.2, 5.3, 5.4, 5.5, 7.5

Tzedakis, P. C., H. Hooghiemstra, and H. Pälike (2006), The last 1.35 million years at Tenaghi Philippon: revised chronostratigraphy and long-term vegetation trends, *Quaternary Science Reviews*, *25*(23), 3416–3430, doi:10.1016/j.quascirev.2006.09.002. 6.6, 6.8

Volkman, J. K. (2006), Lipid Markers for Marine Organic Matter, in *Marine Organic Matter: Biomarkers, Isotopes and DNA*, edited by J. K. Volkman, pp. 27–70, Springer, Berlin, Heidelberg, doi:10.1007/698_2_002. 4.1

Vollmar, N. M., K.-H. Baumann, M. Saavedra-Pellitero, and I. Hernández-Almeida (2022), Distribution of coccoliths in surface sediments across the Drake Passage and calcification of *Emiliania huxleyi* morphotypes, *Biogeosciences*, *19*(3), 585–612, doi: 10.5194/bg-19-585-2022, publisher: Copernicus GmbH. 3.2

Wang, K. J., Y. Huang, M. Majaneva, S. T. Belt, S. Liao, J. Novak, T. R. Kartzinel, T. D. Herbert, N. Richter, and P. Cabedo-Sanz (2021), Group 2i Isochrysidales produce characteristic alkenones reflecting sea ice distribution, *Nature Communications*, *12*(1), 15, doi:10.1038/s41467-020-20187-z. 1, 4.2, 7.2, 7.5

Warren, C. R., and D. E. Sugden (1993), The Patagonian Icefields: A Glaciological Review, *Arctic and Alpine Research*, *25*(4), 316, doi:10.2307/1551915. 6.3

Weber, M. E., P. U. Clark, G. Kuhn, A. Timmermann, D. Sprenk, R. Gladstone, X. Zhang, G. Lohmann, L. Menviel, M. O. Chikamoto, T. Friedrich, and C. Ohlwein (2014), Millennial-scale variability in Antarctic ice-sheet discharge during the last deglaciation, *Nature*, *510*(7503), 134–138, doi:10.1038/nature13397. 6.6, 6.6

Weijer, W., W. Cheng, O. A. Garuba, A. Hu, and B. T. Nadiga (2020), CMIP6 Models Predict Significant 21st Century Decline of the Atlantic Meridional Overturning Circulation, *Geophysical Research Letters*, *47*(12), e2019GL086,075, doi:10.1029/2019GL086075, _eprint: https://onlinelibrary.wiley.com/doi/pdf/10.1029/2019GL086075. 5.4

Weijers, J. W. H., E. Schefuss, S. Schouten, and J. S. S. Damste (2007), Coupled Thermal and Hydrological Evolution of Tropical Africa over the Last Deglaciation, *Science*, *315*(5819), 1701–1704, doi:10.1126/science.1138131. 4.3

Weis, J., Z. Chase, C. Schallenberg, P. G. Strutton, A. R. Bowie, and S. L. Fiddes (2024), One-third of Southern Ocean productivity is supported by dust deposition, *Nature*, *629*(8012), 603–608, doi:10.1038/s41586-024-07366-4, publisher: Nature Publishing Group. 2.2, 6.2

Weiss, B. (1982), The decline of Late Bronze Age civilization as a possible response to climatic change, *Climatic Change*, *4*(2), 173–198, doi:10.1007/BF00140587. (document)

Winckler, G., R. F. Anderson, M. Q. Fleisher, D. McGee, and N. Mahowald (2008), Covariant Glacial-Interglacial Dust Fluxes in the Equatorial Pacific and Antarctica, *Science*, *320*(5872), 93–96, doi:10.1126/science.1150595, publisher: American Association for the Advancement of Science. 6.6

Wolff, E. W., H. Fischer, F. Fundel, U. Ruth, B. Twarloh, G. C. Littot, R. Mulvaney, R. Röthlisberger, M. De Angelis, C. F. Boutron, M. Hansson, U. Jonsell, M. A. Hutterli, F. Lambert, P. Kaufmann, B. Stauffer, T. F. Stocker, J. P. Steffensen, M. Bigler, M. L. Siggaard-Andersen, R. Udisti, S. Becagli, E. Castellano, M. Severi, D. Wagenbach, C. Barbante, P. Gabrielli, and V. Gaspari (2006), Southern Ocean sea-ice extent, productivity and iron flux over the past eight glacial cycles, *Nature*, *440*(7083), 491–496, doi:10.1038/nature04614. 6.7, 6.6, 6.8, 7.5

Wu, L., D. J. Wilson, R. Wang, X. Yin, Z. Chen, W. Xiao, and M. Huang (2020), Evaluating Zr/Rb Ratio From XRF Scanning as an Indicator of Grain-Size Variations of Glaciomarine Sediments in the Southern Ocean, *Geochemistry, Geophysics, Geosystems*, *21*(11), doi:10.1029/2020GC009350. 5.5

Wu, S., G. Kuhn, B. Diekmann, L. Lembke-Jene, R. Tiedemann, X. Zheng, S. Ehrhardt, H. W. Arz, and F. Lamy (2019), Surface sediment characteristics related to provenance and ocean circulation in the Drake Passage sector of the Southern Ocean, *Deep Sea Research Part I: Oceanographic Research Papers*, *154*, 103,135, doi:10.1016/j.dsr.2019.103135. 3.2

Wu, S., L. Lembke-Jene, F. Lamy, H. W. Arz, N. Nowaczyk, W. Xiao, X. Zhang, H. C. Hass, J. Titschack, X. Zheng, J. Liu, L. Dumm, B. Diekmann, D. Nürnberg, R. Tiedemann, and G. Kuhn (2021), Orbital- and millennial-scale Antarctic Circumpolar Current variability in Drake Passage over the past 140,000 years, *Nature Communications*, *12*(1), 3948, doi:10.1038/s41467-021-24264-9. 1, 2.2, 5.2, 5.3, 5.3, 5.4, 5.4, 5.4, 5.5

Yin, Q. (2013), Insolation-induced mid-Brunhes transition in Southern Ocean ventilation and deep-ocean temperature, *Nature*, *494*(7436), 222–225, doi:10.1038/nature11790, number: 7436 Publisher: Nature Publishing Group. 2.1, 5.4, 7.2, 7.5

Zemp, M., M. Huss, E. Thibert, N. Eckert, R. McNabb, J. Huber, M. Barandun, H. Machguth, S. U. Nussbaumer, I. Gärtner-Roer, L. Thomson, F. Paul, F. Maussion, S. Kutuzov, and J. G. Cogley (2019), Global glacier mass changes and their contributions to sea-level rise from 1961 to 2016, *Nature*, *568*(7752), 382–386, doi:10.1038/s41586-019-1071-0. 6.3

Zhang, X., G. Lohmann, G. Knorr, and C. Purcell (2014), Abrupt glacial climate shifts controlled by ice sheet changes, *Nature*, *512*(7514), 290–294, doi:10.1038/nature13592. 1

Zheng, Q., R. Bingham, and O. Andrews (2023), Using Sea Level to Determine the Strength, Structure and Variability of the Cape Horn Current, *Geophysical Research Letters*, *50*(21), e2023GL105,033, doi:10.1029/2023GL105033, _eprint: https://onlinelibrary.wiley.com/doi/pdf/10.1029/2023GL105033. 3.2, 3.2, 8

Zonneveld, K. A. F., K. Harper, A. Klügel, L. Chen, G. De Lange, and G. J. M. Versteegh (2024), Climate change, society, and pandemic disease in Roman Italy between 200 BCE and 600 CE, *Science Advances*, *10*(4), eadk1033, doi:10.1126/sciadv.adk1033, publisher: American Association for the Advancement of Science. (document)

Acknowledgements

To Frank, a friend and mentor, for giving the freedom to explore the world and to think both profound and trivial matters (always related to the Southern Hemisphere!). I am proud to have learned from you,

To Nicoletta, for your sincerity and kindness. Your "pressure" saved me from procrastination. Without you both, this thesis could not have been written, and I would have missed the chance to say "*Ich habe Fertig*",

To Ralf, notably for letting me board PS128 with you. Your love of visiting France in a campervan and your passion for science are truly inspiring.

To Gisela, Carina and Helge, for answering my questions with enthusiasm around brunch, dinner, sauna and Campari sessions,

To MarGeo, for welcoming me as a family. The list is long, but each of you contributed to this work. A perfect mix of administrative support and scientific endeavor, from you I have witnessed German efficiency (apart from Deutsch Bahn),

To Michèlle, Henrik and Julia, the elders, for your kind encouragements,

To the sedimentary archive U1542, every morning I woke up eager to work with you,

To Dampfloks und Freunde von fiets; running and paddling are better with buddies,

Aux copains d'enfance et à ceux rencontrés en chemin,

À la famille partie et à celle qui arrive,

Of course, to Kristine for much more than providing vitamin D,

Et à Jacko, Laura, Sébastien, Grand maman et Maman pour tout le reste,

Merci !!